



**HAL**  
open science

# Matériaux conducteurs mixtes ioniques et électroniques pour le couplage oxydant du méthane

Marie Rochoux

► **To cite this version:**

Marie Rochoux. Matériaux conducteurs mixtes ioniques et électroniques pour le couplage oxydant du méthane. Catalyse. Université Claude Bernard - Lyon I, 2014. Français. NNT : 2014LYO10234 . tel-01127436

**HAL Id: tel-01127436**

**<https://theses.hal.science/tel-01127436>**

Submitted on 7 Mar 2015

**HAL** is a multi-disciplinary open access archive for the deposit and dissemination of scientific research documents, whether they are published or not. The documents may come from teaching and research institutions in France or abroad, or from public or private research centers.

L'archive ouverte pluridisciplinaire **HAL**, est destinée au dépôt et à la diffusion de documents scientifiques de niveau recherche, publiés ou non, émanant des établissements d'enseignement et de recherche français ou étrangers, des laboratoires publics ou privés.

# THESE DE L'UNIVERSITE DE LYON

Présentée devant

L'UNIVERSITE CLAUDE BERNARD LYON 1

École doctorale de Chimie

Pour l'obtention du **DIPLOME DE DOCTORAT**

(arrêté du 7 août 2006)

soutenue publiquement le 24 octobre 2014

par

**Marie ROCHOUX**

## **Matériaux conducteurs mixtes ioniques et électroniques pour le couplage oxydant du méthane**

Directeur de thèse : Dr. David FARRUSSENG

Co-directeur : Dr. Yves SCHUURMAN

<b>Pr. Mélaz TAYAKOUT-FAYOLLE</b>	Enseignant-Chercheur (UCBL, Lyon1)
<b>Dr. Elisabeth SIEBERT</b>	Directeur de recherche (LEPMI, Grenoble) – <u>rapporteur</u>
<b>Pr. Henny BOUWMEESTER</b>	Associate Professor (University of Twente, Netherlands)– <u>rapporteur</u>
<b>Dr. Jean-Marc BASSAT</b>	Directeur de recherche (ICMCB, Bordeaux)
<b>Dr. Yves SCHUURMAN</b>	Directeur de recherche (IRCELyon, Villeurbanne)
<b>Dr. David FARRUSSENG</b>	Directeur de recherche (IRCELyon, Villeurbanne)



# UNIVERSITE CLAUDE BERNARD - LYON 1

## Président de l'Université

**M. François-Noël GILLY**

Vice-président du Conseil d'Administration

M. le Professeur Hamda BEN HADID

Vice-président du Conseil des Etudes et de la Vie Universitaire

M. le Professeur Philippe LALLE

Vice-président du Conseil Scientifique

M. le Professeur Germain GILLET

Directeur Général des Services

M. Alain HELLEU

## ***COMPOSANTES SANTE***

Faculté de Médecine Lyon Est – Claude Bernard

Directeur : M. le Professeur J. ETIENNE

Faculté de Médecine et de Maïeutique Lyon Sud – Charles Mérieux

Directeur : Mme la Professeure C. BURILLON

Faculté d'Odontologie

Directeur : M. le Professeur D. BOURGEOIS

Institut des Sciences Pharmaceutiques et Biologiques

Directeur : Mme la Professeure C. VINCIGUERRA

Institut des Sciences et Techniques de la Réadaptation

Directeur : M. le Professeur Y. MATILLON

Département de formation et Centre de Recherche en Biologie Humaine

Directeur : Mme. la Professeure A-M. SCHOTT

## ***COMPOSANTES ET DEPARTEMENTS DE SCIENCES ET TECHNOLOGIE***

Faculté des Sciences et Technologies

Directeur : M. F. DE MARCHI

Département Biologie

Directeur : M. le Professeur F. FLEURY

Département Chimie Biochimie

Directeur : Mme Caroline FELIX

Département GEP

Directeur : M. Hassan HAMMOURI

Département Informatique

Directeur : M. le Professeur S. AKKOUCHE

Département Mathématiques

Directeur : M. Georges TOMANOV

Département Mécanique

Directeur : M. le Professeur H. BEN HADID

Département Physique

Directeur : M. Jean-Claude PLENET

UFR Sciences et Techniques des Activités Physiques et Sportives

Directeur : M. Y. VANPOULLE

Observatoire des Sciences de l'Univers de Lyon

Directeur : M. B. GUIDERDONI

Polytech Lyon

Directeur : M. P. FOURNIER

Ecole Supérieure de Chimie Physique Electronique

Directeur : M. G. PIGNAULT

Institut Universitaire de Technologie de Lyon 1

Directeur : M. C. VITON

Ecole Supérieure du Professorat et de l'Education

Directeur : M. A. MOUGNIOTTE

Institut de Science Financière et d'Assurances

Directeur : M. N. LEBOISNE



---

## Résumé en français

Le couplage oxydant du méthane (OCM) permet la transformation directe du méthane en éthylène ( $C_2$ ). A ce jour, le procédé catalytique n'atteint pas les critères requis de sélectivité et de rendement. La présence d'oxygène gazeux à haute température ( $T > 700^\circ C$ ) favorise l'oxydation totale. L'utilisation d'un réacteur à membrane (RM) dense, composé de matériaux conducteurs ioniques et électroniques limite la présence de  $O_2(g)$  dans le compartiment de réaction améliorant ainsi la sélectivité en  $C_2$ . Cette thèse a pour cadre le développement de membranes catalytiques ayant un flux d'oxygène assez élevé pour atteindre une conversion supérieure à 25% et dont le revêtement catalytique entraîne une sélectivité en  $C_2$  à 80%.

Une méthode innovante, basée sur une approche microcinétique, a été développée pour déterminer le flux d'oxygène à travers les membranes à partir de mesures sur les poudres correspondantes (échange isotopique et ATG). Les constantes d'adsorption et de diffusion obtenues sont ensuite intégrées dans une équation de flux simulant la semi-perméabilité. Cette méthodologie, validée sur trois matériaux :  $Ba_{0.5}Sr_{0.5}Co_{0.8}Fe_{0.2}O_{3-\delta}$  (BSCF),  $La_{0.6}Sr_{0.4}Co_{0.2}Fe_{0.8}O_{3-\delta}$  et  $Ba_{0.95}La_{0.05}FeO_{3-\delta}$ , permettra d'accélérer la découverte de nouveaux matériaux conducteurs d'oxygène. Les tests d'OCM ont été réalisés sur une membrane BSCF modifiée en surface par une couche mince catalytique. Deux catalyseurs ont été sélectionnés :  $Mn/NaWO_4$  très sélectif et  $LaSr/CaO$  très actif. Le rendement en réacteur membranaire est limité à 6%. Une analyse critique a été réalisée afin de concevoir une géométrie de réacteur membranaire optimale pour cette réaction.

---

### Titre en anglais-English title :

Mixed ionic and electronic conducting material for the oxidative coupling of methane

---

### Résumé en anglais– English summary:

The oxidative coupling of methane (OCM) allowed the direct transformation of methane into ethylene ( $C_2$ ). Until now, the catalytic process does not reach the required criteria of selectivity and yield. The presence of gaseous oxygen at high temperature ( $T > 700^\circ C$ ) favors the total oxidation. The use of a dense membrane reaction (MR), made of mixed ionic and electronic materials, limits the gaseous oxygen in the reaction compartment and thus improve the  $C_2$  selectivity. The goal of this PhD is to develop catalytic membranes exhibiting a flux high enough to reach a conversion higher than 25% and of which the catalytic coating leads to a  $C_2$  selectivity of 80%.

An innovative method, based on a microkinetic approach, has been developed to determine the oxygen flux across a membrane from measurements on corresponding powders (isotopic exchange and TGA). The adsorption and diffusion constants obtained are then introduced in the flux equation simulating the semi-permeability. The methodology, validated on three materials:  $Ba_{0.5}Sr_{0.5}Co_{0.8}Fe_{0.2}O_{3-\delta}$  (BSCF),  $La_{0.6}Sr_{0.4}Co_{0.2}Fe_{0.8}O_{3-\delta}$  et  $Ba_{0.95}La_{0.05}FeO_{3-\delta}$ , will allow to accelerate the discovery of new oxygen conducting. The OCM tests have been achieved on BSCF membrane modified by a thin layer of catalyst. Two catalysts have been selected:  $Mn/NaWO_4$  highly selective and  $LaSr/CaO$  highly active. The yield in membrane reactor cannot overstep 6%. A critical analysis has been achieved in order to design an optimal membrane reactor geometry for this reaction.

---

### Discipline :

Catalyse

---

### Mots-clés :

Couplage oxydant du méthane, réacteur membranaire, pérovskite, SSITKA, ATG, modélisation du flux

---

### Intitulé du laboratoire :

Institut de Recherches sur la Catalyse et l'Environnement de Lyon, UMR 5256,

2, av. A. Einstein 69626 VILLEURBANNE



Les travaux relatifs à l'élaboration de cette thèse ont été menés à

Institut de Recherches sur la Catalyse et l'Environnement de Lyon

(IRCELYON)

UMR CNRS 5256

2, avenue A. Einstein,

69626 VILLEURBANNE



Au sein du Groupe INGENIERIE

Dans le cadre du projet



# Mixed Ionic and Electronic conducting Materials for the Oxidative coupling of methane

---

*An integrated project within the European Union's Seventh Framework Programme for research, technological development and demonstration under grant agreement no 263007*

---



A mes deux grands pères,



# Remerciements

---

Ce travail a été réalisé à l'Institut de Recherches sur la Catalyse et L'Environnement de Lyon (IRCELYON), Unité Mixte de Recherches 5256 CNRS-Université de Lyon 1 de septembre 2011 à août 2014. Je remercie tout d'abord la Commission Européenne qui a financé cette thèse à travers le projet CARENA.

Je tiens ensuite à remercier M. Michel Lacroix, directeur de l'IRCELYON, pour son accueil au sein de l'institut et de la mise à disposition des services scientifiques et administratifs nécessaires à ce travail.

Je voudrais également remercier Mme Elisabeth Siebert ainsi que M. Henny Bouwmeester d'avoir accepté de juger ce travail. Ainsi que Mme Mélaz Tayakout-Fayolle et M. Jean-Marc Bassat d'avoir accepté de participer à ce jury de thèse.

Je remercie tout particulièrement M. David Farrusseng, directeur de recherches à l'IRCELYON et l'encadrant de cette thèse, pour avoir eu la patience d'écouter mes idées, pour avoir réussi à les structurer et pour avoir su m'aider lorsque j'en avais besoin et m'avoir laissée me débrouiller seule quand je le souhaitais. Je voulais aussi remercier M. Yves Schuurman pour m'avoir montrée les points importants pour mener à bien mon modèle et pour m'avoir enseignée sa rigueur.

Je souhaitais également remercier Mmes Elizabeth Shotton et Anna Kroner pour l'opportunité qu'elles m'ont donnée de faire des manipulations sur un synchrotron à Diamond, Mmes Marianne Ponceau et Nicole Schoedel de Linde pour leur expertise scientifique et MM. Gregory Largiller du CEA de Grenoble et Adam Stevenson de Saint-Gobain pour la mise en forme de membrane ainsi que Mme Maria Rivas-Velazco et M. William McDonnell de Johnson Matthey (Royaume-Uni) pour leur synthèse de catalyseurs.

Je voulais ensuite remercier Mmes Laurence Burel, Bernadette Jouguet, Françoise Bosselet, Noëlle Cristin et M. Yoann Aizac pour leur expertise et leurs conseils avisés tout au long de cette thèse et surtout leur patience malgré des demandes quelques fois originales. Je voulais également remercier Gilles D'Orazio pour son aide pour la construction de réacteurs.

Je remercie Mmes Youmin Guo, Lamia Dreibine et MM. Claude Mirodatos, Thomas Serres pour leurs enseignements, leurs conseils et leurs idées pour faire avancer ce projet. Je voudrais aussi remercier MM. Emmanuel Landrison, Mehdi Bessaa et Florian Chapon pour leur support technique sans qui les petits problèmes d'appareillages auraient pu se transformer en des mois d'arrêts de manipulations.

Je voulais ensuite sincèrement remercier Mme Cécile Daniel pour sa patience et son soutien tout au long de ma thèse, et pour m'avoir permis de décompresser le midi en allant courir, nager ou tout simplement en partageant nos repas. Je tenais aussi à remercier tous les membres de l'équipe ingénierie pour leur aide et leur bonne humeur, ceux avec qui j'ai partagé mon bureau : Thomas, Fabien, Nico, Alina mais aussi Mathilde, Anaëlle, Linh, Jérôme et tous les autres.

Je voulais aussi remercier mes parents et mes deux petites sœurs qui m'ont fait confiance et qui m'ont soutenue tout au long de thèse. Je les remercie également d'avoir sincèrement essayé de comprendre mon sujet de thèse bien que le résumé de ma thèse se limite à des membranes cassées qui énervent.

Et je voulais tout particulièrement remercier Pierre pour m'avoir soutenue jusqu'à démissionner de son poste à Paris pour s'installer à Lyon. Et surtout pour m'avoir soutenue même dans les moments difficiles où ce n'était pas forcément agréable de vivre avec moi.





# Résumé

---

Les importantes réserves en gaz naturel, essentiellement constituées de méthane, rendent ce composé un substitut possible au pétrole pour la production d'éthylène. La réaction du couplage oxydant du méthane (OCM) dans un réacteur à membrane dense, composée de matériaux conducteurs ioniques et électroniques, permettrait de rendre cette réaction industrialisable grâce à une plus grande sélectivité en éthylène. Ce type de réacteur diminuerait les coûts de production en couplant OCM et séparation de l'oxygène de l'air dans un unique réacteur. De plus, cela limiterait la taille des usines de transformation du méthane.

L'intégration de l'OCM dans un réacteur membranaire a déjà été étudiée et les résultats sont prometteurs. Ces réacteurs ont été testés avec et sans catalyseur. La nécessité d'utiliser un catalyseur a été mise en avant. Cependant, le catalyseur était ajouté sous forme de lit fixe dans le compartiment réaction du réacteur. Les résultats obtenus étaient proches du lit fixe et l'intérêt d'un tel réacteur était donc perdu. En revanche, aucun réacteur composé d'une membrane dense avec une couche mince de catalyseur n'a été étudié. Il a été prouvé que ce procédé est basé sur un équilibre sensible entre les réactions de surface et les réactions en phase gazeuse et que l'oxygène activé présent sur la surface de la membrane permet la production de radicaux méthyles, intermédiaires clés de la réaction d'OCM. La conduction ionique entre la membrane et le catalyseur, tout en évitant la recombinaison d'oxygène dans la phase gaz, n'est possible qu'avec le dépôt d'une couche mince de catalyseur à la surface de la membrane. Ce concept permettrait donc d'améliorer la sélectivité de la réaction par rapport au lit fixe. L'étude présente le développement de ce type de réacteur. Le choix du matériau de la membrane constitue une partie essentielle du développement. Les matériaux utilisés sont les pérovskites qui présentent de grands flux en oxygène ionique à travers la membrane. La caractérisation des performances de ces matériaux ainsi que leur optimisation sont très compliquées et demandent de nombreux tests longs et coûteux. La première partie de ce travail est basée sur le développement d'une méthode microcinétique afin de déterminer les paramètres cinétiques régissant le transport d'oxygène à travers la membrane sur les poudres correspondantes. La méthode est basée sur le couplage d'une méthode d'analyse de l'évolution de la phase gaz lors de l'échange d'oxygène isotopique (entre l'oxygène 16 et 18) en phase stationnaire (SSITKA) et d'une méthode d'analyse thermogravimétrique. Les constantes d'adsorption, désorption et le coefficient de diffusion de l'oxygène obtenues sont ensuite intégrées dans une équation de flux tenant compte des conditions expérimentales d'utilisation de ces membranes, c'est-à-dire, la température, la pression partielle d'oxygène de part et d'autre de la membrane et l'épaisseur de cette dernière.

Cette méthodologie a été appliquée à trois différents matériaux :  $\text{Ba}_{0.5}\text{Sr}_{0.5}\text{Co}_{0.8}\text{Fe}_{0.2}\text{O}_{3-\delta}$  (BSCF),  $\text{La}_{0.6}\text{Sr}_{0.4}\text{Co}_{0.2}\text{Fe}_{0.8}\text{O}_{3-\delta}$  (LSCF) et  $\text{Ba}_{0.95}\text{La}_{0.05}\text{FeO}_{3-\delta}$  (BLF). BSCF présente le flux d'oxygène le plus élevé dans cette configuration (membrane d'environ 2 mm, température comprise entre 800 et 900°C, pression partielle de l'oxygène de 21 kPa dans le compartiment air et de 1 kPa dans le compartiment de réaction). En revanche, le flux d'oxygène dans le cas de LSCF est bien trop faible. Cette composition ne sera donc plus étudiée dans la suite du travail. BLF pourra être considérée comme une alternative à BSCF si l'alimentation en oxygène est le facteur limitant pour la réaction d'OCM. En effet BLF présente un flux en oxygène bien plus faible que BSCF dans les conditions expérimentales choisies, mais l'utilisation de membranes denses minces supportées permet d'obtenir un flux plus élevé avec BLF (membrane totale entre 1 et 2 mm avec une couche poreuse côté air et une couche fine entre 20 et 120  $\mu\text{m}$  côté réaction).

La seconde partie de cette étude s'est focalisée sur le développement d'un réacteur pour l'OCM. La membrane était composée de BSCF. Les manipulations ont d'abord été réalisées sans catalyseur. Les résultats obtenus étaient prometteurs mais la sélectivité en éthylène ainsi que la conversion en méthane était trop faible. L'impact de l'addition d'une couche mince de catalyseur a alors été étudié. Les catalyseurs pour l'OCM ont été très étudiés au cours de ces 30 dernières années et plus aucun effort n'est nécessaire dans ce sens. Deux catalyseurs ont alors été sélectionnés, le premier MnWNa pour sa grande sélectivité en éthylène (supérieure à 70%) mais présentant une activité réduite et LaSrCa considéré comme le catalyseur le plus actif pour l'OCM. L'addition d'une couche mince de MnWNa a provoqué une diminution importante du flux d'oxygène à travers la membrane, environ 10 fois plus faible. Cependant les résultats obtenus ont montré une très grande sélectivité en éthylène mais une faible productivité. La productivité était très fortement limitée par la conversion du méthane. Pour LaSrCa, la productivité en éthylène est bien plus élevée, mais est limitée cette fois-ci non pas par la conversion du méthane mais par la quantité de sites actifs. Afin d'augmenter la quantité de sites actifs, une plus importante couche de catalyseur a été ajoutée. Ceci a provoqué la perte de sélectivité en éthylène et donc la perte de productivité. La quantité de sites actifs doit être augmentée tout en conservant une épaisseur très fine. La solution possible est de modifier la forme de la membrane, afin d'obtenir une surface plus importante au regard de la phase gaz. L'utilisation de ce type de réacteur ainsi qu'un revêtement mince de catalyseur a été validé mais la forme du réacteur doit maintenant être optimisée en prenant en compte des cinétiques associées au transport d'oxygène à travers la membrane et des cinétiques décrivant le couplage oxydant du méthane.





# Nomenclature

---

Notation		Units
$a_v$	surface of exchange / volume of the solid phase	$m^{-1}$
$C_T$	total concentration of vacancies	$mol\ cm^{-3}$
$d_{crys}$	crystallite diameter	cm
$D^*$	self-diffusion of oxygen	$cm^2\ s^{-1}$
$D_e$	effective axial diffusivity	$m_G^3\ m_R^{-1}\ s^{-1}$
$D_v, D'_v, D''_v$	oxygen vacancy transport diffusion: global, rich side, and lean side, resp.	$cm^2\ s^{-1}$
$D_{vXu}$	global oxygen vacancy diffusion coefficient, determined on dense membrane; flux fitting based on Xu and Thomson model	$cm^2\ s^{-1}$
$E_{dXu}$	activation energy associated to $D_{vXu}$	$kJ\ mol^{-1}$
$E'_f, E''_f$	activation energy of adsorption	$kJ\ mol^{-1}$
$E_{fXu}$	activation energy associated to $k_{fXu}$	$kJ\ mol^{-1}$
$E'_r, E''_r$	activation energy of desorption	$kJ\ mol^{-1}$
$E_{rXu}$	activation energy associated to $k_{rXu}$	$kJ\ mol^{-1}$
$f^*$	perovskite correction factor	(-)
$F$	Faraday constant	$C\ mol^{-1}$
$F_{air}, F_{sweep}$	total flow rate at the air side and at the sweep side	$cm^3\ min^{-1}$
$h^\circ$	electron hole	(-)
$J_{O_2}$	oxygen flux	$mol\ cm^{-2}\ s^{-1}$ or $ml\ cm^{-2}\ min^{-1}$
$K$	Langmuir constant	$Pa^{-1}$
$k$	global surface rate	$cm\ s^{-1}$
$k_f, k'_f, k''_f$	adsorption coefficient: global, rich side, and lean side	$Pa^{-1}\ s^{-1}$
$k_{fXu}$	global adsorption coefficient determined on dense membrane; flux fitting based on Xu and Thomson model	$cm\ atm^{-0.5}\ s^{-1}$
$k_r, k'_r, k''_r$	desorption coefficient: global, rich side, and lean side	$s^{-1}$
$k_{rXu}$	global desorption coefficient determined on dense	$mol\ cm^{-2}\ s^{-1}$

	membrane; flux fitting based on Xu and Thomson model	
$K, K', K''$	Langmuir coefficient: global, rich side and lean side, resp.	$\text{Pa}^{-1}$
$L$	thickness of the membrane	cm
$L_t$	number of active sites	$\text{mol m}^{-3}_s$
$n_v(T, P_{O_2})$	oxygen vacancy concentration	(-)
$O_{0,s}^X, O_{0,b}^X$	surface oxygen and bulk oxygen, respectively	(-)
$P'_{O_2}, P''_{O_2}$	partial pressure of oxygen on the rich side and on the lean side, respectively	atm
$r$	crystallite radius	$\mu\text{m}$
$r_j$	reaction rate of step j	$\text{s}^{-1}$
$R$	gas constant	$\text{J mol}^{-1} \text{K}^{-1}$
$S$	surface area of the dense membrane	$\text{cm}^2$
$S_{(\text{BET})}$	BET surface area	$\text{cm}^2 \text{g}^{-1}$
$T$	absolute temperature	K
$U$	superficial velocity	$\text{cm s}^{-1}$
$\nu_{ij}$	stoichiometric coefficient for species i in reaction j	(-)
$V_m$	molar volume	$\text{mol cm}^{-3}$
$V_{0,s}^{\cdot\cdot}, V_{0,b}^{\cdot\cdot}$	surface oxygen vacancies and bulk oxygen vacancies, respectively	(-)
$x_{O_2}$	molar ratio of oxygen	(-)
$z$	axial reactor coordinate	$m_R$
$\epsilon_b$	inter-granular void space	$\text{m}^3_G \text{m}^{-3}_R$
$\delta$	oxygen non-stoichiometry	(-)
$\Delta H$	oxygen adsorption enthalpy	$\text{kJ mol}^{-1}$
$\rho$	solid density	$\text{g cm}^{-3}$
$\sigma_o$	oxygen conductivity	$\text{S cm}^{-1}$
$\theta_v, \theta_{^{16}\text{O}}, \theta_{^{18}\text{O}}$	vacancy coverage, $^{16}\text{O}$ coverage and $^{18}\text{O}$ coverage	(-)





# Outline

---

<b>REMERCIEMENTS</b>	<b>11</b>
<b>RESUME</b>	<b>15</b>
<b>NOMENCLATURE</b>	<b>19</b>
<b>OUTLINE</b>	<b>23</b>
<b>INTRODUCTION</b>	<b>29</b>
<b>BIBLIOGRAPHY</b>	<b>32</b>
<b>CHAPTER 1-CONTEXT AND BIBLIOGRAPHIC STUDY</b>	<b>35</b>
<b>I. OCM CHEMISTRY</b>	<b>35</b>
I.1. OCM TYPICAL CATALYST	36
I.2. ENGINEERING ASPECTS – MEMBRANE REACTORS	41
I.3. CONCLUSION	43
<b>II. TRANSPORT IN MEMBRANE REACTOR CHARACTERIZATION</b>	<b>45</b>
II.1. TRANSPORT MECHANISMS	45
II.2. CHARACTERIZATION AND TRANSPORT MODELLING	48
<b>III. STRATEGY FOLLOWED IN THIS WORK</b>	<b>58</b>
<b>BIBLIOGRAPHY</b>	<b>60</b>
<b>CHAPTER 2-EXPERIMENTAL PROCEDURES:</b>	<b>65</b>
<b>IV. PEROVSKITE MATERIAL AND MEMBRANE CHARACTERIZATION</b>	<b>65</b>
IV.1. PEROVSKITE SYNTHESIS:	65
IV.2. SCANNING ELECTRON MICROSCOPY (SEM)	66
IV.3. SPECIFIC AREA MEASUREMENT BY THE BET METHOD	66
IV.4. X-RAY DIFFRACTION (XRD)	67
IV.5. THERMO GRAVIMETRIC ANALYSIS (TGA)	68
	23

IV.6. IODOMETRIC TITRATION	69
IV.7. X-RAY ABSORPTION NEAR EDGE STRUCTURE (XANES)/ EXTENDED X-RAY ADSORPTION FINE STRUCTURE (EXAFS)	71
<b>V. KINETIC PARAMETERS DETERMINATION: OXYGEN ISOTOPIC EXCHANGE, SSITKA EXPERIMENTS</b>	<b>76</b>
V.1. EXPERIMENTAL SET UP	76
V.2. DETERMINATION OF THE OPTIMAL PARAMETER	78
V.3. APPARATUS CALIBRATION	82
<b>VI. MEMBRANE REACTOR SET-UP</b>	<b>84</b>
<b>VII. OXIDATIVE COUPLING OF METHANE IN MEMBRANE REACTOR</b>	<b>88</b>
VII.1. CATALYST SYNTHESIS	88
VII.2. CATALYST COATING	90
VII.3. CATALYTIC PERFORMANCE MEASUREMENTS	92
VII.4. RESIDENCE TIME	93
<b>BIBLIOGRAPHY</b>	<b>94</b>

### **CHAPTER 3-DETERMINATION OF OXYGEN ADSORPTION-DESORPTION RATES AND DIFFUSION RATE**

#### **COEFFICIENTS IN PEROVSKITES** **97**

<b>I. INTRODUCTION</b>	<b>97</b>
I.1. ELECTRICAL CONDUCTIVITY RELAXATION	97
I.2. OXYGEN ISOTOPIC EXCHANGE TECHNIQUES	98
I.3. STRATEGY FOLLOWED IN THIS CHAPTER	99
<b>II. MODELLING</b>	<b>100</b>
II.1. SURFACE EXCHANGE COEFFICIENTS AND RATES	100
II.2. DEVELOPMENT OF THE MICRO KINETIC MODEL	101
II.3. GLOBAL MASS BALANCE:	102
<b>III. BSCF: CASE STUDY</b>	<b>103</b>
III.1. VACANCIES CHARACTERIZATION	103
III.2. MODELLING OF OXYGEN ISOTOPIC EXCHANGE AND ESTIMATION OF SURFACE EXCHANGE KINETIC COEFFICIENT ( $K_R, K_F$ )	108
III.3. ESTIMATION OF DIFFUSION COEFFICIENTS FROM CHARACTERISTIC TIME	111
<b>IV. GENERAL DISCUSSION</b>	<b>116</b>
<b>V. CONCLUSIONS</b>	<b>116</b>

<b>BIBLIOGRAPHY</b>	<b>117</b>
---------------------	------------

---

<b>CHAPTER 4-PREDICTION OF OXYGEN FLUX IN DENSE PEROVSKITE MEMBRANES FROM MICROKINETIC CONSTANTS</b>	<b>121</b>
--	------------

---

<b>I. INTRODUCTION</b>	<b>121</b>
<b>II. BASIC PRINCIPLES AND MODEL</b>	<b>122</b>
<b>III. FLUX EQUATION</b>	<b>125</b>
<b>IV. RESULTS</b>	<b>130</b>
IV.1. OXYGEN PERMEATION MEASUREMENTS ON $\text{Ba}_{0.5}\text{Sr}_{0.5}\text{Co}_{0.8}\text{Fe}_{0.2}\text{O}_{3-\Delta}$ MEMBRANE	130
IV.2. PARAMETER ESTIMATION	132
IV.3. SIMULATION OF OXYGEN FLUX BASED USING MICROKINETIC PARAMETERS OBTAINED FROM POWDER.	134
IV.4. SIMULATION OF THE IMPACT OF MEMBRANE THICKNESS ON THE OXYGEN FLUX	136
<b>V. CONCLUSIONS</b>	<b>140</b>

<b>BIBLIOGRAPHY</b>	<b>141</b>
---------------------	------------

---

<b>CHAPTER 5-APPLICATION OF THE MICROKINETIC METHODOLOGY TO LSCF AND BLF MEMBRANES</b>	<b>143</b>
--	------------

---

<b>I. INTRODUCTION</b>	<b>143</b>
<b>II. STUDY OF LSCF MATERIALS AND MEMBRANES</b>	<b>144</b>
II.1. CHARACTERIZATION OF LSCF MATERIAL	144
II.2. MODELLING OF THE OXYGEN FLUX OF LSCF MEMBRANE	149
II.3. CONCLUSIONS ON LSCF MATERIAL AND MEMBRANE	153
<b>III. BLF: A GOOD ALTERNATIVE TO BSCF</b>	<b>154</b>
III.1. CHARACTERIZATION OF THE SAMPLE	154
III.2. ESTIMATION OF THE OXYGEN FLUX THROUGH THE DENSE MEMBRANE:	161
III.3. CONCLUSION ON BLF MATERIAL	164
<b>IV. CONCLUSIONS</b>	<b>165</b>

<b>BIBLIOGRAPHY</b>	<b>166</b>
---------------------	------------

---

<b>CHAPTER 6-OXIDATIVE COUPLING OF METHANE IN MEMBRANE REACTOR</b>	<b>169</b>
--	------------

---

<b>I. INTRODUCTION</b>	<b>169</b>
<b>II. DESCRIPTION OF THE MEMBRANE REACTOR</b>	<b>170</b>
II.1. OCM RESULTS ON BARE BSCF MEMBRANE	172
II.2. DISCUSSION	177
II.3. STABILITY OF BSCF MEMBRANE IN OCM CONDITIONS	177
<b>III. I.1. OCM RESULTS USING A CATALYST COATING ON BSCF MEMBRANE</b>	<b>181</b>
III.1. TUNGSTEN BASED CATALYST	181
III.2. LANTHANUM BASED CATALYST	185
III.3. STABILITY OF LASRCA CATALYTIC COATING ON BSCF MEMBRANE	198
III.4. DISCUSSION	200
<b>IV. CONCLUSIONS</b>	<b>203</b>
<b><u>BIBLIOGRAPHY</u></b>	<b>204</b>
<b><u>CONCLUSIONS &amp; PERSPECTIVES</u></b>	<b>207</b>





# Introduction

Ethylene is the most widely produced organic compound in the world. It is essentially exploited as a monomer in the polymer industry<sup>1</sup>. Indeed, 75% of its consumption is by the polymer industry, to generate mainly polyethylene and various co-polymers (Figure 1). Ethylene oxide corresponds to 4%<sup>1</sup> of the use of ethylene, either directly uses in detergent industry or converts to ethylene glycol used for example as anti frost. Ethylene is also used to produce ethylene dichloride for the vinyl chloride production or is directly added to lead gasoline as a lead scavenger. In 2012, the total demand of ethylene was of 129 Million Metric tons. The average growth of demand in ethylene is increasing of 5.85 Million Metric tons per year (4.1%)<sup>1</sup>.

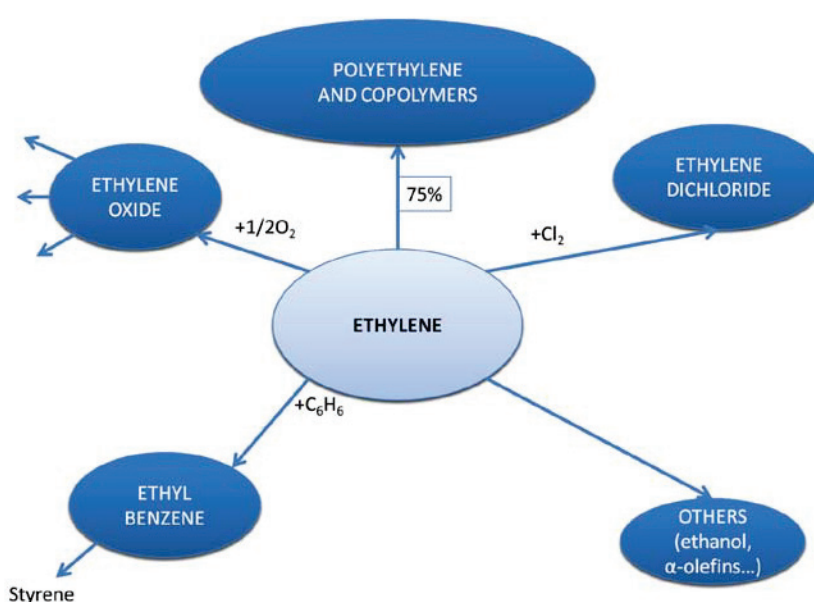


Figure 1 Ethylene consumption by end products in 2012 (source IHS: [www.ihs.com](http://www.ihs.com)<sup>1</sup>).

Over the past decade the world has experienced a widening gap between the predicted future demand for oil and known reserves<sup>2</sup>. The rapid increase in consumption, fuelled particularly by the growth of new economies like China and India, has led to unprecedented increases in the oil price. Innovation with respect to chemical processes in order to use alternative feedstock's in the medium and long term is essential for the future of the chemical industry. In its annual report<sup>3</sup>, the International Energy Agency (IEA) presents the world global energy supply over the years (Figure 2). The objective is to increase the variety of resource used to support the crude oil to provide enough energy with the increase of the demand. The estimated resources in oil are of 1.7 trillion of barrels (about 265 billion of cubic meters) against 187 trillion cubic meters for natural gas (NG). The world production of barrel is of 86 million barrels per year for a consumption of 90 thousand barrels daily. With this consumption the total resource should decline within 50 years. About the natural gas, the

consumption is about 3 trillion cubic meters per year against a production of 3 trillion cubic meters per year<sup>4</sup>.

Currently, ethylene is extracted from crude oil by naphtha cracking. The two other existing ways are based on ethane valorisation: the thermal (non-oxidative) dehydrogenation and the oxidative dehydrogenation of ethane from oil or from natural gas. The loading of ethane in natural gas depends on the source. The natural gas can be classified in two categories known as dry or wet depending on the amount of  $C_{2+}$  hydrocarbons (wet gas for  $C_{2+}$  content higher than 10 vol%)<sup>5</sup>. But in main case, the natural gas contains at least 75%vol of methane and mainly in a range of 87.0 to 97.0%<sup>6</sup>. Methane can be valorised into  $C_{2+}$  hydrocarbons by the oxidative coupling of methane.

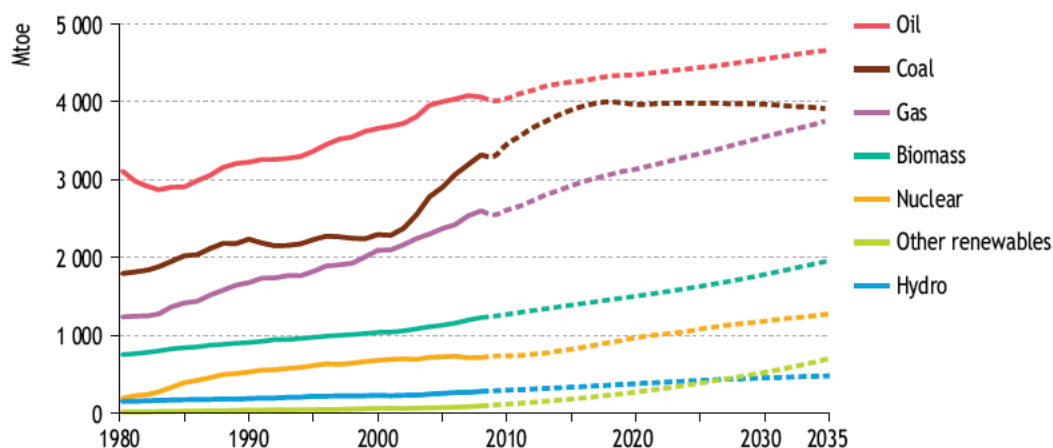


Figure 2 World oil primary energy demand by fuel, International Energy Agency<sup>3</sup>.

This work has been part of CARENA project. CARENA stands for CAlytic membrane REactors based on New mATERIALs for C1-C4 valorisation (Figure 3). The objective of the CARENA project is to develop catalytic membrane reactors for the efficient conversion of light alkanes into higher value chemicals resulting in the reduction of the number of process steps and an increase in feedstock flexibility for the European chemical industry. Different partners have enrolled in this project industrial (Akzonobel, Arkema, Johnson Matthey, Saint Gobain; Tecnimont KT SPA (TKT), Linde, Process Design Center BV (PDC) and Acktar) as well academic groups: universities (Leibniz University, UTwente, Technion, Salerno) and research organisations (CNRS-IRCELYON, SINTEF, ECN, CEA, CNRS-IEM, Diamond).

To valorise methane from natural gas, three alternatives are considered the production of syngas, of ethylene based on the oxidative coupling of methane (OCM) and of methanol. Our participation is in the development of optimised reactor for the oxidative coupling of methane.

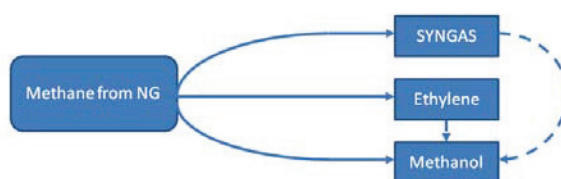


Figure 3 Methane valorisation: CARENA approach

The aim of this study is to optimize the design of a membrane reactor for the oxidative coupling of methane (OCM). The strategy of this work is described by Figure 4. The first chapter will establish a state of the art of the knowledge on OCM reaction as well as the advantages of a membrane reactor and the source of membrane reactor design enhancement. Then the experimental methods used would be described in the second chapter. A novel approach to determine the intrinsic kinetic parameter describing the oxygen flux across the dense membrane would be developed on a case study material  $\text{Ba}_{0.5}\text{Sr}_{0.5}\text{Co}_{0.8}\text{Fe}_{0.2}\text{O}_{3-\delta}$  (chapter 3). These parameters would be integrated in a new flux equation and the flux across  $\text{Ba}_{0.5}\text{Sr}_{0.5}\text{Co}_{0.8}\text{Fe}_{0.2}\text{O}_{3-\delta}$  would be characterised (chapter 4). All this methodology would be tested on to other materials  $\text{La}_{0.6}\text{Sr}_{0.4}\text{Co}_{0.2}\text{Fe}_{0.8}\text{O}_{3-\delta}$  and  $\text{Ba}_{0.95}\text{La}_{0.05}\text{FeO}_{3-\delta}$  (chapter 5).  $\text{Ba}_{0.5}\text{Sr}_{0.5}\text{Co}_{0.8}\text{Fe}_{0.2}\text{O}_{3-\delta}$  membrane would be then integrated in an OCM membrane reactor (chapter 6). An optimal design would be discussed (conclusion).

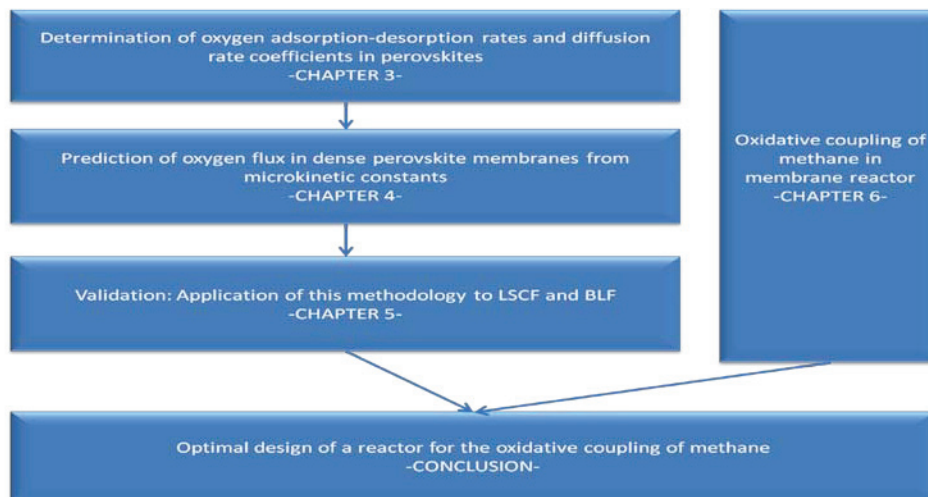


Figure 4 Work strategy

# Bibliography

---

1. IHS Inc., <http://www.ihs.com/products/chemical/planning/ceh/ethylene.aspx>, 2011.
2. International Energy Agency, *Worldwide engagement for sustainable energy strategies 2013*, 2013.
3. International Energy Agency, *World Energy Outlook*, 2010.
4. B. Petroleum, *BP Statistical Review of World Energy*, 2013.
5. M. Tagliabue, D. Farrusseng, S. Valencia, S. Aguado, U. Ravon, C. Rizzo, A. Corma and C. Mirodatos, *Chem. Eng. J.*, 2009, **155**, 553–566.
6. uniongas, [www.uniongas.com/about-us/about-natural-gas/Chemical-Composition-of-Natural-Gas](http://www.uniongas.com/about-us/about-natural-gas/Chemical-Composition-of-Natural-Gas).





# CHAPTER 1-CONTEXT AND BIBLIGRAPHIC STUDY

---

## I. OCM CHEMISTRY

The oxidative coupling of methane to C<sub>2</sub> and higher hydrocarbons has seen a promising way to upgrade natural gas since the work of Keller and Bhasin<sup>1</sup> and continues to attract both industrial as well as academic interest. Different authors have worked on developing a method to characterize the kinetics of the oxidative coupling of methane (OCM). The first results were obtained on fixed bed reactor<sup>2-5</sup>. The transformation of methane to ethane and ethylene by OCM is performed via these two global reactions (1) and (2), respectively:



Both transformations are exothermic; hence ideally there is no need for an external energy supply to keep the reactants at temperatures high enough to perform the reaction.

However, as methane is a very stable molecule (C-H binding energy=438.4 kJ mol<sup>-1</sup>), its activation implies operating at temperature higher than 600°C. The biggest challenge of OCM relates to the fact that at such high temperatures any presence of oxygen in gas phase leads easily to a follow-up oxidation of desired reaction products, i.e. ethane and ethylene, into carbon oxides and may also favour the total oxidation of methane(3) and (4). Moreover, the reactants are more stables than the products (Ethane C-H binding energy=419.5 kJ mol<sup>-1</sup> and Ethylene C-H binding energy=444.0 kJ mol<sup>-1</sup>).



OCM mechanism is based on both surface reaction and gas phase reaction. In absence of a catalyst, the typical elementary reaction network for oxidative coupling of methane consists of 39 gas-phase reactions<sup>6</sup>, and 14 equations describe the catalytic reactions. This network can be simplified as shown in Figure 5. The main and rate-determining step (RDS) is the homolytic activation of one of C-H bond in the methane molecule on an O- oxygen surface species, leading to the formation of a methyl radical:



This RDS step can be kinetically described as an Eley-Rideal process<sup>7-11</sup>. Hence, almost all active OCM catalysts reported in literature are metal oxides, able to generate the electrophilic surface oxygen ( $O^*$ ).

On Figure 5, the competition between the gas phase reaction and the surface reaction is simplified. Two methyl radical molecules recombine to form an ethane molecule during the coupling step in the gas phase. Then, successive ethane dehydrogenation leads to ethylene formation. The methyl radical in presence of oxygen produces  $CO_x$ . Moreover, the adsorption of methyl radicals on the surface of the catalyst leads only to  $CO_x$  species. The choice of the catalyst has a strong impact on the selectivity in  $C_{2+}$  and on the conversion of methane. For example, a good catalyst should have a low sticking coefficient for methyl radicals<sup>12,13</sup>, in order to avoid re-adsorption and total oxidation of the initial methane molecule.

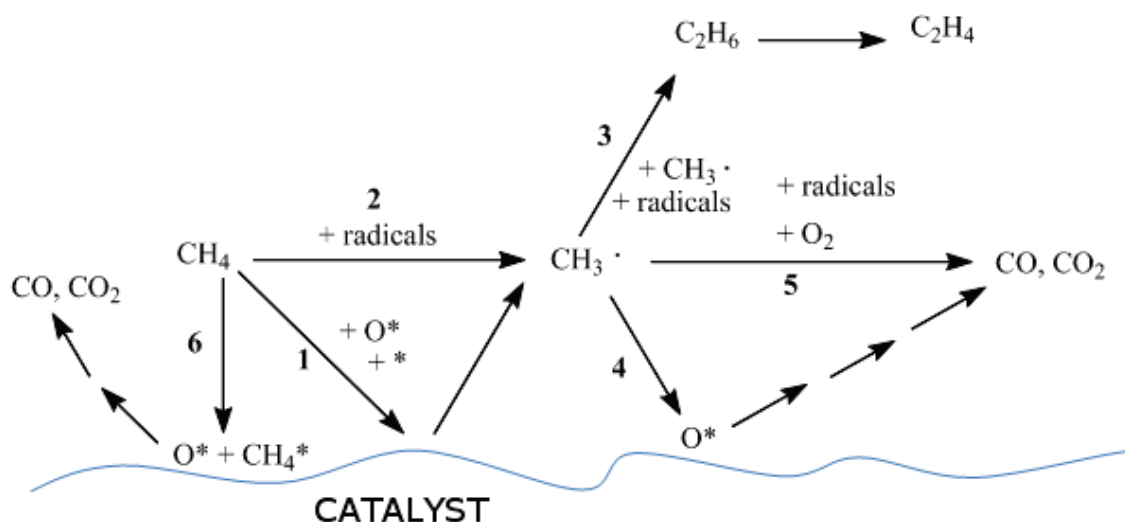
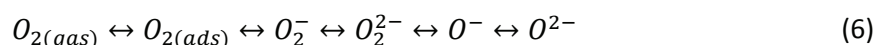


Figure 5 OCM mechanistic scheme

### 1.1. OCM typical catalyst

The main research effort on OCM materials spent over the last 30 years, started with simple oxide compounds and evolved towards multi-promoted mixed oxide materials with increased performances. Keller and Bhasin<sup>1</sup> made a first screening of potential OCM catalysts using air as oxidant. They tested various metal oxides. Oxides of Sn, Pb, Sb, Bi, Cd and Ln were found to be most active, while Li, Mg, Zn, Ti, Zr, Mo, Fe, Cr, W, Cu, Ag, Pt, Ce, V, B and Al oxides showed poor or no activity. All their catalysts were prepared by wet impregnation on  $\alpha$ -alumina. The conversion of methane and selectivity in  $C_2$  did not meet the expectation for a viable process (i.e.  $CH_4$  conversion > 30% and  $C_2$  selectivity > 90%). After their work, a lot of efforts were put on mixed metal oxide materials.

Many surface phenomena are matter of debates. However, several key features are now commonly accepted. The basic surface sites lead to the surface activation of oxygen. C-H bond activation proceeds on this activated oxygen. The minimal rate of catalyst re-oxidation is also need as compared to OCM reaction. Finally, the sticking properties of CH<sub>3</sub> radicals on the surface should be low<sup>12,13</sup>. Indeed, the termination reaction in the gas phase mainly leads to C<sub>2</sub> products while the adsorption of methyl radicals on the surface leads to the production of CO<sub>x</sub>. Several authors<sup>12,14-21</sup> investigated the acid-base properties of a catalyst for the C<sub>2</sub> selectivity. Among all ionic oxygen species present on the catalyst, according to the equilibrium (6):



The most reactive species O<sup>2-</sup> are also the most basic and the least electrophilic<sup>22</sup>. Reactivity and Lewis-type basicity of these sites depend on the coordination state of the oxygen, i. e. on the associated metal cation playing a key role as stabilizer. The strongly basic species O<sup>2-</sup> associated to a vacancy is able to activate reversible O<sub>2</sub> and CO<sub>2</sub> leading to either O<sup>-</sup> or carbonate on the surface. In the case of a very basic oxide, the pair O<sup>2-</sup>/Oxygen vacancies would even perform heterolytic methane dissociation. O<sup>-</sup> and O<sub>2</sub><sup>-</sup> as less basic sites are assumed to be responsible for methyl and ethyl radical formation, via homolytic dissociation of methane, and total oxidation of CO and CO<sub>2</sub><sup>23</sup>. As basicity of an oxide is strongly influenced by the cation, doping or promoting a simple metal oxide with another metal can easily strengthen mild basicity of the oxide. Best combinations reported in the literature are Li<sub>2</sub>O/MgO, La<sub>2</sub>O<sub>3</sub>(SrO)/CaO and MnNa<sub>2</sub>WO<sub>4</sub>/SiO<sub>2</sub>.

Louis et al.<sup>24</sup> used of high temperature parallel screening to determine the optimal catalyst for OCM reaction. In this graph are recorded their best results (Figure 6). Three main families are highlighted, tungsten based catalyst, which showed a very low C<sub>2</sub> productivity, Li based catalyst and La based catalyst. The second family have been intensively studied for their good selectivity in C<sub>2</sub><sup>21,25,26</sup> but the final yield remains too low and their stability under reaction poor. The highest productivity is showed for a La based catalyst: 10%La-20%Sr/CaO (LaSrCa). After this work, several authors focused on this catalyst<sup>27,28</sup>.

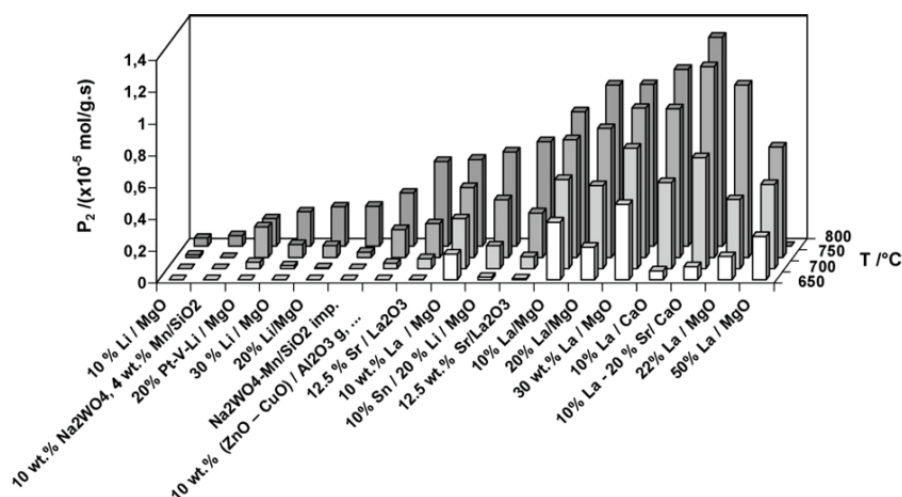


Figure 6  $C_2$  productivity of active catalyst after several hours on stream screening on a 6 parallel fixed bed with a feed flow rate of  $100\text{ml min}^{-1}$ , composition (Ar:CH<sub>4</sub>:O<sub>2</sub>)=(90:6.7:3.3) at temperature from 650 to 800°C. Formulations are given in %wt<sup>24</sup>

In 2011, Zavyalova et al.<sup>12</sup> recorded all the previous catalytic results on OCM reaction. Regarding the expectation for a viable process, they summarised all the good catalysts tested in fixed bed reactor. Figure 7 is extracted from their work. The numbers in brackets correspond to their bibliography. For high  $C_2$  selectivity, two main families are highlights: Na-Mn-W based catalyst and Li-Mn based catalyst. Tungsten based catalysts exhibit the highest  $C_2$  selectivity up to 80% but the conversion of methane is lower than for the other catalysts which leads to a maximum yield of 35%. For Lithium based catalyst, the average methane conversion varies from 40 to 50% and  $C_2$  selectivity from 50 to 70%. The  $C_2$  yield is about 35%. Lithium based catalysts seem to be the best catalysts. But, no good stability has been reported over time. Indeed after few hours, the methane conversion and  $C_2$  selectivity drop drastically<sup>29</sup>.

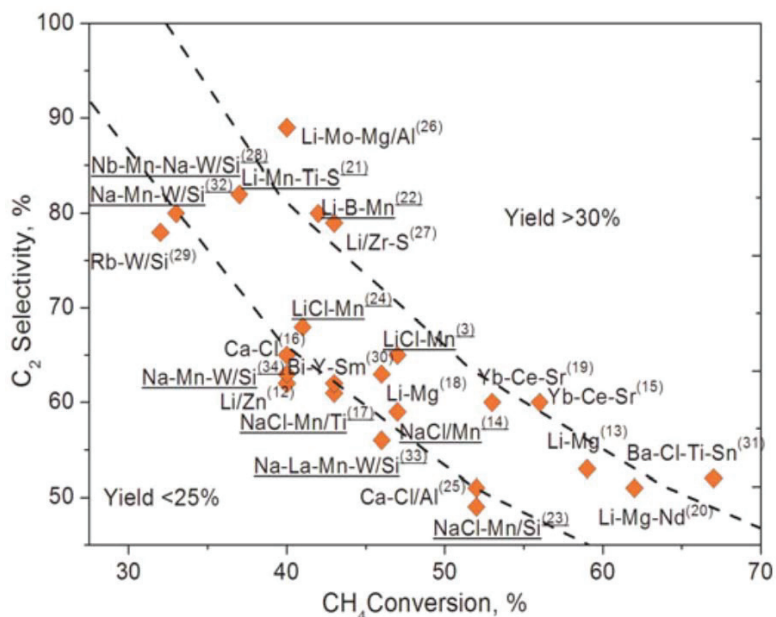


Figure 7 Elemental compositions of OCM-catalysts with Y(C<sub>2</sub>) 25% reported in the literature. All the catalysts were tested in a fixed bed reactor, in co-feed mode under atmospheric pressure at temperature from 9473 to 1223K; p(CH<sub>4</sub>)/p(O<sub>2</sub>)=1.7-9.0; and contact time from 0.2 to 5,5<sup>12</sup>

Na-Mn-W based catalysts have been extensively studied for their very high C<sub>2</sub> selectivity and their good stability over time<sup>30</sup>. To industrialise a process, the highest selectivity is researched even if it is at the expense of the methane conversion. Tungsten based catalyst meets the best expectations.

A comparative study between LaSrCaO catalysts and 13.3/18.3/4.6 wt% Mn-Na<sub>2</sub>WO<sub>4</sub>/SiO<sub>2</sub> (Na-Mn-W) catalysts has been done by Serres<sup>31</sup>. These catalysts have been tested in different reactor configurations from the fixed bed reactor, to the micro reactor to the tubular reactor. In these three reactors, methane and oxygen were mixed in the feed. In order to compare these configurations, the catalytic results have been plotted as a function of the V/S ratio, V stands for the volume of the gas phase and S for the active surface of the catalyst. C<sub>2</sub> selectivity increases with V/S ratio with no dependence with the reactor design (Figure 8). Na-Mn-W catalyst shows a high selectivity in C<sub>2</sub> that reaches a maximum of 70% for V/S ratio equal to 6 μm. In the case for LaSrCa catalyst, the selectivity in C<sub>2</sub> is much lower and reaches its maximum of 45% for a V/S ratio of 3.5 μm. Previous studies have confirmed the low conversion of methane for Na-Mn-W catalyst.

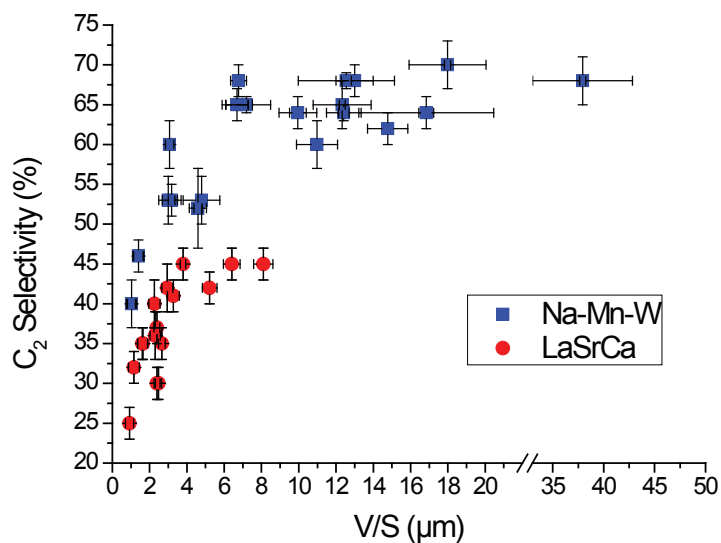


Figure 8 C<sub>2</sub> selectivity of LaSrCa and Na-Mn-W catalysts in the two different reactors as a function of V/S parameter at 800°C, CH<sub>4</sub>/O<sub>2</sub>=4

The productivity in ethylene also increases as a function of V/S ratio for these two catalysts (Figure 9). For both catalysts, the productivity in ethylene follows the same trend as the C<sub>2</sub> selectivity. But LaSrCa shows productivity eight times higher than the tungsten based catalyst. The low methane conversion of methane in the case of the tungsten based catalyst explains the low productivity.

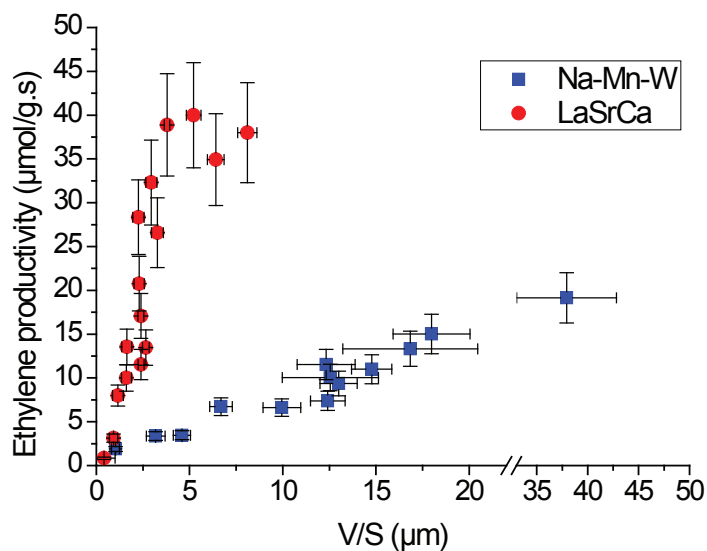


Figure 9 Ethylene productivity for Na-Mn-W and LaSrCa in two reactors as a function of V/S at 800°C and CH<sub>4</sub>/O<sub>2</sub>=4



this reactor enhances the  $C_2$  selectivity and allows reaching the same selectivity as the fixed bed reactor but does not overstep it. This can be explained by the recombination of oxygen in the gas phase which is not favourable to obtain a higher  $C_2$  selectivity in the membrane reactor. About the  $CH_4$  conversion and the  $C_2$  yield, they both increase with the temperature; the same observations can be done between the three set-ups. The ratio  $C_2H_4/C_2H_6$  increases with the temperature. This ratio is much higher in the case of the membrane reactor. In the membrane reactor, the formation of ethane can be followed by an adsorption of this molecule on the surface of the membrane, the oxidative dehydrogenation (ODHE) occurs. The ODHE reaction in membrane reactor gives very good results with a ethylene selectivity from 60% to 100% and a conversion of ethane from 40% to 100%<sup>34</sup>.

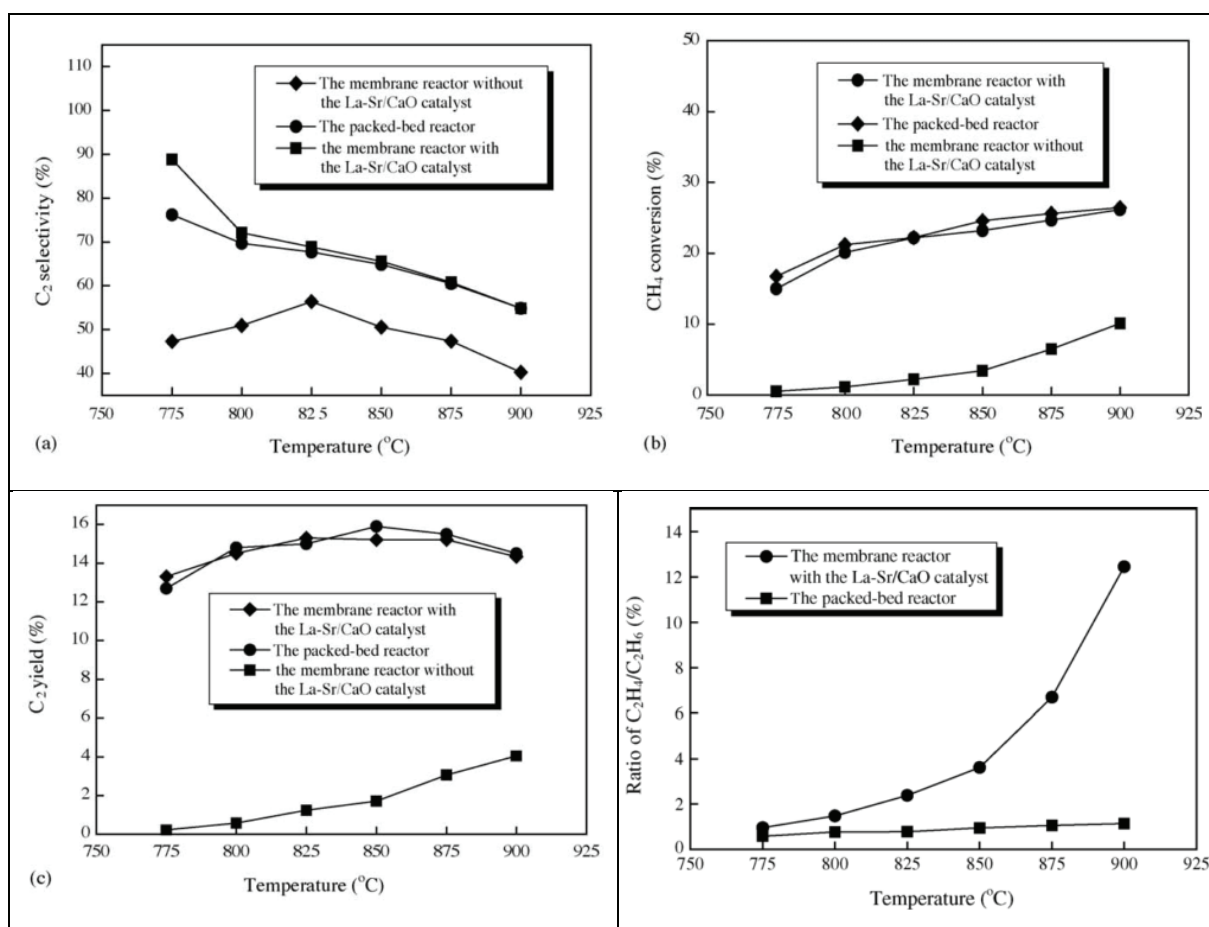


Figure 11 Comparison of  $C_2$  selectivity,  $CH_4$  conversion and  $C_2$  yield for packed-bed and the ratio  $C_2H_4/C_2H_6$  reactor without catalyst and membrane reactor with La-Sr/CaO catalyst. Flow rate  $CH_4=20.67\text{mL}\cdot\text{min}^{-1}$ ,  $He=79.75\text{mL}\cdot\text{min}^{-1}$ ,  $air=300\text{mL}\cdot\text{min}^{-1}$ <sup>28</sup>

It has been proved<sup>35</sup> that the presence of activated oxygen and the absence of gaseous oxygen is favourable for the selectivity of OCM reaction. A lot of effort has been made to avoid this mixture mainly based on membrane reactor design<sup>36</sup>. Indeed, membrane reactors based on ceramic dense membrane allowed a high flux of ionic oxygen and a constant feed of adsorb oxygen on the membrane avoiding all contact between methane and oxygen in the gas phase. LSCF has been tested in both fixed bed reactor and disk reactor. The results show an enhancement of the selectivity in the membrane reactor but the conversion is much lower. The  $C_2$  yield is in the same range. Looking at

the reaction of LaSrCa in fixed bed, the conversion and the selectivity are good, but the addition of this catalyst in the membrane reactor leads to a drop of the methane conversion contrary to Wang et al.<sup>28</sup> results. This can be explained by a limitation of the oxygen feeding in this configuration. The membrane reactor design should be improved to enhance the methane conversion. Moreover, a highest conversion of methane is obtained when the temperature is increased, the selectivity slightly decreases. An optimum should be found between increases of the temperature to enhance the CH<sub>4</sub> conversion and avoiding decreasing too much the C<sub>2</sub> selectivity. About the tungsten based catalyst no results have been published about this catalyst in a membrane reactor. The use of this catalyst in a fixed bed reactor leads to a very high C<sub>2</sub> selectivity. The current design of membrane reactor with a catalytic bed does not exhibit better results than the fixed bed reactor (Table 1).

**Table 1** Summary of the catalytic results obtain in membrane reactor or fixed bed with LaSrCa catalyst, W-Mn/SiO<sub>2</sub> and LiLaNi reported in the literature

Membrane	T °C	Shape	Catalyst	X <sub>CH4</sub> %	S <sub>C2</sub> %	C <sub>2</sub> H <sub>4</sub> /C <sub>2</sub> H <sub>6</sub>	Ref
La <sub>0.6</sub> Sr <sub>0.4</sub> Co <sub>0.8</sub> Fe <sub>0.2</sub> O <sub>3-δ</sub>	800	FB	-	12	21	1.3	37
La <sub>0.6</sub> Sr <sub>0.4</sub> Co <sub>0.8</sub> Fe <sub>0.2</sub> O <sub>3-δ</sub>	850	FB	-	20	38	3.3	
La <sub>0.6</sub> Sr <sub>0.4</sub> Co <sub>0.8</sub> Fe <sub>0.2</sub> O <sub>3-δ</sub>	800	Disk	-	1	100	0.5	
La <sub>0.6</sub> Sr <sub>0.4</sub> Co <sub>0.8</sub> Fe <sub>0.2</sub> O <sub>3-δ</sub>	850	Disk	-	4	100	0.3	
-	800	FB	La-Sr/CaO	33	57	0.8	24
Ba <sub>0.5</sub> Sr <sub>0.5</sub> Co <sub>0.8</sub> Fe <sub>0.2</sub> O <sub>3-δ</sub>	800	tube	La-Sr/CaO	2	48		28
Ba <sub>0.5</sub> Sr <sub>0.5</sub> Co <sub>0.8</sub> Fe <sub>0.2</sub> O <sub>3-δ</sub>	850	tube	La-Sr/CaO	5	47		
Ba <sub>0.5</sub> Sr <sub>0.5</sub> Co <sub>0.8</sub> Fe <sub>0.2</sub> O <sub>3-δ</sub>	800	Disk	LiLaNiO/γ-Al <sub>2</sub> O <sub>3</sub>	1	48	-	38
Ba <sub>0.5</sub> Sr <sub>0.5</sub> Co <sub>0.8</sub> Fe <sub>0.2</sub> O <sub>3-δ</sub>	875	Disk	LiLaNiO/γ-Al <sub>2</sub> O <sub>3</sub>	3	73		
-	820	FB	W-Mn/SiO <sub>2</sub>	30	68	1.6	39

### I.3. Conclusion

For industrialization, the expected conversion of methane should be higher than 30% and the C<sub>2</sub> selectivity should overstep 90%. In the presenting results no formulation can meet these two criteria. The catalyst composition has been intensively studied over the last 30 years, Zavyalova et al.<sup>12</sup> reported over 1870 datasets on catalyst compositions and their performance in OCM. No more work is needed in this field; the remaining solution is to work on the reactor design. The cited results have been obtained in fixed bed configuration. 10%La-20%Sr/CaO and 13.3/18.3/4.6 wt% Mn-Na<sub>2</sub>WO<sub>4</sub>/SiO<sub>2</sub> are known to be among the best OCM catalysts. The first one for is high activity and the

second one for is high selectivity. Moreover, with the two best catalysts, Serres<sup>31</sup> worked on micro reactor and did not manage to overstep these results. The use of membrane reactor should improve the production of methyl radicals which leads to a higher conversion of methane. Moreover avoiding gaseous oxygen in the reaction compartment should leads to an enhancement of the C<sub>2</sub> selectivity. Sadly, no results on a membrane reactor validate this hypothesis. The development of an optimal reactor design is limited by a lack of understanding of the mechanism and the predominance of the gas phase in the current reactor.

Many authors used perovskite based ceramic membrane for this reaction such as Ba<sub>0.5</sub>Sr<sub>0.5</sub>Co<sub>0.8</sub>Fe<sub>0.2</sub>O<sub>3-6</sub> (BSCF) which known to permeate well oxygen<sup>40</sup>. The first studies have been done with no catalyst on the surface, which limits the reaction due to the low surface area of the membrane and the low selectivity (Figure 12 A). In order to increase this selectivity, a catalyst coating has been added on the membrane surface (Figure 12 B). This approach leads to a recombination of oxygen in the gas phase, and the main interest of the membrane design is lost. The last option which has not been studied yet is the addition of a thin layer of catalyst on the membrane allowing the conduction of ionic oxygen to the surface of the catalyst (Figure 12 C). And so there is a contact between the activated oxygen, the catalyst and the methane.

The objective of this work is to do thin layers of catalyst (Figure 12 C) in order to avoid the recombination of oxygen into the gas phase and to conduct the oxygen to the surface to react with methane species to produce methyl radicals. In order to obtain the best results, a BSCF membrane has been selected for its high oxygen permeation and 10%La-20%Sr/CaO and 13.3/18.3/4.6 wt% Mn-Na<sub>2</sub>WO<sub>4</sub>/SiO<sub>2</sub> have been selected as the best catalysts.

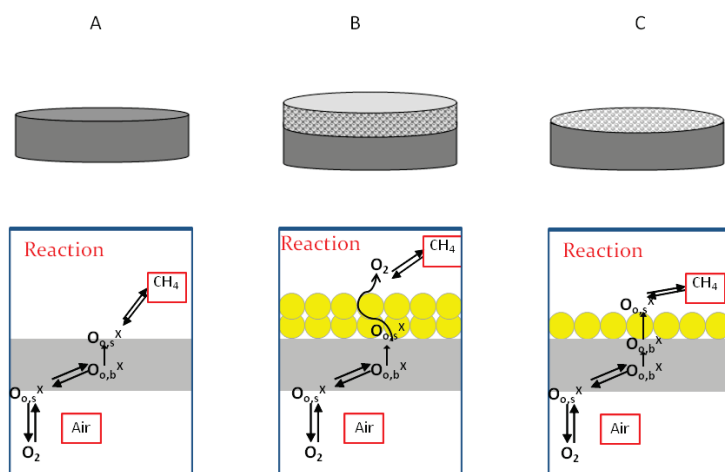


Figure 12 Concepts for reactor for the oxidative coupling of methane

## II. Transport in membrane reactor characterization

Mixed ionic and electronic conductors (MIECs) are an important class of materials that can be potentially employed in high temperature applications where simultaneous reaction and separation is advantageous<sup>41</sup>. Researches have been conducted on partial oxidation of methane to syngas<sup>42,43</sup>, oxidative coupling of methane<sup>44</sup> or oxidative dehydrogenation of ethane to ethylene<sup>34</sup>. These materials are also proposed for separation applications with cathodes for SOFCs<sup>45</sup>. Among MIEC ceramic membranes, perovskites have been extensively studied.

Perovskites, named after  $\text{CaTiO}_3$ , are studied for their high conductivity capabilities; they are mixed ionic and electronic conductors. They are described by the formula  $\text{ABO}_{3-\delta}$ . The A site is constituted of alkaline earth metals. B site is formed of transition metals.  $\delta$  is known as the quantity of oxygen vacancies. It is a thermodynamical value. Indeed the oxidative state of A cation is  $n$  (2 or 3), while the oxidative state of B cation is  $m$  (2, 3 or 4). In order to respect the electro neutrality of the solid, all oxygen sites are not occupied, which define the quantity of oxygen vacancies ( $\delta$ ). Indeed, when  $n+m=6$ , then  $\delta=0$ , when  $n+m=6-x$ , then  $\delta=x/2$ .

Since the early 1980s, perovskites materials have been used as cathode materials in solid oxide fuel cells (SOFC) and oxygen separation membranes<sup>46-49</sup>. Perovskites and related structures are conductors that exhibit the highest oxygen semi-permeability.

The oxygen transport through these materials can be described by three major steps. The dissociative adsorption of  $\text{O}_2$  on the surface of the perovskite leading to the formation of anionic oxygen  $\text{O}^{2-}$ , then its diffusion by an activated hopping mechanism with oxygen vacancies ( $V_{\text{O},s}^{\bullet\bullet}$ ) and finally the desorption/recombination of  $\text{O}_2$  on the permeate side<sup>50</sup>. Different experimental techniques are used to measure the flux of oxygen. Associated models have been developed to estimate the adsorption and desorption kinetics and diffusion coefficient that govern the oxygen flux in perovskite membranes.

### II.1. Transport mechanisms

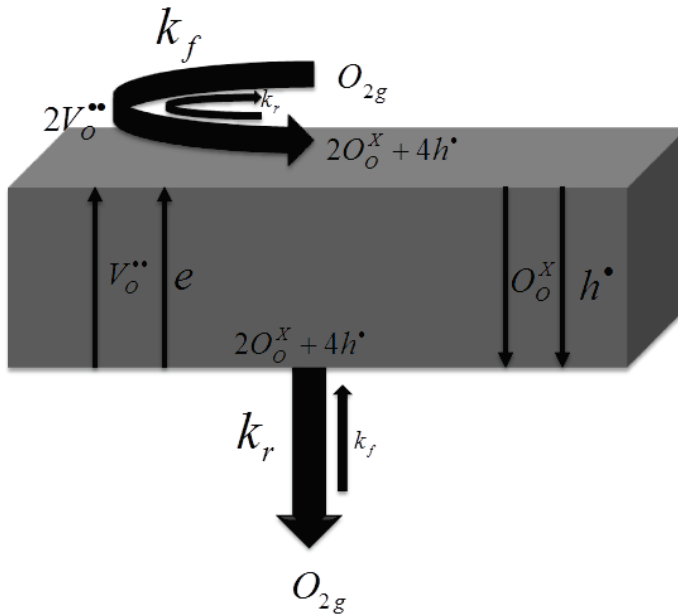
All the mechanisms associated to the oxygen transport steps, (adsorption, desorption and diffusion) would be written in Kröger and Vink notation reported in Table 2.

Table 2 Kröger-Vink notation for point defects in crystals. Divalent ions are chosen as example with MO as a compound formula with  $M^{2+}$ ,  $O^{2-}$  as cation and anion, respectively<sup>50</sup>

Symbol	Type of defect
$V_M''$	Metal ion vacancy: vacant metal site with effective charge of -2 (with the respect of the ideal lattice)
$V_O^{\bullet\bullet}$	O ion vacancy: vacant O site with effective charge of +2 (with the respect of the ideal lattice)
$M_M^X, O_O^X$	Metal respectively, O ion at their normal lattice position (neutral)
$L_M'$	$L^+$ dopant ion on metal site with effective charge of -1 (with the respect of the ideal lattice)
$N_M^{\bullet}$	$N^{3+}$ dopant ion on metal site with effective charge of +1 (with the respect of the ideal lattice)
$e'$	(Quasi)-free electron in conduction band
$h^{\bullet}$	(Quasi)-free electron in hole in valence band
$M_i^{\bullet\bullet}$	Interstitial metal ion with effective charge +2 (with respect to the ideal lattice)
$O_i''$	Interstitial O ion with effective charge -2 (with respect to the ideal lattice)
$M_M'$	Monovalent metal ion on $M^{2+}$ position (localised electron, only possible if the metal M has multiple vacancies)
$M_M^{\bullet}$	Trivalent metal ion on $M^{2+}$ position (localised electron hole, only possible if the metal M has multiple vacancies)

The oxygen transport through a dense membrane occurs thank to the oxygen partial pressure gradient which leads to the existence of an oxygen chemical potential gradient across the membrane<sup>49</sup>.

Gelling et al.<sup>50</sup> described the different processes governing the oxygen flux through a dense membrane by three main steps (Figure 13). The Kröger-Vink<sup>50</sup> notation is used to describe these phenomena. Gaseous oxygen physisorbs on the surface of the membrane then dissociates and incorporates into a surface oxygen vacancy ( $V_{O,s}^{\bullet\bullet}$ ). The adsorbed oxygen surface species are described as  $O_{O,s}^X$  and  $h^{\bullet}$  stands for the electronic defects. The adsorbed oxygen then diffuses through the dense membrane via bulk oxygen vacancies. Finally, the oxygen desorbs on the other side of the membrane, via the reverse process described above for the air side



**Figure 13 Transport through dense membranes: main steps of a p type MIEC**

The following table (Table 3) describes the main reactions which could occur during the oxygen transport in the dense membrane. The three first equations designate adsorption phenomena on the membrane in the higher oxygen partial pressure compartment. The two next steps represent the diffusion through the dense membrane, and finally the three last reactions illustrate the desorption on the lower oxygen partial pressure side. Phases with a ' correspond the air side and with a '' to the reaction side.

**Table 3 Oxygen transport through the dense membrane: detail mechanism**

Exchange step	$\frac{1}{2} O_{2(g')} \leftrightarrow \frac{1}{2} O_{2(s')}$	(7)
Exchange step	$\frac{1}{2} O_{2(s')} \leftrightarrow O_{(s')}$	(8)
Exchange step	$O_{(s')} + V_{O(s')}^{\bullet\bullet} \leftrightarrow O_{O(s')}^X + 2h_{(s')}^{\bullet}$	(9)
Diffusion step	$O_{O(s')}^X \leftrightarrow O_{O(s'')}^X$	(10)
Diffusion step	$h_{(s')}^{\bullet} \leftrightarrow h_{(s'')}^{\bullet}$	(11)
Exchange step	$O_{O(s'')}^X + 2h_{(s'')}^{\bullet} \leftrightarrow O_{(s'')} + V_{O(s'')}^{\bullet\bullet}$	(12)
Exchange step	$O_{(s'')} \leftrightarrow \frac{1}{2} O_{2(s'')}$	(13)
Exchange step	$\frac{1}{2} O_{2(s'')} \leftrightarrow \frac{1}{2} O_{2(g'')}$	(14)

Oxygen diffusion occurring in dense membrane can be via vacancy, via interstitial site or by pushing neighbour atom (Figure 14). The (a) type is based on the diffusion of an oxygen atom in a oxygen vacancy naturally present in the perovskite material. The second diffusion type (b) is based on diffusion across the interstitial site, this phenomena requires a cell parameter big enough. The

diffusion can finally be described as (c) which is based on the pushing of the neighbour atom. All authors agreed to validate the hypothesis (a) for perovskite materials. The oxygen vacancies concentration<sup>51</sup> in the perovskite materials plays an major role in the diffusion phenomena. Their characterization as a function of the experimental conditions has lead to a high quantity of studies.

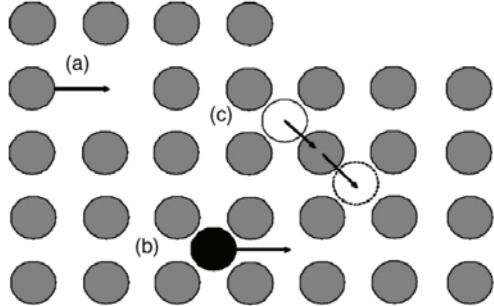


Figure 14 Various lattice diffusion mechanisms (a) via vacancy, (b) via interstitial site and (c) pushing neighbour atom<sup>52</sup>

The quantity of vacancies is a key parameter in the oxygen transport in the dense membrane and should be well characterized. It is defined by the electro neutrality law.

$$A^{(n+)}B^{(m+)}O_{3-\delta} \quad (15)$$

$$\delta = 3 - \frac{n + m}{2} \quad (16)$$

Different kinds of characterizations and  $\delta$  measurements have been developed. Lankhorst et al.<sup>53</sup> used the coulometric titration in order to determine  $\Delta\delta$ . The coulometric titration is based on the evolution of the current of electrochemical cell over the time. The second method is X-ray Absorption Spectroscopy<sup>54,55</sup>. The last method cited by many authors<sup>56</sup> is thermo gravimetric analysis (TGA). This technique is based on the relative mass variation during the increase of the temperature of the sample. The initial point should be determined by another technique as the coulometric titration, the TGA under pure H<sub>2</sub> or the iodometric titration<sup>49</sup>.

## II.2. Characterization and transport modelling

The experiment set up used to characterize the oxygen flux through a dense membrane is based on a two chamber reactor (Figure 15). On one side, the reactor is fed by air and on the other side by inert gas. For tubular membrane reactor, in order to avoid mechanical stress, tubes are dead-end tubes and the air flows either inside or outside the tube.

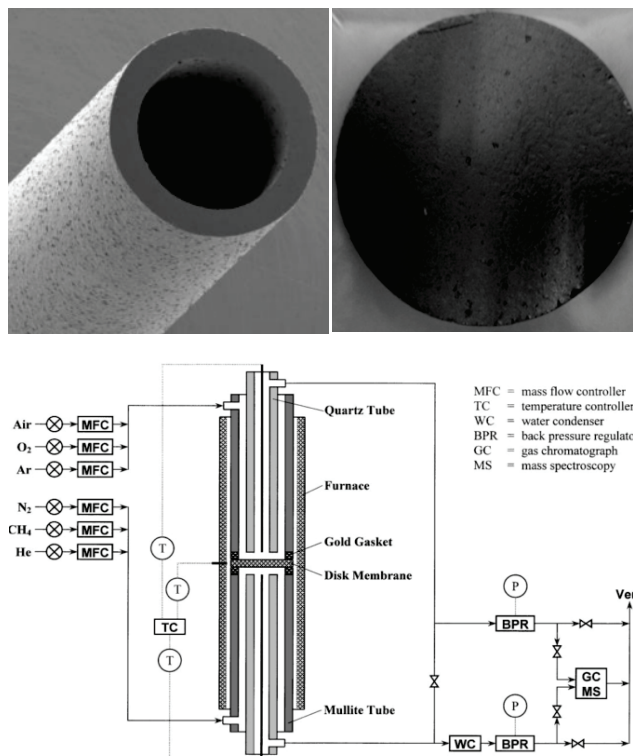


Figure 15 Tubular membrane and planar membrane-membrane set-up<sup>57</sup>

The outlet flow can be characterized either by gas chromatography or mass spectrometry. The flux is studied under various conditions (variation of the oxygen partial pressure in the air side, the total flow rate on each side, the total pressure, the temperature or the membrane thickness).

The experimental data give only little information on the oxygen flux mechanism and could not be used as final data to enhance the design of the reactor. Direct flux measurements give a qualitative approach of the flux of oxygen through the dense membrane. No information can be obtained on the intrinsic mechanism occurring during the oxygen transport across the dense membrane. No kinetic parameter governing the flux could be obtained. Thus the optimization of the design of the reactor could not be done.

Many authors worked on the valorisation of these flux data. Indeed some of them measured the oxygen conductivity through the dense membrane which leads to a flux equation, other on the structure-flux empirical equations and the last ones worked on developing flux equation based on apparent kinetic parameters.

### II.2.1. Measurement of the oxygen semi-permeation and the oxygen activity drop on both membrane faces

The oxygen semi permeation was measured using the setup in Figure 16. On one side, air gas flow was applied and on the other side, pure argon flow in order to create oxygen partial pressure gradient. These tests were done in a temperature range from 973 K to 1273 K by steps of 20 K.

Different oxygen partial pressures were recorded in order to measure the flux.  $P_1$  is the oxygen partial pressure on the air side.  $P_2$  and  $P_3$  are measured on the other side, the first one is the inlet (pure Argon flux) and the second one is the outlet (Argon richer in oxygen).

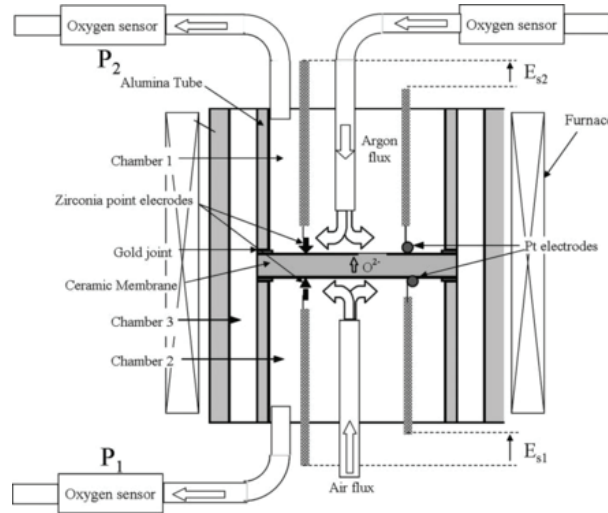


Figure 16 Schematic diagram of oxygen semi-permeation flux system with the oxygen activity measurements at membrane surfaces<sup>58,59</sup>

Knowing these oxygen partial pressures, Geffroy et al.<sup>60</sup> were able to calculate an oxygen flux using equation (17).

$$J_{O_2} = \frac{D_{Ar}}{V_M} \frac{(P_{2out} - P_{2in})}{S} \quad (17)$$

$J_{O_2}$  is the oxygen semi-permeation flux through the dense membrane ( $\text{mol m}^{-2} \text{s}^{-1}$ ).  $D_{Ar}$  is the Argon flow in  $\text{l s}^{-1}$  ( $=3.33 \times 10^{-3} \text{ l s}^{-1}$ ),  $V_m$  is the gas molar volume at 298 K under 100 kPa.

The electromotive force is given by each Yttria-Stabilized Zirconia (YSZ)-oxygen sensor used for the measurement of the oxygen pressure in the flowing gases,  $E_{\text{sensor}}$ , between both opposite faces of the zirconia tube (use of the Nernst Law, equation (18)).

$$E_{\text{sensor}} = \frac{RT}{4F} \ln \frac{P_{2out}}{P_{O_2(\text{air})}} \quad (18)$$

They measure then the drop of activity on both side of the membrane, which lead to equations (19) and (20).

$$E_{s1} = \frac{RT}{4F} \ln \frac{a_1}{a'_1} = \frac{\Delta\mu_{O_2}^{surf(Ox)}}{4F} \quad (19)$$

$$E_{s2} = \frac{RT}{4F} \ln \frac{a_2}{a'_2} = \frac{\Delta\mu_{O_2}^{surf(Ox)}}{4F} \quad (20)$$

The dioxygen activity in air (resp. In sweep side) is  $a_1$  (resp  $a_2$ ) which is equal to the oxygen partial pressure of oxygen, noted  $P_1$  (resp  $P_2$ ).  $a'_1$ (resp  $a'_2$ ) is the dioxygen activity at the rich surface of the membrane (resp lean surface of the membrane). Then  $\Delta\mu_{O_2}^{surf(ox)}$  (resp  $\Delta\mu_{O_2}^{surf(red)}$ ) is the drop of chemical potential on at the oxygen rich surface of the membrane (resp lean surface of the membrane).

The oxygen activity gradient through the membrane volume,  $E_v$ , is calculated as function of  $E_{sensor}$ ,  $E_{s1}$  and  $E_{s2}$ , as equation (21):

$$E_v = \frac{RT}{4F} \ln \frac{a'_1}{a'_2} = E_{sensor} - E_{s1} - E_{s2} = \frac{\Delta\mu_{O_2}^{bulk}}{4F} \quad (21)$$

They used these activity values to determine the rate limiting step. The flux is then described by three main steps (Figure 17).

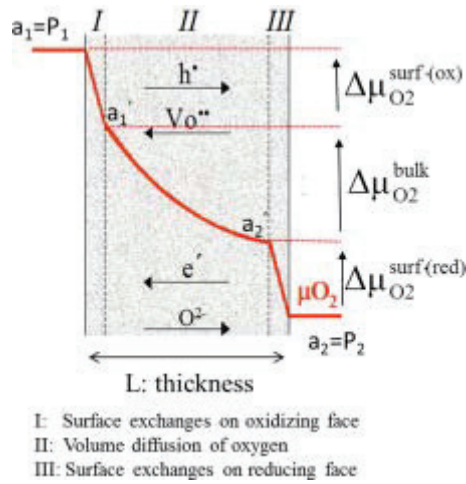


Figure 17 Oxygen activity gradient through the membrane involving three main steps for the oxygen transport<sup>42</sup>

### II.2.2. Establishment of Structure-Flux properties

Among attempts to establish Structure-Flux properties, Ullmann, et al.<sup>61</sup> correlated the Thermal Expansion Coefficient (TEC) with the oxygen ionic conductivity on a series of 23 different  $AA'BB'O_{3-\delta}$  perovskites membranes, as shown on Figure 18. However, this empirical trend does not hold for materials with other structures (such as  $LaSrGaMgO_3$ ). Looking at other well known perovskite such as  $Ba_{0.5}Sr_{0.5}Co_{0.8}Fe_{0.2}O_{3-\delta}$ , the empirical law established by Ullmann et al.<sup>61</sup> could not be used; the  $\log\sigma_o$  is higher than for La based perovskite for a similar TEC. Indeed, Wei et al.<sup>62</sup> determined the specific TEC of BSCF between 50-1000°C:  $TEC_{BSCF} = 19.95 \cdot 10^{-6} K^{-1}$  with  $\log\sigma_o = 1.53 S cm^{-1}$ .

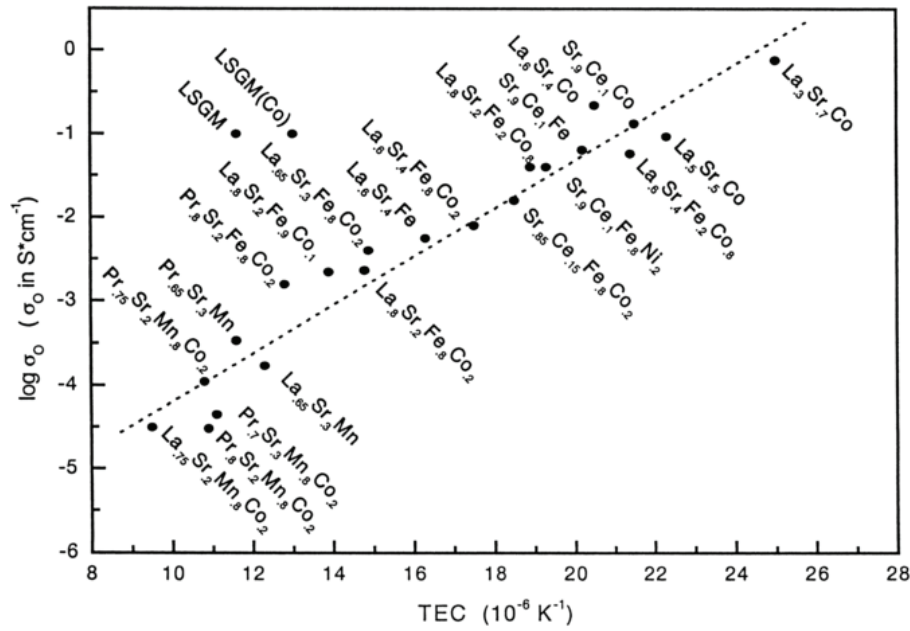


Figure 18 Correlation between thermal expansion TEC (30-1000°C) and ionic conductivity  $\sigma_0$  (800°C,air) for perovskite-type oxides. Excluding the points for LSGM electrolyte materials, the correlation reads as:  $\log(\sigma_0) = -7.08 + 2.9 \times 10^{-5} \text{TEC}$

The Nernst-Einstein equation links the oxygen conductivity ( $\sigma_0$ ) to the self diffusion of oxygen ( $D^*$ ), and the quantity of oxygen vacancies ( $\delta$ ):

$$\sigma_0 = \frac{4F^2(3 - \delta)D^*}{RTV_m} \quad (22)$$

F is the Faraday constant, R the gas constant and  $V_m$  the molar volume.

### II.2.3. Transport modelling

Oxygen transport through the dense membrane involves three phenomena. Adsorption/dissociation on the surface, the diffusion through the membrane and then desorption/recombination on the other side. Two main theories have developed to characterize this transport. The first one doesn't take in account surface phenomena, and is based on the ionic conduction across the membrane. This theory is known as the Wagner theory. The second one has been developed by Xu/Thomson and describes well all phenomena occurring within the oxygen transport.

### II.2.4. Oxygen ionic conduction based theory: Wagner

Wagner theory is based on the oxygen conduction through the dense membrane. This is a thermodynamical equation based on an irreversible phenomena. Moreover, the surface is considered in equilibrium with the  $P_{O_2}$ . As a consequence, the model assumes that the transport is diffusion limited. This equation can be used in case of diffusion limitation. The overall equation (23):

$$J_{O_2} = \frac{1}{4F^2L} \int_{\mu_{O_2}(II)}^{\mu_{O_2}(I)} t_i t_e \sigma_t d\mu_{O_2} \quad (23)$$

$$t_i = \frac{\sigma_i}{\sigma_i + \sigma_e} = \frac{\sigma_i}{\sigma_t} \quad (24)$$

$t_i$  and  $t_e$  are the ionic and electronic transfers numbers and  $\sigma_t$  is the overall conductivity.

In the case of perovskites, the electronic conductivity dominates, and the limiting step is oxygen vacancies diffusion, so  $\sigma_e \gg \sigma_i$ . Moreover, the chemical potential of oxygen is given by:

$$d\mu_{O_2} = RT d \ln P_{O_2} \quad (25)$$

And the Nernst-Einstein equation gives:

$$\sigma_i = \frac{4F^2[V_{O''}]D_v}{RTV_m} \quad (26)$$

An average value of  $\sigma_i$  is taken, and finally the flux equation becomes:

$$J_{O_2} = \frac{RT}{4F^2L} \bar{\sigma}_i \ln \frac{P'_{O_2}}{P''_{O_2}} \quad (27)$$

The Wagner theory is very powerful when the flux is limited by the diffusion. Moreover, the oxygen conductivity can be measured by various methods. But, in many conditions, the oxygen flux through the dense membrane is not limited by the diffusion, but by the oxygen exchange on the surface of the membrane.

The oxygen flux is limited either by the diffusion rate ( $D/L$ ) or by the surface exchange rate ( $k$ ). When  $D/L \ll k$ , the oxygen flux is limited by the diffusion and when  $D/L \gg k$ , the oxygen flux is limited by the surface-exchange rate. The critical length ( $L_c$ ), defined by  $D/k$  is the limit between one case and the other.

Figure 19 is an example of the variation of the oxygen flux as a function of the thickness of the membrane on  $La_{1-x}Sr_xCo_{1-y}Fe_yO_{3-\delta}$  perovskites.  $L_c$  is equal to  $400\mu m$  in that case. For a thickness  $L$  lower than  $400\mu m$ , the oxygen flux does not depend on the thickness. The surface-exchange rate is the kinetic determining step. While for thickness higher than  $400\mu m$ , the kinetic determining step is the diffusion rate.

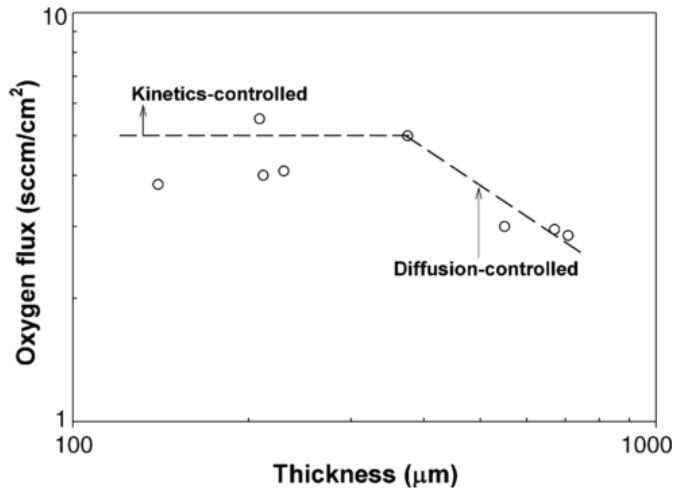


Figure 19 Variation of regime bulk-diffusion to surface-exchange reaction limited with decreasing membrane thickness for  $\text{La}_{1-x}\text{Sr}_x\text{Co}_{1-y}\text{Fe}_y\text{O}_{3-\delta}$  wherein  $x$  ranges from 0.1 to 1.0,  $y$  ranges from 0.05 to 1.0 and  $\delta$  ranges from 0.5 to 0<sup>63</sup>. On a large range of temperature, some authors point out the variation of limiting step depending on the experimental temperature. Indeed, Rebeilleau et al.<sup>34</sup> show that over 1000 K the apparent activation energy associated to the transport phenomena decreases (from 84  $\text{kJ mol}^{-1}$  to 46  $\text{kJ mol}^{-1}$ ) (Figure 20).

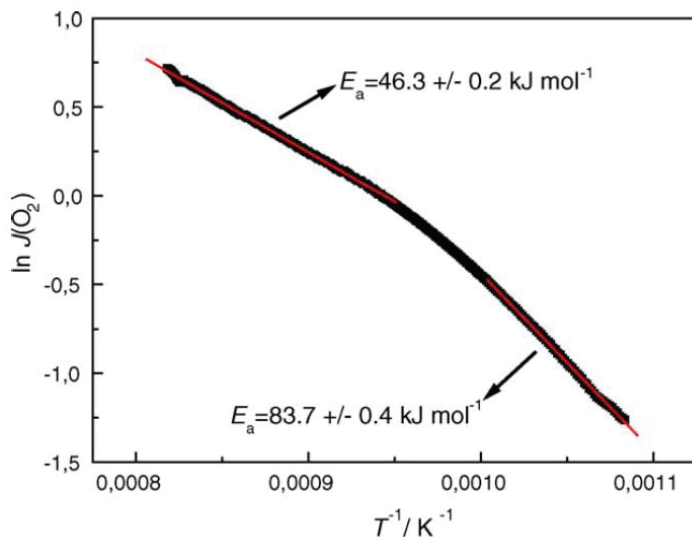


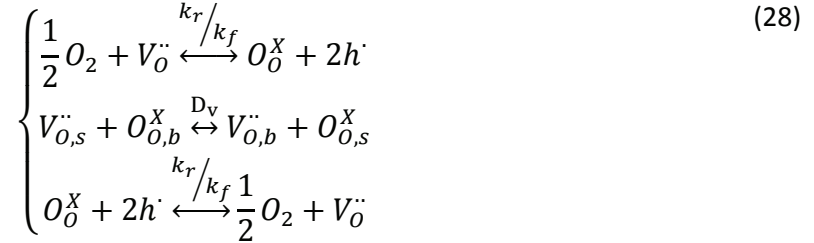
Figure 20 Determination of the activation energy for oxygen permeation in the case of a bare membrane<sup>34</sup>

Although Wagner's model is a powerful model and easy to apply, but it cannot describe many experimental conditions. Consequently, it cannot be used to optimize a reactor design. Other authors worked on the description of the oxygen flux in various conditions. Xu/Thomson developed a model able to describe a wider range of conditions.

### II.2.5. Oxygen elementary steps based theory: Xu/Thomson

Xu and Thomson<sup>57</sup> have developed a membrane transport model which allows determining the

adsorption and desorption kinetics and diffusion coefficients of the membrane materials from oxygen flux experimental data. The model is based on the following assumptions: Gas transfers are much faster than oxygen transport in the materials and are not rate-controlling. Because of the overwhelming electrons conductivities of perovskite over electronic conductivity, the transport resistance for electron-holes can be neglected<sup>49</sup>.



About the diffusion, Xu and Thomson<sup>57</sup> assumed that the oxygen permeation rate across a perovskite membrane is overwhelmingly governed by the flux of oxygen vacancies  $J_v$ . Heyne, et al.<sup>64</sup> described this flux by the following equation:

$$J_v = -\frac{\sigma_v}{4F^2} (\nabla\mu_v + 2F\nabla\Phi) \quad (29)$$

Where  $\sigma_v$  is the oxygen vacancy conductivity;  $\nabla\mu_v$  and  $\nabla\Phi$  are the gradients of the chemical potential and the electric field, respectively. Because of the fast movement of electron-holes inside the open circuit membrane, a steady-state electric field gradient is not established and  $\nabla\Phi = 0$ . And assuming ideal behavior, the chemical potential gradient can be correlated to the concentration of oxygen vacancies by:  $\nabla\mu_v = RT\nabla \ln C_v$

Since the thickness of the membrane disks are small compared with their diameters, radial diffusion has been neglected. So finally, with these equations as well as the Einstein relation ( $\sigma_v = (4F^2/RT)C_v D_v$ ), they obtained:

$$J_v = -D_v \frac{dC_v}{dx} \quad (30)$$

Once the steady state structure is established under certain temperatures,  $D_v$  can be considered constant and not to be a function of the position from the membrane wall. Based on this analysis and considering  $J_{O_2} = -\frac{1}{2}J_v$ .

$$J_{O_2} = \frac{D_v}{2L} (C_v'' - C_v') \quad (31)$$

Where  $L$  is the membrane thickness,  $C_v'$  and  $C_v''$  are the concentration of oxygen vacancies at the high and low oxygen pressure sides of the membrane respectively.

Finally they described the flux using the following equation system:

$$\begin{cases} J_{O_2} = k_f P_{O_2}^{\prime 0.5} C_v' - k_r \\ J_{O_2} = \frac{D_v}{2L} (C_v'' - C_v') \\ J_{O_2} = k_r - k_f P_{O_2}^{\prime \prime 0.5} C_v'' \end{cases} \quad (32)$$

They arrive at the following expression for the oxygen flux across a thin ceramic membrane:

$$J_{O_2} = \frac{D_v k_r (P_{O_2}^{\prime 0.5} - P_{O_2}^{\prime \prime 0.5})}{2L k_f (P_{O_2}^{\prime} P_{O_2}^{\prime \prime})^{0.5} + D_v (P_{O_2}^{\prime} + P_{O_2}^{\prime \prime})} \quad (33)$$

The 6 parameters of the expression accounting for pre-exponential factors of the diffusion, forward reaction and reverse reaction ( $D_v^\circ$ ,  $k_f^\circ$ ,  $k_r^\circ$ ) and associated activation energy ( $E_d$ ,  $E_f$ ,  $E_r$ ) have been estimated by regression on two different membranes and using 126 different experimental conditions of oxygen partial pressures and temperatures. This equation can be used to predict the oxygen permeation for a dense membrane as a function of the operating conditions, provided that the kinetic ( $k_f$ ,  $k_r$ ) and transport ( $D_v$ ) constants are known.

A parity plot has been obtained with the results on the 3 different membranes (Figure 21). Disk #1 is LSCF based membrane of 3.99 mm thickness. In these conditions, they are highly limited by the diffusion across the membrane. This membrane has been tested in various conditions:  $1023 < T(^{\circ}C) < 1223$  K,  $21 < P'_{O_2} < 100$  kPa; the model gives very good results. Disk #2 is based on the same material, but its thickness is only 1.65mm (and disk 3 of 1.68 mm thick). This membrane has been tested in the same range of temperature with  $P'_{O_2} = 21$  kPa, while Disk #3 was under  $P'_{O_2} = 1$  kPa. The results on membrane 2 are very concluding; the model seems to be appropriate. But on membrane 3, the results do not fit with this model. Although, this model can described properly the flux of oxygen through the dense membrane, if the conditions are too extreme (as high oxygen partial pressure gradient on a thin membrane), this model cannot predict the behaviour of the membrane.

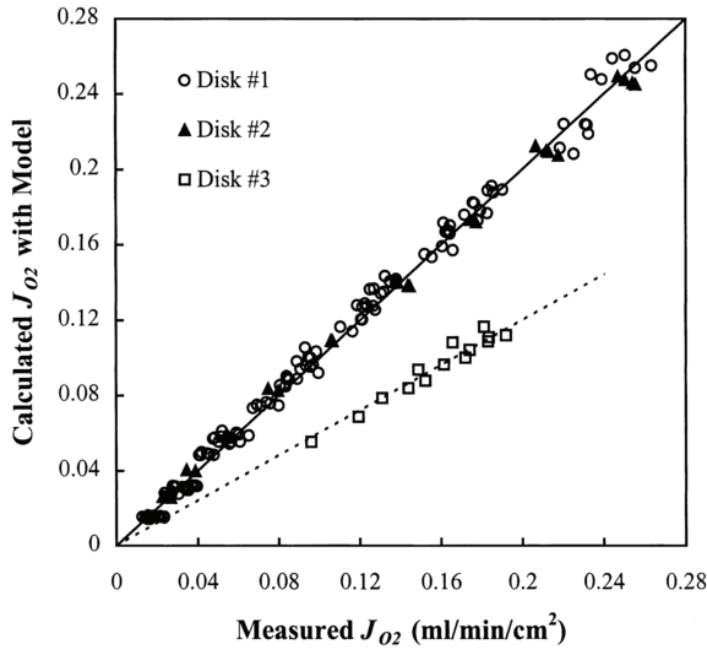


Figure 21 Comparison of oxygen flux measurements with model predictions on LSCF: Disk 1:  $L=3.99\text{mm}$ ;  $750 < T(^{\circ}\text{C}) < 950$ ,  $0.21 < P'_{\text{O}_2} < 1\text{atm}$ ; Disk 2:  $L=1.65\text{mm}$ ;  $750 < T(^{\circ}\text{C}) < 950$ ,  $P'_{\text{O}_2}=0.21\text{atm}$ ; Disk 3:  $L=1.68\text{mm}$ ;  $750 < T(^{\circ}\text{C}) < 950$ ,  $P'_{\text{O}_2}=1\text{atm}$ .<sup>57</sup>

A new model should be developed in order to describe all the experimental conditions to design an optimal reactor in the working conditions without testing all the various possibilities. Moreover, some experiments have been run with catalyst coated on the dense membrane (Figure 22). Rebeilleau et al.<sup>34</sup> studied the impact of V/MgO coating and Pd coating on the flux of  $\text{Ba}_{0.5}\text{Sr}_{0.5}\text{Co}_{0.8}\text{Fe}_{0.2}\text{O}_{3-\delta}$ . The obtained fluxes are higher in the case of coated membranes.

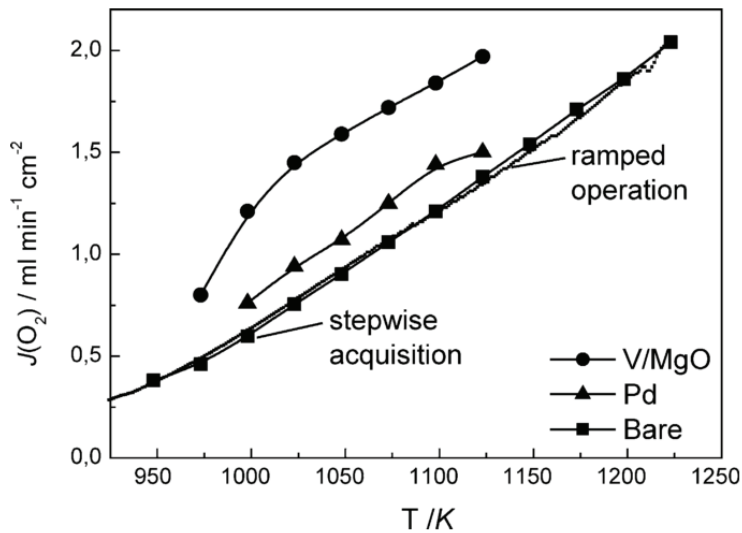


Figure 22 Oxygen permeation fluxes of bare (square scatter), Pd nano cluster modified (up triangle scatter) and V/MgO micron grain modified (circle scatter) membrane as a function of the temperature. The air side compartment was fed with  $50\text{ml min}^{-1}$ , the permeation side was swept with  $30\text{ml min}^{-1}$  He at total pressure of  $110\text{ kPa}$  on both sides<sup>34</sup>.

### III. STRATEGY FOLLOWED IN THIS WORK

The development of dense membranes is a very tedious procedure through mainly trial and error. The experimental procedures are difficult and time-consuming as often a disk or tubular shape membranes have to be fabricated to measure the oxygen permeation flux under varying operating conditions. The high temperatures required for good permeability often cause sealing issues with disks or tubes. Moreover, the testing of membrane free from external mass and heat transfer limitations is challenging as pressure gradients are difficult to be controlled. As a result variations of the oxygen permeability of one order of magnitude for the same material are reported. The handling of materials in powder form is much easier and faster experimentation. Hence, there is a strong incentive to develop alternative approaches, which does not involve membrane testing. To determine oxygen transport in the dense membrane from powders, each elementary step should be precisely known to obtain a set of parameter describing all the experimental conditions. We will work on a possible route to determine all kinetic parameters governing the oxygen flux from the corresponding powder (chapter 3). It would be assumed that the oxygen vacancies concentration has a strong impact on the kinetic parameters which is not in agreement with the literature.

Once these parameters obtained, they would be integrated in a flux equation (chapter 4). The Wagner's model as well as the Xu/Thomson can describe the oxygen flux through the dense membrane in well defined conditions. These models are based on apparent kinetic parameters determined from fitting on membrane oxygen flux. No current model is able to describe the oxygen flux based on intrinsic kinetic parameters. A new model should be developed taking into account all the variation occurring when the oxygen is transported from one side of the membrane to another. Some assumptions will be done on the profile of the diffusion across the membrane, as the diffusion would have been determined as a function of the oxygen vacancies.

The methodology of chapter 3 and 4 would be developed on  $\text{Ba}_{0.5}\text{Sr}_{0.5}\text{Co}_{0.8}\text{Fe}_{0.2}\text{O}_{3-\delta}$  (BSCF) membrane which is known to exhibit a high oxygen flux. In order to validate this method, the same procedure would be applied on two other perovskites (chapter 5). The first one,  $\text{La}_{0.6}\text{Sr}_{0.4}\text{Co}_{0.2}\text{Fe}_{0.8}\text{O}_{3-\delta}$  (LSCF) have been first studied in the late 1980s by Teraoka et al.<sup>48</sup>. Moreover, Xu and Thomson developed their flux model on it. Then we will look at a cobalt-free alternative to both  $\text{La}_{0.6}\text{Sr}_{0.4}\text{Co}_{0.2}\text{Fe}_{0.8}\text{O}_{3-\delta}$  and  $\text{Ba}_{0.5}\text{Sr}_{0.5}\text{Co}_{0.8}\text{Fe}_{0.2}\text{O}_{3-\delta}$ . Indeed, new existing regulations are set up to remove cobalt oxide in chemistry industry. Many groups worked on cobalt-free perovskites:  $\text{La}_{1-x}\text{Sr}_x\text{FeO}_{3-\delta}$ <sup>65</sup>,  $\text{CaTi}_{0.8}\text{Fe}_{0.2}\text{O}_{3-\delta}$ <sup>66</sup>,  $\text{Ba}_{0.3}\text{Sr}_{0.7}\text{FeO}_{3-\delta}$ <sup>67</sup>,  $\text{La}_{0.6}\text{Sr}_{0.4}\text{Ga}_{0.6}\text{Fe}_{0.4}\text{O}_{3-\delta}$ <sup>68</sup>,  $\text{BaFe}_{1-y}\text{Ce}_y\text{O}_{3-\delta}$ <sup>69</sup> and  $\text{Ba}_{0.5}\text{Sr}_{0.5}\text{Fe}_{0.8}\text{Zn}_{0.2}\text{O}_{3-\delta}$ <sup>70</sup>. In the late 2000s,  $\text{BaFeO}_{3-\delta}$  based cobalt free family has been developed in a Japanese group<sup>71,72</sup>. They pointed out the high oxygen permeation of  $\text{Ba}_{0.95}\text{La}_{0.05}\text{FeO}_{3-\delta}$  (BLF) ( $1.96 \text{ ml min}^{-1} \text{ cm}^{-2}$  at  $930 \text{ }^\circ\text{C}$  for 1 mm

thickness). It is why we choose to study this material in order to know if it can be a suitable alternative to BSCF. Finally an optimal design of the membrane would be discuss.

Then, BSCF membrane would be integrated in a membrane reactor for OCM. For now, no breakthrough results have been obtained on this design. The coupling of a thin catalytic layer avoiding oxygen recombination and an optimal design of the reactor may give a better understanding of the reaction and lead to a good reactor (chapter 6).

This work would be concluded on a discussion on the optimal design regarding the membrane and the reactor conception in order to reach a high C<sub>2</sub> selectivity and productivity.

# Bibliography

---

1. G. E. Keller and M. M. Bhasin, *J. Catal.*, 1982, **73**, 9–19.
2. S. Lacombe, H. Zanthoff and C. Mirodatos, *J. Catal.*, 1995, **155**, 106–116.
3. V. . Choudhary, V. H. Rane and R. . Gadre, *J. Catal.*, 1994, **145**, 300–311.
4. O. V. Buyevskaya, M. Rothaemel, H. W. Zanthoff and M. Baerns, *J. Catal.*, 1994, **150**, 71–80.
5. G. T. Baronetti, C. Padre, O. A. Scelza and A. A. Castro, *Appl. Catal. A Gen.*, 1993, **101**, 167–183.
6. Q. Chen, J. H. B. J. Hoebink and G. B. Marin, *Ind. Eng. Chem. Res.*, 1991, **30**, 2088–2097.
7. T. Ito, J. Wang, C. H. Lin and Lun, *J. Am. Chem. Soc.*, 1985, **18**, p5062–5068.
8. L. M. Aparicio, S. A. Rossini, D. G. Sanfilippo, J. E. Rekoske, A. A. Treviio and J. A. Dumesic, *Ind. Eng. Chem. Res.*, 1991, **30**, 2114–2123.
9. J. G. McCarty, in *Methane Conversion by Oxidative processes*, Springer Netherlands, New York, E.E. Wolf., 1992, pp. 320–350.
10. S. C. Reyes, E. Iglesia and C. P. Kelkar, *Chem. Eng. Sci.*, 1993, **48**, 2643–2661.
11. O. V. Krylov, in *Kinetics and Catalysis*, 1993, p. 250.
12. U. Zavyalova, M. Holena, R. Schlögl and M. Baerns, *Chem Cat Chem*, 2011, **3**, 1935–1947.
13. V. I. Alexiadis, J. W. Thybaut, P. N. Kechagiopoulos, M. Char, A. C. Van Veen, M. Muhler and G. B. Marin, *Appl. Catal. B Environ.*, 2014, **150-151**, 496–505.
14. Y. Moro-oka, *Catal. Today*, 1998, **45**, 3–12.
15. G. D. Moggridge, J. P. . Badyal and R. M. Lambert, *J. Catal.*, 1991, **132**, 92–99.
16. J. a. Duffy, *J. Solid State Chem.*, 1986, **62**, 145–157.
17. A. M. Maitra, *Appl. Catal. A Gen.*, 1994, **114**, 65–81.
18. J. A. P. Carreiro and M. Baerns, *J. Catal.*, 1989, **117**, 396–403.
19. W. Bytyn and M. Baerns, *Appl. Catal. A Gen.*, 1986, **28**, 199–207.
20. V. R. Choudhary and V. H. Rane, *J. Catal.*, 1991, **422**, 411–422.

21. P. Kässner and M. Baerns, *Appl. Catal. A Gen.*, 1996, **139**, 107–129.
22. J.-L. Dubois and C. J. Cameron, *Appl. Catal.*, 1990, **67**, 49–71.
23. D. Dissanayake, J. H. Lunsford and M. P. Rosynek, *J. Catal.*, 1994, **146**, 613–615.
24. L. Olivier, S. Haag, H. Pennemann, C. Hofmann, C. Mirodatos and a Vanveen, *Catal. Today*, 2008, **137**, 80–89.
25. Z. Stansch, L. Mleczko and M. Baerns, *Ind. Eng. Chem. Res.*, 1997, 2568–2579.
26. M. Traykova, N. Davidova, J. Tsaih and A. H. Weiss, *Appl. Catal. A Gen.*, 1998, **169**, 237–247.
27. J. W. Thybaut, J. Sun, L. Olivier, A. C. Van Veen, C. Mirodatos and G. B. Marin, *Catal. Today*, 2011, **159**, 29–36.
28. H. Wang, Y. Cong and W. Yang, *Catal. Today*, 2005, **104**, 160–167.
29. S. Arndt, 2010.
30. S. Arndt, T. Otremba, U. Simon, M. Yildiz, H. Schubert and R. Schomäcker, *Appl. Catal. A Gen.*, 2012, **425-426**, 53–61.
31. T. Serres, Univerty of Lyon 1, 2013.
32. L. Mleczko and M. Baerns, *Fuel Process. Technol.*, 1995, **42**, 217–248.
33. P. . Couwenberg, Technische Universiteit Eindhoven, 1995.
34. M. Rebeilleau-Dassonneville, S. Rosini, a. C. Van Veen, D. Farrusseng and C. Mirodatos, *Catal. Today*, 2005, **104**, 131–137.
35. J. H. White, E. A. Needham, R. L. Cook and A. F. Sammells, *Solid State Ionics*, 1992, **53-56**, 149–161.
36. Y. Lu, A. G. Dixon, W. R. Moser and Y. H. Ma, 2000, **55**, 4901–4912.
37. Z. Taheri, K. Nazari, A. A. Safekordi and N. Seyed-matin, *J. Mol. Catal. A Chem.*, 2008, **286**, 79–86.
38. Z. Shao, H. Dong, G. Xiong, Y. Cong and W. Yang, 2001, **183**, 181–192.
39. J. Wang, L. Chou, B. Zhang, H. Song, J. Zhao, J. Yang and S. Li, *J. Mol. Catal. A Chem.*, 2006, **245**, 272–277.
40. P. Zeng, Z. Chen, W. Zhou, H. Gu, Z. Shao and S. Liu, *J. Memb. Sci.*, 2007, **291**, 148–156.
41. A. Thursfield and I. S. Metcalfe, *J. Mater. Chem.*, 2004, **14**, 2475.
42. H. J. M. Bouwmeester, *Catal. Today*, 2003, **82**, 141–150.

43. H. Dong, Z. Shao, G. Xiong, J. Tong, S. Sheng and W. Yang, *Catal. Today*, 2001, **67**, 3–13.
44. J. E. Elshof, H. J. M. Bouwmeester and H. Verweij, *Appl. Catal.*, 1995, **130**, 195–212.
45. Z. Shao and S. M. Haile, *Nature*, 2004, **431**, 170–3.
46. T. Schiestel, M. Kilgus, S. Peter, K. Caspary, H. Wang and J. Caro, *J. Memb. Sci.*, 2005, **258**, 1–4.
47. C. Tablet, Universität Hannover, 2006.
48. Y. Teraoka, Z. Hua-Min, S. Furukawa and N. Yamazoe, *Chem. Lett.*, 1985, 1743–1746.
49. J. Sunarso, S. Baumann, J. M. Serra, W. a. Meulenber, S. Liu, Y. S. Lin and J. C. Diniz da Costa, *J. Memb. Sci.*, 2008, **320**, 13–41.
50. P. J. Gellings and H. J. M. Bouwmeester, *Catal. Today*, 2000, **58**, 1–53.
51. J. B. Goodenough, *Proc. R. Soc. Lond.*, 1984, 215–234.
52. P. Kofstad, *Wiley-Interscience, Toronto*, 1972.
53. M. H. R. Lankhorst, J. E. Elshof, T. La and S. Mo, *J. Solid State Chem.*, 1997, **310**, 302–310.
54. D. C. Koningsberger and R. (eds) Prins, 1988.
55. A. V Chadwick, C. Colli, C. Maltese, G. Morrison, I. Abrahams and A. Bush, *Solid State Ionics*, 1999, **119**, 79–84.
56. S. Kim, Y. L. Yang, A. J. Jacobson and B. Abeles, *Solid State Ionics*, 1998, **106**, 189–195.
57. S. J. Xu and W. J. Thomson, *Chem. Eng. Sci.*, 1999, **54**, 3839–3850.
58. A. Julian, E. Juste, P. M. Geffroy, V. Coudert, S. Degot, P. Del Gallo, N. Richet and T. Chartier, *J. Memb. Sci.*, 2009, **333**, 132–140.
59. P. M. Geffroy, J. M. Bassat, A. Vivet, S. Fourcade, T. Chartier, P. Del Gallo and N. Richet, *J. Memb. Sci.*, 2010, **354**, 6–13.
60. P. M. Geffroy, M. Reichmann, J. Fouletier, N. Richet and T. Chartier, *Chem. Eng. Sci.*, 2013, **104**, 817–828.
61. H. Ullmann, N. Trofimenko, F. Tietz, D. Stöver and a. Ahmad-Khanlou, *Solid State Ionics*, 2000, **138**, 79–90.
62. B. Wei, Z. Lu, X. Huang, J. Miao, X. Sha, X. Xin and W. Su, *J. Eur. Ceram. Soc.*, 2006, **26**, 2827–2832.
63. 1995, US Patent 5.240.480.
64. L. Heyne, in *Solid Electrolytes*, ed. S. Beler, Springer, New York, 1977, pp. 169–221.

65. J. E. Elshof, H. J. M. Bouwmeester and H. Verweij, *Solid State Ionics*, 1995, **81**, 97–109.
66. H. Iwahara, T. Esaka and T. Mangahara, *J. Appl. Electrochem.*, 1988, **18**, 173–177.
67. Y. Teraoka, H. Shimokawa, C. Kang, H. Kusaba and K. Sasaki, *Solid State Ionics*, 2006, **177**, 2245–2248.
68. T. Ishihara, T. Yamada, H. Arikawa, H. Nishiguchi and Y. Takita, *Solid State Ionics*, 2000, **135**, 631–636.
69. X. Zhu, H. Wang and W. Yang, *Solid State Ionics*, 2006, **177**, 2917–2921.
70. H. Wang, C. Tablet, A. Feldhoff and J. Caro, *Adv. Mater.*, 2005, **17**, 1785–1788.
71. K. Watanabe, S. Ninomiya, M. Yuasa, T. Kida, N. Yamazoe, H. Haneda and K. Shimanoe, *J. Am. Ceram. Soc.*, 2010, **93**, 2012–2017.
72. K. Watanabe, M. Yuasa, T. Kida, Y. Teraoka, N. Yamazoe and K. Shimanoe, *Adv. Mater.*, 2010, **22**, 2367–70.



# Chapter 2-Experimental procedures:

---

The experimental work of the PhD is divided in three main parts: the synthesis and the characterization of the powder of perovskite in order to determine microkinetic parameter; the measurement of the oxygen flux through the dense membrane of the corresponding composition; and finally, the study of the oxidative coupling of methane in the membrane reactor bench with or without catalyst.

## IV. Perovskite material and membrane characterization

### IV.1. Perovskite synthesis:

Perovskite materials were synthesized using a sol gel method. 0.05 mol (about 10 g) of perovskite can be synthesized in one run. All the precursors were nitrates from Sigma Aldrich (pur: 99.5%).  $\text{La}(\text{NO}_3)_3 \cdot 6\text{H}_2\text{O}$  ( $433.01 \text{ g mol}^{-1}$ ),  $\text{Ba}(\text{NO}_3)_2$  ( $261.34 \text{ g mol}^{-1}$ ),  $\text{Sr}(\text{NO}_3)_2$  ( $211.63 \text{ g mol}^{-1}$ ),  $\text{Fe}(\text{NO}_3)_3 \cdot 9\text{H}_2\text{O}$  ( $404.00 \text{ g mol}^{-1}$ ) and finally  $\text{Co}(\text{NO}_3)_2 \cdot 6\text{H}_2\text{O}$  ( $291.03 \text{ g mol}^{-1}$ ). These components were weighted then stirred in distilled water until total dissolution of the components.

Meanwhile, Ethylenediaminetetraacetic acid (EDTA,  $292.24 \text{ g mol}^{-1}$ ) and citric acid ( $192.12 \text{ g mol}^{-1}$ ) were mixed in distilled water. One molar equivalent of EDTA was added for each molar equivalent of total metal ion (0.1 mol) and two molar equivalent of citric acid (0.2 mol). This mixture was stirred until total dissolution of both components. Ammonia solution was then slowly added until obtaining a transparent solution (about 70 mL,  $\text{pH}=6\sim 8$ ).

This second mixture was then slowly added to the first one. The solution was heated to  $100^\circ\text{C}$  and stirred until a gel like formation. The gel was cooled down and then heated for 6 hours at  $250^\circ\text{C}$  in a pre-heated furnace. Finally the powders were sintering at high temperature (from  $950$  to  $1150^\circ\text{C}$ ) for 5 hours depending on the perovskite in order to obtain a pure phase, (Figure 23). The optimal sintering temperature for each sample is recorded in Table 4.

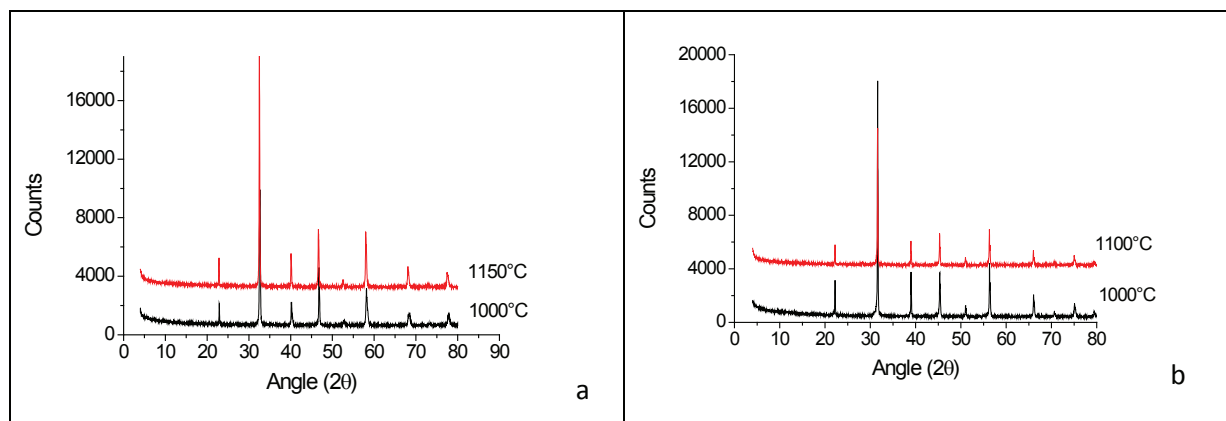


Figure 23 XRD of a)  $\text{La}_{0.6}\text{Sr}_{0.4}\text{Co}_{0.2}\text{Fe}_{0.8}\text{O}_{3-\delta}$  after sintering for 5 hours at different temperatures b)  $\text{Ba}_{0.95}\text{La}_{0.05}\text{FeO}_{3-\delta}$  after sintering for 5 hours at different temperatures

Table 4 Optimized sintering temperature to obtain pure phase perovskites

Perovskites	$\text{La}_{0.6}\text{Sr}_{0.4}\text{Co}_{0.2}\text{Fe}_{0.8}\text{O}_{3-\delta}$	$\text{Ba}_{0.95}\text{La}_{0.05}\text{FeO}_{3-\delta}$	$\text{Ba}_{0.5}\text{Sr}_{0.5}\text{Co}_{0.8}\text{Fe}_{0.2}\text{O}_{3-\delta}$
Name(in this work)	LSCF	BLF	BSCF
Firing temperature(°C)	1150	1000	1000

As the large amount of perovskite was needed for the membrane formulation, BSCF and BLF were then ordered at Marion Technologies.

## IV.2. Scanning electron microscopy (SEM)

Scanning electron microscopy was achieved on a JEOL JSM5800LV working at 15 kV. This technique was used to control nature the surface of samples and membranes before and after experiments, their morphology and the composition. Depending on the sample, line scanning or mapping were carried out. It was also applied on powder to estimate the crystallite size.

The electron beam was focused on the sample surface and scanned a sample area. The interaction between these electrons and the one from the sample involve radiation emissions of different types (back diffused elementary electrons, secondary, Auger, transmitted and X Ray electrons). The secondary electron detection allowed the surface topography rebuilding.

## IV.3. Specific area measurement by the BET method

The specific area of our samples was determined by nitrogen adsorption-desorption at 77 K with B.E.T method (Brunauer, Emmett, Teller) using ASAP 2020 apparatus. The adsorbed nitrogen quantity was measured in a pressure range  $P/P_0$  from 5 to 30 Pa.  $P_0$  is the nitrogen saturation vapour pressure at 77 K.

First of all, samples were desorbed under vacuum for a night at 673 K. Each point was repeated three times in order to make sure of the validity of our results. The specific area of our samples was included between 0.15 and 3 m<sup>2</sup> g<sup>-1</sup> which is the low limit of validity of the apparatus.

#### IV.4. X-Ray diffraction (XRD)

X-Ray diffraction was applied for different purposes. This method allowed different phase of the material identification using the Bragg's equation  $2 \cdot d_{hkl} \cdot \sin \theta = n\lambda$ . A detector measured the X ray diffraction angles due to the solid crystalline plans.

Two different apparatus were used.

The first one, a Bruker D8 Advance A25 diffractometer (Bragg-Brentano para-focusing geometry, reflection mode, Cu K<sub>α</sub> radiation 0.154184 nm, nickel filter) equipped with a 1-dimensional multistrip detector (LynxEye, 192 channels on 2.9476°) was used for standard analysis at room temperature under air. Standard measurements were recorded from 4 to 80°(2θ) with 0.02047° step and 0.5s per step for a total acquisition time of 32min .

The second one, a Panalytical X'Pert Pro MPD diffractometer (Bragg-Brentano para-focusing geometry, reflection mode, Cu K<sub>α</sub> radiation 0.154184 nm, diffracted beam graphite monochromator) equipped with a 1-dimensional multistrip detector (X'Celerator, 127 channels on 2.118°) was used for in-situ measurements. This apparatus allowed to collect X-ray powder patterns of samples at controlled temperature and under different gases.

The samples were mounted in an atmosphere-controlled Anton Paar XRK 900 reactor chamber. The Temperature-regulated glass-ceramic sample holder was open to allow the gas to flow through the sample. Samples were heated by steps up to 1073 K at a rate of 2K min<sup>-1</sup> under a 20mL min<sup>-1</sup> flow rate of 1%O<sub>2</sub> in Argon or under synthetic air (gas mixture consisting of N<sub>2</sub> : 20 mL min<sup>-1</sup> and O<sub>2</sub> : 5 mL min<sup>-1</sup>). The diffractograms were collected under isothermal conditions from 6 to 95°(2θ) with 0.0334° step and 250 s per step (90 min per scan) after a stabilization time of 1 h between each temperature modification.

Phase identification was performed using the DiffracSuite Eva software (Bruker) and the ICDD-PDF4+ database. The lattice parameters were calculated with TOPAS software.

## IV.5. Thermo gravimetric Analysis (TGA)

The thermo gravimetric analysis coupled with the differential thermal analysis (DTA) was used to study the variation of oxygen vacancies concentration in perovskites as a function of the temperature and the oxygen partial pressure<sup>1</sup>. Oxygen contents in perovskites were measured using Setsys Evolution 12 thermo gravimetric analyzer from SETARAM.

The measurements were made up 1173 K with a heating ramp of 5 K.min<sup>-1</sup> with two partial pressures of oxygen,  $P_{O_2}=21$  kPa and 1kPa using 80 mg of sample. The sample was pre-treated in an oxygen/helium mixture for 2 h hours at 1173 K in order to remove all traces of water and carbonates. The changes in the gas composition were continuously monitored by a mass spectrometer, PFEIFFER, Omnistar model (m/e=32,34,36,40,17,18,44,45&28). Inlet flows were controlled with BROOKS mass flow controllers. The structure of the perovskites was checked before and after TGA by XRD analysis. To obtain the initial point, authors used TGA under hydrogen until obtaining a mixture of metals and monometallic metals. The total reduction of the perovskite allows the determination of the initial content of oxygen. In order to validate this method, we did a XRD under hydrogen (Figure 24), the perovskite is reduced very fast but pure metals and monometallic metals mixture was not obtained, we obtained a mixture of bimetallic oxides. So we decided to use another method to determine the starting point: iodometric titration.

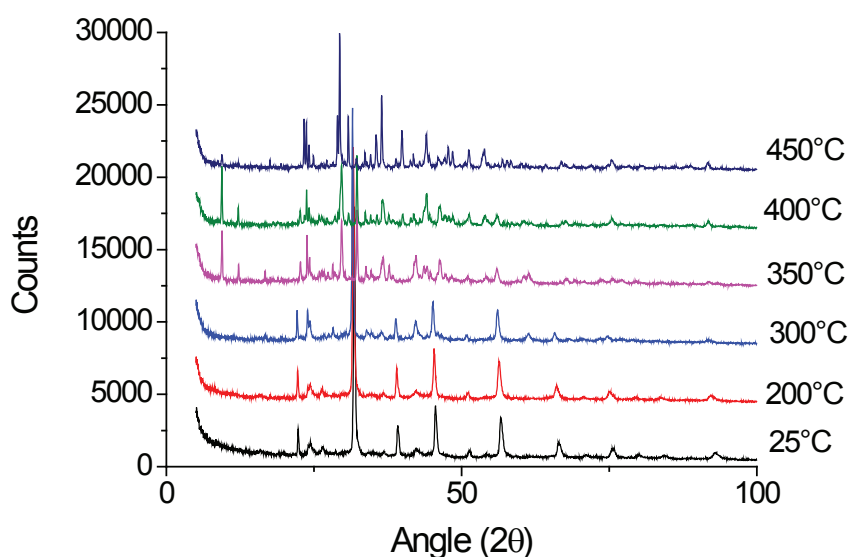
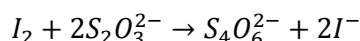


Figure 24 XRD of  $Ba_{0.5}Sr_{0.5}Co_{0.8}Fe_{0.2}O_{3-\delta}$  under pure hydrogen at different temperatures

## IV.6. Iodometric titration

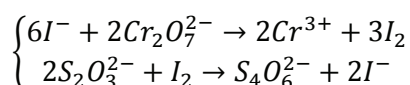
The method was described elsewhere by Manthiram, et al.<sup>2</sup>. This titration was used to calibrate the initial oxygen vacancy value under air at room temperature. The reduction of the metal ion was achieved by potassium iodide added in excess in the solution (oxidized in I<sub>2</sub>). I<sub>2</sub> was then titrated by sodium thiosulfate.



To prepare Na<sub>2</sub>S<sub>2</sub>O<sub>3</sub> (158.11 g mol<sup>-1</sup>) solution, 1L of distilled water was boiled for several minutes, then cooled down. 25 g of Na<sub>2</sub>S<sub>2</sub>O<sub>5</sub> (Sigma-Aldrich, puriss. p.a. 190.11 g mol<sup>-1</sup>), 5H<sub>2</sub>O and 0.1g Na<sub>2</sub>CO<sub>3</sub> (Sigma-Aldrich, >99%, 105.99 g mol<sup>-1</sup>) were added. This mixture was stirred until the total dissolution of the crystals and transferred to a clean brown bottle and stored in dark.

For each titration, the starch indicator was prepared the morning for a titration in the afternoon. 1 g of starch (Sigma Aldrich) was grinded into 10mL of distilled water. It was stirred thoroughly and boiled for a minute until getting a transparent solution.

The sodium thiosulfate concentration was controlled by potassium dichromate (K<sub>2</sub>Cr<sub>2</sub>O<sub>7</sub>, Sigma Aldrich, pur. 99.9%, 294.18 g mol<sup>-1</sup>) titration. About 0.15 g of K<sub>2</sub>Cr<sub>2</sub>O<sub>7</sub> was dry for 2h at 140°C. Then 0.10 g (with a precision of 0.0001 g) of K<sub>2</sub>Cr<sub>2</sub>O<sub>7</sub> was weight in an iodometric flask, dissolved in 25mL of distilled water. Then 2g of KI (Sigma Aldrich, pur. 99.9%, 166.00 g mol<sup>-1</sup>) were added and the solution was stirred gently until dissolution. 20 mL of 20% of potassium sulfate (K<sub>2</sub>SO<sub>4</sub>, Sigma Aldrich, pur >99.9%, 174.26 g mol<sup>-1</sup>) solution was added; the top was covered and then stirred gently. The flask was then put in the dark for 10 minutes. Then the titration was done with Na<sub>2</sub>S<sub>2</sub>O<sub>3</sub> (0.01 mol L<sup>-1</sup>) until the colour becomes light yellow. At this point, 2 mL of starch indicator was added. The endpoint signal is the disappearance of the blue starch-iodine complex and light green colour appears.



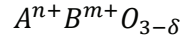
$$[S_2O_3^{2-}] = 6 \times \frac{m_{K_2Cr_2O_7}}{M_{K_2Cr_2O_7} \times V_{eq}}$$

Error calculation:

$$\bullet \quad \Delta[S_2O_3^{2-}] = [S_2O_3^{2-}] \times \left( \frac{\Delta m_{K_2Cr_2O_7}}{m_{K_2Cr_2O_7}} + \frac{\Delta V_{eq}}{V_{eq}} \right)$$

About 0.1 g of perovskites was weighted in a iodometric flask, and walls were cleaned with a small amount of water. Then 3 g of KI (Sigma Aldrich, pur. 99.9%) were added. Then the perovskite was dissolved in HCl ((Sigma) 36.5-38.0%; HCl / H<sub>2</sub>O; 1:1 volume). The solution was stirred until the total

dissolution of the solid. Then the titration was done as before. The endpoint signal is the disappearance of the blue starch-iodine complex and light pink colour appears.



The electro neutrality in a crystal leads to:

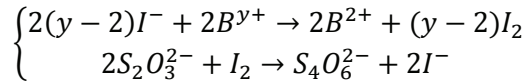
$$\delta = 3 - \frac{xn_A + yn_B}{2 \times n_O}$$

Moreover:  $n_A = n_B = n_{ABO_{3-\delta}}$

Finally:

$$\delta = 3 - \frac{(x - y)m_{ABO_{3-\delta_i}}}{2 \times n_O \times M_{ABO_{3-\delta_i}}}$$

In our case, A is not reducible and stays in its oxidative state. In the case of BSCF, x=2. In the following, B stands for Fe and Co mixture, y range can be from 2 to 4. The quantity of I<sub>2</sub> formed is used to determine the initial global oxidative state of B site. After reduction in iodine, the oxidative state of B site is always 2+.



This system leads to the following equation:

$$y = \frac{V_{eq}[S_2O_3^{2-}]}{n_{ABO_{3-\delta_f}}} - 2$$

Then to calculate  $\delta$ :

$$\delta = 3 - \frac{(x - y)m_{ABO_{3-\delta_f}}}{2 \times n_O \times M_{ABO_{3-\delta_f}}}$$

The estimation is done until:  $M_{ABO_{3-\delta_i}} = M_{ABO_{3-\delta_f}}$

Error calculation:

- $\Delta\delta = \delta \times \left( \frac{\Delta[S_2O_3^{2-}]}{[S_2O_3^{2-}]} + \frac{\Delta m_{ABO_{3-\delta_f}}}{m_{ABO_{3-\delta_f}}} + \frac{\Delta V_{eq}}{V_{eq}} \right)$

The experiments were achieved 10 times each, in order to have a better precision. It has been possible to determine error bars.

## IV.7. X-ray Absorption Near Edge Structure (XANES)/ Extended X-Ray Adsorption Fine Structure (EXAFS)

X-ray Absorption Spectroscopy (XAS) is an established technique providing essential element specific information about the local atomic geometry and about the chemical state of the absorbing atom. The technique is not limited to the crystalline phase materials, but may be used with highly disordered amorphous, liquid and gaseous samples. XANES (X-ray Absorption Near Edge Structure) and EXAFS (Extended X-Ray Adsorption Fine Structure) experiments were carried out in Diamond facilities in Didcot (UK). XANES is based on the absorption of an X-Ray photon and gives information of the oxidative state of the studied element. EXAFS gives information on the atomic environment of the studied element.

This technique was used in order to understand the reduction and oxidation phenomena occurring while the perovskite was heated under various gas mixtures (various ratio of oxygen in Helium) (Figure 25 and Figure 26).

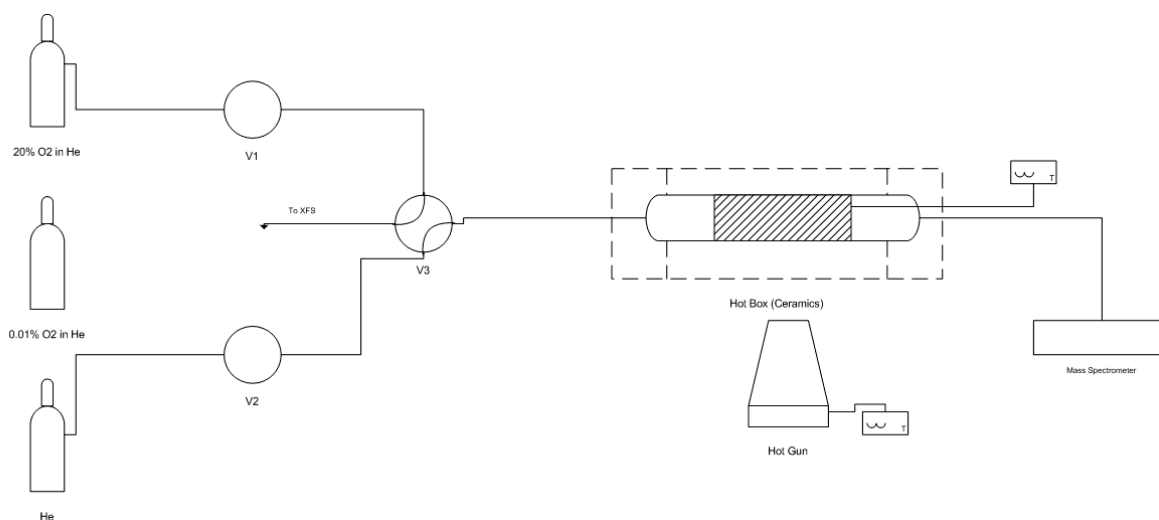


Figure 25 Experimental set-up

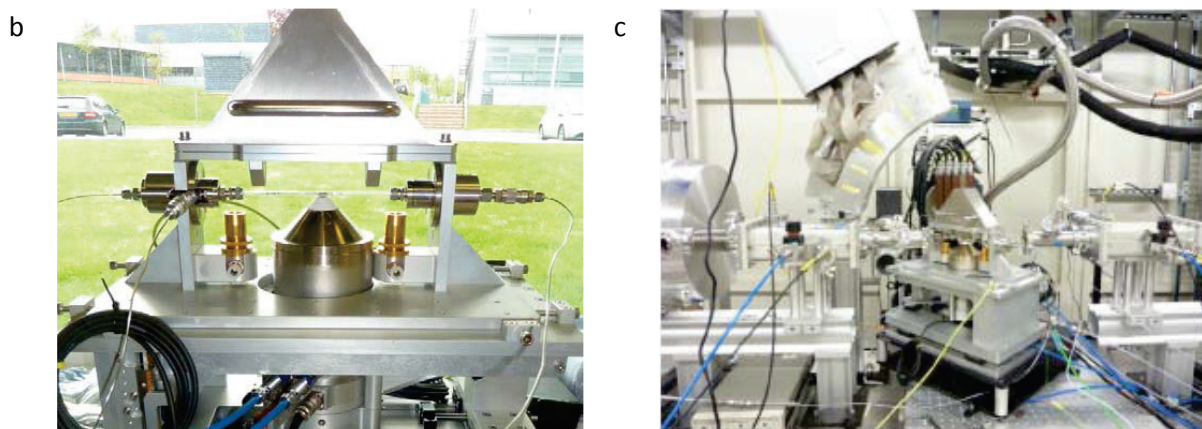
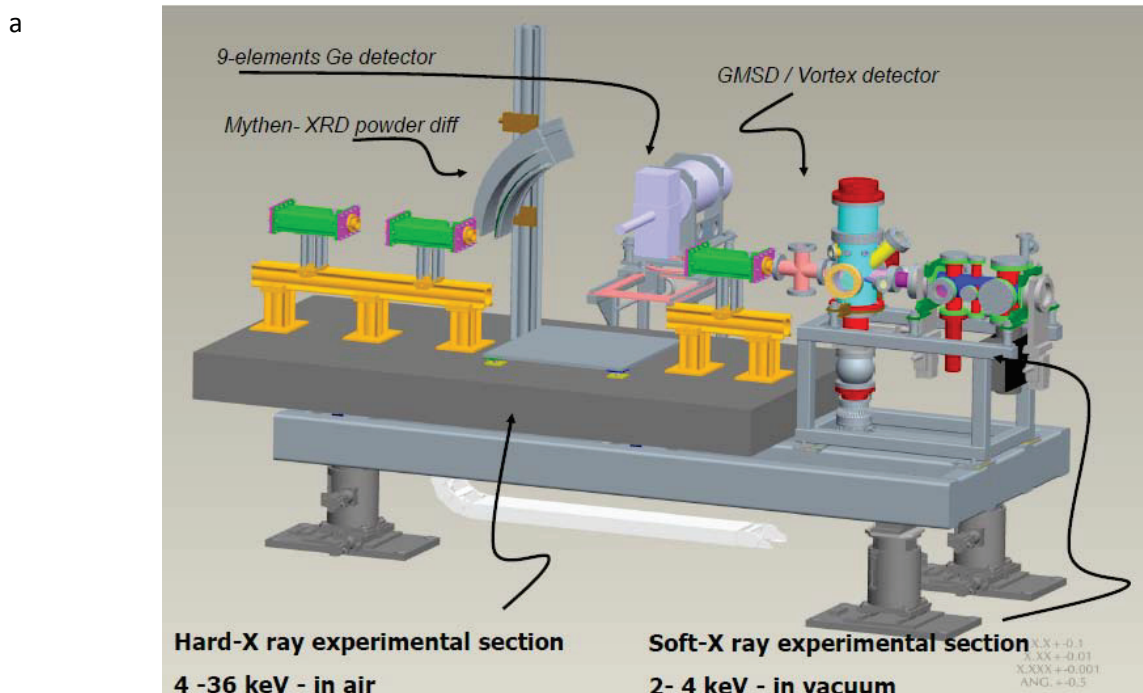


Figure 26 Diamond set-up. a) EXAFS/XANES set-up; b) Reactor set-up; c) Reactor set up on the beamline

The capillary was in quartz (density=2.65 and thickness=140  $\mu\text{m}$ ) which leads to a signal intensity lost (Figure 27). The quality of the results was directly impacted. The energy range for this beamline is from 2.05 to 20.5 keV. To get good data, we need to have 0.6 transmission factor or above.

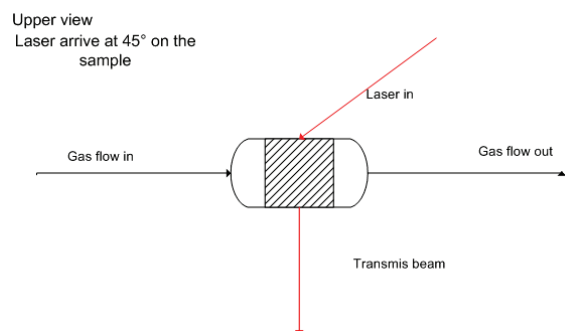


Figure 27 Reactor set up

Thanks to CXRO website (X-rays Interactions with matter)<sup>3</sup>, the quality of the results can be estimated, depending on the energy of the source and the energy we are looking at. The Figure 28 shows the value of the transmission factor depending of the photon energy.

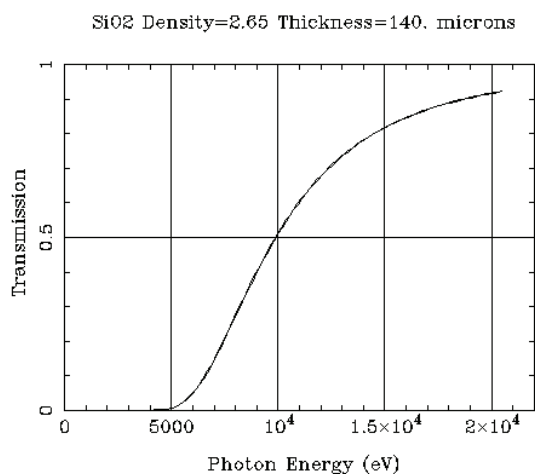


Figure 28 Transmissions value on the beamline full range

The Cobalt (resp. Iron) K-edge is from 7500 eV to 8450 eV (resp. from 7000 to 7600 eV). The transmission values obtain are from 0.1 to 0.3 (Figure 29), which will affect the results. The resolution would be not as good as hoped. For 10000 counts for Iron, the result will be of 1000 counts.

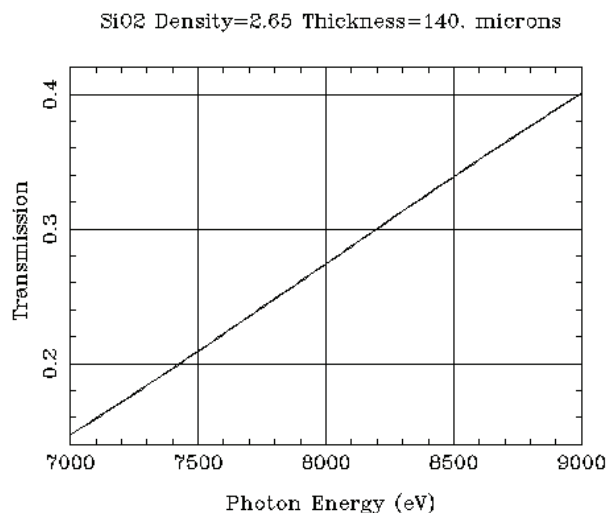


Figure 29 Transmission values for photon energy for Iron and Cobalt K-Edge range

About the Barium L-edge (4450-5550 eV) and the Lanthanum L-edge (4650-5800 eV), the energy use should be from 4450 eV to 6000 eV, which is different from the energy of Co and Iron K-edge, two acquisitions should be run for each point. As the transmission is from 0.01 to 0.05 (Figure 30 a) and the oxidative state of lathanum and barium are not evolving in these conditions, the data aquisition for this range has not been achieved.

The K edge of these compounds, which around 34keV could have been studied, but the detector limitation is of 20.5 keV.

About Strontium, the K-edge is between 14150 and 15900 eV. This energy will lead to high quality results (Figure 30 b) but as for Lanthanum and Barium, the Strontium is not reduced in these conditions.

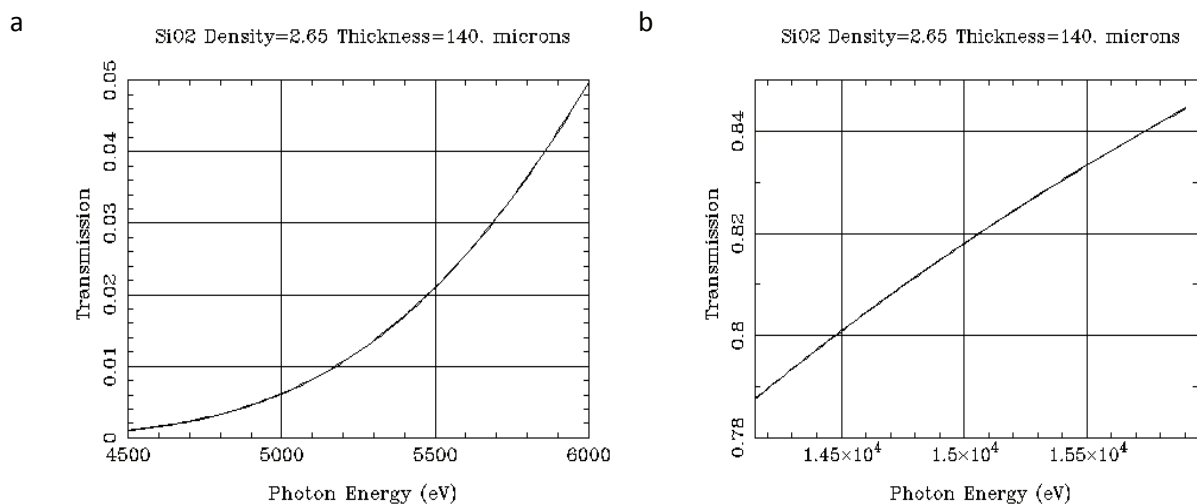


Figure 30 a) Transmission values for photon energy for Barium and Lanthanum L-Edge range; b) Transmission values for photon energy for Strontium K-Edge range

X-ray Adsorption Spectroscopy (XAS) measurements were performed on a series of mixed oxide perovskite type samples to investigate the oxidation state of only Co and Fe under two different oxygen partial pressures (20%-0.01%) in the temperature range of 295-1273 K.

XANES data were collected at the Fe and Co K-edge. Scans were collected in both transmission and fluorescence modes. In transmission mode, two ion chambers, filled with a mixture of Ar/He, were used: one installed before the sample to measure the intensity of the incident beam on the sample ( $I_0$ ), another one after the sample to measure the intensity of the transmitted ( $I_t$ ).

Fluorescence spectra from samples loaded in quartz capillary cells were acquired using  $I_0$  and a high count rate fluorescence 9-element Ge detector windowed on the Fe and Co K fluorescence peaks. The elastic scattering contribution was incoming beam. Acquisition time of the XAS spectrum for each edge was about 3 minutes.

In order to calculate to oxidative state of Co and Fe, some standard samples were done in the same conditions; the results are shown in Figure 31. Typically the shape and position of the absorption edge are used as fingerprints in identifying the valence and the symmetry around the absorbing atoms.

For Iron, samples used were Fe<sub>2</sub>O<sub>3</sub> (Fe(III)), FeO (Fe(II)) and Iron foil (Fe(0)). The results were not relevant. Harvey et al.<sup>4</sup> proved the non negligible presence of Fe(IV) and Co(IV)<sup>4</sup>. A Fe(IV) was calibrated too. As well as for Cobalt, samples used at the beginning were Co(acac)<sub>3</sub> (Co(III)), Co(NO<sub>3</sub>)<sub>2</sub> (Co(II)) and Co foil (Co(0)).

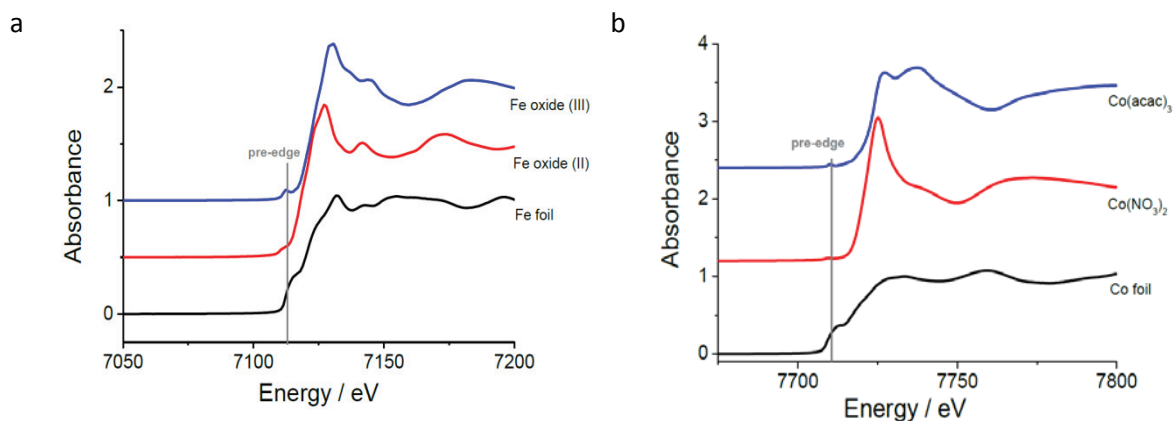


Figure 31 Normalized K-edge XANES spectra a) Fe-Fe foil, Fe oxide (II) and Fe oxide (III) b) For Co- Co foil, Co(acac)<sub>3</sub> and Co(NO<sub>3</sub>)<sub>2</sub>

In order to calibrate Fe (VI) and Co(IV), several studies have been done in the past. Mueller et al.<sup>5</sup> studied the Ba<sub>0.1</sub>Sr<sub>0.9</sub>Co<sub>0.8</sub>Fe<sub>0.2</sub>O<sub>3-6</sub>. They used SrFeO<sub>2.86</sub> to calibrate Fe(IV) and they determine the edge positions. Moreover they used the experimental values from the literature for LaCoO<sub>3</sub> containing Co(IV). We used these values to determine the average oxidative state of our materials (Figure 32).

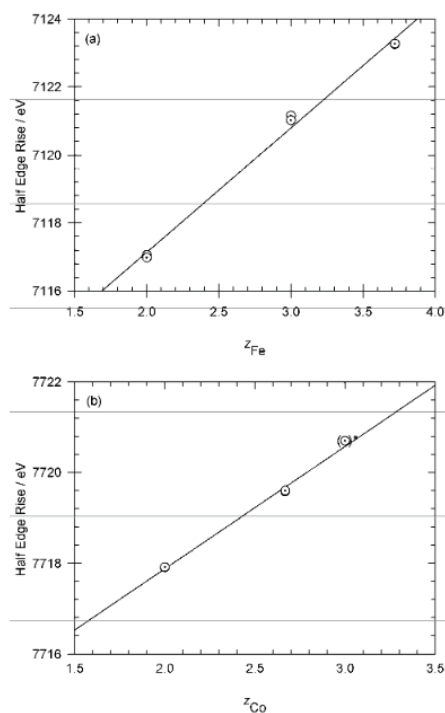


Figure 32<sup>5</sup> Calibration curves for (a) Fe, determined from FeO, Fe<sub>2</sub>O<sub>3</sub> and SrFeO<sub>2.86</sub> and for (b) Co, determined from CoO, Co<sub>3</sub>O<sub>4</sub> and LaCoO<sub>3</sub> (taken from the Literature<sup>6</sup> and indicated in the figure by an asterix). Edges positions were defined as the energy at half the step height of the normalised curves.

## V. Kinetic parameters determination: Oxygen isotopic exchange, SSITKA experiments

### V.1. Experimental set up

The flow chart of the bench is described in Figure 33. The oxygen exchange experiments were carried out in a fixed-bed quartz tube reactor (i.d. 5 mm) containing 50 mg of sieved BSCF. The reactor space before the sample was filled with quartz particles of the same sieve fraction. This bed was then maintained thanks to quartz wool plugs (Figure 34). This lowers the dead volume, preheats the gas, and establishes a plug flow before the sample. A thermocouple was inserted directly into the sample zone to monitor the sample temperature. Experiments were carried out from 873 K to 1173 K with a step every 50 K and at a pressure between 120-160 kPa. Inlet flows were controlled with mass flow controllers. A gas mixture of 50 mL min<sup>-1</sup> of x% <sup>16</sup>O<sub>2</sub> (Air Liquide, 99.999%) + (100-x)% Ar was replaced by a mixture of 50 mL min<sup>-1</sup> of x% <sup>18</sup>O<sub>2</sub> (EurisoTop 98% <sup>18</sup>O<sub>2</sub> and 2% <sup>16</sup>O<sub>2</sub>) + 5% N<sub>2</sub> + (95-x)% Ar, where x was either 21% or 1%. After this experiment, a back-switch was performed. The changes in the gas composition were continuously monitored by a mass spectrometer (m/e=32 (<sup>16</sup>O<sub>2</sub>), 34(<sup>16</sup>O<sup>18</sup>O), 36(<sup>18</sup>O<sub>2</sub>), 40(Ar) and 28(N<sub>2</sub>)) with an acquisition rate of approximately 1 point/s. Nitrogen was added to the feed gas as an inert tracer to measure the gas holdup of the system. The highest oxygen exchange rate was measured at 900°C and amounted to 1.5\*10<sup>-4</sup> mol/kg/s. Under these conditions, the Carberry number, which characterizes external diffusion limitations, amounts to 2\*10<sup>-6</sup>. This is well below the value of 0.05 at which diffusion limitations may occur. Similarly, the Weisz modulus of 10<sup>-5</sup> is well below the critical value of 0.08 for pore diffusion limitations. BROOKS and MS were calibrated before experiments.

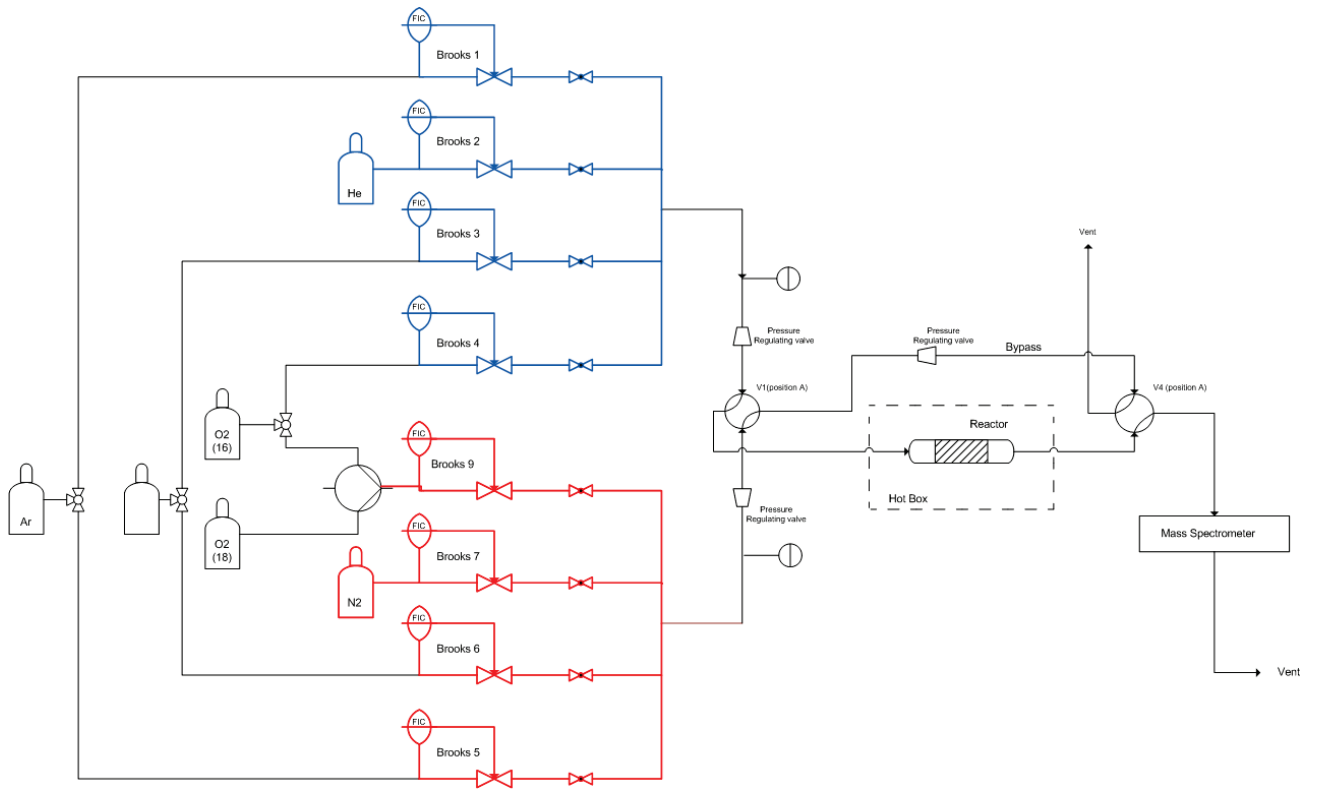


Figure 33 SSITKA bench: flow chart

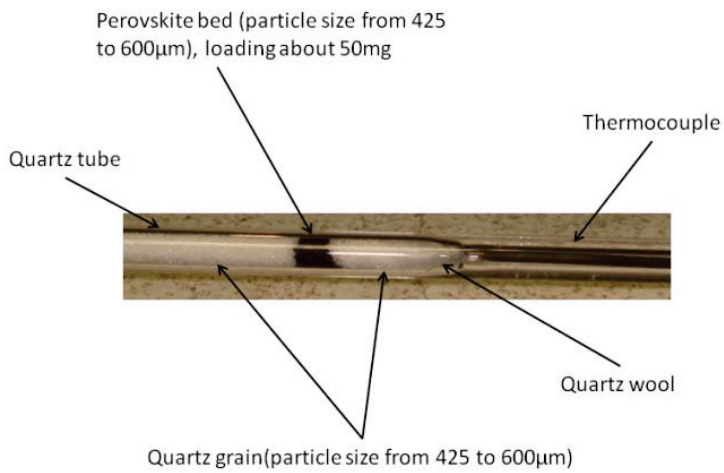


Figure 34 SSITKA experiments reactor

## V.2. Determination of the optimal parameter

### V.2.1. Total flow rate

The impact of the flow rate from 30 mL min<sup>-1</sup> to 70 mL min<sup>-1</sup> did not change the quality of the signal. We used 50 ml min<sup>-1</sup> which is the optimal value between the limit of detection of the mass spectrometer and a high flux involving a stronger pressure drop at higher temperature.

In order to obtain a good signal for the SSITKA analysis, two equivalent mixtures are flowing simultaneously in the bench. One is passing through the catalytic bed and the other through the bypass. The total pressure in each line should be the same in order to avoid any jump of the signal. A needle valve has been added after the bypass and before valve V<sub>4</sub> in order to homogenise the pressure in each line. It should be noticed that a small difference of pressure is observed between the two lines. At room temperature, the pressure in M<sub>1</sub> (<sup>16</sup>O<sub>2</sub>) line is 1 kPa lower than the one in M<sub>2</sub> (<sup>18</sup>O<sub>2</sub>). This is due to the addition of Nitrogen in M<sub>2</sub> as an inert gas. Taking in account this information, at each new temperature, the needle valve should be adjust as follow (Table 5):

Table 5 Adjustment of the pressure in each line

Mixture flowing in the reactor	Pressure in the reactor P1	Pressure in the bypass P2
M <sub>1</sub> ( <sup>16</sup> O <sub>2</sub> containing mixture)	P <sub>1M1</sub>	P <sub>2M2</sub> =P <sub>1M1</sub> +0.01Bar
M <sub>2</sub> ( <sup>18</sup> O <sub>2</sub> containing mixture)	P <sub>1M2</sub> = P <sub>1M1</sub> +0.01Bar	P <sub>2M1</sub> = P <sub>1M1</sub>

#### V.2.1.1. Gas controlling the pneumatic valve and indicator gas

Valve 1 before the reactor is a pneumatic valve. This valve is controlled manually to avoid time loss due to the information sending from the computer to the bench. The valve was originally fed by nitrogen. Figure 35 shows the signal of the mass spectrometer using a valve feed with nitrogen and the Helium as indicator. The switch was too low and some information was missing. Indeed, at t=0s, Mass(32) should be higher at Mass (36) at t=600 s. The composition of the bottle of <sup>18</sup>O<sub>2</sub> is 2%<sup>16</sup>O<sub>2</sub> in <sup>18</sup>O<sub>2</sub>, [MASS(32), t=0]=[MASS(36), t=600]+0.5[MASS(34, t=600)].

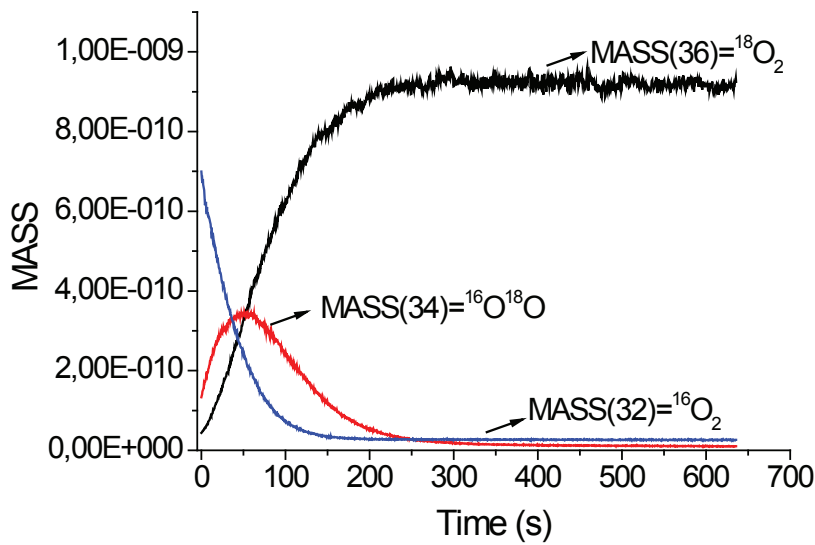


Figure 35 Profile of MASS(32) to MASS(36) after a switch of the valve feed with nitrogen

In order to solve the problem, Nitrogen has been replaced by Helium. Figure 36 shows the first results obtained with Helium as a feed for the pneumatic valve. For the switch of the valve from  $M_1$  to  $M_2$ , the total concentration of oxygen which should be constant varies a lot. Results seem better for the switch of  $V_1$  from  $M_2$  to  $M_1$ . The signal from 0 to 10 s is typical for a switch of valve with a different pressure in the two lines (cf chapter 3). While Helium has been used in the valve, it was still used as an indicator to know if the valve turning has occurred:  $M_1$  to  $M_2$ : Helium signal,  $M_2$  to  $M_1$  no Helium signal. The valve turning increases the consumption of Helium in the line, which modified the pressure in the Brooks and so the pressure in  $M_2$ , that explained why the signal was better in a condition than in the other.

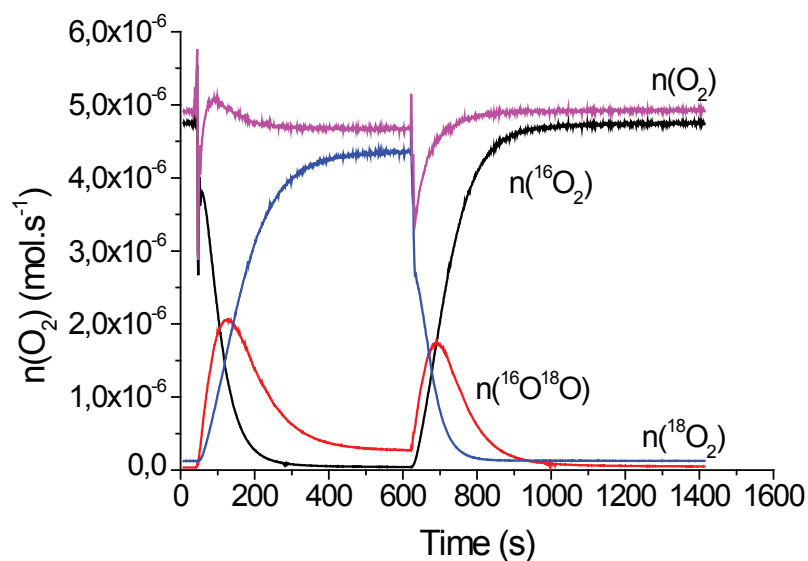


Figure 36 Concentration of different isotope of oxygen and the total oxygen concentration with the pneumatic valve feeds with Helium and Helium used as an indicator.

To obtain optimal results,  $V_1$  was fed with Helium and Nitrogen has been chosen as an indicator.

### *V.2.1.2. Perovskite bed*

The objective is to obtain the lowest granulometry in order to have the highest exchange surface avoiding too high pressure drop (Table 6). Indeed, the pressure in the reactor should be lower than 3 bar to protect the mass spectrometer. Moreover the test is run from 600°C to 950°C.

Table 6 Impact of the bids size on the total pressure

	$P_1(873\text{ K})$ Ramp= 10 K min <sup>-1</sup>	$P_1(973\text{ K})$ Ramp= 5 K min <sup>-1</sup>	$P_1(1073\text{ K})$ Ramp= 5 K min <sup>-1</sup>
<b>BSCF (200-300<math>\mu\text{m}</math>)</b>	370 kPa	230 kPa	280 kPa
<b>BSCF (425-600<math>\mu\text{m}</math>)</b>	190 kPa	120 kPa	130 kPa

The size of the perovskite grains have been chosen in a range of 425-600  $\mu\text{m}$ . The heating ramp has been chosen equal to 5 K min<sup>-1</sup>.

### *V.2.1.3. Powder preparation*

The objective of this method is to be able to determine kinetic parameters on powder to predict the flux across the membrane. The powder is obtained by crushing a sintered membrane. Indeed if the membrane is not sintered and only pressed the powder is an agglomeration of smaller bids (Figure 37).

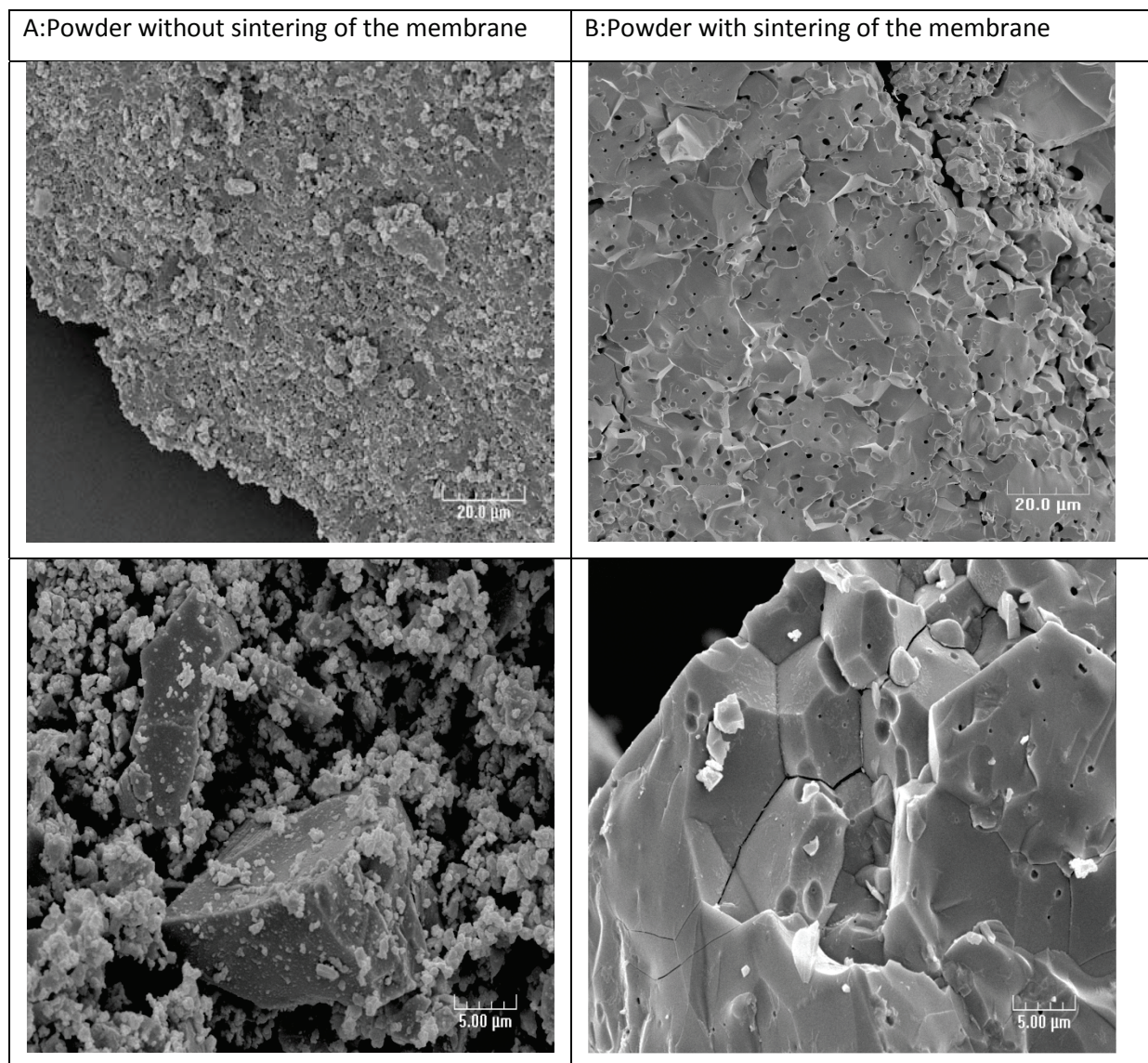


Figure 37 Comparison between: (A) powder from press membrane and sintering after the membrane crushing (x1000 and x4000) and (B) powder obtain with crushing a already sintered membrane (x1000 and x4000)

The powder has been pressed under 30 Mpa for 1 minute to obtain a perovskite membrane. This membrane was then sintered at 1173 K for 4h. After this treatment, the membrane was crushed in a mortar into 425-600  $\mu\text{m}$  perovskite bids.

#### V.2.1.4. Quartz bids

In order to limit the void volume, the perovskite bed was surrounded by inert bids. The bids were of the same size of the perovskite grains. 0.5 g was added before the perovskite bed and 1.5 g after the catalytic bed (Table 7).

Table 7 Amount of exchange oxygen depending on the type of inert

	Oxygen exchange	Max quantity for BSCF	% Oxygen exchange
	10 kmol m <sup>-3</sup> of catalyst	10 kmol m <sup>-3</sup> of catalyst	
SiC bids (425-600µm)	10	2,2	455%
Quartz bids (425-600µm)	2.1	2,2	96%

The quantity of oxygen exchange in the case of SiC is much higher than the maximum quantity of oxygen which can be exchanged. SiC take part of the oxygen exchange. Quartz bids have been chosen as an inert for the experiment. A blank experiment has been run with a reactor filled of quartz bids, the signal of <sup>18</sup>O<sub>2</sub> follows the signal of inert gas.

The total quantity of oxygen exchange during the experiments was calculated integrated <sup>16</sup>O<sub>2</sub> signal and <sup>16</sup>O<sup>18</sup>O, the quantity of oxygen exchange is given by:

$$\text{Exchange oxygen} = 2 * \text{integration of } ^{16}\text{O}_2 \text{ signal} + \text{integration of } ^{16}\text{O}^{18}\text{O}$$

Areas integrated to determine the quantity of oxygen 16 exchanges are coloured on Figure 38.

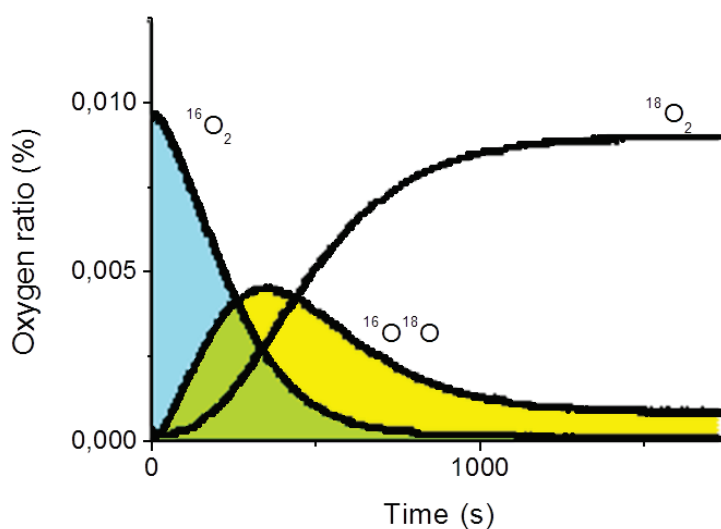


Figure 38 Calculation of the exchange oxygen

### V.3. Apparatus calibration

The BROOKS were calibrated using a digital flow meter (Drycal 0-500 mL min<sup>-1</sup> from Serv'Instrument). All the BROOKS were calibrated using nitrogen (Figure 39).

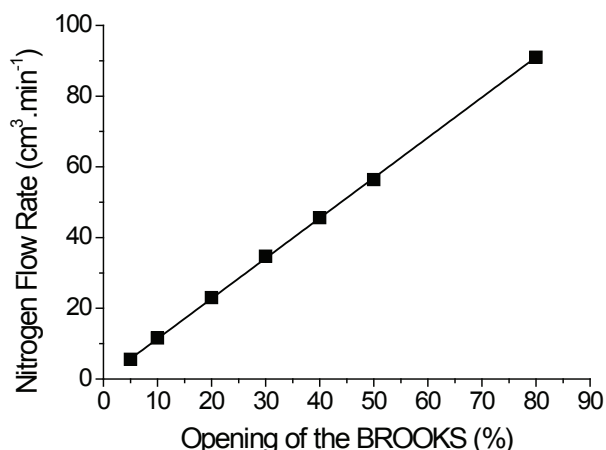


Figure 39 Calibration of a 100 ml min<sup>-1</sup> full range BROOKS at 23°C

Then the gas flow depending on the gas used was calculated with the following formula:

$$F_i = C_i \times F_{N_2}$$

$F_i$  is the flow rate of the specie  $i$  in cm<sup>3</sup>·min<sup>-1</sup>,  $C_i$  is the calibration factor for  $i$  given by Serv'Instruments (Table 8) and  $F_{N_2}$  is the nitrogen flow rate.

Table 8 Calibration factors provided by Serv'Instruments

Gaz	Calibration factor
He	1.385
Ar	1.395
N <sub>2</sub>	1
CH <sub>4</sub>	0.805
O <sub>2</sub>	0.988

In the case for mixture such as  $aA_i/A_j$ ,  $a$  (resp.  $1-a$ ) is the molar fraction of  $A_i$  (resp  $A_j$ ), and  $C_i$  (resp.  $C_j$ ) is calibration factor.

The calibration factor is calculated by the following equation:

$$C_{mixture} = \frac{1}{a/C_i + (1-a)/C_j}$$

For low partial pressure of oxygen, a bottle of mixture was used (10%O<sub>2</sub> in Argon). The calculated calibration factor was: 1.340.

The BROOKS were calibrated with nitrogen and not directly with the operating species as the bench were equipped of quick-connect connector which gives a higher flexibility for this bench. Indeed, depending on the oxygen dilution in inert gas different size of BROOKS could have been used (for 50 ml min<sup>-1</sup> full range to 100 ml min<sup>-1</sup>).

The mass spectrometer was also calibrated. The calibrated gas was diluted in the operating inert gas (in this case Argon). The total flow rate used was in the range of the experiment (50 ml min<sup>-1</sup>) and the dilution of the species in the range of the experiment (from 1% to 25% of oxygen in Argon).

$$n_a = \frac{I_a}{I_s} \times \frac{n_s}{sens_a}$$

$$I_a^* = \frac{I_a}{I_s}$$

$n_a$  (resp.  $s$ ) is the flow rate of the specie  $a$  (resp. solvent  $s$ ) in mol s<sup>-1</sup>;  $I_a$  is the intensity of a compound on the mass spectrometer. In the case of <sup>16</sup>O<sub>2</sub> (Figure 40),  $I_a$  correspond to M(32) signal.  $sens_a$  is the sensibility of  $a$  in the diluents  $S$ .  $sens_a$  is defined for one compound in a define inert for a certain signal (Mass). The following figure shows the calibration of <sup>16</sup>O<sub>2</sub> in Argon for M(32) with a total flow rate of 50 ml min<sup>-1</sup>.

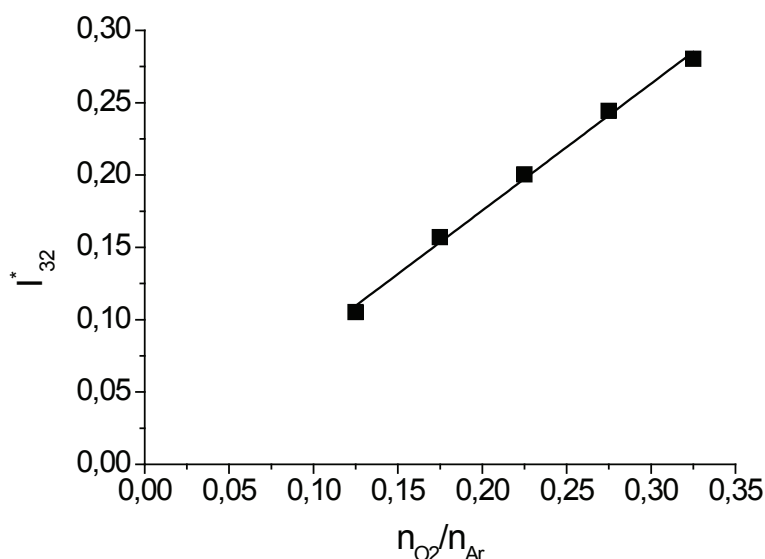


Figure 40  $I_{32}^*$  as a function of the flow rate of O<sub>2</sub> in Argon.

The sensibility was regularly measured in order to insure a good quality of results. For all the tests, the sensibility factor for O<sub>2</sub> in Argon for M(32) was about 0.88.

## VI. Membrane reactor set-up

Oxygen permeation studies were carried out in a membrane reactor. Perovskite disks (about 2 mm thick) were sealed in between two dense alumina tubes (outer diameter of 25 mm, i.d. 21 mm of

exposed surface) using gold rings as chemically inert sealant, by heating to 1193 K for one hour (Figure 41 and Figure 42).



Figure 41 Membrane surface on the alumina tube (left), and membrane edge between the two alumina tubes

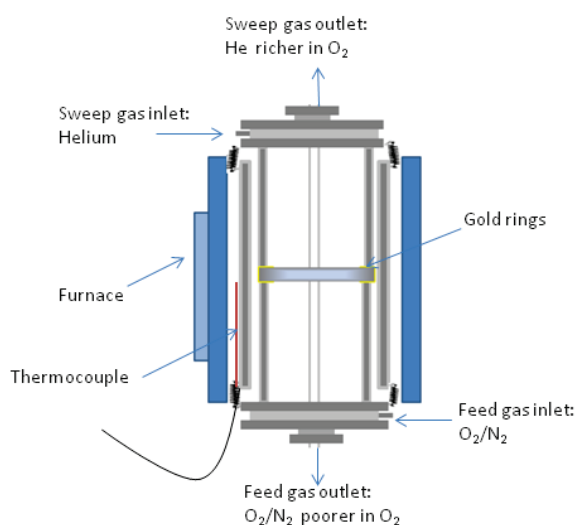


Figure 42 Reactor set-up

The membrane reactor flow chart is described on the following figure (Figure 43). The oxygen-rich side was fed at a constant total flow rate of  $200 \text{ ml min}^{-1}$  of a mixed  $\text{O}_2$  and  $\text{N}_2$  stream individually controlled by mass flow controllers. The reaction side was fed by helium; the total flow rate was adjusted for the experiment at different oxygen partial pressure on the lean side. To evaluate the performances of different membranes experiments were performed in the temperature range of 873–1123 K, partial pressure of oxygen on the air side from 4 to 100 kPa, the total flow rate on the lean side from  $50 \text{ mL min}^{-1}$  to  $300 \text{ mL min}^{-1}$ . The sweep side gases ( $\text{O}_2$ , He,  $\text{N}_2$ ) were analyzed by on-line micro gas chromatography (microGC). Membrane gas leak free conditions were ensured by monitoring nitrogen concentration on the reacting side.

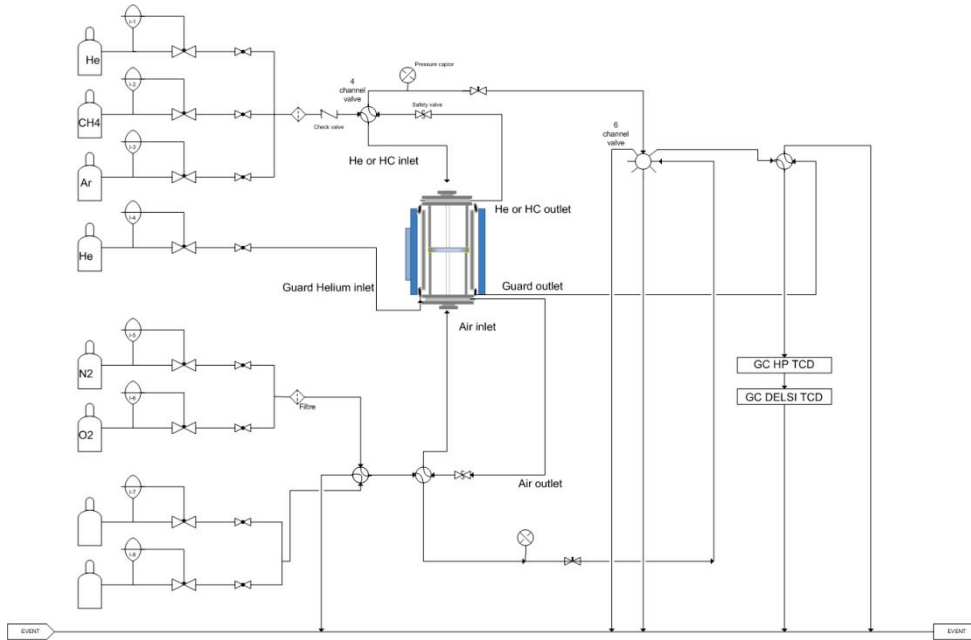


Figure 43 Membrane reactor: flow chart

For this reactor, the BROOKS were calibrated using a digital flow meter, and each BROOKS was calibrated with the operating specie.

The oxygen flux through the membrane was then calculated:

$$P_{O_2}(total) = k_{O_2} \times A_{O_2}$$

$A_{O_2}$  is the oxygen area,  $k_{O_2}$  is  $O_2$  calibration coefficient

$$J_{O_2} \left( \frac{ml}{min.cm^2} \right) = \left[ \frac{k_{O_2} \times A_{O_2}}{P_{tot}} \right] \times \frac{F_{He}}{S}$$

Nitrogen can cross the membrane, so the total oxygen flux is not only due to the oxygen semi-permeation, the calculation should then be corrected:

$$P_{O_2}(leak) = k_{N_2} \times A_{N_2} \times \frac{x_{O_2}}{x_{N_2}}$$

With  $A_{N_2}$  nitrogen area,  $k_{N_2}$  is  $N_2$  calibration coefficient,  $x_{O_2}$  (resp  $x_{N_2}$ ) is the oxygen resp nitrogen) ratio in the gas phase.

The oxygen fraction coming from the semi permeability is :

$$x_{O_2}(perm) = \left[ P_{O_2}(total) - P_{O_2}(leak) \right] \times \frac{1}{P_{tot}}$$

Finally the oxygen permeation flux through the dense membrane is given by :

$$J_{O_2} \left( \frac{ml}{min. cm^2} \right) = x_{O_2} (perm) \times \frac{F_{He}}{S}$$

$$J_{O_2} \left( \frac{ml}{min. cm^2} \right) = \left[ \frac{k_{O_2} \times A_{O_2}}{P_{tot}} - \frac{k_{N_2} \times A_{N_2}}{P_{tot}} \times \frac{x_{O_2}}{x_{N_2}} \right] \times \frac{F_{He}}{S}$$

With,  $F_{He}$  is the helium flow rate in the sweep side and  $S$  is the membrane surface.

In order to refine the flow calculation, Shao et al.<sup>7</sup> used the Knudsen flow to determine the leak flow rate. Indeed,  $P_{O_2} (leak)$  is due to the flux of the gaseous nitrogen and oxygen through the pores (if exists) and so the flow becomes:

$$J_{O_2} (leak) = \left[ \frac{k_{N_2} \times A_{N_2}}{P_{tot}} \times \frac{x_{O_2}}{x_{N_2}} \times \sqrt{\frac{28}{32}} \right] \times \frac{F_{He}}{S}$$

So finally, the flow rate equation is:

$$J_{O_2} \left( \frac{ml}{min. cm^2} \right) = \left[ \frac{k_{O_2} \times A_{O_2}}{P_{tot}} - \frac{k_{N_2} \times A_{N_2}}{P_{tot}} \times \frac{x_{O_2}}{x_{N_2}} \times \sqrt{\frac{28}{32}} \right] \times \frac{F_{He}}{S}$$

## VII. Oxidative coupling of methane in membrane reactor

### VII.1. Catalyst synthesis

Three OCM catalysts were used:

- 1wt% Sr/La<sub>2</sub>O<sub>3</sub> (Johnson-Matthey)
- 10%La-20%Sr/ CaO (LSC catalysts, Synthetize at IRCElyon and also provided by Johnson-Matthey)
- 13.3/18.3/4.6 wt% Mn/W/NaSiO<sub>2</sub> (MWN catalysts)

10%La-20%Sr/ CaO catalysts were prepared via the nitrate and citric acid sol-gel method [1]. Lanthanum, strontium and calcium nitrate (La(NO<sub>3</sub>)<sub>3</sub>, 6H<sub>2</sub>O, pur.99.5%, 433.01 g mol<sup>-1</sup>; pur.99.5%, Sr(NO<sub>3</sub>)<sub>2</sub>, pur.99.5%, 211.63 g mol<sup>-1</sup>; Ca(NO<sub>3</sub>)<sub>2</sub>, 4H<sub>2</sub>O, pur.>99.0%, 236.15 g mol<sup>-1</sup>) were diluted into distilled water at a molar ratio of 0.058:0.18:1. Meanwhile, Ethylenediaminetetraacetic acid (EDTA, 292.24 g mol<sup>-1</sup>) and citric acid (192.12 g mol<sup>-1</sup>) were mixed in distilled water. One molar equivalent of EDTA was added for each molar equivalent of total metal ion (0.1 mol) and two molar equivalent of citric acid (0.2mol). This mixture was stirred until total dissolution of both components. Ammonia solution was then slowly added until obtaining a transparent solution (about 70 mL, pH=6~8). This second mixture was then slowly added to the first one. The solution was heated to 373 K and stirred until a gel like formation. The gel was cool down. The gel was then fired in air according to the following procedure: 2h at 393 K, 3h at 573 K, 3h at 673 K and finally 10h at 1273 K. Temperature rates were fixed at 1K min<sup>-1</sup>.

This sample is characterized in XRD and no pure phase was obtained (Figure 44). Moreover, this sample is compared to LSC provided by Johnson Matthey, the two patterns are different, but we cannot conclude anything about it.

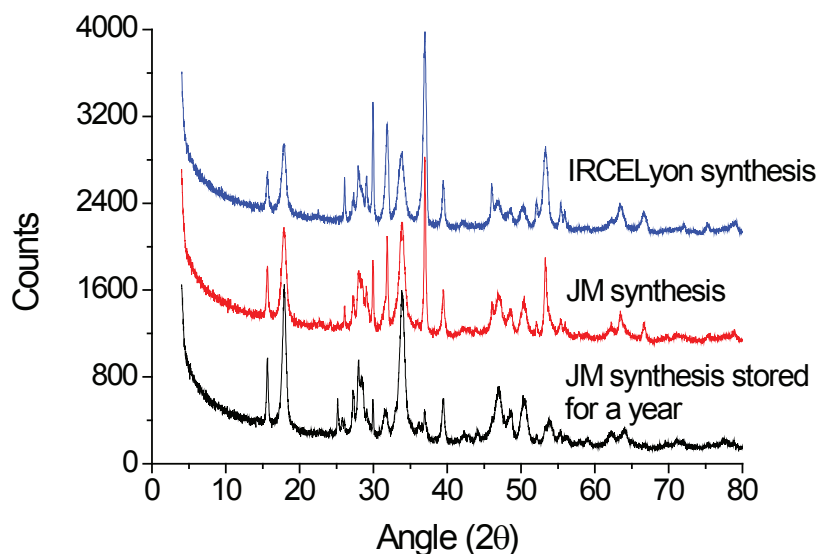


Figure 44 10%La-20%Sr/ CaO synthesis

The 13.3/18.3/4.6 wt% Mn-Na<sub>2</sub>WO<sub>4</sub>/SiO<sub>2</sub> catalyst was prepared via wetness impregnation<sup>8</sup>. Mn(NO<sub>3</sub>)<sub>2</sub> · 4H<sub>2</sub>O (Sigma, pur>97.0%, 251.01 g mol<sup>-1</sup>) and Na<sub>2</sub>WO<sub>4</sub> · 2H<sub>2</sub>O (Sigma-Aldrich, pur>99%, 329.85 g mol<sup>-1</sup>) were dissolved in water and then added to silica support, Silica gel Davisil 646 (Sigma, high purity, 35-70μm, 300m<sup>2</sup> g<sup>-1</sup>, 150Å pore size). After a 12h drying step in air at 383 K, The catalysts were first fired at 673 K for 10h in air to form the metallic oxides and at 1273 K for 2h in air to ensure a complete phase transition of silica to cristobalite.

## VII.2. Catalyst coating

A catalytic layer was added on the membrane surface using two techniques: tape-casting and spray coating method. For both methods, a 22 mm empty circle stencil is prepared in high temperature resistant tape to protect the border of the membrane, in order to ensure a good sealing on the reactor (Figure 45).

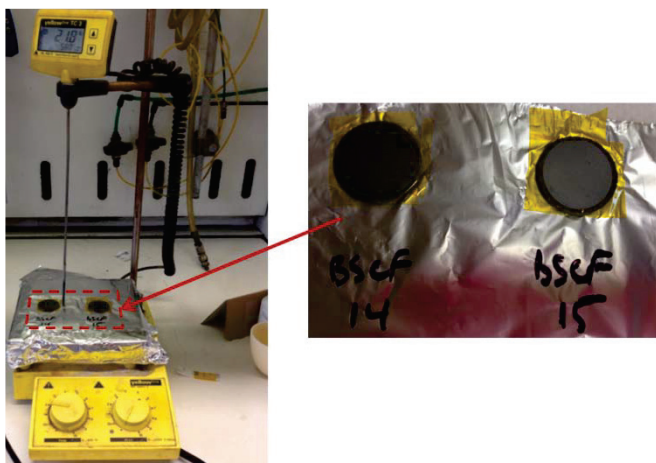


Figure 45 Samples pre-preparation

### VII.2.1. Tape-casting method

Catalysts were crushed and ball-milled to obtain a particle size around 1-5  $\mu\text{m}$ . The preparation of the coating slurry has been described in detail<sup>9</sup>. Catalyst suspensions were prepared by mixing 40 g of distilled water with 20 wt% of catalyst and 0.8 wt% of binder for the Sr/La<sub>2</sub>O<sub>3</sub> sample and 40 g of distilled water with 8 wt% of catalyst and 0.4% binder for La/Sr/CaO sample. Tylose H300 (SE Tylose GmbH, Germany), a cellulose derivative, was used as a binder and a few drops of an anti-foaming agent were added (Poly(propylene glycol)-block-poly(ethylene glycol)-block-poly(propylene glycol) - average Mn  $\sim$ 3,300, Aldrich). The suspension was stirred for at least 48h before the coating procedure.

The membranes were coated following an in-house wash-coating method (Figure 46). The suspension was spread with a syringe on the disk and a razor blade and the coated samples were dried in air at ambient temperature for 24h. The layers were annealed in air in an oven at 873K. Typically the membranes were loaded with 40-50 mg of solids.

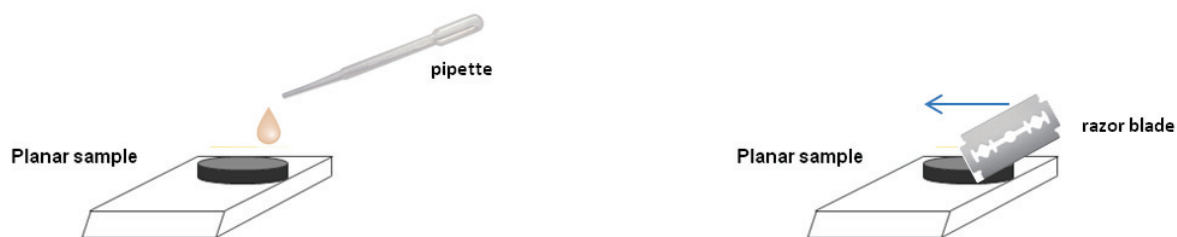


Figure 46 Tape casting method on dense membrane

The adhesion was checked with a cotton bud and ultrasonic bench.

### VII.2.2. Spray coating method

A mixture was prepared with 1 g of catalyst, 10 mL of propanol, 2 mL of ethylen glycol and 1 ml of glycerin. It was then stirred in the ball mill for one hour at 400 rpm. Once the mixture obtained, it was sprayed on the membrane heated at 373 K. A 22 mm empty circle stencil is prepared in high temperature resistant tape to protect the border of the membrane, in order to achieve a good sealing on the reactor.

The catalyst is sprayed on different layers (Figure 47). To add a new layer the previous one should be dry. Once all the catalyst is added the membrane dries for a night at 373 K and then is heated at 873 K for 2h.

The adhesion was checked in the same condition as the tape casting.

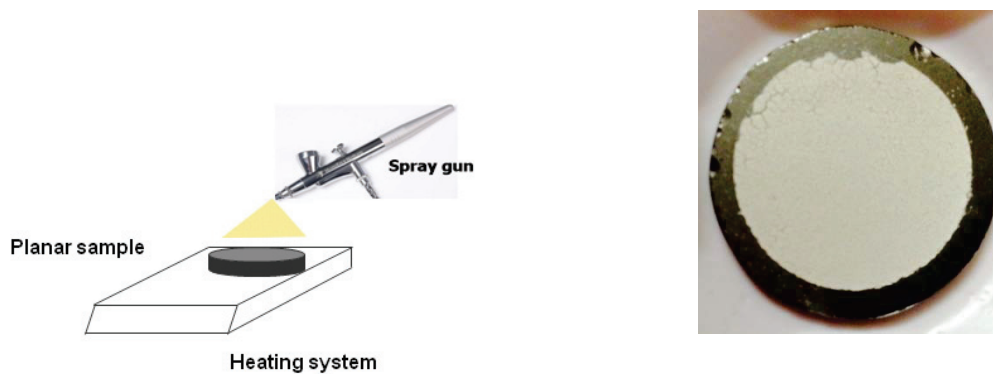


Figure 47 Spray coating method on dense membrane

### VII.3. Catalytic performance measurements

The oxidative coupling of methane was carried out in the same reactor. The catalytic performance was calculated from the different integration picks given by the GC. In order to take in account the possible flux expansion due to an increase of the number of moles during the oxidative coupling of methane, helium has been introduced in the feed gas flow. The expansion coefficient is given by:

$$C_{exp} = \frac{A_{He}^{\circ}}{A_{He}}$$

And the total flow rate is then calculated taking in account this expansion as follows:

$$F_{total} = c_{exp} \times F_{total}^{\circ}$$

And the x component flow rate is given by

$$F_x = \frac{P_x}{P_{total}} \times F_{total}$$

$$P_x = \%X * P_{total} = \frac{Area_x}{\text{calibration values for } X} * P_{total}$$

$P_x$  is the partial pressure of the component in Bar, and  $P_{total}$  the total pressure,  $\%X$  is the molar ratio of the X compound (Table 9).  $Area_x$  is the area determined by the microGC.

Methane conversion (C)	$C = \frac{F_{CH_4}^{\circ} - F_{CH_4}}{F_{CH_4}^{\circ}}$
C <sub>2</sub> selectivity (S)	$S_{C_2} = \frac{2 \times F_{C_2H_4} + 2 \times F_{C_2H_6}}{2 \times F_{C_2H_4} + 2 \times F_{C_2H_6} + F_{CO} + F_{CO_2}}$
C <sub>2</sub> yield (Y)	$Y_{C_2} = \frac{2 \times F_{C_2H_4} + 2 \times F_{C_2H_6}}{2 \times F_{C_2H_4} + 2 \times F_{C_2H_6} + F_{CO} + F_{CO_2} + F_{CH_4}}$
Carbon balance (CB)	$CB = \frac{2 \times F_{C_2H_4} + 2 \times F_{C_2H_6} + F_{CO} + F_{CO_2} + F_{CH_4}}{F_{CH_4}^{\circ}}$
Molar ratio of oxygen in the reaction side ( $x_{O_2}$ )	$x_{O_2} = \frac{0.5F_{H_2O} + 0.5F_{CO} + F_{CO_2}}{F_{total}}$
Estimation of the H <sub>2</sub> O flow rate	$F_{H_2O} = 2F_{CO} + 2F_{CO_2} + 2F_{C_2H_4} + F_{C_2H_6}$

Oxygen flux with reaction ( $J_{O_2}$ ) 
$$J_{O_2} = x_{O_2} \frac{F_{total}}{S}$$

Using this formula for the calculation of the selectivity,  $\sum S_c = 1$ .

$$Prod_{C_2H_4} = S_{C_2} \times n_{C_2H_4} \times A_{CH_4} \times \left( \frac{R}{1 + R} \right)$$

With  $A_{CH_4}$  the activity in mol of converted  $CH_4$   $s^{-1} g^{-1}$  of catalyst and  $n_{C_2H_4}$  the stoichiometric coefficient corresponding to ethylene (0.5 is considered in this case). And R is the ratio between  $C_2H_4$  and  $C_2H_6$ .

Table 9 Calibration values for 100% of each compound

	1/ $k_i$
He	8980.2556
O <sub>2</sub>	2035.9444
N <sub>2</sub>	1315.49
CH <sub>4</sub>	2851.24
CO	1351.45
CO <sub>2</sub>	18204.017
C <sub>2</sub> H <sub>4</sub>	14164.97
C <sub>2</sub> H <sub>6</sub>	15157.63

#### VII.4. Residence time

The contact time and the residence time are key parameters in catalytic reactor. The case of the disk membrane reactor, the calculation of the contact time is not possible. So we will study only the residence time. Knowing the contact is much smaller

Residence time is defined by:

$$Residence\ time = \frac{V_{void}(m^3)}{Volume\ flow\ rate\ (m^3 \cdot s^{-1})}$$

The volume of the gas phase is the same in the two compartments and equal to 14.2 cm<sup>3</sup>. The length of the hot zone is considered equal to 5 cm.

# Bibliography

---

1. S. Kim, Y. L. Yang, A. J. Jacobson and B. Abeles, *Solid State Ionics*, 1998, **106**, 189–195.
2. A. Manthiram, J. S. Swinnea, Z. T. Sui, H. Steinfink and J. B. Goodenough, *Am. Chem. Soc.*, 1987, **109**, 6667–6669.
3. U. CXRO-Website: X-Ray Interactions with Matter, .
4. A. S. Harvey, F. Jochen Litterst, Z. Yang, J. L. M. Rupp, A. Infortuna and L. J. Gauckler, *Phys. Chem. Chem. Phys.*, 2009, **11**, 3010.
5. D. N. Mueller, R. A. De Souza, J. Brendt, D. Samuelis and M. Martin, *J. Mater. Chem.*, 2009, **19**, 1960.
6. V. Efimov, E. Efimova, D. Karpinsky, D. I. Kochubey, V. Kriventsov, a. Kuzmin, S. Molodtsov, V. Sikolenko, S. Tiutiunnikov, I. O. Troyanchuk, a. N. Shmakov and D. Vyalikh, *Phys. Status Solidi*, 2007, **4**, 805–808.
7. Z. Shao, W. Yang, Y. Cong, H. Dong, J. Tong and G. Xiong, *J. Memb. Sci.*, 2000, **172**, 177–188.
8. J. Wang, L. Chou, B. Zhang, H. Song, J. Zhao, J. Yang and S. Li, *J. Mol. Catal. A Chem.*, 2006, **245**, 272–277.
9. G. Germani, a. Stefanescu, Y. Schuurman and a. C. van Veen, *Chem. Eng. Sci.*, 2007, **62**, 5084–5091.





# Chapter 3-Determination of oxygen adsorption-desorption rates and diffusion rate coefficients in perovskites

---

## I. Introduction

The mechanism of oxygen transport through perovskite membranes can be summarized in three major steps. The first step is the dissociative adsorption of O<sub>2</sub> on the surface of the perovskite, leading to the formation of anionic oxygen; the second step is oxygen diffusion by an activated hopping mechanism with oxygen vacancies ( $V_{O,s}^{\bullet\bullet}$ ); and the final step is the desorption/recombination of O<sub>2</sub> on the permeate side<sup>1</sup>. Different experimental techniques and associated modelling approaches have been developed for the measurement and estimation of the surface exchange parameters and diffusion parameters that govern the oxygen flux in MIEC membranes in general and perovskite membranes in particular. The state-of-the-art methods are described below.

### I.1. Electrical conductivity relaxation

Different authors described each parameter (exchange coefficient and diffusion parameter) with various methods such as the electrical conductivity relaxation (ECR). It allows the measurement of the variation of the electronic conductivity as a function of time when the material is oxidized or reduced. The oxygen chemical diffusion parameter,  $D_{chem}$ , is then determined, and the chemical exchange coefficient  $k_{chem}$ . The diffusion parameter depends on  $D_O$  and of the oxygen non stoichiometry<sup>2-4</sup>. Equation (1) describes the relation between  $D_{chem}$  and  $D_O$  and the relation between  $k_{chem}$  and  $k_O$  is described in equation (2):

$$D_{chem} = D_O \Gamma_O \quad (1)$$

$$k_{chem} = k_O \Gamma_O \quad (2)$$

Solid electrolyte coulometry (SEC)<sup>5</sup> is an attractive alternative relaxation technique which is easier to use since measurements are carried out on powders. However, concerns related to non steady-state measurements are raised<sup>5</sup>.

## I.2. Oxygen isotopic exchange techniques

Oxygen isotopic exchange techniques for which oxygen concentration steps are carried out at equilibrium conditions by replacing  $^{16}\text{O}_2$  by  $^{18}\text{O}_2$  are a very appropriate alternative solution. The oxygen isotopic exchange takes place under equilibrium conditions, thus the oxygen partial pressure and the concentration of oxygen vacancies are constant during the measurements. This also greatly simplifies the modelling and the parameter estimation. The technical and modelling advantages of steady-state transient methods have been described by Shannon and Goodwin<sup>6</sup>.

### I.2.1. Secondary Ion Mass Spectrometry (SIMS)

The group of Carter and Steele<sup>7</sup> have developed the isotopic  $^{18}\text{O}_2/^{16}\text{O}_2$  exchange-diffusion profiling (IEDP) technique which allows estimating surface exchange coefficient  $k^*$  and diffusion  $D^*$  coefficients<sup>8,9</sup>. This technique is based on surface thin-film analysis by secondary ion mass spectrometry (SIMS) which measures a three dimensional mapping of the  $^{18}\text{O}$  distribution<sup>10-12</sup>. The assumption for the  $^{18}\text{O}$  transport modelling is that the rate of isotope exchange across the gas/solid interface is assumed to be directly proportional to the difference in isotope concentration between the gas and the solid. The diffusion is defined by the Fick's law, equation (3), and is directly proportional to the exchange kinetics based on the film model.

$$-D^* \left. \frac{\partial C}{\partial x} \right|_{x=0} = k^* (C_s - C_g) \quad (3)$$

$D^*$  is the self diffusion coefficient of oxygen,  $C_g$  and  $C_s$  are respectively the concentration in isotopic oxygen fraction in the gas phase and in the solid phase.

The advantage of IEDP technique is that it is carried out on a dense pellet (2-3mm), which allows direct application of the estimated parameters to transport modelling of the membrane because of the same geometry<sup>8</sup>. On the other hand, it implies that the samples shall be shaped as a dense pellet. In addition, each experimental condition requires a new sample. Hence, sample preparation makes this technique tedious to use. In addition, this method is usually used at  $P_{\text{O}_2}=70$  kPa to get sufficient resolution. This high oxygen partial pressure does not match with membrane processes, which operate at much lower oxygen partial pressures.

### I.2.2. SSITKA

Isotopic  $^{18}\text{O}_2/^{16}\text{O}_2$  exchange has also been carried out on samples in powder form for the estimation of the rate of adsorption and desorption, the concentration of oxygen on the catalyst, and the diffusion coefficient of oxygen in the bulk<sup>13</sup>. In contrast to the IEDP technique, in which the  $^{16}\text{O}/^{18}\text{O}$

gradient is measured in the solid after a given time, steady-state isotopic transient kinetic analysis (SSITKA) is a time-resolved method that analyzes the evolution of the isotope concentration in the gas phase by online mass spectrometry. It might seem that carrying out the measurements over the powder-form sample could be a drawback of this approach, as this powder might not be representative of the microstructure of the membrane material. As already stated above, however, the use of powders accelerates the experimental part of the work, while the use of intrinsic kinetic and transport parameters allows a coherent description of oxygen permeation through the membrane. The latter is accomplished only by describing all the processes on the microkinetic scale (at the level of the elementary steps) and not, like most approaches reported in the literature so far, by lumped apparent parameters (a macrokinetic approach). By combining the microkinetic model with a hydrodynamic model (*e.g.*, mass transfer) of the membrane configuration, the overall oxygen permeation can be correctly predicted. This is basically the same methodology as for reactor modeling<sup>14</sup>. Nonetheless, the issues of transport modelling when crystallite boundaries come into play are acknowledged to be a scientific challenge, one which remains incompletely addressed.

### I.3. Strategy followed in this chapter

In summary, the measurement of oxygen semi-permeability on membranes, along with modelling using the Xu and Thomson model, is currently the only solution for the estimation of both forward and backward kinetic parameters for oxygen adsorption-desorption on MIEC materials. Other characterization techniques such as ECR and IEDP, which are carried out on shaped materials, give access to global kinetic rate parameters only. Hence, there is a strong incentive to develop straightforward approaches that do not involve membrane testing under relevant (steady-state) conditions for the measurement of microkinetic constants.

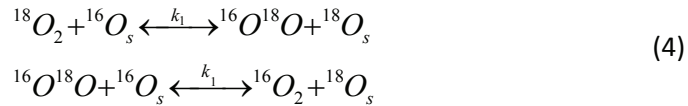
In this chapter, we describe a methodology based on oxygen exchange measurements on perovskites in powder form, for the microkinetic modelling of oxygen transport under conditions applied during membrane operation. The originality of our method consists in the integration of oxygen vacancy concentration measurements by thermogravimetric analysis (TGA) with isotopic oxygen exchange experiments ( $^{16}\text{O}_2/^{18}\text{O}_2$ ) in a microkinetic model. All necessary kinetic and transport parameters can be estimated and used as input for an oxygen membrane flux model. The prediction of oxygen semi-permeability from the estimated kinetic constants obtained over powder samples will be described in chapter 4. The proof of principle has been carried out on  $\text{Ba}_{0.5}\text{Sr}_{0.5}\text{Co}_{0.8}\text{Fe}_{0.2}\text{O}_{3-\delta}$  (BSCF), which is one of the most-studied perovskites<sup>15</sup>. The results section is divided into three parts: (i) determination of the adsorption equilibrium constant (K) and the degree of oxygen non-stoichiometry ( $\delta$ ) from TGA experiments, (ii) estimation of kinetic rate parameters ( $k_f$ ,  $k_r$ ) from oxygen isotopic exchange experiments, and (iii) estimation of the oxygen self-diffusion rate ( $D^*$ ).

## II. Modelling

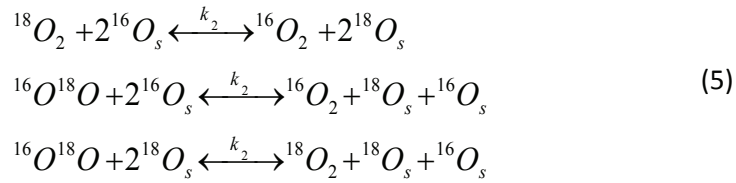
### II.1. Surface exchange coefficients and rates

Oxygen exchange between gas-phase oxygen and solid oxides such as perovskites can occur according to three global reactions in which zero, one or two oxygen atoms are exchanged with the solid<sup>16,17,18,19</sup>.

The different isotopic exchange equations can be described as follow, (1) the simple hetero-exchange is between one atom from the gas phase and one atom from the solid phase



(2) the double hetero-exchange occurs between an oxygen molecule from the gas phase with two atoms from the oxide



The equation (3) describes the homo-exchange in which the oxide do not participate to the exchange.



Rate equations are defined as follows<sup>16,17,18,19</sup>. For each equation,  $k_x$  is equal to  $k_{-x}$ , as there are no isotopic effects. Finally, for the single hetero-exchange, the reaction rates are defined, as follow,

$$\begin{aligned} r_1 &= k_1 P_{^{18}\text{O}_2} \theta_{^{16}\text{O}} - k_1 P_{^{18}\text{O}^{16}\text{O}} \theta_{^{18}\text{O}} \\ r_2 &= k_1 P_{^{18}\text{O}^{16}\text{O}} \theta_{^{16}\text{O}} - k_1 P_{^{16}\text{O}_2} \theta_{^{18}\text{O}} \end{aligned} \quad (7)$$

For the double hetero-exchange,

$$\begin{aligned} r_3 &= k_2 P_{^{18}\text{O}_2} \theta_{^{16}\text{O}} \theta_{^{16}\text{O}} - k_2 P_{^{16}\text{O}_2} \theta_{^{18}\text{O}} \theta_{^{18}\text{O}} \\ r_4 &= k_2 P_{^{18}\text{O}^{16}\text{O}} \theta_{^{16}\text{O}} \theta_{^{16}\text{O}} - k_2 P_{^{16}\text{O}_2} \theta_{^{18}\text{O}} \theta_{^{16}\text{O}} \\ r_5 &= k_2 P_{^{18}\text{O}^{16}\text{O}} \theta_{^{16}\text{O}} - k_2 P_{^{18}\text{O}_2} \theta_{^{18}\text{O}} \theta_{^{16}\text{O}} \end{aligned} \quad (8)$$

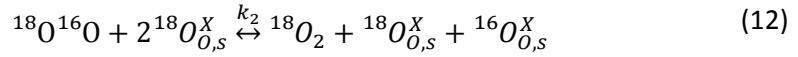
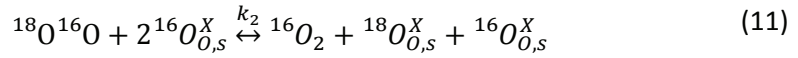
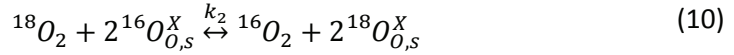
And for the homo-exchange,

$$r_6 = k_3 P_{18O_2} P_{16O_2} - k_3 P_{18O^{16}O} P_{18O^{16}O} \quad (9)$$

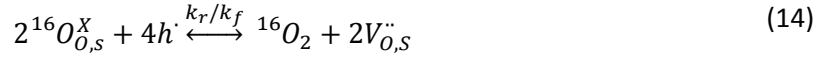
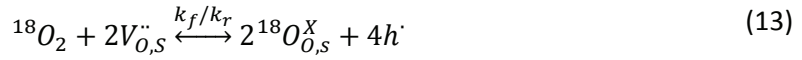
For the homo exchange when the mixture is changed from  $^{16}O_2$  and  $^{18}O_2$  to  $^{16}O^{18}O$  the gas phase is directly changed. There is exchange with the oxygen from the material.

## II.2. Development of the micro kinetic model

Based on the best fit, model discrimination was carried out in order to select most appropriate exchange model. A double hetero exchange was found, which is described by following equations:



The proposed micro kinetic model involves the integration of oxygen vacancies ( $V_{O}^{\cdot\cdot}$ ) in the description of oxygen adsorption-desorption rate at the surface. Equations (13) and (14) are the corresponding elementary steps for equation (10). The equilibrium between  $O_{O,S}^X$  and  $O_O^X$  is included in equations (13) and (14), no assumptions are made on this.



The kinetic rate parameters in equation (13) and (14) are the same because the kinetic isotope effect between  $^{18}O_2$  and  $^{16}O_2$  is negligible at these conditions. The kinetic constants,  $k_f$  and  $k_r$ , are expressed in the following units  $Pa^{-1} s^{-1}$  and  $s^{-1}$ , respectively,  $E_f$  and  $E_r$  the associated activation energy in  $kJ mol^{-1}$ .

$$k_r = k_r^0 \exp\left(\frac{-E_r}{RT}\right)$$

$$k_f = k_f^0 \exp\left(\frac{-E_f}{RT}\right)$$

The reaction rate for this exchange step according to the law of mass action then reads:

$$r = k_f P_{18O_2} \theta_v^2 - k_r \theta_{18O}^2 \quad (15)$$

$$r = k_r \theta_{16O}^2 - k_f P_{16O_2} \theta_v^2 \quad (16)$$

To complete the oxygen exchange kinetics a third rate equation for  $P_{16O^{18}O}$  is necessary:

$$r = k_f P_{16O_{18O}} \theta_v^2 - k_r \theta_{18O} \theta_{16O} \quad (17)$$

The total bulk oxygen site balance gives  $\theta_{16O} + \theta_{18O} + \theta_v = 1$ , where  $\theta_{16O}$  ( $\theta_{18O}$ ) is the fraction of sites occupied by  $^{16}O$  (resp.  $^{18}O$ ), and  $\theta_v$  is the fraction of vacant sites ( $V_{O,s}$ ).

The concentration of surface species ( $V_{O,s}$ ,  $^{18}O_{O,s}^X$ ,  $^{16}O_{O,s}^X$ ) are calculated by assuming a Langmuir adsorption isotherm. This implies that only one site exists (all sites are energetically equivalent and there is no interaction between the oxygen species), which is either occupied or vacant, and that the oxygen surface species are in equilibrium with the gas phase. The equilibrium constant  $K$  which can be expressed as a Van't Hoff expression, is equal to the ratio  $k_f/k_r$ .  $K = A_K^\circ \exp\left(-\frac{\Delta H}{RT}\right)$  with

$$\Delta H = E_f - E_r.$$

$$K = \frac{(1 - \theta_v)^2}{P_{O_2} \theta_v^2} \quad (18)$$

The oxygen non-stoichiometry ( $\delta$ ) is related to the fraction of vacancies through:  $\theta_v = \delta/3$  according to the perovskite general formula  $ABO_{3-\delta}$ .

### II.3. Global mass balance:

The oxygen transport model is based on the one dimensional pseudo-homogeneous diffusion convection equation for a fixed bed reactor implying the usual assumptions<sup>14</sup> coupled with the oxygen exchange kinetics at the surface and oxygen diffusion through the bulk, described by equation (21)

$$\frac{\partial P_i}{\partial t} = -\frac{u_s}{\varepsilon_b} \frac{\partial P_i}{\partial z} + \frac{De}{\varepsilon_b} \frac{\partial^2 P_i}{\partial z^2} - \frac{(1 - \varepsilon_b)}{\varepsilon_b} RT L_t \sum_{j=1}^3 \nu_{ij} r_j \quad (19)$$

Where  $P_i$  (Pa) is the partial pressure of oxygen in the gas phase ( $i=^{18}O_2$ ,  $^{16}O_2$ ,  $^{16}O^{18}O$ ),  $t$  (s) time,  $u_s$  ( $m^3_G m^{-2}_R s^{-1}$ ) the superficial gas velocity,  $L_t$  is number of active sites ( $mol m^{-3}_s$ ), and  $\varepsilon_b$  ( $0.5 m^3_G m^{-3}_R$ ) is the inter-granular void space,  $D_e$  ( $m^3_G m^{-1}_R s^{-1}$ ) the effective axial diffusivity,  $z$  ( $m_R$ ) the axial reactor coordinate,  $R$  ( $J mol^{-1} K^{-1}$ ) the gas constant,  $T$  (K) the absolute temperature,  $\nu_{ij}$  (-) the stoichiometric coefficient for species  $i$  in reaction  $j$  and  $r_j$  ( $s^{-1}$ ) the reaction rate of step  $j$  (equations (17) to(19)). Note that all 4 terms in equation (21) have as dimensions  $Pa s^{-1}$ .

The following boundary conditions were used:

$$z=0, P_i=P_i^0$$

$$z=L, \left. \frac{\partial P_i}{\partial z} \right|_{z=L} = 0$$

Fick's law is used for the oxygen tracer diffusion transport in the bulk. Assuming spherical perovskite particles with radius  $r^\circ$  (m) Fick's second law then reads:

$$\frac{\partial \theta_{18O}}{\partial t} = D^* \left( \frac{\partial^2 \theta_{18O}}{\partial r^2} + \frac{2}{r} \frac{\partial \theta_{18O}}{\partial r} \right) \quad (20)$$

Taking  $R = \frac{r}{r^\circ}$

$$\frac{(r^\circ)^2}{D^*} \frac{\partial Q}{\partial t} = \frac{\partial^2 Q}{\partial R^2} + \frac{2}{R} \frac{\partial Q}{\partial R} \quad (21)$$

With  $D^*$  ( $m^2 s^{-1}$ ), the oxygen tracer diffusion coefficient,  $\theta_{18O,r(-)}$ , the  $^{18}O$  fraction in the perovskite (equal to  $C_{18O}/(C_{18O} + C_{16O} + C_V)$ ,  $C_V$  ( $mol/m^3$ ) being the oxygen vacancy concentration) and  $r$  ( $m$ ) the radial coordinate of the perovskite sphere.

Boundary conditions:

At  $r=R_p$

$$-\frac{3D^*}{R_p} \frac{\partial \theta_{18O}}{\partial r} \Big|_{r=R_p} = \sum_{j=1}^3 \nu_{ij} r_j \quad (22)$$

At  $r=0$

$$\frac{\partial \theta_{18O}}{\partial r} \Big|_{r=0} = 0 \quad (23)$$

For the initial conditions, at  $t < 0$ , the entire solid and the gas phase oxygen is assumed to be only  $^{16}O$  isotope as the perovskite has been pre-treated at the same temperature under a  $^{16}O_2$  flow. ( $P_i = P_{16O_2}$  and  $\theta_o(r) = 0$ ). Then at  $t = 0$  the partial pressure of  $^{18}O_2$  is defined by equation (26) with  $cst$  ( $s^{-1}$ ) is a constant depending on the 4 way switching valve.

$$P_{18O_2} = P_{18O_2}^0 \frac{1 - \exp(-cst \times t)}{1 + \exp(-cst \times t)} \quad (24)$$

The first-order differential equations were numerically integrated using the ODEPACK library<sup>20</sup>. The non-linear least-square regression analysis to estimate  $k_r$ ,  $k_f$  and  $D^*$  has been performed by a Levenberg-Marquardt minimization algorithm<sup>21,22</sup>. After regression analysis a statistical test was performed<sup>23</sup>.

## III.BSCF: Case study

### III.1. Vacancies characterization

The evolution of oxygen non-stoichiometry ( $\delta$ ) and thus oxygen vacancies ( $\theta_v$ ) of  $Ba_{0.5}Sr_{0.5}Co_{0.8}Fe_{0.2}O_{3-\delta}$  with the temperature at fixed oxygen partial pressure can be followed by thermogravimetric analysis (TGA). Prior to TG analysis, the initial oxygen non-stoichiometry ( $\delta$ ) of  $Ba_{0.5}Sr_{0.5}Co_{0.8}Fe_{0.2}O_{3-\delta}$  at room temperature has been determined by iodometric titration<sup>24,25</sup>. Series of 10 repetitive measurements gives a value of non-stoichiometry ( $\delta$ ) equal to  $0.41 \pm 0.01$  corresponding to a fraction

of oxygen vacancies ( $\theta_v$ ) of 0.137 (Table 10). Figure 48 shows the evolution of the fraction of vacancies as a function of temperature as calculated from the weight loss of the TGA curve ( $\theta_v = \delta/3$ ) under two different fixed oxygen partial pressures. The partial pressure of 21 kPa of  $O_2$  (solid line) and under 1 kPa of  $O_2$  (dashed line) correspond typically at conditions applied for air separation in a membrane process, for the oxygen rich side (air feed) and for the oxygen lean side (permeate side), respectively. The fraction of vacancies remains ( $\theta_v$ ) constant until 473 K, then increases with a linear trend with temperature in the case of  $P_{O_2}=21$  kPa<sup>3,26,27</sup>. For lower oxygen pressure ( $P_{O_2}=1$  kPa), we can observe a marked oxygen loss at 550-650K accounting for a larger reduction of the solid followed by a linear trend parallel to the former. Hence, we can observe an almost constant difference of oxygen vacancy concentration between the oxygen rich and lean conditions over the temperature range of interest. Our data fall within the typical range of oxygen non-stoichiometry generally found for BSCF<sup>28</sup> and in very good agreement with the data of Kriegel et al<sup>26</sup>.

Table 10 Iodometric titration on BSCF

BSCF	Mass (g)	$V_{eq}$ (mL)	$[Na_2S_2O_3]$ (mol L <sup>-1</sup> )	$\delta$	$M_{BSCFi}$ (g mol <sup>-1</sup> )	$\Delta\delta$
1	0.010	5.7	0.0995	0.40	212.45	0.05
2	0.109	29.3	0.0199	0.43	211.88	0.02
3	0.100	32.1	0.0172	0.41	212.22	0.02
4	0.107	29.7	0.0199	0.42	212.14	0.02
5	0.116	33.4	0.0199	0.40	212.50	0.02
6	0.109	29.3	0.0199	0.43	211.86	0.02
7	0.107	29.7	0.0199	0.41	212.21	0.02
8	0.102	28.9	0.0199	0.40	212.42	0.02
9	0.102	28.3	0.0199	0.41	212.21	0.02
10	0.101	28.1	0.0199	0.41	212.21	0.02

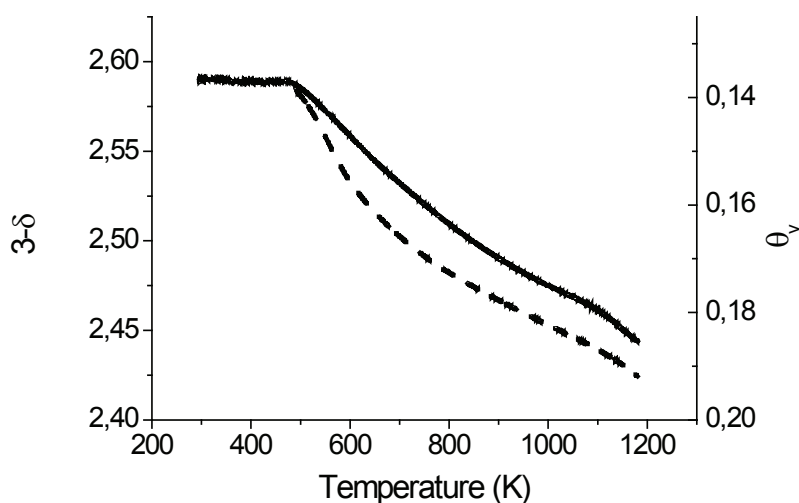


Figure 48 TGA of BSCF powder under O<sub>2</sub>/N<sub>2</sub> flow, with P<sub>O<sub>2</sub></sub>=21 kPa (solid line) and P<sub>O<sub>2</sub></sub>=1 kPa (dashed line).

In addition, TGA measurements were carried out by keeping the sample for a longer time at a constant temperature before ramping to a next temperature level. A dwell type temperature program gave similar non-stoichiometry values  $\delta$  as those obtained by a continuous temperature ramp (Figure 49). We can therefore conclude that the oxygen adsorption/desorption and transport is fast and in quasi-equilibrium compared to the change in temperature.

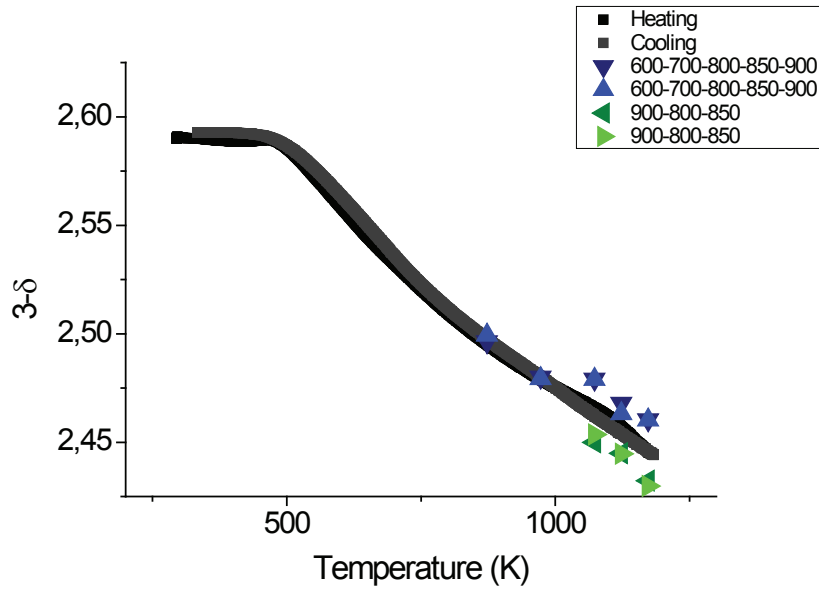


Figure 49 TGA of BSCF powder under  $O_2/N_2$  flow, with  $P_{O_2}=21\text{kPa}$ : while heating (—); while cooling (---); with different dwell: 600-700-800-850-900°C before dwell ( $\blacktriangledown$ ) and after ( $\blacktriangle$ ), and 900-800-850°C: before dwell ( $\blacktriangleleft$ ) and after one hour at the same temperature ( $\blacktriangleright$ ).

No consensus exists in the literature on the stability of the material during TGA measurements. Stable behavior<sup>27</sup> and a slow partial decomposition<sup>28–30</sup> have been reported in separate studies. We have observed that after TGA measurements, cell parameters remain constant (Table 11) within measurement errors (Figure 50). In addition, we do not observe the formation of a new phase. Hence, the modification of the  $Ba_{0.5}Sr_{0.5}Co_{0.8}Fe_{0.2}O_{3-6}$  material during TGA experiments, if occurring, is at least reversible.

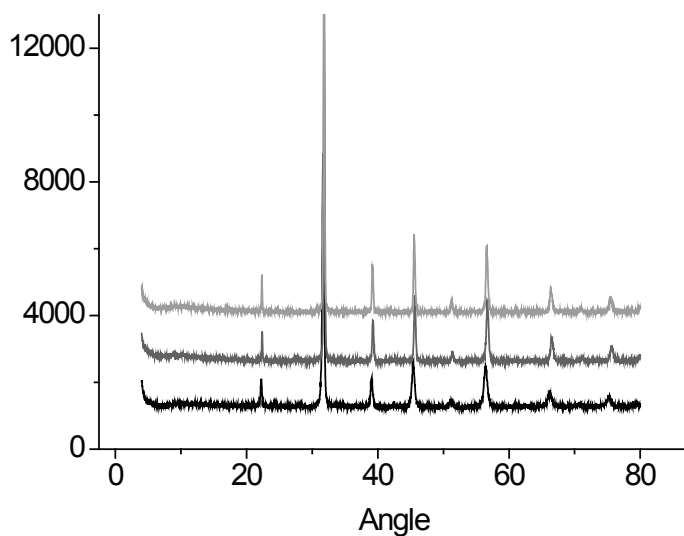


Figure 50 XRD analysis on the different sample, BSCF before analysis (black line), BSCF after TGA under  $P_{O_2}=0.21$  bar (grey line), BSCF after TGA under  $P_{O_2}=0.01$  bar (light grey line)

Table 11 Mesh parameter of BSCF before and after experiment

BCSF (Cubic structure)	Under 21% O <sub>2</sub> in N <sub>2</sub>	Under 1% O <sub>2</sub> in N <sub>2</sub>
	Mesh (error)	Mesh (error)
	Å	Å
Before experiment	3.9791(2)	3.979(1)
After experiment	3.9781(6)	3.977(1)

The adsorption equilibrium constant (K) was calculated at each temperature with equation (20). This is the simplest possible model used to describe oxygen non-stoichiometry in perovskites<sup>31</sup>. A Van't Hoff type equation was used to describe the temperature dependence (Figure 51). The corresponding parameters are presented in Table 12.

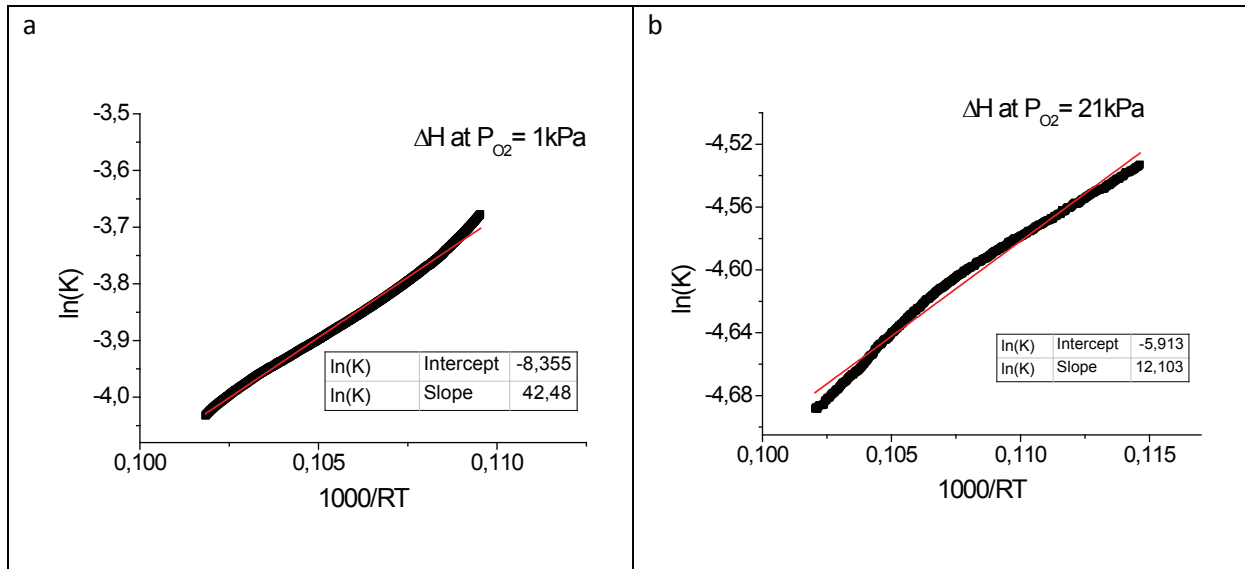


Figure 51 Determination of  $\Delta H$  from TGA experiments for BSCF at  $P_{O_2}=1 \text{ kPa}$  (a) and  $P_{O_2}=21 \text{ kPa}$  (b)

Table 12 Parameter estimates of the apparent adsorption equilibrium constant (K) by equation (20) for two oxygen partial pressures.

$P_{O_2}$ (kPa)	$K^\circ(1 \text{ Pa}^{-1})$	$\Delta H$ (kJ mol <sup>-1</sup> )
1	$(2.4 \pm 0.05) 10^{-4}$	$-42.5 \pm 0.9$
21	$(2.7 \pm 0.05) 10^{-3}$	$-12.1 \pm 0.1$

For both oxygen partial pressures significantly different parameters are found which relates to a difference in adsorption-desorption properties. The physical interpretation of these data is rather problematic. Thermodynamic models that describe the defect chemistry have been developed<sup>32</sup>, but no specific model for BSCF has yet been reported. The oxygen non-stoichiometry behaviour of BSCF is complex due to the presence of both cobalt and iron cations in three different valence states<sup>33</sup>. The higher enthalpy at lower partial pressure of oxygen is consistent with an enthalpy that decreases with increasing oxygen vacancy concentration (or  $\delta$ ), as observed by Mizusaki *et al.* for  $\text{La}_{0.9}\text{Sr}_{0.1}\text{CrO}_{3-\delta}$ <sup>32</sup>.

The semi-empirical model  $\left(\delta = \frac{3KP_{O_2}^n}{1+KP_{O_2}^n}\right)$  proposed by Yang and Lin<sup>34</sup> did not work either for BSCF as  $n$  varied at each temperature (Table 13).

Table 13 Determination of  $n$  from the formula of Yang and Lin<sup>34</sup>

Temperature (K)	$\delta_{TGA}(P_{O_2}= 21\text{kPa}, T)$	$\delta_{TGA}(P_{O_2}= 1\text{kPa}, T)$	$n$
773	0.49	0.51	0.0158
873	0.51	0.53	0.0153
973	0.52	0.54	0.0151
1073	0.53	0.55	0.0148

As we are proposing a straightforward and versatile method for the screening of perovskites powders to extract transport parameters in order to predict the oxygen semi-permeability we continue using the simplified model as given by Xu/Thomson equation (chapter 1) with two sets of values: one on the air side and one on the permeate side. The development of a theoretically based-model for the full description the defect chemistry as a function of oxygen partial pressures and temperatures will be developed in the next chapter.

### III.2. Modelling of oxygen isotopic exchange and estimation of surface exchange kinetic coefficient ( $k_r$ , $k_f$ )

The TGA data could not be described over the whole range of oxygen pressures by a simple one parameter defect model. In order to avoid the development of a full defect model, isotopic oxygen exchange measurements were carried out at same conditions applied for TGA measurement, namely 1 kPa and 21 kPa. By fixing the equilibrium oxygen adsorption constant at the values obtained from TGA experiments, the forward adsorption rate constant can be estimated from the isotopic oxygen exchange experiments.

Figure 52 shows an example of oxygen exchange experiments for two partial pressures of oxygen at three temperatures. The exchange takes about an order of magnitude longer at  $P_{O_2}=1$  kPa than at  $P_{O_2}=21$  kPa. On the other hand the temperature has initially at low temperatures an effect but the effect levels out quickly above 900 K. Integration of the  $0.5 \cdot P^{32}O_2 + P^{16}O^{18}O$  signals gives the amount of exchanged oxygen. At  $P_{O_2}=21$  kPa, 95% of all oxygen atoms in BSCF are exchanged. At  $P_{O_2}=1$  kPa this amounts to only 50%, due to the lower exchange rate, the exchange curves were not recorded until the end of the exchange.

The oxygen exchange curves ( $P^{16}O_2$  and  $P^{16}O^{18}O$ ) were modelled for each level of oxygen partial pressure separately, but including all temperatures simultaneously. Initial regression analysis showed that quasi-equilibrium of the exchange rates was established at the time scale of the experiment.

Thus only the forward rate parameters ( $k_f$ ) were estimated during the regression analysis, and the reverse rate parameters ( $k_r$ ) were calculated from the equilibrium rate constants ( $K=k_f/k_r$ ) determined from the TGA experiments (Table 12). Using the electroneutrality condition, the electron hole concentration  $[h]$  was estimated to be on the order of  $2 \cdot \theta_v$ . The value of the rate constant was adjusted accordingly. In the temperature interval between 650-900°C the concentration  $[h]$  varies roughly 30%, which is negligible compared to the change in the oxygen exchange rate. Thus an intrinsic activation energy can be obtained from the exchange experiments. In addition to the oxygen exchange parameters, the characteristic time constant ( $D/r^2$ ) for oxygen transport was estimated from the isotopic exchange response curves. Figure 52 compares the model predicted response curves with the experimental ones. A good fit is obtained at both oxygen partial pressures and at all temperatures. The surface reaction parameter and diffusion estimates are reported in Table 14 and Table 15, respectively.

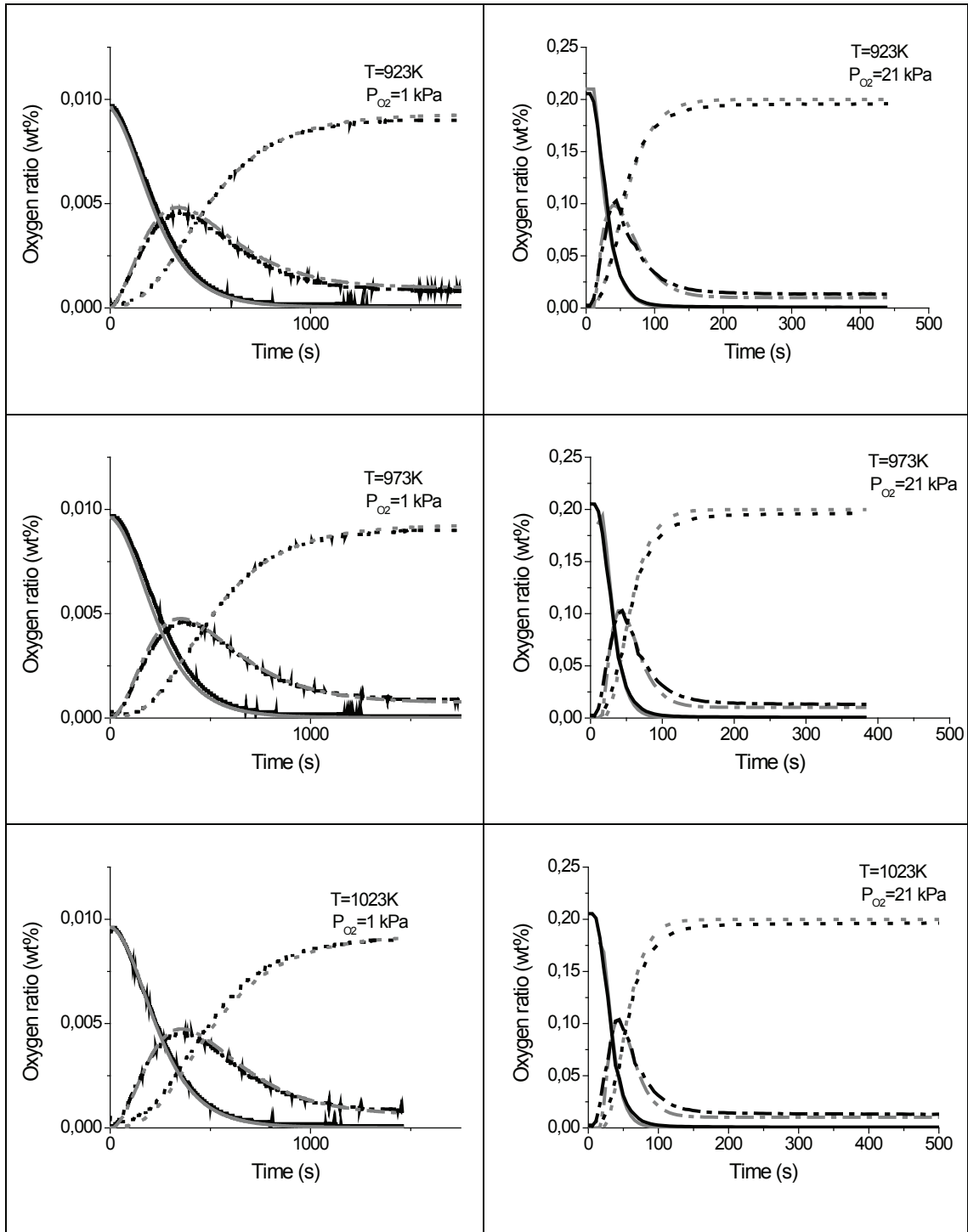


Figure 52 SSITKA experiments (black) and model curve (light grey),  $^{16}\text{O}_2(\text{g})$  (solid line),  $^{16}\text{O}-^{18}\text{O}(\text{g})$  (dash),  $^{18}\text{O}_2(\text{g})$  (dot) at different partial pressure of oxygen and different temperatures.

Table 14 Kinetic parameters estimated from regression analysis of the isotopic oxygen exchange response curves. The confidence intervals estimated at 95%. For comparison, the estimated parameters obtained on LSCF membrane semi-permeability data from Xu and Thomson model are reported.

			Surface reverse kinetic parameter		Surface forward kinetic parameter		ref
		$P_{O_2}$ kPa	$k_r^\circ$ $s^{-1}$	$E_r$ $kJ.mol^{-1}$	$k_f^\circ$ $Pa^{-1}.s^{-1}$	$E_f$ $kJ.mol^{-1}$	
BSCF	Powder	21	$(1.3\pm0.6).10^{11}$	216±45	$(3.1\pm1.9) 10^7$	204±45	This work
BSCF	Powder	1	$(1.7\pm0.2). 10^{11}$	241±20	$(1.4\pm0.2) 10^7$	199±21	This work
			$mol cm^{-2} s^{-1}$	$kJ mol^{-1}$	$cm atm^{-0.5} s^{-1}$	$kJ mol^{-1}$	
BSCF	Powder	21	$(1.3\pm0.6).10^6$	216±45	$(1.2\pm0.1) 10^8$	204±45	This work
BSCF	Powder	1	$(1.6\pm0.2). 10^6$	241±20	$(5.7\pm0.1) 10^7$	199±21	This work
LSCF	Membrane	NA	$(2.07\pm0.02) 10^4$	241.3±0.1	$(5.90\pm0.08) 10^6$	226.9±0.2	<sup>35</sup>

We can observe a significant difference in the activation energy of the reverse (desorption) reaction at rich and lean oxygen pressures whereas for the forward (adsorption) reaction the activation energies are very similar. Unfortunately, to the best of our knowledge no data related to intrinsic kinetic parameters have been reported in the literature for BSCF materials, but only surface exchange coefficients<sup>36,37</sup> which does not allow direct comparison with our data. Moreover, the values of the surface exchange coefficients in the two studies vary by two orders of magnitude<sup>36,37</sup>. The surface exchange kinetic parameters over BSCF powder are compared with data obtained over LSCF membrane by modelling the semi-permeability data using the model by Xu and Thomson, Table 14. Although the comparison of surface kinetic data needs to be taken with care since they are obtained from different materials, activation energies fall in the same range.

### III.3. Estimation of diffusion coefficients from characteristic time

Oxygen exchange experiments give access to the characteristic diffusion time, which is the ratio of the diffusion coefficient to the square of the characteristic length ( $D^*/r^2$ ). This is similar for all other techniques used to measure diffusion coefficients. If the diffusion measurements are carried out directly on the shape and material for the intended application, then the value of  $D^*/r^2$  can be used directly. In our context, the method we develop aims at predicting the permeation of membranes from kinetic modelling carried out on corresponding powders. In this case the characteristic length of diffusion is not the same. For the membrane application the length corresponds to the thickness of the membrane. For the measurements on powder it corresponds to the crystallite size. Therefore,

the crystallite size for the powders used in this study needs to be determined. The diameter of crystallite can be estimated directly from SEM image analysis (Figure 53). The size distribution of the crystallites was measured by counting 250 crystallites (Figure 53). The distribution is centred at 7  $\mu\text{m}$  using a non linear Gauss curve fit (Figure 54). The BET surface area is equal to  $150 \pm 1 \text{ m}^2 \text{ kg}^{-1}$  which lead to a crystallite diameter ( $d_{\text{crys}}$ ) of 7.2  $\mu\text{m}$  in good agreement with SEM image analysis. Thus we set the crystallite radius ( $r$ ) equal to 3.5  $\mu\text{m}$  for the estimation of diffusion parameter.

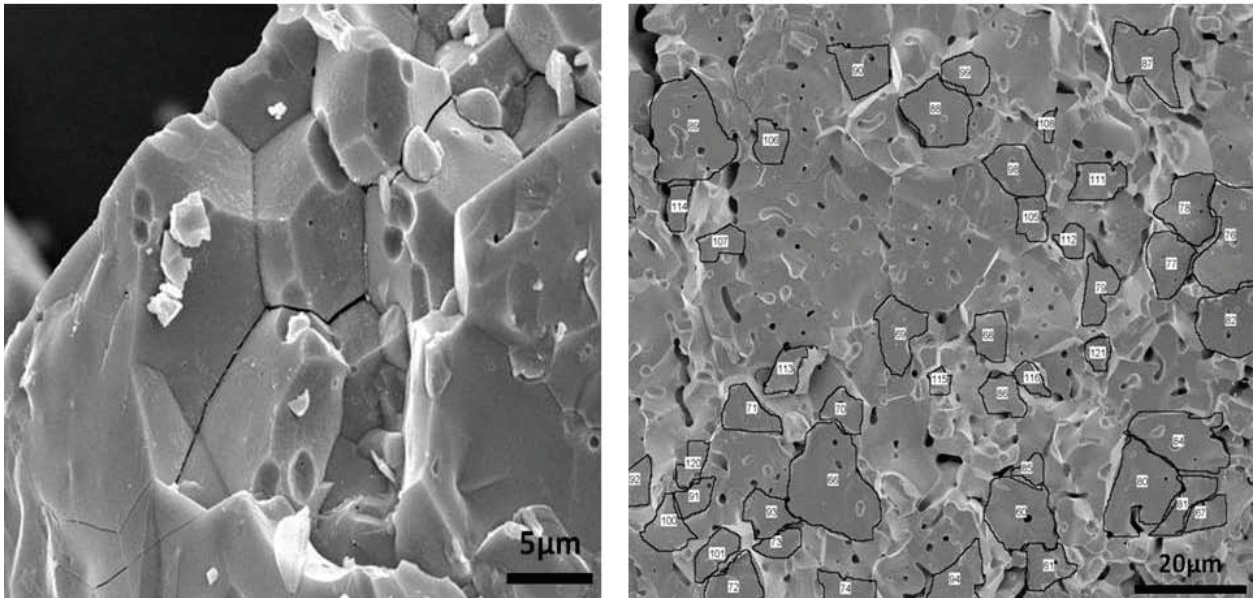


Figure 53 SEM images of a BSCF grain, surface of a grain (x4000)(left), bulk (x1000) (right). Crystallite size distribution measurement using ImageJ software

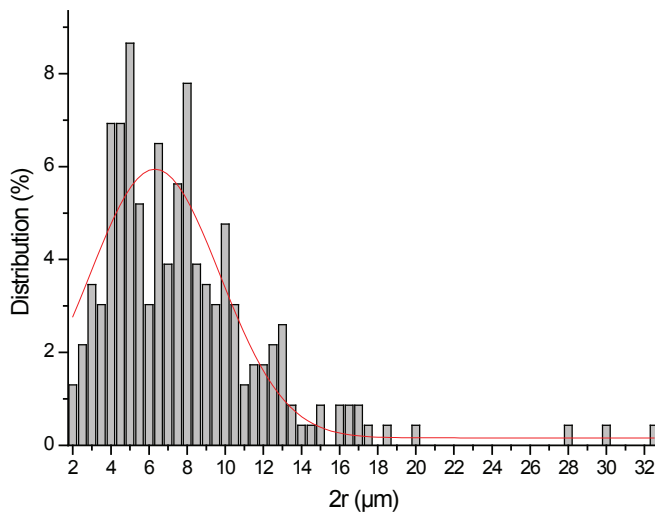


Figure 54 Distribution of the crystallite size from SEM image analysis

Isotopic exchange measurements are carried out on sieved powder with a mean grain size of about 500  $\mu\text{m}$ . Assuming a crystallite mean radius ( $r$ ) of 3.5  $\mu\text{m}$ , a grain consists on average of 5,000 crystallites. The transport measurement in a grain is thus representative of the transport phenomena

occurring in a continuous body such as film or a membrane. Besides, we can also conclude that SSITKA measurements that are carried out over powders include transport phenomena in grain boundaries. In other words, the crushing of the membrane in grain of 500  $\mu\text{m}$  does not alter the microstructure of the solid.

From SSITKA modelling, the self-diffusion parameters ( $D^*$ ) are calculated at two different oxygen partial pressures using the estimated characteristic diffusion times and the mean crystallite radius of 3.5 $\mu\text{m}$  (Table 15). The largest value of the diffusion activation energy is obtained at a low partial pressure of oxygen. This is in line with the dependence of the diffusion activation energy on the oxygen partial pressure found over  $\text{La}_{0.9}\text{Sr}_{0.1}\text{CrO}_{3-\delta}$ <sup>32</sup>.

The activation energy for the diffusion has been calculated from the Arrhenius law, modelling the diffusion at different temperatures (Figure 55). The model was not able to model directly the activation using different temperatures.

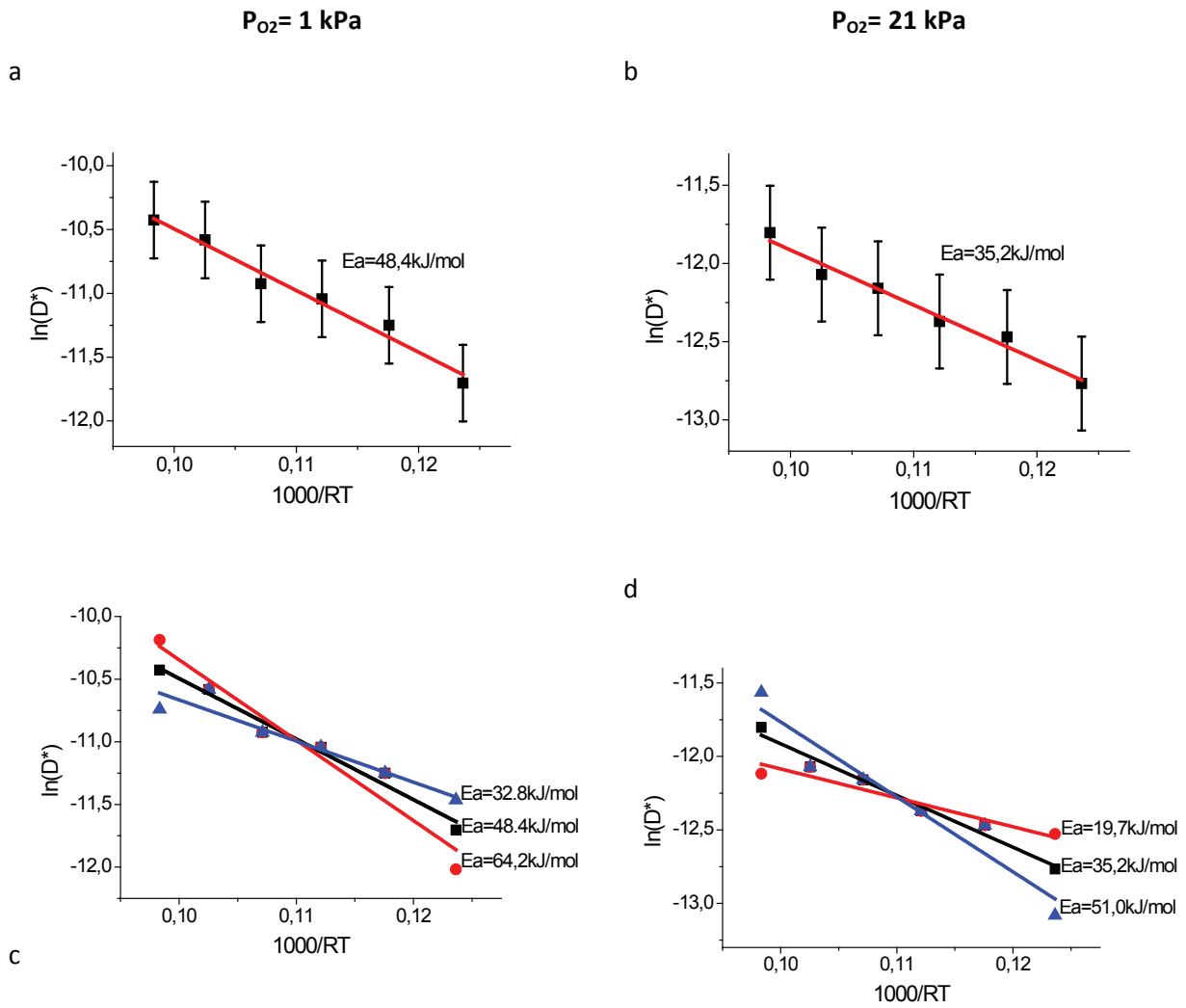


Figure 55 Activation energy for the diffusion according to Arrhenius equation for 1kPa (a); 21kPa (b) and the error from the modelling for 1 kPa (c) and 21 kPa (d).

Table 15 Characteristic time constants for diffusion estimates from regression analysis of the oxygen exchange response curve between 700-900°C, and self diffusion parameter calculated using the crystallite radius ( $r$ ) equal to 3.5 $\mu$ m. The confidence intervals estimated at 95% level.

$P_{O_2}$ (kPa)	$D^*/r^2$ ( $s^{-1}$ )	$D^*$ ( $cm^2 s^{-1}$ )	$E_d$ ( $kJ mol^{-1}$ )
21	$(2.3 \pm 0.4) 10^2$	$(6.5 \pm 0.4) 10^{-5}$	$35 \pm 16$
1	$(7.4 \pm 0.9) 10^3$	$(9.1 \pm 0.9) 10^{-4}$	$48 \pm 16$

Self diffusion rates calculated at give conditions of temperature and oxygen pressures are compared with the literature results available on  $Ba_{0.5}Sr_{0.5}Co_{0.8}Fe_{0.2}O_{3-\delta}$  (Table 16). A good agreement is found with the values of the tracer diffusion study, but a not those by relaxation conductivity. The origin of the latter deviation is not obvious since it can arise either from a different material microstructure or by the measurement technique which is not a steady state method.

Table 16 Comparison of calculated oxygen self diffusion rate coefficients at given conditions with literature on  $Ba_{0.5}Sr_{0.5}Co_{0.8}Fe_{0.2}O_{3-\delta}$ .

Formulation	Method	T(K)	P' <sub>O<sub>2</sub></sub> (kPa)	D* (cm <sup>2</sup> s <sup>-1</sup> )	Reference
Membrane	Tracer diffusion	973	50	8.0 10 <sup>-7</sup>	Wang et al. <sup>38</sup>
Membrane	Conductivity relaxation	973	2.1	1.09 10 <sup>-7</sup>	Bucher and al. <sup>3</sup>
Membrane	Conductivity relaxation	973	1	3.99 10 <sup>-8</sup>	Bucher and al. <sup>3</sup>
Powder	SSITKA	973	21	8.6 10 <sup>-7</sup>	Our work
Powder	SSITKA	973	1	2.41 10 <sup>-6</sup>	Our work

The Nernst-Einstein equation allows calculating the oxygen conductivity ( $\sigma_0$ ) from the oxygen self diffusion ( $D^*$ ) according to the formula:

$$\sigma_0 = \frac{4F^2(3 - \delta)D^*}{RTV_m} \quad (25)$$

F is the Faraday constant, R the gas constant and  $V_m$  the molar volume in mol.cm<sup>-3</sup>.

In order to determine the molar volume of the perovskite in various conditions XRD experiments have been run on BSCF. XRD patterns have been done under two oxygen partial pressures at various temperatures. The mesh parameters have been determined by TOPAS software and used to calculate the molar volume of BSCF (Table 17).

Table 17 Mesh Parameter calculated with TOPAS for BSCF and  $V_m$  at  $P_{O_2}=21\text{kPa}$  and  $P_{O_2}=1\text{kPa}$

BCSF (Cubic structure)		Under 21% O <sub>2</sub> in N <sub>2</sub>		Under 1% O <sub>2</sub> in Ar	
Temperature	Mesh (error)	$V_m$	Mesh (error)	$V_m$	
K	Å	cm <sup>3</sup>	Å	cm <sup>3</sup>	
293	3.9791(2)	37.94	3.979(1)	37.94	
873	4.0154(2)	38.99	4.019(1)	39.09	
923	4.0196(2)	39.11	4.023(1)	39.21	
973	4.0245(2)	39.25	4.028(1)	39.36	
1023	4.0294(4)	39.40	4.032(1)	39.47	
1073	4.0321(7)	39.48	4.036(1)	39.59	
Initial condition	3.9718(6)		3.976(1)		

The oxygen conductivities calculated at 973K, at 1 kPa and 21 kPa are 0.70 and 0.11 S cm<sup>-1</sup> respectively. At the same conditions, Bucher and al.<sup>3</sup> find a conductivity of 0.033 and 0.018 S cm<sup>-1</sup>. The increase of the oxygen conductivity ( $\sigma_0$ ) at lower oxygen partial pressure is also well documented in the literature<sup>33,39</sup>.

## IV. GENERAL DISCUSSION

We have presented a new methodology to measure the parameters needed to predict oxygen permeation through dense perovskite membranes. Rather than measuring the permeation flux over a membrane or thin film, which is delicate and time-consuming to produce, measurements are directly carried out on the powder sample. The measurements consist of a combination of TGA and isotopic oxygen exchange experiments. Both techniques are straightforward. In a TGA experiment the sample is ramped up or down temperature under a controlled oxygen flow. In the case study presented here, the kinetic and transport parameters for  $\text{Ba}_{0.5}\text{Sr}_{0.5}\text{Co}_{0.8}\text{Fe}_{0.2}\text{O}_{3-6}$  have been determined by this methodology. The chosen approach is general for reducible oxides that form oxygen vacancies. If necessary more complicated oxygen non-stoichiometry thermodynamic models can be integrated into the approach, thus making it applicable to other MIEC's.

## V. CONCLUSIONS

We have described a novel and powerful method based on a microkinetic approach for the estimation of oxygen transport parameters of  $\text{Ba}_{0.5}\text{Sr}_{0.5}\text{Co}_{0.8}\text{Fe}_{0.2}\text{O}_{3-6}$  powder. The originality and relevancy of the reported approach is that surface kinetic rate constants are measured on a sample as powder. In contrast to previous IEDP, ERC and SSITKA studies which can determine the global exchange kinetic parameter, our microkinetic modelling approach allows the estimation of the forward and reverse kinetic rate accounting for oxygen vacancy concentration. Besides, self diffusion rate parameter has been estimated at different oxygen partial pressures. This microkinetic approach which combines SSITKA and TGA measurements shall significantly accelerate the characterization of oxygen transport in perovskite and related materials. In this study, the kinetic parameters have been measured in a temperature window between 873 K and 1173 K and at two conditions 21 kPa and 1 kPa and, relevant for simulating the semi-permeability of oxygen in a membrane in an oxygen separation process from air. The simulation of oxygen permeability of BSCF membrane using the estimated parameter from the corresponding powder is reported in the next chapter.

# Bibliography

---

1. P. J. Gellings and H. J. M. Bouwmeester, *Catal. Today*, 2000, **58**, 1–53.
2. S. Yakovlev, C.-Y. Yoo, S. Fang and H. J. M. Bouwmeester, *Appl. Phys. Lett.*, 2010, **96**.
3. E. Bucher, A. Egger, P. Ried, W. Sitte and P. Holtappels, *Solid State Ionics*, 2008, **179**, 1032–1035.
4. P. F. Haworth, S. Smart, J. M. Serra and J. C. Diniz da Costa, *Phys. Chem. Chem. Phys.*, 2012, **14**, 9104–11.
5. M. Sahibzada, W. Morton, A. Hartley, D. Mantzavinos and I. S. Metcalfe, *Solid State Ionics*, 2000, **137**, 991–996.
6. S. L. Shannon and J. G. Goodwin, *Chem. Rev.*, 1995, **95**, 677–695.
7. C. Ftikos, S. Carter and B. C. H. Steele, *J. Eur. Ceram. Soc.*, 1993, **12**, 79–86.
8. R. A. De Souza, J. A. Kilner and B. C. H. Steele, *Solid State Ionics*, 1995, **77**, 180–184.
9. T. Kawada, T. Horita, N. Sakai, H. Yokokawa and M. Dokiya, *Solid State Ionics*, 1995, **79**, 201–207.
10. R. A. De Souza and J. A. Kilner, *Solid State Ionics*, 1998, **106**, 175–187.
11. R. a De Souza and M. Martin, *Phys. Chem. Chem. Phys.*, 2008, **10**, 2356–67.
12. S. Carter, A. Selcuk, R. J. Chater, J. Kajda, J. A. Kilner and B. C. H. Steele, *Solid State Ionics*, 1992, **56**, 597–605.
13. R. H. Nibbelke, J. Scheerova, M. H. J. M. De Croon and G. B. Marin, *J. Catal.*, 1995, **156**, 106–119.
14. G. B. Froment and K. B. Bischoff, *John Wiley, New York*, 1979.
15. J. Sunarso, S. Baumann, J. M. Serra, W. a. Meulenberg, S. Liu, Y. S. Lin and J. C. Diniz da Costa, *J. Memb. Sci.*, 2008, **320**, 13–41.
16. G. K. Boreskov and V. S. Muzykantov, *Ann. N. Y. Acad. Sci.*, 1973, **213**, 137–60.
17. G. K. Boreskov, *Discuss. Faraday Soc.*, 1966, **41**, 263.
18. E. R. S. Winter, *J. Am. Chem. Soc. A*, 1968, 2889–2902.
19. K. Klier, J. Novakova and P. Jiru, *J. Catal.*, 1963, **484**, 479–484.

20. A. Hindmarsh, *Amsterdam: Elsevier*, 1983.
21. K. Levenberg, *Q. Appl. Math*, 1944, **11**, 164–168.
22. D. W. Marquardt, *J. Soc. Ind. Appl. Math.*, 1963, **11**, 431–441.
23. G. F. Froment and L. H. Hosten, *Catal. Sci. Technol. JR, Boudart M. Eds) Springer Verlag, Berlin*, 1981.
24. A. Manthiram, J. S. Swinnea, Z. T. Sui, H. Steinfink and J. B. Goodenough, *Am. Chem. Soc.*, 1987, **109**, 6667–6669.
25. L. Rørmark, K. Wiik and T. Grande, *Society*, 2002.
26. R. Kriegel, R. Kircheisen and J. Töpfer, *Solid State Ionics*, 2010, **181**, 64–70.
27. S. Mcintosh, J. F. Vente, W. G. Haije, D. H. A. Blank and H. J. M. Bouwmeester, *Solid State Ionics*, 2006, **177**, 1737 – 1742.
28. D. N. Mueller, R. A. De Souza, J. Brendt, D. Samuelis and M. Martin, *J. Mater. Chem.*, 2009, **19**, 1960.
29. S. Svarcova, K. Wiik, J. Tolchard, H. J. M. Bouwmeester and T. Grande, *Solid State Ionics*, 2008, **178**, 1787–1791.
30. Z. Shao, W. Yang, Y. Cong, H. Dong, J. Tong and G. Xiong, *J. Memb. Sci.*, 2000, **172**, 177–188.
31. G. . Carini II, H. U. Anderson, D. M. Sparlin and M. M. Nasrallah, *Solid Stat Ionics*, 1991, **49**, 233–243.
32. J. Mizusaki, S. Yamauchi, K. Fueki and A. Ishikawa, *Solid State Ionics*, 1984, **12**, 119–124.
33. J.-I. Jung, S. T. Misture and D. D. Edwards, *Solid State Ionics*, 2012, **206**, 50–56.
34. Z. Yang and Y. S. Lin, *Solid State Ionics*, 2002, **150**, 245–254.
35. S. J. Xu and W. J. Thomson, *Chem. Eng. Sci.*, 1999, **54**, 3839–3850.
36. A. Berenov, A. Atkinson, J. Kilner, M. Ananyev, V. Eremin, N. Porotnikova, A. Farlenkov, E. Kurumchin, H. J. M. Bouwmeester, E. Bucher and W. Sitte, *Solid State Ionics*, 2014, **268**, 102–109.
37. D. Chen and Z. Shao, *Int. J. Hydrogen Energy*, 2011, **36**, 6948–6956.
38. L. Wang, R. Merkle, J. Maier, T. Acartürk and U. Starke, *Appl. Phys. Lett.*, 2009, **94**, 071908.

39. H. Arikawa, T. Yamada, T. Ishihara, H. Nishiguchi and Y. Takita, *Chem. Lett.*, 1999, **135**, 1257–1258.



# CHAPTER 4-Prediction of oxygen flux in dense perovskite membranes from microkinetic constants

---

## I. INTRODUCTION

The Xu & Thomson model, acknowledged as the state of the art model for oxygen permeation through dense membranes, allows the simulation of the perovskite membrane flux on a large window of conditions of temperature and pressure. In the later macro-kinetic approach, the surface kinetics and diffusion rate constants are estimated by regression analysis of the membrane fluxes which is operated at different conditions ( $T$ ,  $P'_{O_2}$ ,  $P''_{O_2}$ ) and the variation of the oxygen vacancy concentrations is lumped. To the best of our knowledge, the prediction of oxygen membrane fluxes from transport parameters determined over powder samples has not been reported. In addition, the variation of oxygen vacancies transport diffusion as function of membrane thickness has not been addressed so far.

In this chapter, we present a novel method to predict the oxygen permeability of MIEC membranes with kinetic and transport parameters determined from the corresponding powder. The membrane  $Ba_{0.5}Sr_{0.5}Co_{0.8}Fe_{0.2}O_{3-\delta}$  (BSCFO)<sup>1</sup> has been selected as first case study. The originality lies on the integration of a microkinetic modelling. The estimation of microkinetic surface rate constants ( $k_f$ ,  $k_r$ ) and oxygen self-diffusion constants under conditions representative of membrane operation can be found in a previous study. Firstly, we identify the prediction limits of Xu and Thomson model over a wide range of temperature and oxygen pressures. We then develop three flux models based on different assumptions of oxygen vacancies diffusion ( $D_v$ ) gradient across membrane thickness. Model discrimination is carried out based on best fits with observed fluxes. Finally, we show that our model match with data from the literature and can predict performances as a function of different experimental conditions.

## II. Basic principles and model

P.J Gelling et H.J.M. Bouwmeester described the different processes governing the oxygen flux through a dense membrane<sup>2</sup> as illustrated in Figure 56. The Kröger-Vink<sup>2</sup> notation is used to describe these phenomena. Gaseous oxygen adsorbs on the membrane surface then dissociates and incorporates into a surface oxygen vacancy ( $V_{O,s}^{\bullet\bullet}$ ). The adsorbed oxygen surface species are described as  $O_{O,s}^X$  and  $h^\circ$  stands for electronic holes. Anionic oxygen then diffuses through the dense membrane via bulk oxygen vacancies. Finally, the oxygen desorbs on the other side of the membrane, via the reverse process. We stress that different diffusion constants are encountered in the literature. The self diffusion of oxygen, known as  $D^*$  is measured under equilibrium conditions, with for example techniques using  $^{18}O_2/^{16}O_2$  exchange<sup>3</sup>. The vacancies diffusivity,  $D_v$ , describes the rate of oxygen vacancies transport. Vacancy diffusion constant ( $D_v$ ) is usually obtained from regression analysis from membrane permeation data. The self diffusion of oxygen ( $D^*$ ) and oxygen vacancies diffusion coefficients ( $D_v$ ) are linked through the oxygen vacancy molar fraction  $\theta_v$  by the following expression(1).

$$D_v = \frac{D^*(T, P_{O_2}) (1 - \theta_v(T, P_{O_2}))}{f^* \theta_v(T, P_{O_2})} \quad (1)$$

Ishigaki et al.<sup>4</sup> calculated the correlation factor ( $f^*$ ) of 0.69 for perovskites.

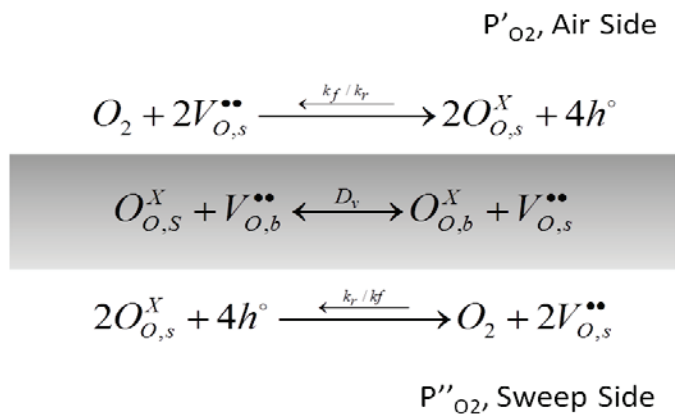


Figure 56 Oxygen permeation flux through the dense membrane

Xu & Thomson assume that the adsorption and desorption constants for the equations shown in chapter 1-II.2.5,  $k_f$  and  $k_r$ , are independent of the oxygen partial pressure, and equal on both membrane interfaces. Similarly  $D_v$  is assumed to be constant across the membrane assuming constant gradient of oxygen vacancies across the membrane. In chapter 3, we have measured different  $k_f$ ,  $k_r$  and  $D^*$  values under oxygen rich an oxygen lean conditions, which are representative

of conditions applied for oxygen separation using MIEC membrane. Values are reported in Table 18 for feed compartment ( $P'_{O_2}=21$  kPa) and sweep compartment ( $P''_{O_2}=1$  kPa). The variation of  $k_f$  and  $k_r$  rates at different oxygen partial pressures invalidates the assumption made by Xu and Thomson in their membrane flux model (Figure 56). At 1173K,  $k'_f=31$  s<sup>-1</sup> at  $P_{O_2}=21$ kPa against  $k''_f=3.2$  s<sup>-1</sup> at  $P_{O_2}=1$ kPa, and  $k'_r=0.03$  Pa<sup>-1</sup> s<sup>-1</sup> at  $P_{O_2}=21$ kPa while at  $P_{O_2}=1$ kPa,  $k''_r=0.02$  Pa<sup>-1</sup> s<sup>-1</sup>.

Table 18 Kinetic parameters estimated from regression analysis of the oxygen exchange response curves. The confidence intervals estimated at 95% level. (Obtained in chapter 3)

P <sub>O2</sub> kPa	Surface reverse kinetic parameter		Surface forward kinetic parameter		Diffusion parameter	
	k <sub>r</sub> <sup>o</sup> s <sup>-1</sup>	E <sub>r</sub> kJ.mol <sup>-1</sup>	k <sub>f</sub> <sup>o</sup> Pa <sup>-1</sup> .s <sup>-1</sup>	E <sub>f</sub> kJ.mol <sup>-1</sup>	D <sup>*o</sup> cm <sup>2</sup> s <sup>-1</sup>	E <sub>d</sub> kJ mol <sup>-1</sup>
21	(1.3±0.6).10 <sup>11</sup>	216±45	(3.1±1.9) 10 <sup>7</sup>	204±45	(6.5±0.4)10 <sup>-5</sup>	35±16
1	(1.7±0.2). 10 <sup>11</sup>	241±20	(1.4±0.2) 10 <sup>7</sup>	199±21	(9.1±0.9)10 <sup>-4</sup>	48±16

The vacancy diffusion constants ( $D_v$ ) were calculated for each condition from  $D^*$  and oxygen vacancy ( $\theta_v$ ) using equation (1) (Figure 57). Bucher et al.<sup>5</sup> calculated two different self diffusion coefficients as a function of the partial pressure of oxygen, using their self diffusion parameter and their vacancies concentration, we observed that they obtained a  $D_v=9.67 \cdot 10^{-7}$  cm<sup>2</sup> s<sup>-1</sup> at  $P_{O_2}=2.1$  kPa and  $D_v=3.51 \cdot 10^{-7}$  cm<sup>2</sup> s<sup>-1</sup> at  $P_{O_2}=1$  kPa at 973K.

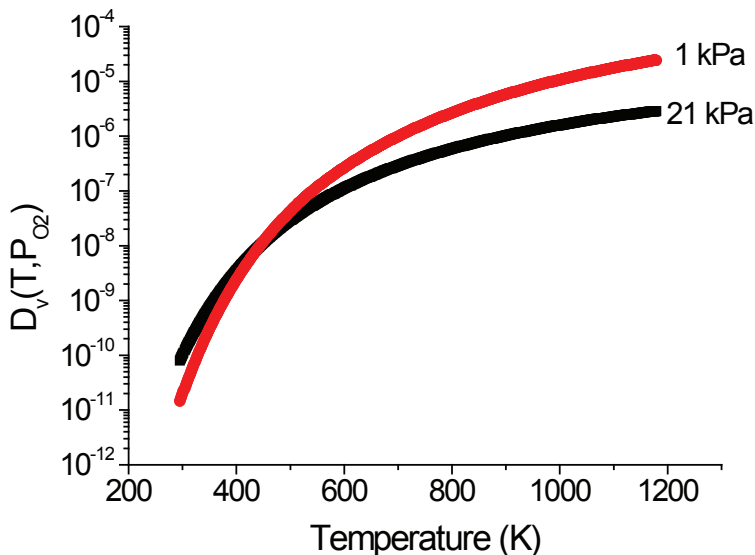


Figure 57 Oxygen vacancies diffusivity as a function of the temperature for  $P_{O_2}=1$  kPa and  $P_{O_2}= 21$  kPa calculated for each point with equation (1).

Support for an oxygen dependant diffusion coefficient comes from an experimental measurement of the oxygen conductivity.

Oxygen conductivity of BSCF has been calculated from 293K to 1173K for two partial pressure from  $D^*$  and  $\theta_v$  according the Nernst-Einstein equation (2)<sup>5</sup> (Figure 58).

$$\sigma_o = \frac{4F^2(3 - \delta)D^*}{RTV_m} \quad (2)$$

F is the Faraday constant, R the gas constant and  $V_m$  the molar volume in mol cm<sup>-3</sup>. An average value of 38.5 mol cm<sup>-3</sup> is taken in this range of temperature and pressure.

The oxygen conductivity depends on the partial pressure of oxygen. Moreover, over the temperature range, the ratio between the oxygen conductivity calculated for  $P_{O_2} = 1$  kPa and for  $P_{O_2} = 21$  kPa varies from 0.1 to 10 (Figure 58). Many authors<sup>6</sup> agree on the linear variation of oxygen conductivity and of the thermal expansion coefficient. Geffroy et al.<sup>7</sup> studied the thermal expansion coefficient of perovskite-type materials at different partial pressures of oxygen. They showed that for  $T < 320^\circ\text{C}$ , the thermal expansion coefficient is slightly higher for high partial pressure of oxygen. From 320-850°C, this coefficient is more or less the same for both conditions and finally at higher temperature this coefficient is much higher at the lower partial pressures of oxygen. Figure 58 shows the evolution of the oxygen conductivity of BSCF calculating this oxygen conductivity from equation (2). It is in good agreement with the observation of Geffroy et al.<sup>7</sup> about the variation of the TEC.

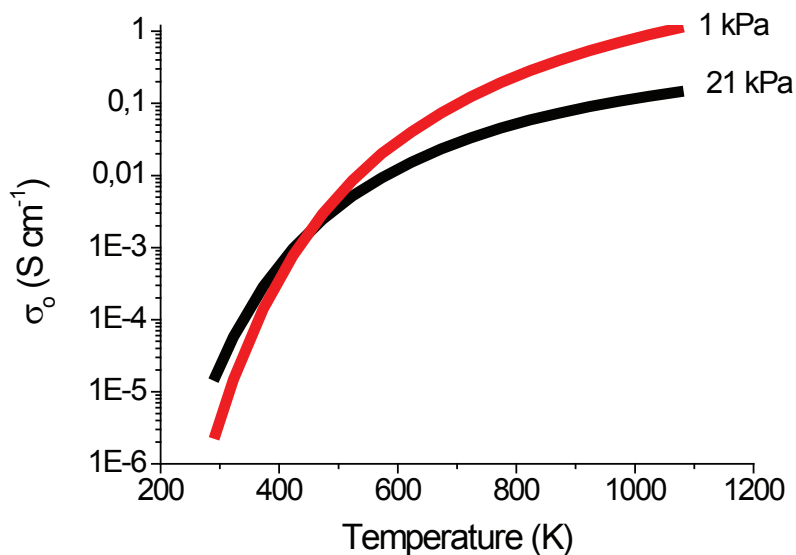


Figure 58 Oxygen conductivity as a function of the temperature at  $P_{O_2}=1$  kPa and  $P_{O_2}=21$  kPa calculated from  $D^*$  and  $\theta_v$  with equation (2).

### III. Flux equation

The general methodology of the integration of microkinetic rate constants in an hydrodynamic model of mass and heat transfers can be found elsewhere<sup>8</sup>. In the model presented here, surface kinetics depend on the oxygen partial pressure  $k(P_{(O_2)}, T)$  and therefore are different on rich and lean oxygen sides. The diffusion parameter is dependent on the temperature and the concentration of vacancies. The transport in the bulk is overwhelming by the diffusion of the oxygen vacancies<sup>9,10</sup>. The oxygen vacancies diffusion has been first described by Heyne<sup>9</sup> and Kofstad<sup>10</sup> by the following equation:

$$J_v = -\frac{\sigma_v}{4F^2}(\nabla\mu_v + 2F\nabla\phi) \quad (3)$$

Where  $\sigma_v$  is the oxygen vacancy conductivity;  $\nabla\mu_v$  and  $\nabla\phi$  are the gradients of the chemical potential and the electric field, respectively. Because of the fast movement of the electron holes,  $\nabla\phi$  is taken equal to 0. And  $\nabla\mu_v = RT\nabla C_v$ . About the vacancies conductivity, with  $D_v$  constant over the thickness,  $\sigma_v = \frac{4F^2}{RT} C_v D_v$ .

So finally the oxygen vacancies flux is defined by equation (4).

$$J_v = -D_v \frac{\partial(C_v)}{\partial x} \quad (4)$$

If  $D_v$  is not constant on the thickness and depend on the position in the membrane then:

$$J_v = -\frac{\partial(D_v, C_v)}{\partial x}$$

In order to simplify the integration, the membrane has been divided into many layers (Figure 59), with  $D_v$  is constant in one layer. Moreover, the oxygen flux is equal in each layer.

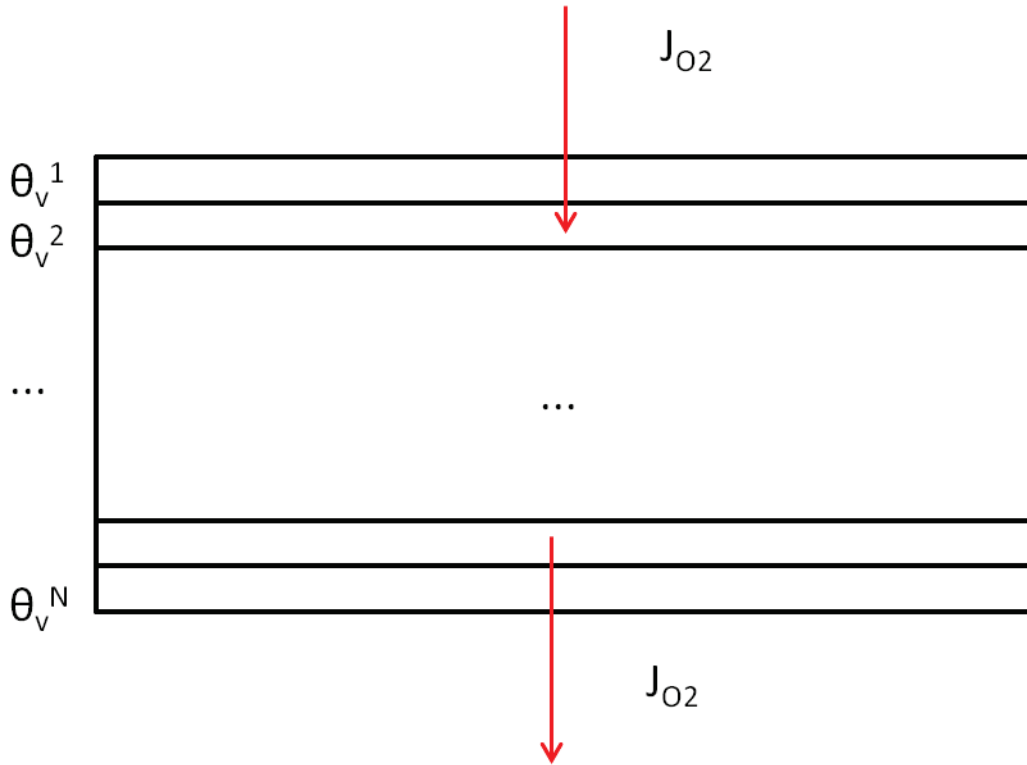


Figure 59 Multi-layer Scenario

Using the hypothesis, that  $J_{O_2} = -1/2J_v$ , we finally obtain equation (5)

$$J_{O_2} = \frac{C_T D_v^i}{2L} (\theta_v^{i+1} - \theta_v^i) \quad (5)$$

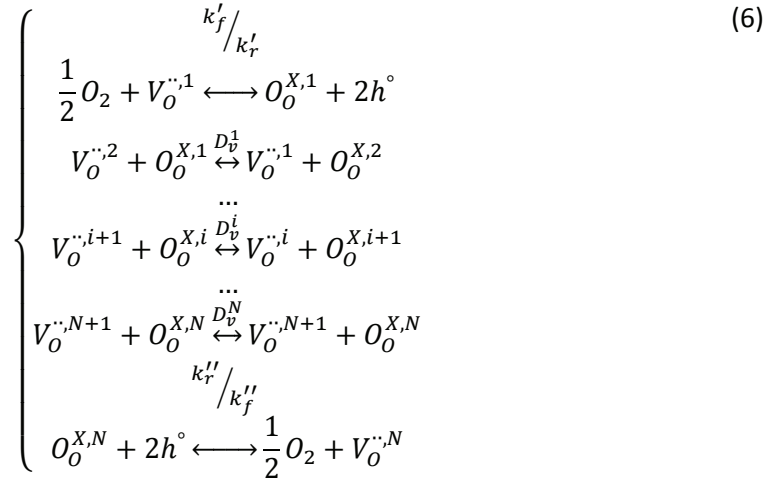
Where  $L$  is the membrane thickness, With  $N$ , the number of layer,  $D_v^i$  ( $\text{cm}^2 \text{ s}^{-1}$ ) the diffusion parameter in the layer,  $\theta_v^i$  the quantity of oxygen vacancies at the inlet of the layer and  $\theta_v^{i+1}$  at the outlet of the layer.  $L$  is the thickness of the membrane and  $N$  the number of layer.

Three main cases can be highlighted:

- $\theta_v^{i+1} - \theta_v^i = \text{constant}$ ,  $J_{O_2}$  is constant so  $D_v^i$  is also constant
- $\theta_v^2 - \theta_v^1 < \dots < \theta_v^{N+1} - \theta_v^N$ ,  $J_{O_2}$  is constant, so  $D_v^1 > \dots > D_v^N$
- $\theta_v^2 - \theta_v^1 > \dots > \theta_v^{N+1} - \theta_v^N$ ,  $J_{O_2}$  is constant, so  $D_v^1 < \dots < D_v^N$

In this work,  $D_v^1 < D_v^N$

So the oxygen transport is described by the following system:



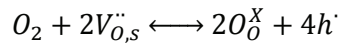
$k_f$  is the adsorption coefficient ( $\text{Pa}^{-1} \cdot \text{s}^{-1}$ ),  $k_r$  the desorption coefficient ( $\text{s}^{-1}$ ),  $D_v$  is the oxygen vacancy diffusion coefficient ( $\text{cm}^2 \cdot \text{s}^{-1}$ ) which are function of the position along the membrane thickness,  $D_v(z)$ .

$$\left\{ \begin{array}{l} J_{O_2} = a'_v C_T (k'_f P_{O_2} (\theta_v^1)^2 - k'_r (1 - \theta_v^1)^2) \\ J_{O_2} = \frac{C_T D_v^1}{2L} (\theta_v^2 - \theta_v^1) \\ \dots \\ J_{O_2} = \frac{C_T D_v^i}{2L} (\theta_v^{i+1} - \theta_v^i) \\ \dots \\ J_{O_2} = \frac{C_T D_v^N}{2L} (\theta_v^{N+1} - \theta_v^N) \\ J_{O_2} = a''_v C_T (k''_r (1 - \theta_v^{(N+1)})^2 - k''_f P_{O_2} (\theta_v^{(N+1)})^2) \end{array} \right. \quad (7)$$

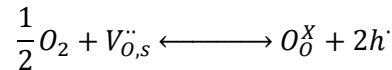
With  $C_T$  ( $\text{mol}/\text{m}^3$ ) is the total concentration of vacancies,  $a_v$  is the ratio between the solid phase volume and the surface of exchange (m), in our case,  $a'_v = a''_v$ .

Depending on the reaction stoichiometry chosen for oxygen, there are two equations:

$$\frac{k_f}{k_r} \quad (8)$$



$$\frac{k_{f1/2}}{k_{r1/2}} \quad (9)$$



$k_r/k_f$  are associated to a stoichiometry 1 for  $O_2$  and  $k_{r1/2}/k_{f1/2}$  to a stoichiometry 0.5 for  $O_2$ .

And finally, we find two rate equations:

$$R = k_f P_{O_2} \theta_v^2 - k_r (1 - \theta_v)^2 \quad (10)$$

$$R_{1/2} = k_{f1/2} P_{O_2}^{0.5} \theta_v - k_{r1/2} (1 - \theta_v) \quad (11)$$

The equations are linked as follow:

$$R = 2R_{1/2} \quad (12)$$

The kinetic parameters in the two equations are linked:

$$\begin{cases} k_f P_{O_2} \theta_v^2 = 2k_{f1/2} P_{O_2}^{0.5} \theta_v \\ k_{f1/2} = \frac{1}{2} k_f P_{O_2}^{0.5} \theta_v \end{cases} \quad (13)$$

Using Langmuir equilibrium on the surface, we found the quantity of vacancies can be described as follow  $\theta_v = 1/(1+(KP_{O_2})^{0.5})$  With:  $K = k_f/k_r$ .

The system is then given by:

$$\begin{cases} k_{f1/2} = \frac{1}{2} k_f \frac{P_{O_2}^{0.5}}{1 + \sqrt{KP_{O_2}}} \\ k_{r1/2} = \frac{1}{2} k_r \frac{\sqrt{KP_{O_2}}}{1 + \sqrt{KP_{O_2}}} \end{cases} \quad (14)$$

All the parameters are described by  $X'$  for the rich oxygen side and  $X''$  for the poor oxygen side.

In the end, the initial surface equation system becomes:

$$\begin{cases} J_{O_2} = a'_v C_T (k'_{f1/2} P_{O_2}^{0.5} \theta'_v - k'_{r1/2} (1 - \theta'_v)) \\ J_{O_2} = a''_v C_T (k''_{r1/2} (1 - \theta''_v) - k''_{f1/2} P_{O_2}^{0.5} \theta''_v) \end{cases} \quad (15)$$

And the flux equation:

$$J_{O_2} = \frac{C_T D_v (k''_{r1/2} (k'_{f1/2} P_{O_2}^{0.5} + k'_{r1/2}) - k'_{r1/2} (k''_{f1/2} P_{O_2}^{0.5} + k''_{r1/2}))}{D_v \left( \frac{1}{a'_v} (k'_{f1/2} P_{O_2}^{0.5} + k'_{r1/2}) + \frac{1}{a''_v} (k''_{f1/2} P_{O_2}^{0.5} + k''_{r1/2}) \right) + 2L (k'_{f1/2} P_{O_2}^{0.5} + k'_{r1/2}) (k''_{f1/2} P_{O_2}^{0.5} + k''_{r1/2})} \quad (16)$$

When the flux equation is determined,  $D_v$  appears to be equal to:

$$D_v = \frac{\prod_{i=1}^N D_v^i}{\sum_{j=1}^N \frac{\prod_{i=1}^N D_v^i}{D_v^j}} \quad (17)$$

The variation of  $D_v^i$  depends on the variation of the oxygen vacancies gradient,  $(\theta_v^{i+1} - \theta_v^i)$ . Three boundary cases could be described (Figure 60).

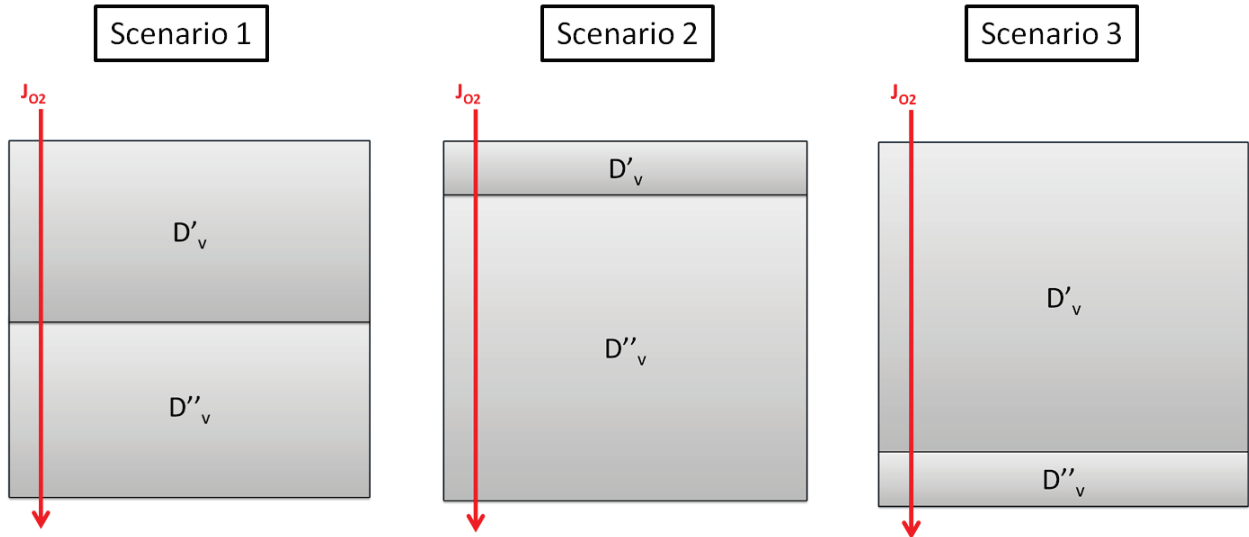


Figure 60 Three different scenarios to ensure the continuity of the model

- **Hypothesis 1:** Linear variation of the gradient:  $(\theta_v^{i+1} - \theta_v^i) = Cst.(\theta_v^{i+2} - \theta_v^{i+1})$ , with A a constant (-), so  $D_v^i = (1/A)D_v^{i+1}$ ,  $D_v$  becomes then:

Model 1 
$$D_v = \frac{2D'_v D''_v}{D'_v + D''_v} \quad (18)$$

- **Hypothesis 2:** High variation of the gradient at the beginning  $[(\theta_v^2 - \theta_v^1) = B(\theta_v^3 - \theta_v^2)]$  (implies:  $D_v^1 = 1/B \cdot D_v^2$ ), then the gradient remains constant:  $[(\theta_v^{i+1} - \theta_v^i) = (\theta_v^{i+2} - \theta_v^{i+1})] (D_v^2 = D_v^i = D_v^N)$

Model 2 
$$D_v = \frac{ND'_v D''_v{}^N}{(N-1)D'_v D''_v{}^{(N-1)} + D''_v{}^N} \quad (19)$$

- **Hypothesis 3:** High variation of the gradient at the end  $[(\theta_v^{N+1} - \theta_v^N) = C(\theta_v^N - \theta_v^{N-1})]$  (implies:  $D_v^{N-1} = 1/C \cdot D_v^N$ ), then the gradient remains constant:  $[(\theta_v^{i+1} - \theta_v^i) = (\theta_v^{i+2} - \theta_v^{i+1})] (D_v^{N-1} = D_v^i = D_v^1)$

Model 3 
$$D_v = \frac{ND''_v D'_v{}^N}{(N-1)D''_v D'_v{}^{(N-1)} + D'_v{}^N} \quad (20)$$

With N=10.

Introducing kinetic parameters associated to the oxygen stoichiometry equal to 1 (equation (8)), we obtain the following equation (21):

(21)

$$J_{O_2} = \frac{C_T \sqrt{P'_{O_2} P''_{O_2}} (k'_f k''_r \sqrt{K'' P'_{O_2}} - k''_f k'_r \sqrt{K' P''_{O_2}})}{\left(1/a''_v (1 + \sqrt{K'' P''_{O_2}}) (k'_f P'_{O_2} + k'_r \sqrt{K' P'_{O_2}}) + 1/a'_v (1 + \sqrt{K' P'_{O_2}}) (k''_f P''_{O_2} + k''_r \sqrt{K'' P''_{O_2}}) + 2L/D_v (k'_f P'_{O_2} + k'_r \sqrt{K' P'_{O_2}}) (k''_f P''_{O_2} + k''_r \sqrt{K'' P''_{O_2}})\right)}$$

## IV. Results

### IV.1. Oxygen permeation measurements on Ba<sub>0.5</sub>Sr<sub>0.5</sub>Co<sub>0.8</sub>Fe<sub>0.2</sub>O<sub>3-δ</sub> membrane

Oxygen fluxes through a dense Ba<sub>0.5</sub>Sr<sub>0.5</sub>Co<sub>0.8</sub>Fe<sub>0.2</sub>O<sub>3-δ</sub> membrane have been measured under isothermal conditions from 1073 to 1173 K. At a fixed feed pressure (P'<sub>O<sub>2</sub></sub>= 21 kPa), the oxygen flux through the dense membrane decreased when the partial pressure of oxygen at the sweep side increased (Figure 61). At a fixed oxygen pressure at the sweep side (P''<sub>O<sub>2</sub></sub>=1, 2 and 3 kPa) (Figure 62), the experimental oxygen flux increased with an increasing oxygen partial pressure at the feed side (P'<sub>O<sub>2</sub></sub>) and levels off at P'<sub>O<sub>2</sub></sub>>60 kPa. The variation of the membrane fluxes are expected and relate mainly to the different oxygen potential which are applied at both membrane sides. At 1173 K using a membrane of 2 mm thick, the oxygen flux was limited by the diffusion through the dense membrane<sup>11</sup>.

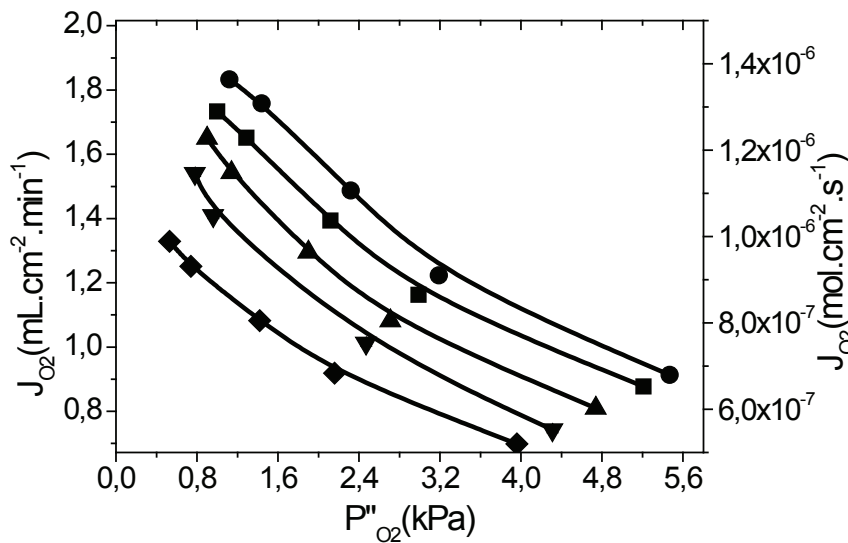


Figure 61 Oxygen flux as a function of the partial pressure of oxygen in the sweep side at different temperature with 21% of oxygen in nitrogen in the air side with a total flow rate of 200 ml min<sup>-1</sup> (STP), at 1073 K (◆), at 1098 K (▼), at 1123 K (▲), at 1158 K (■); at 1173 K (●).

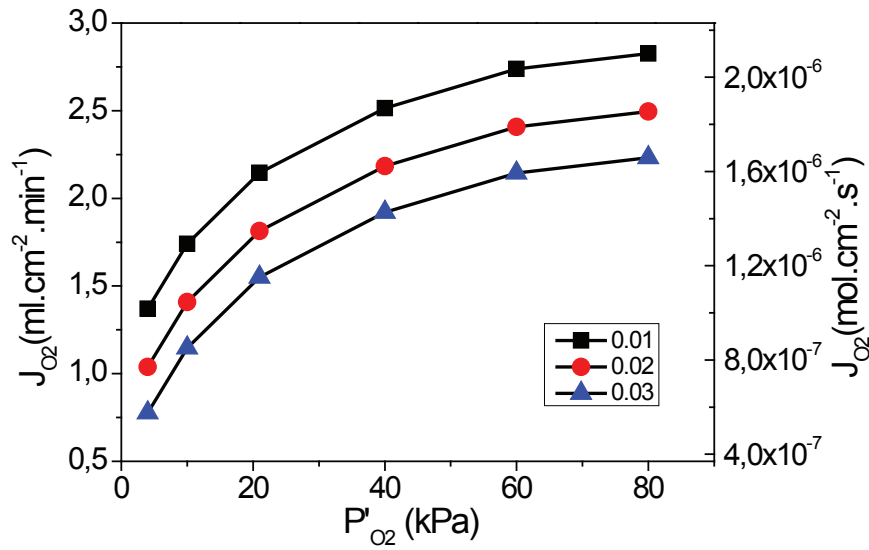


Figure 62 Oxygen flux as a function of the partial pressure of oxygen in the air side with a total flow rate of  $200 \text{ ml min}^{-1}$  (STP) on both side of the membrane at  $1173 \text{ K}$  and different partial pressure of oxygen in the sweep side: (■)  $P''_{\text{O}_2}=1 \text{ kPa}$ ; (●)  $P''_{\text{O}_2}=2 \text{ kPa}$  and (▲)  $P''_{\text{O}_2}=3 \text{ kPa}$ .

Under isobaric conditions on both membrane sides ( $P'_{\text{O}_2}=21 \text{ kPa}$  and  $P''_{\text{O}_2}=1,2 \text{ and } 3 \text{ kPa}$ ), the oxygen fluxes increased with temperature (Figure 63). The phenomenon is consistent with an activated diffusion process of oxygen as measured over powder (Table 18).

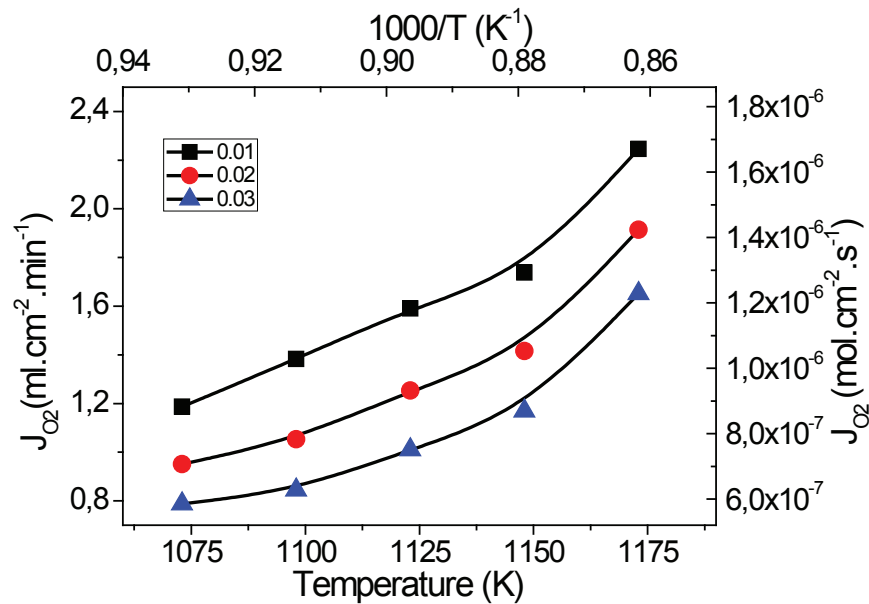


Figure 63 Oxygen flux as a function of the temperature with  $P'_{\text{O}_2}=21 \text{ kPa}$  in the air side and a total flow rate of  $200 \text{ ml min}^{-1}$  (STP) in the sweep side the partial pressure of oxygen is fixed to: (■)  $P''_{\text{O}_2}=1 \text{ kPa}$ ; (●)  $P''_{\text{O}_2}=2 \text{ kPa}$  and (▲)  $P''_{\text{O}_2}=3 \text{ kPa}$

Observed fluxes fall in the same range as in most literature reports (Table 19). We stress that in most studies the membrane surfaces are significantly smaller and the oxygen partial pressure at the sweep side are generally not reported, which makes the comparison not straightforward. In addition, membranes may not have the same thickness as in the case of Van Veen<sup>12</sup> et al.

Table 19 Literature data

Reference	L	S	Q <sub>air</sub>	Q <sub>sweep</sub>	T	P' <sub>O<sub>2</sub></sub>	P'' <sub>O<sub>2</sub></sub>	Oxygen flux
	cm	cm <sup>2</sup>	ml min <sup>-1</sup>	ml min <sup>-1</sup>	K	kPa	kPa	ml.cm <sup>-2</sup> .min <sup>-1</sup>
<sup>13</sup>	0.1	0.50	50	30	973	21	1	0.54
<sup>14</sup>	0.15	0.85	150	30	973	21	1	0.23
<sup>15</sup>	0.15	0.79	150	60	973	21	1	0.80
This work	0.2	3.5	200	200	973	21	1	0.85
<sup>13</sup>	0.1	0.50	50	30	1073	21	2	1.05
<sup>14</sup>	0.15	0.85	150	30	1073	21	2	0.64
<sup>15</sup>	0.15	0.79	150	60	1073	21	2	1.35
This work	0.2	3.5	200	200	1073	21	2	1.14
<sup>13</sup>	0.1	0.50	50	30	1173	21	3	1.45
<sup>14</sup>	0.15	0.85	150	30	1173	21	3	1.09
<sup>15</sup>	0.15	0.79	150	60	1173	21	3	2.00
This work	0.2	3.5	200	200	1173	21	3	1.63

## IV.2. Parameter estimation

The observed oxygen permeation data were fitted with the state of the art model of Xu and Thomson<sup>16</sup> (Figure 64). The parameter estimates are obtained by non-linear regression analysis (Table 20). Although surface kinetic rate constants for Ba<sub>0.5</sub>Sr<sub>0.5</sub>Co<sub>0.8</sub>Fe<sub>0.2</sub>O<sub>3-δ</sub> have not been reported in the literature using this approach, values (Table 20) are of the same order of magnitude as those obtained by Xu and Thomson<sup>16</sup> over La<sub>0.6</sub>Sr<sub>0.4</sub>Co<sub>0.2</sub>Fe<sub>0.8</sub>O<sub>3-δ</sub> (LSCF). We note however that the diffusion energy is significantly lower for BSCF (40 kJ mol<sup>-1</sup>) than for LSCF (74 kJ mol<sup>-1</sup>)<sup>16</sup>. Simulated and observed oxygen fluxes are plotted as function of operating conditions in figure 6. The Xu & Thomson model describes properly the membrane flux as a function of the oxygen partial pressure on the sweep side, but overestimates the oxygen flux when the oxygen partial pressure is low at the feed side. The temperature dependence is not properly described. In the seminal publication Xu & Thomson reported a major departure of the model with the oxygen partial pressure at the feed side for LSCF membrane.

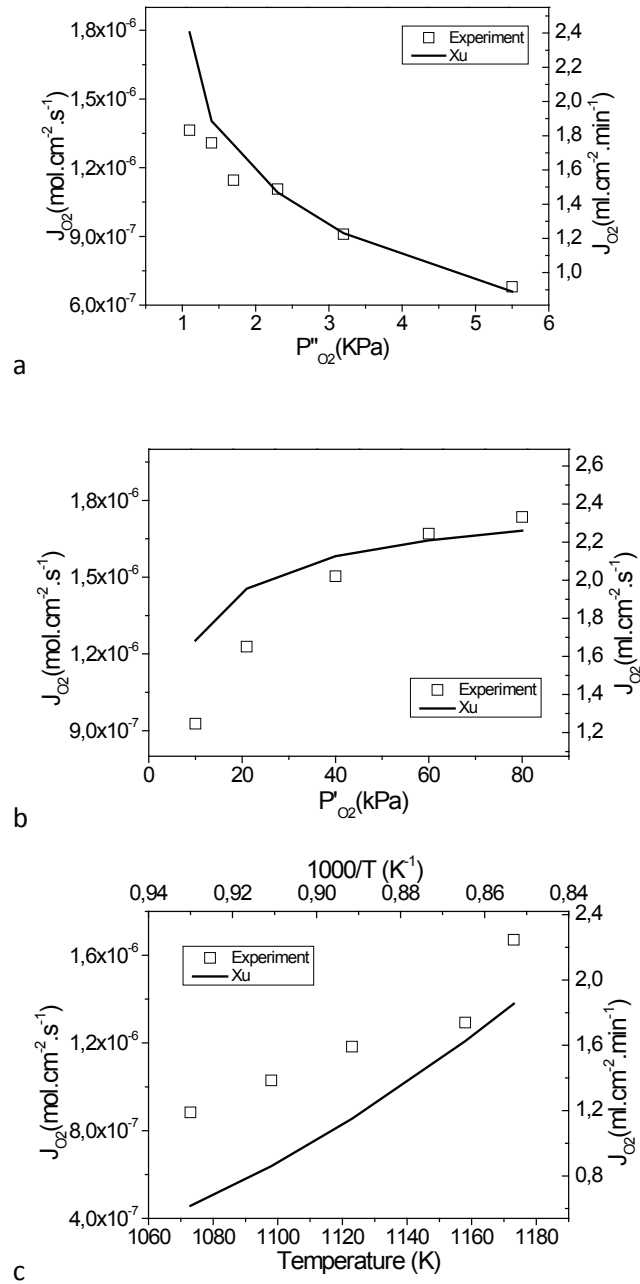


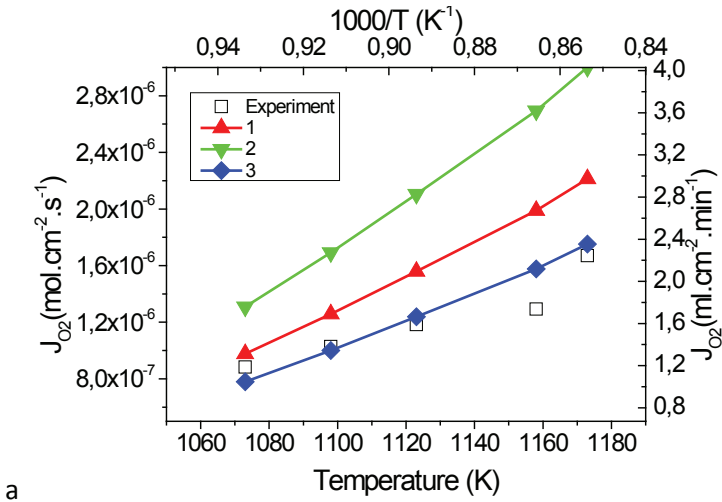
Figure 64 Comparison of the calculated flux (-) from Xu/Thomson model as a function of  $P''_{O_2}$  (at 1173 K and  $P'_{O_2}=80$  kPa)(a) and  $P'_{O_2}$  (at 1173 K and  $P''_{O_2}=1$  kPa) (b) and temperature ( $P'_{O_2}=21$  kPa and  $P''_{O_2}=1$  kPa) (c) and experimental data in the same conditions ( $\square$ )

Table 20 Parameters used for Xu/Thomson model estimated from oxygen flux on BSCF membrane operated under conditions described in Figure 64.

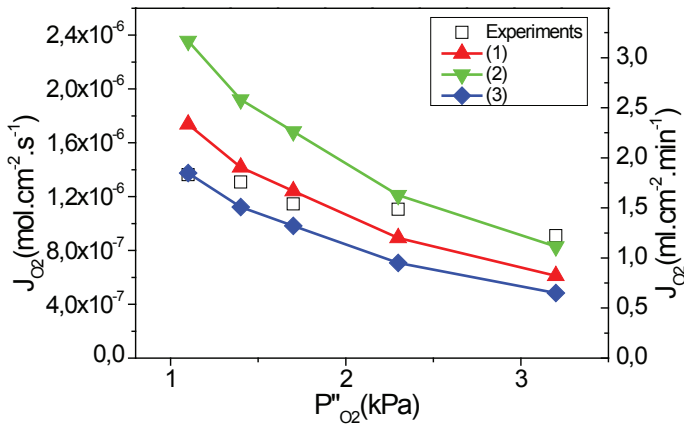
Surface reverse kinetic rate parameter		Surface forward kinetic rate parameter		Oxygen vacancies diffusion parameter	
$k_{rXu}^{\circ}$	$E_{rXu}$	$k_{fXu}^{\circ}$	$E_{fXu}$	$D_{vXu}^{\circ}$	$E_{dXu}$
$\text{mol cm}^{-2} \text{s}^{-1}$	$\text{kJ mol}^{-1}$	$\text{cm atm}^{-0.5} \text{s}^{-1}$	$\text{kJ mol}^{-1}$	$\text{cm}^2 \text{s}^{-1}$	$\text{kJ mol}^{-1}$
$3.21 \cdot 10^4$	212.0	$6.36 \cdot 10^6$	182	$2.40 \cdot 10^{-2}$	40

### IV.3. Simulation of oxygen flux based using microkinetic parameters obtained from powder.

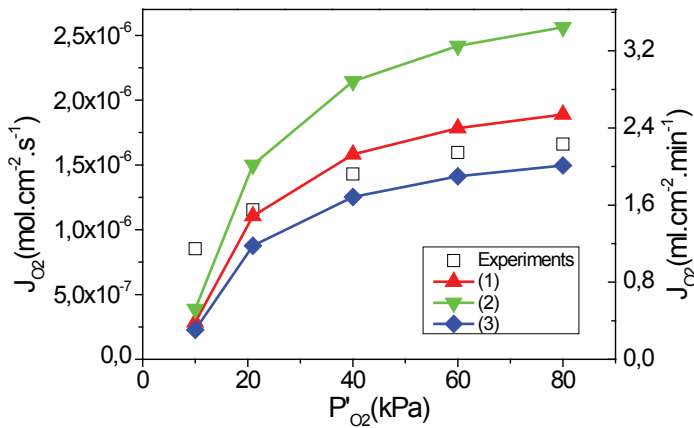
The three oxygen flux models are compared with experimentally observed oxygen fluxes through the  $\text{Ba}_{0.5}\text{Sr}_{0.5}\text{Co}_{0.8}\text{Fe}_{0.2}\text{O}_{3-\delta}$  membrane under a wide range of conditions (Figure 65). Obviously, the model #2, which assumes a high mean value of  $D_v$ , systematically overestimates the oxygen permeation flux. On the other hand models #1 and #3 describe properly the observed absolute values and trends, rivalling one other depending on the operating variable. We stress here that the simulated fluxes are obtained directly with microkinetic parameters obtained from measurements obtained on the corresponding powder samples (Table 18) and that we did not carry out any further parameter adjustments. We can however note a deviation of the model, which tends to underestimate the flux at high oxygen partial pressure ( $P''_{\text{O}_2} > 2 \text{ kPa}$ ) at the sweep side. This is likely due to the fact that the microkinetic  $k_f''$  and  $k_r''$  rate constants were estimated at  $P''_{\text{O}_2} = 1 \text{ kPa}$  and are strictly valid on a rather narrow window of the oxygen pressure partial pressure. This confirms our main hypothesis that adsorption-desorption rate coefficients shall be estimated on both sides of the membrane under conditions that represent membrane operation. Under the window of conditions of temperatures and pressures, the comparison between experimental and simulated data does not allow discriminating between the flux models #1 and #3.



a



b



c

Figure 65 Comparison between the experimental flux (□) and different flux models (#1, ▲), (#2, ▼), (#3, ◆) as a function of the temperature at  $P'_{O_2}=21$  kPa and  $P''_{O_2}=1$  kPa (top), of the partial pressure of oxygen on the sweep side at 1173 K and  $P'_{O_2}=70$  kPa (medium) and of the partial pressure of oxygen on the feed side at 1173 K and  $P''_{O_2} = 1$  kPa (bottom).

#### IV.4. Simulation of the impact of membrane thickness on the oxygen flux

The prediction of the impact of the membrane thickness on the oxygen flux is very important for a rational design of membranes. Betz et al<sup>17,18</sup> show that the reduction of BSCF membrane thickness of 88% increases only the membrane flux by 30%. It is thus important to identify what are the limiting factors that govern the flux. On the other hand, the comparison of simulated flux with experimental data obtained on membranes with different thickness may support model discrimination. The simulations are carried out at 1010K for flux models # 1 and #3 (Table 21, Figure 66). The decrease of the membrane thickness from 2 mm to 0.7 mm has a strong effect on the membrane flux whereas further reduction of the thickness (below 0.1 mm) exhibit very limited impact.

Table 21 Input conditions for modeling of Figure 66

$P'_{O_2}$ (kPa)	$P''_{O_2}$ (kPa)	Temperature (K)	Thickness (mm)	N
21	1	1010	0.07 to 2	10

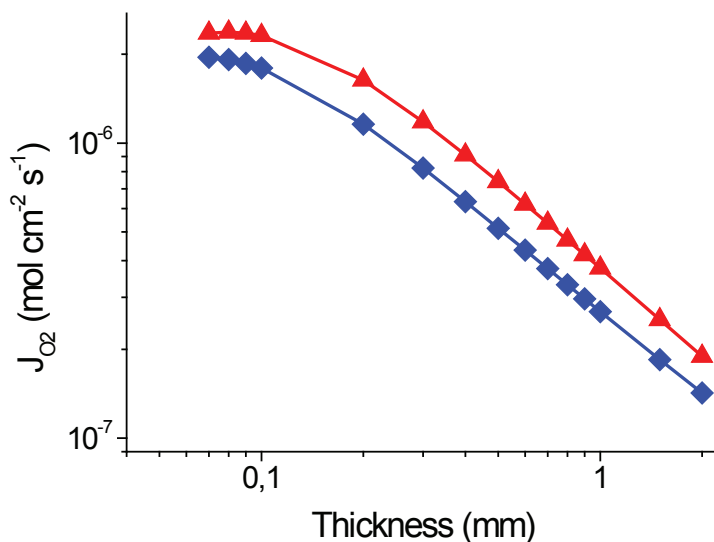


Figure 66 Different model flux as a function of the thickness at 1010 K: #1 predicted model with  $D_v$  a linear function of the thickness (▲) #3 predicted model with  $D_v$  constant on air side (◆).

With the purpose of discriminating models #1 and #3, simulation data are compared with observed data from literature. Fluxes have been simulated with model #1 and #3 as function of  $1000/T$  for 2 different thicknesses, 1 mm and 120  $\mu$ m, corresponding to membranes tested in the study of Betz et al<sup>17,18</sup> (Table 22, Figure 67). The model #1 overestimates the effect of thickness whereas the model (#3) perfectly matches with experimental data obtained by Betz and al<sup>17</sup>. It is an outstanding result

since no fitting of experimental membrane fluxes have been carried out for the simulation. Hence, we can conclude that the model #3 for which the  $D_v$  value increases close to the lean side is a scenario which can be considered for  $Ba_{0.5}Sr_{0.5}Co_{0.8}FeO_{3-\delta}$  membranes although model #2 cannot be rule out at this stage since the overall pressure drop in the porous support has not been taken into account in our simulation. Furthermore, we cannot generalize the conclusions on the evolution of  $D_v$  to other type of MIEC membranes.

Table 22 Input conditions for modeling of Figure 67

$P'_{O_2}$ (kPa)	$P''_{O_2}$ (kPa)	Temperature (K)	Thickness (mm)	N
21	1	1023 to 1173	1	10
21	2	1023 to 1173	0.12	10

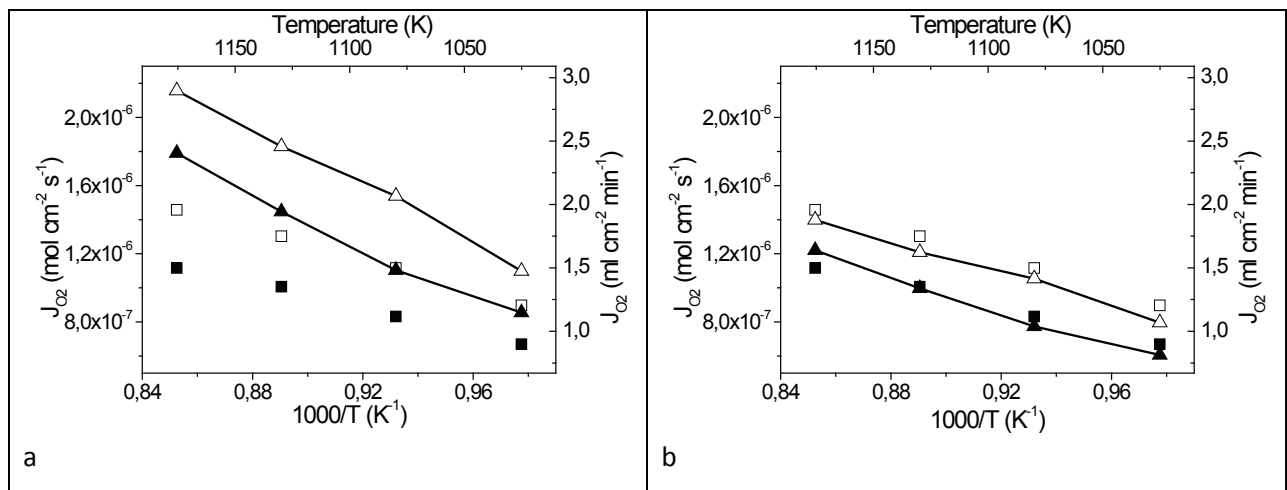


Figure 67 Oxygen flux as a function of  $1000/T$  for different thicknesses: Comparison between the dataset of Betz et al.(fig. 5<sup>17</sup>) ( $\square$   $L=1$  mm;  $\blacksquare$   $L=120$   $\mu$ m) and two modelled flux: simulated flux with model #1 -linear evolution of  $D_v$  (a) ( $\Delta L=1$  mm;  $\blacktriangle$   $L=120$   $\mu$ m); simulated flux with model #3 -  $D_v$  constant on air side (b) ( $\diamond L=1$  mm;  $\blacklozenge$   $L=120$   $\mu$ m).

In this last section, flux simulations are carried out in order to provide guidelines for the design of performing  $Ba_{0.5}Sr_{0.5}Co_{0.8}Fe_{0.2}O_{3-\delta}$  membranes and the identification of operational leverage conditions. Recently Baumann et al.<sup>19</sup> showed that very high fluxes have been achieved in thin  $Ba_{0.5}Sr_{0.5}Co_{0.8}Fe_{0.2}O_{3-\delta}$  supported membranes when the oxygen partial pressure is  $P'_{O_2}=100$ kPa. In contrast, we showed that in the case of a thick membrane (2mm), a partial pressure higher than 21 kPa in the feed side has a relative low impact on the total oxygen flux (Figure 62). In order to evaluate the combined effect of the reduction of membrane thickness and larger feeding pressure, flux simulations using model #3 were carried out. The simulation conditions and microkinetic parameters were estimated to match with experimental conditions of the work of Baumann et al.<sup>19</sup> which developed supported thin BSCF layer of 70  $\mu$ m. Simulated fluxed and observed data from Baumann et al.<sup>19</sup> are compared in Figure 68 (Input conditions for modelling are reported in Table 23).

Here again, we can observe a very good description of our model. The ability of our modelling approach arises from microkinetic rate constants that are intrinsic to the materials and therefore can be extrapolated to some extent without major deviation.

Table 23 Input conditions for modeling of Figure 68

$P'_{O_2}$ (kPa)	$P''_{O_2}$ (kPa)	Temperature (K)	Thickness (mm)	N
100	15	973 to 1273	0.3	10
21	2	973 to 1273	0.3	10

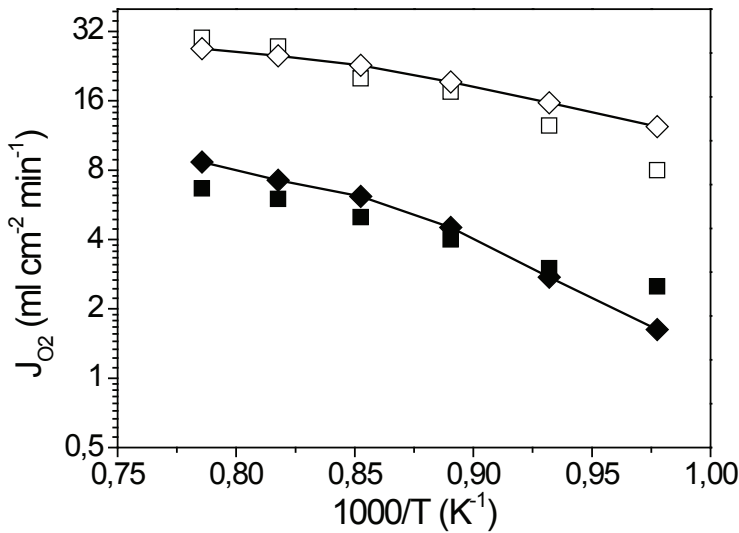


Figure 68 Comparison between literature dataset (fig. 5<sup>19</sup>) ( $\square$   $P'_{O_2}$ =100 kPa;  $\blacksquare$   $P'_{O_2}$ =21 kPa) and our model (3) (line- $\diamond$   $P'_{O_2}$ =100 kPa;  $\blacklozenge$   $P'_{O_2}$ =21 kPa) as a function of  $1/T$ .

The simulations are extended to different membrane thicknesses in order to estimate the leverage effect of the oxygen partial pressure for thin membranes (Table 24, Figure 69). As we can observe the effect of the oxygen partial pressure at the feed side is very limited for thicknesses larger than 0,5mm. There is an increasing leverage effect of the pressure when the membrane is thinner. When the partial pressure increases from 20 to 100kpa (factor 5) the flux increases by a factor 4.5 for a membrane of 62.5 $\mu$ m against only 2 for a membrane of 1mm.

Table 24 Input conditions for modeling of Figure 69

$P'_{O_2}$ (kPa)	$P''_{O_2}$ (kPa)	Temperature (K)	Thickness ( $\mu$ m)	N
21 to 100	15	1123	1000	10
21 to 100	2	1123	500	10
21 to 100	15	1123	250	10
21 to 100	2	1123	125	10
21 to 100	15	1123	62.5	10

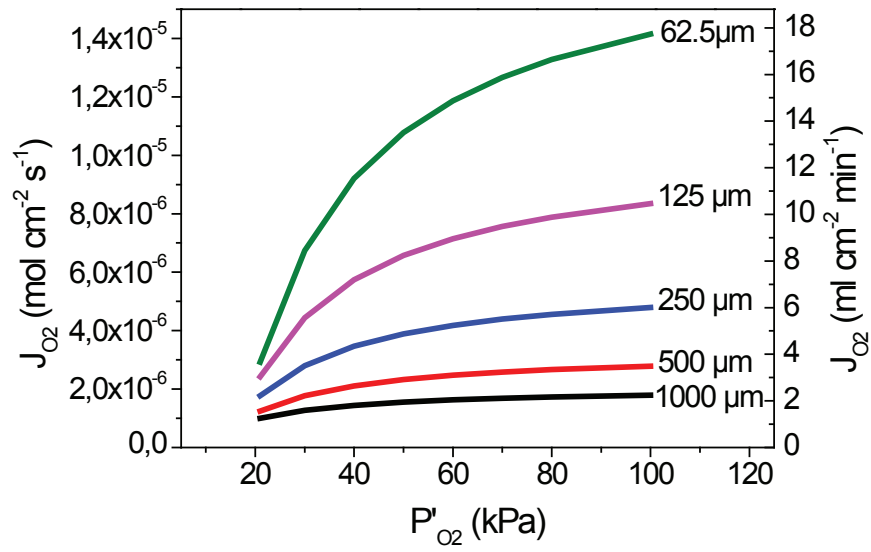


Figure 69 Impact of the partial pressure of oxygen in the air side on the flux with different thickness of the membrane  $t=1173\text{K}$ .

## V. CONCLUSIONS

Fluxes of  $\text{Ba}_{0.5}\text{Sr}_{0.5}\text{Co}_{0.8}\text{Fe}_{0.2}\text{O}_{3-6}$  membrane have been modelled from microkinetic parameters in a flux model without using any fitting on experimental membrane data. The model properly describes the variation of experimental conditions (temperature and oxygen partial pressures) as well as membrane thickness. The microkinetic parameters accounting for surface kinetic reaction rates and diffusion coefficients are measured from corresponding  $\text{Ba}_{0.5}\text{Sr}_{0.5}\text{Co}_{0.8}\text{Fe}_{0.2}\text{O}_{3-6}$  materials as powder (chapter 3). The model that accounts for different rate constants and diffusion coefficient due to the difference of oxygen gradient in the membrane describes experimental oxygen fluxes remarkably well.

In contrast to macrokinetic approaches in which the measured rate constants are apparent, microkinetic parameters are intrinsic to the features of the solids and therefore can be applied in different flux models such as in a fixed bed or in a planar membrane cell (this study). Using the same approach, the modelling of flux with a different membrane geometry in which internal and external surfaces are different can be carried out. The modelling of a membrane device having a coated porous activation layer is possible in principle but goes beyond the scope of this work. Besides the ability of integration of microkinetic parameters in various reactor/membrane devices, the microkinetic rate constants remain valid in a larger operational window of temperature and pressure which allows predicting performances in which experimental data can be hardly obtained, such as with ultrathin membranes.

Simulations carried out on thin  $\text{Ba}_{0.5}\text{Sr}_{0.5}\text{Co}_{0.8}\text{Fe}_{0.2}\text{O}_{3-6}$  membranes demonstrate that high fluxes can be obtained by increasing the oxygen partial pressure at the feed side. We believe that the combination of high feed pressure and thin membrane is a powerful leverage to significantly increase oxygen flow in  $\text{Ba}_{0.5}\text{Sr}_{0.5}\text{Co}_{0.8}\text{Fe}_{0.2}\text{O}_{3-6}$  membranes. Nevertheless, we recognize that mechanical stability shall become an issue at a certain point.

The application of this microkinetic modelling approach will be extended to other type of MIEC membranes in the next chapter.

# Bibliography

---

1. Z. Shao and S. M. Haile, *Nature*, 2004, **431**, 170–3.
2. P. J. Gellings and H. J. M. Bouwmeester, *Catal. Today*, 2000, **58**, 1–53.
3. L. Wang, R. Merkle, J. Maier, T. Acartürk and U. Starke, *Appl. Phys. Lett.*, 2009, **94**, 071908.
4. T. Ishigaki, S. Yamauchi, K. Kishio, J. Mizusaki and K. Fueki, *J. Solid State Chem.*, 1988, **187**, 179–187.
5. E. Bucher, A. Egger, P. Ried, W. Sitte and P. Holtappels, *Solid State Ionics*, 2008, **179**, 1032–1035.
6. H. Ullmann, N. Trofimenko, F. Tietz, D. Stöver and A. Ahmad-Khanlou, *Solid State Ionics*, 2000, **138**, 79–90.
7. A. Vivet, P. M. Geffroy, T. Chartier, P. Del Gallo and N. Richet, *J. Memb. Sci.*, 2011, **372**, 373–379.
8. G. B. Froment and K. B. Bischoff, *John Wiley, New York*, 1979.
9. L. Heyne, in *Solid Electrolytes*, ed. S. Beler, Springer, New York, 1977, pp. 169–221.
10. P. Kofstad, *Bin. Met. Oxides*, 1972, 100–105.
11. US Patent, 5.240.480, 1995.
12. A. C. van Veen, M. Rebeilleau, D. Farrusseng and C. Mirodatos, *Chem. Commun. (Camb.)*, 2003, **33**, 32–3.
13. M. Rebeilleau-Dassonneville, S. Rosini, a. C. Van Veen, D. Farrusseng and C. Mirodatos, *Catal. Today*, 2005, **104**, 131–137.
14. Z. Shao, W. Yang, Y. Cong, H. Dong, J. Tong and G. Xiong, *J. Memb. Sci.*, 2000, **172**, 177–188.
15. A. Behrouzifar, A. A. Asadi, T. Mohammadi and A. Pak, *Ceram. Int.*, 2012, **38**, 4797–4811.
16. S. J. Xu and W. J. Thomson, *Chem. Eng. Sci.*, 1999, **54**, 3839–3850.
17. M. Betz, F. Schulze-Küppers, S. Baumann, W. A. Meulenber and D. Stöver, *Adv. Sci. Technol.*, 2010, **72**, 93–98.
18. W. A. Meulenber, S. Baumann and J. M. Serra, in *International Workshop Inorganic Membrane Technology Advanced Production and Design*, 2011.
19. S. Baumann, J. M. Serra, M. P. Lobera, S. Escolástico, F. Schulze-Küppers and W. a. Meulenber, *J. Memb. Sci.*, 2011, **377**, 198–205.



# CHAPTER 5-Application of the microkinetic methodology to LSCF and BLF membranes

---

## I. Introduction

$\text{La}_{1-x}\text{Sr}_x\text{Co}_{1-y}\text{Fe}_y\text{O}_{3-\delta}$  have been first studied in the late 1980s by Teraoka et al.<sup>1</sup>. These membranes were in the centre of interest for their capabilities to generate pure oxygen. They started to be used for technological applications in the early 1990s for solid oxide fuel cells (SOFCs), electrochemical oxygen pump (EOP) and oxygen sensors. In the middle of the 1990s, a wider range of application was considered especially for selective oxidation of hydrocarbons. Despite intensive efforts to obtain higher fluxes, the oxygen flux remains too moderate for industrial perspectives. Xu and Thomson developed a flux model based on  $\text{La}_{0.6}\text{Sr}_{0.4}\text{Co}_{0.2}\text{Fe}_{0.8}\text{O}_{3-\delta}$  (LSCF).

We will determine the kinetic parameters for this composition in order to validate our methodology, and our simulation results would be compared to Xu Thomson results.

Then we will look at an Co-free alternative to both  $\text{La}_{0.6}\text{Sr}_{0.4}\text{Co}_{0.2}\text{Fe}_{0.8}\text{O}_{3-\delta}$  and  $\text{Ba}_{0.5}\text{Sr}_{0.5}\text{Co}_{0.8}\text{Fe}_{0.2}\text{O}_{3-\delta}$ . Indeed, regulations are set up to remove cobalt oxide in for applications outside the use in chemical industry. Many groups have been working on cobalt-free perovskites such as  $\text{La}_{1-x}\text{Sr}_x\text{FeO}_{3-\delta}$ <sup>2</sup>,  $\text{CaTi}_{0.8}\text{Fe}_{0.2}\text{O}_{3-\delta}$ <sup>3</sup>,  $\text{Ba}_{0.3}\text{Sr}_{0.7}\text{FeO}_{3-\delta}$ <sup>4</sup>,  $\text{La}_{0.6}\text{Sr}_{0.4}\text{Ga}_{0.6}\text{Fe}_{0.4}\text{O}_{3-\delta}$ <sup>5</sup>,  $\text{BaFe}_{1-y}\text{Ce}_y\text{O}_{3-\delta}$ <sup>6</sup> and  $\text{Ba}_{0.5}\text{Sr}_{0.5}\text{Fe}_{0.8}\text{Zn}_{0.2}\text{O}_{3-\delta}$ <sup>7</sup>. The material  $\text{Ba}_{0.95}\text{La}_{0.05}\text{FeO}_{3-\delta}$  has been developed by a Japanese group<sup>8,9</sup> in the late 2000s. They developed  $\text{BaFeO}_{3-\delta}$  based cobalt free families. They pointed out a high oxygen permeation of  $\text{Ba}_{0.95}\text{La}_{0.05}\text{FeO}_{3-\delta}$  (BLF). They found a flux of  $1.96 \text{ ml min}^{-1} \text{ cm}^{-2}$  at  $930 \text{ }^\circ\text{C}$  for 1mm thickness which is 20% higher than BSCF in comparable conditions.

We choose to study  $\text{Ba}_{0.95}\text{La}_{0.05}\text{FeO}_{3-\delta}$  (BLF) material in order to evaluate a Co-free alternative to  $\text{Ba}_{0.5}\text{Sr}_{0.5}\text{Co}_{0.8}\text{Fe}_{0.2}\text{O}_{3-\delta}$ .

BLF membrane are prepared and characterized in order to obtain the microkinetic parameters. Then, oxygen fluxes are measured in semi-permeability tests. These results are compared to the modelled oxygen flux.

## II. Study of LSCF materials and membranes

### II.1. Characterization of LSCF material

#### II.1.1. Oxygen vacancies characterization and adsorption constants estimation

The evolution of oxygen non-stoichiometry ( $\delta$ ) and thus oxygen vacancies ( $\theta_v$ ) of  $\text{La}_{0.6}\text{Sr}_{0.4}\text{Co}_{0.2}\text{Fe}_{0.8}\text{O}_{3-\delta}$  with the temperature at fixed oxygen partial pressure are measured by thermogravimetric analysis (TGA). Prior to TGA, the initial oxygen non-stoichiometry ( $\delta$ ) of  $\text{La}_{0.6}\text{Sr}_{0.4}\text{Co}_{0.2}\text{Fe}_{0.8}\text{O}_{3-\delta}$  at room temperature has been determined by iodometric titration<sup>10,11</sup> (Table 25). Series of 10 repetitive measurements gives a value of non-stoichiometry ( $\delta$ ) equal to  $0.08 \pm 0.005$  corresponding to a fraction of oxygen vacancies ( $\theta_v$ ) of 0.03.

Table 25 Iodometric titration on LSCF

LSCF	mass	Ve <sub>q</sub>	[Na <sub>2</sub> S <sub>2</sub> O <sub>3</sub> ]	$\delta$	M <sub>LSCFi</sub>	$\Delta\delta$
1	0.050	17.7	0.0199	0.03	222.38	0.007
2	0.086	36.5	0.0169	0.03	222.38	0.004
3	0.084	33.2	0.0169	0.01	222.70	0.001
4	0.100	43.7	0.0169	0.04	222.22	0.005
5	0.102	44.1	0.0169	0.03	222.38	0.005
6	0.095	40.2	0.0169	0.03	222.38	0.005
7	0.085	34.9	0.0169	0.03	222.38	0.005
8	0.105	49.2	0.0169	0.02	222.54	0.003
9	0.083	32.8	0.0169	0.03	222.38	0.005
10	0.083	34.5	0.0169	0.04	222.22	0.005

$\delta_{\text{LSCF}} = 0.03 \pm 0.005$

The evolution of the fraction of vacancies as a function of temperature has been determined from the weight loss of the TGA curve ( $\theta_v = \delta/3$ ) under two different fixed oxygen partial pressures (Figure 70). The partial pressure of 21 kPa of O<sub>2</sub> (solid line) and under 1 kPa of O<sub>2</sub> (dashed line) correspond typically at conditions applied for air separation in a membrane process, for the oxygen rich side (air feed) and for the oxygen lean side (permeate side), respectively. The fraction of vacancies is stable until 823K under P<sub>O<sub>2</sub></sub>=1 kPa and then increases linearly. Under P<sub>O<sub>2</sub></sub>=21 kPa, until 1050 K, the quantity of vacancies remains constant, we observe a linear trend parallel to the former. Hence, we can observe an almost constant difference of oxygen vacancy concentration between the oxygen rich and lean conditions over the temperature range of interest. We have observed that after TGA

measurements, cell parameters remain constant within measurement errors. In addition, XRD does not reveal the formation of additional phases.

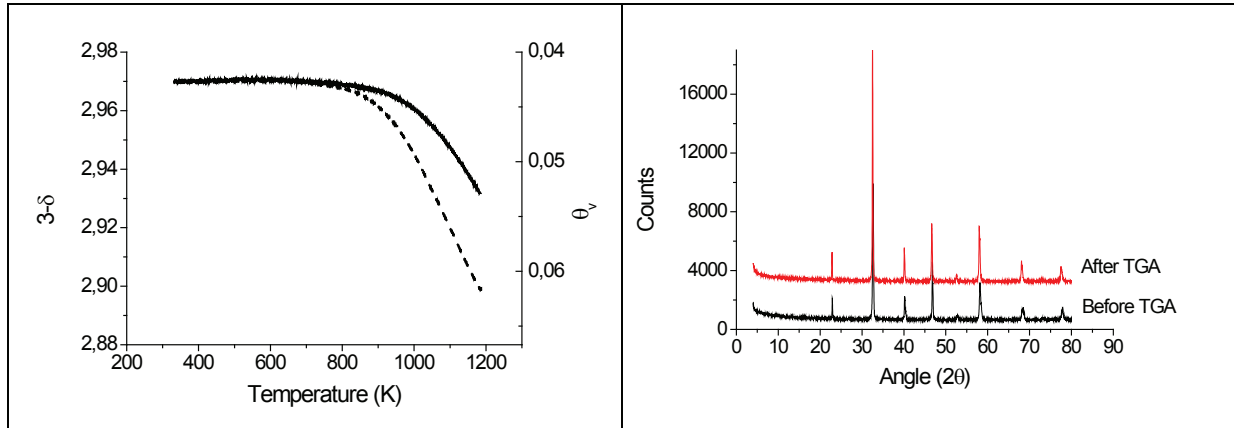


Figure 70 TGA on LSCF powder under O<sub>2</sub>/N<sub>2</sub> flow, with P<sub>O<sub>2</sub></sub>=21 kPa (plain line) and P<sub>O<sub>2</sub></sub>=1 kPa (Dash line) and XRD before and after experiments.

Langmuir adsorption constants as well as the adsorption enthalpies are calculated at the two different oxygen pressures (1 and 21kPa) from the evolution of (δ)(Figure 71). These values are recorded in Table 26.

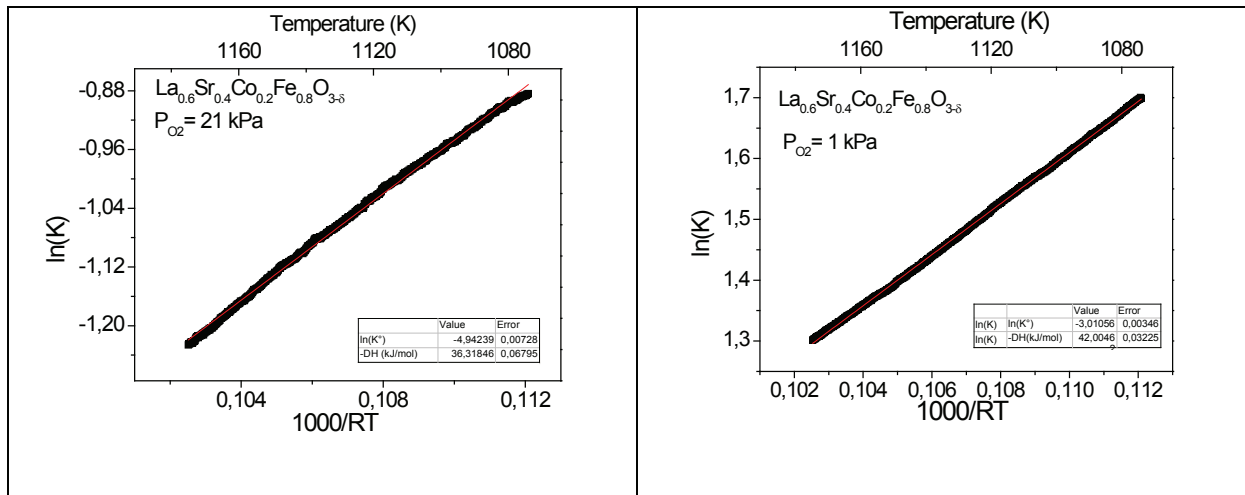


Figure 71 Determination of Langmuir adsorption constants from TGA measurement

Table 26 Langmuir adsorption equilibrium constants

P <sub>O<sub>2</sub></sub> (kPa)	K°(1 Pa <sup>-1</sup> )	ΔH (kJ mol <sup>-1</sup> )
21	7.2 10 <sup>-2</sup>	-36.3
1	5.0 10 <sup>-2</sup>	-41.6

### II.1.2. Estimation of the kinetic parameters by SSITKA experiments

When comparing qualitatively the oxygen isotope exchange experiments, the exchange times last about an order of magnitude longer at  $P_{O_2}=1$  kPa than at  $P_{O_2}=21$  kPa (Figure 72). On the other hand the temperature has a slight effect at low temperatures but the effect levels out quickly above 900 K. The integration of the  $0.5 \cdot P^{32}O_2 + P^{16}O^{18}O$  signals gives the amount of exchanged oxygen. At  $T=973$  K and  $P_{O_2}=21$  kPa, 86% of all oxygen atoms in LSCF are exchanged. At  $P_{O_2}=1$  kPa this amounts to only 50%, due to the lower exchange rate, the exchange curves were not recorded until the end of the exchange.

The oxygen exchange curves ( $P^{16}O_2$  &  $P^{16}O^{18}O$ ) have been modelled for each level of oxygen partial pressure separately, but including all temperatures simultaneously. Initial regression analysis showed that quasi-equilibrium of the exchange rates is established at the time scale of the experiment. Thus only the forward rate parameters ( $k_f$ ) have been estimated during the regression analysis and the reverse rates parameters ( $k_r$ ) are calculated from the equilibrium rate constants ( $K=k_f/k_r$ ) determined from the TGA experiments (Table 26). The characteristic time constant ( $D/r^2$ ) for oxygen transport is estimated simultaneously to the fitting of oxygen exchange parameters. Figure 72 compares the model predicted response curves with the experimental ones. A good fit is obtained at both oxygen partial pressures and at all temperatures. The surface parameter and diffusion estimates are reported in Table 27 and Table 28, respectively.

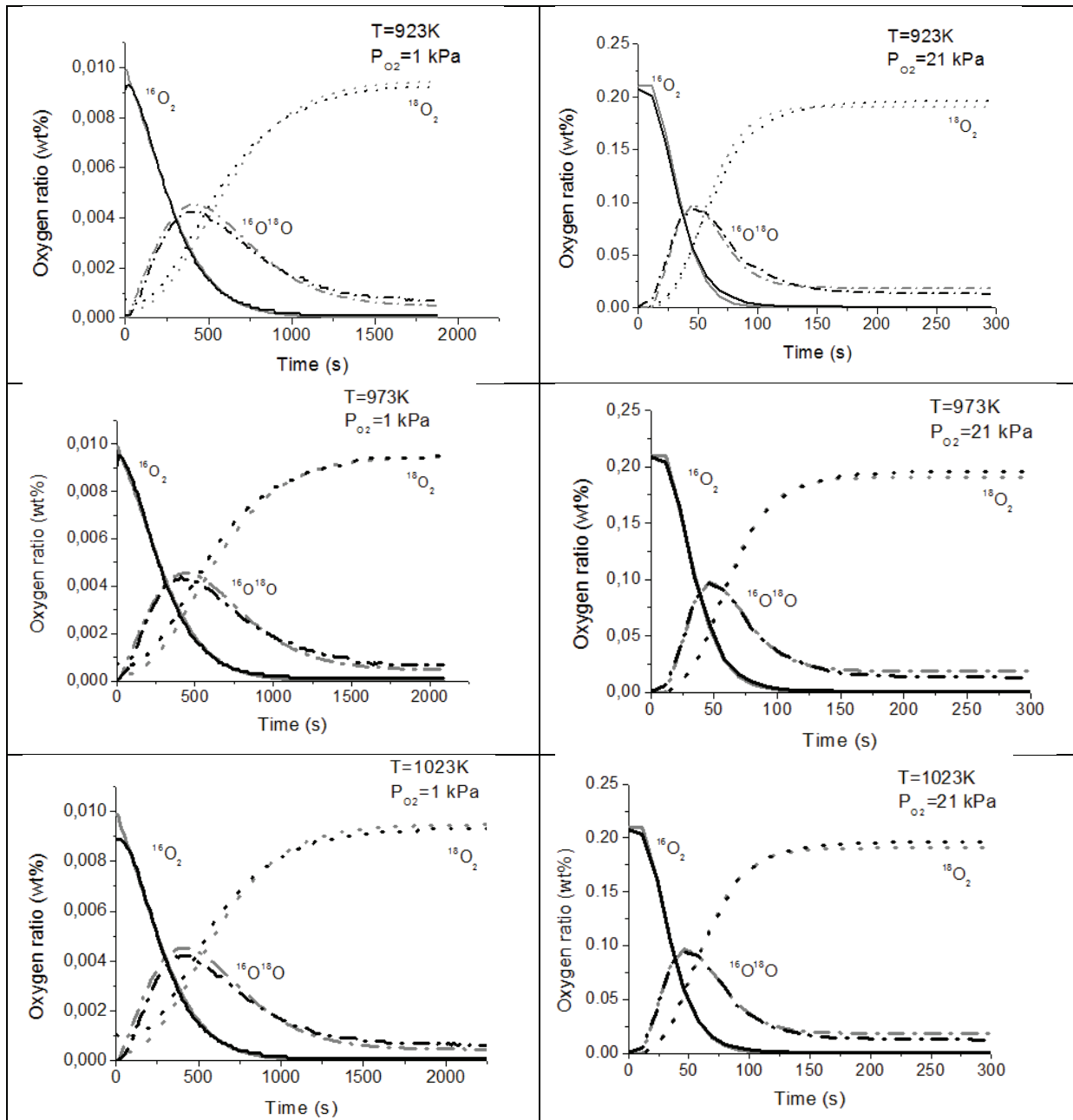


Figure 72 SSITKA experiments (plain) and model curve (dash),  $^{16}O_2(g)$ ,  $^{16}O^{18}O(g)$ ,  $^{18}O_2(g)$  at different partial pressure of oxygen at 923, 973 and 1023K.

The obtained kinetic parameters have been compared to the kinetic parameters obtained by Xu/Thomson (Table 27). They are in the same order of magnitude. The desorption activation energy of Xu/Thomson is included in between desorption activation energy obtained at  $P_{O_2} = 1 \text{ kPa}$  and  $P_{O_2} = 21 \text{ kPa}$ . In contrast, the adsorption activation energies (at low and high  $P_{O_2}$ ) are significantly lower than the value found by Xu/Thomson.

Table 27 Kinetic parameters estimated from regression analysis of the isotopic oxygen exchange response curves for LSCF. The confidence intervals estimated at 95%. For comparison, the estimated parameters obtained on LSCF membrane semi-permeability data from Xu and Thomson model are reported. Kinetic constants are calculated in two different units in order to allow direct comparison with literature data.

Shape	Surface reverse kinetic parameter			Surface forward kinetic parameter		ref
	P <sub>O<sub>2</sub></sub> kPa	k <sub>r</sub> <sup>°</sup> s <sup>-1</sup>	E <sub>r</sub> kJ.mol <sup>-1</sup>	k <sub>f</sub> <sup>°</sup> Pa <sup>-1</sup> .s <sup>-1</sup>	E <sub>f</sub> kJ.mol <sup>-1</sup>	
Powder	21	(2.7±0.07) 10 <sup>11</sup>	239±25	(8.1±0.1) 10 <sup>7</sup>	198±25	This work
Powder	1	(2.7±0.07) 10 <sup>11</sup>	243±25	(4.4±0.05) 10 <sup>7</sup>	207±25	This work
	kPa	mol cm <sup>-2</sup> s <sup>-1</sup>	kJ mol <sup>-1</sup>	cm atm <sup>-0.5</sup> s <sup>-1</sup>	kJ mol <sup>-1</sup>	
Powder	21	(5.5±0.15) 10 <sup>4</sup>	239±25	(5.9±0.1) 10 <sup>6</sup>	198±25	This work
Powder	1	(5.5±0.15) 10 <sup>4</sup>	243±25	(3.2±0.03) 10 <sup>6</sup>	207±25	This work
Membrane	NA	2.07 10 <sup>4</sup>	241.3±0.1	5.90 10 <sup>6</sup>	226.9	<sup>12</sup>

#### Estimation of diffusion coefficients

Oxygen exchange experiments give access to the characteristic diffusion time, which is the ratio of the diffusion coefficient to the square of the characteristic length ( $D^*/r^2$ ). The mean diameter of crystallite with an accessible surface was determined by N<sub>2</sub> adsorption measurements at 77 K. The BET surface area is equal to 3.2 m<sup>2</sup> g<sup>-1</sup> and  $\rho=5.89$  g cm<sup>-3</sup> which leads to a crystallite diameter ( $d_{\text{cryst}}$ ) of 0.32  $\mu\text{m}$ . Thus, we set the crystallite radius ( $r$ ) to 0.16  $\mu\text{m}$  for the estimation of the diffusion parameter. Finally, results are recorded in Table 28.

Table 28 Characteristic time constants for diffusion estimates from regression analysis of the oxygen exchange response curve between 700-900°C, and self diffusion parameter calculated using the crystallite radius ( $r$ ) equal to 0.16  $\mu\text{m}$ . The confidence intervals estimated at 95% level.

Pressure	D <sup>*°</sup> /r <sup>2</sup>	D <sup>*°</sup>	E <sub>d</sub>
kPa	s <sup>-1</sup>	cm <sup>2</sup> s <sup>-1</sup>	kJ mol <sup>-1</sup>
21	(2.0±0.4)10 <sup>5</sup>	(5±1)10 <sup>-5</sup>	76.9±10
1	(3.0±0.6)10 <sup>5</sup>	(7.6±1.5)10 <sup>-5</sup>	76.9±10

The Nernst-Einstein equation allows calculating the oxygen conductivity ( $\sigma_0$ ) from the oxygen self diffusion ( $D^*$ ) according to the formula:

$$\sigma_0 = \frac{4F^2(3 - \delta)D^*}{RTV_m} \quad (22)$$

F is the Faraday constant, R the gas constant and  $V_m$  the molar volume is  $38.5 \text{ mol cm}^{-3}$ . In air, Ullman et al.<sup>13</sup> found an oxygen conductivity of  $0.007 \text{ S cm}^{-1}$ . In our work, the oxygen conductivities calculated at 1073K, at 1 kPa and 21 kPa are 0.003 and  $0.005 \text{ S cm}^{-1}$  respectively. Our results are in good agreement with the literature.

## II.2. Modelling of the oxygen flux of LSCF membrane

We did not prepare LSCF membranes. All permeation data were collected from literature for allowing comparison between experimental observed fluxes and simulated from the kinetic model. As Xu-Thomson found high quality modelling results we will use their data set in order to obtain the tendencies for the experimental fluxes. Xu and Thomson fitted their model on 126 experimental data points in various conditions, their results are summarized in Table 29. They obtained a good fit with their experimental data. But they obtained a strong deviation for a membrane of 1.5mm and a partial pressure of oxygen in the air side of 100 kPa (Disk #3-Figure 73).

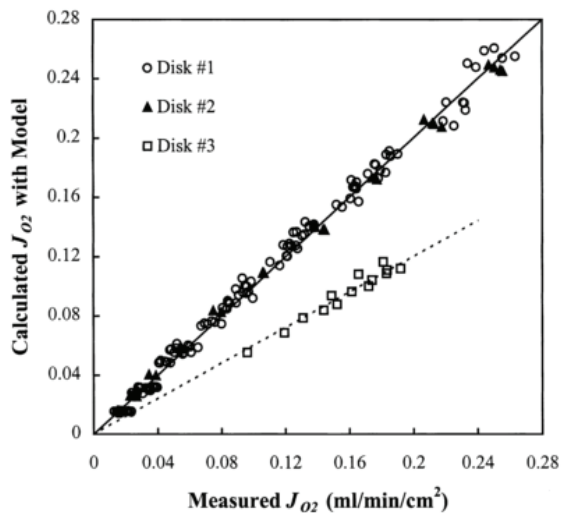


Figure 73 Comparison of oxygen flux measurements with model predictions from Xu & Thomson (fig. 4<sup>12</sup>)

Table 29 Pre-exponential coefficient and activation energy of  $k_r$ ,  $k_f$  and  $D_v$ <sup>12</sup> for the Xu-Thomson model.

$k_r^\circ$	$E_r$	$k_f^\circ$	$E_f$	$D_v^\circ$	$E_D$
$\text{mol cm}^{-2} \text{s}^{-1}$	$\text{kJ mol}^{-1}$	$\text{cm atm}^{-0.5} \text{s}^{-1}$	$\text{kJ mol}^{-1}$	$\text{cm}^2 \text{s}^{-1}$	$\text{kJ mol}^{-1}$
$(2.07 \pm 0.02) 10^4$	$241.3 \pm 0.1$	$(5.90 \pm 0.08) 10^6$	$226.9 \pm 0.2$	$(1.58 \pm 0.01) 10^{-2}$	$73.6 \pm 0.2$

### II.2.1. Simulation of oxygen fluxes on LSCF membrane using microkinetic parameters

The microkinetic parameters obtained for LSCF (Table 27 and Table 28) are used in flux model presented in chapter 4. Simulated fluxes have been calculated in a wide range of conditions of temperature (from 923 K to 1173 K),  $P''_{O_2}$  (from 1 kPa to 6 kPa) and  $P'_{O_2}$  (from 4 kPa to 80 kPa).

The variation of the predicted flux as a function of the kind of diffusion (linear, constant and the beginning then strong variation or the opposite) is very little (Figure 74 a). In order to simplify the understanding of the graphs we will only calculate the flux of oxygen from the model #3 which has been validated for BSCF in the previous chapter 4 (Figure 74 b and c). The trends describe by our model are in good agreement with the Xu/Thomson model flux. We can observe a significant deviation with the Xu/Thomson model at high  $P'_{O_2}$  and low temperature. Xu/Thomson plotted their measured flux against the calculated flux from their model, they obtained an excellent parity plot for Disk #1 (3.99 mm) under air and from 750°C to 950°C, Disk #2 (1.65mm) in the same conditions. On the other hand, the model underestimated the oxygen flux under  $P_{O_2}=100$  kPa for the Disk #3 (1.68 mm). Our modelling results are in good agreement with the Xu/Thomson model results. This validates our kinetic parameters and our flux equation. About the high  $P_{O_2}$  (=100kPa), our model is in agreement with the Xu/Thomson model and not with the experimental data, we cannot conclude on the validity of the model in these conditions.

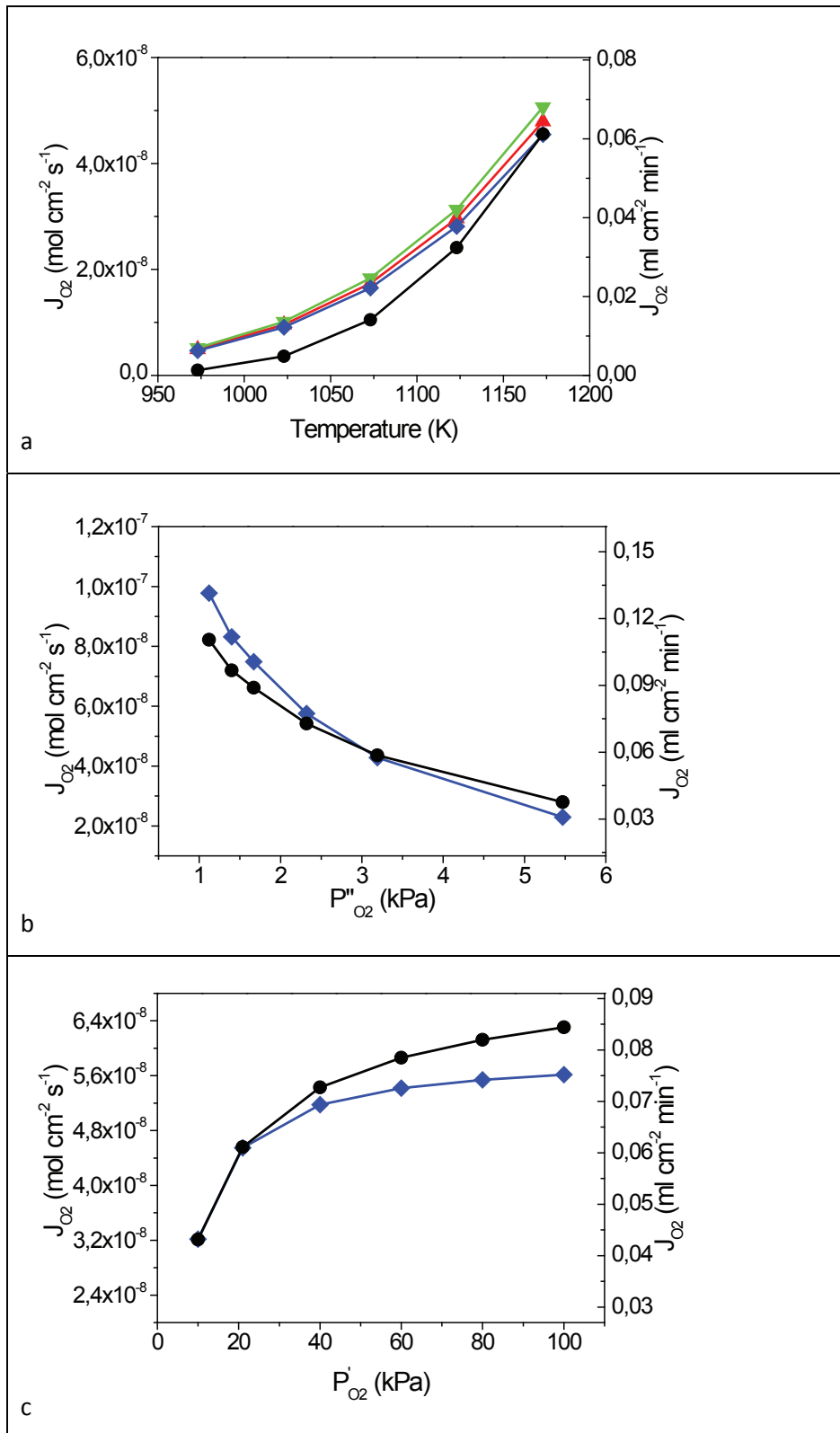


Figure 74 Comparison between Xu/Thompson model results (●) and our model data with model #1 (▲) #2 (▼) and #3 (◆): a) as a function of the temperature with  $P'_{O_2}=21$  kPa and  $P''_{O_2}= 1$  kPa, b) as a function of  $P''_{O_2}$  with  $T=1173$ K and  $P'_{O_2}=21$ kPa c) as a function of  $P'_{O_2}$  with  $P''_{O_2}= 3$  kPa and  $T= 1173$  K

## II.2.2. Simulation of the oxygen flux as a function of the thickness

Betz et al.<sup>14</sup> studied the impact of the thickness of the dense membrane as a function of the thickness. They used a dense LSCF membrane of 1mm thick and a supported dense membrane of 20 $\mu$ m thick. They observed that at low temperature, the flux of oxygen in the supported membrane is lower than the one for the thicker. We estimated oxygen fluxes in the same conditions (Table 31) and plotted the results on the same figure than Betz et al. results (Figure 75). Thus, we can confirm that in the case of LSCF the porous support limited the adsorption of oxygen on the surface. Then the oxygen flux increases rapidly. To model this experiments, we studied a membrane of 1mm thick with  $P'_{O_2}=21$  kPa and  $P''_{O_2}=2$  kPa and a membrane of 20  $\mu$ m thick  $P'_{O_2}= 21$ kPa and  $P''_{O_2}= 10$  kPa. About the fully dense membrane, the model flux predicted well the experimental flux. But, for the supported membrane, the oxygen flux is strongly overestimated at low temperature. In our model, the limitation due to the transport of oxygen in the porous support is not taken in account.

Table 30 Input conditions for modelling of Figure 75

$P'_{O_2}$ (kPa)	$P''_{O_2}$ (kPa)	Temperature (K)	Thickness (mm)	N
21	1	1023 to 1173	1	10
21	2	1023 to 1173	0.12	10

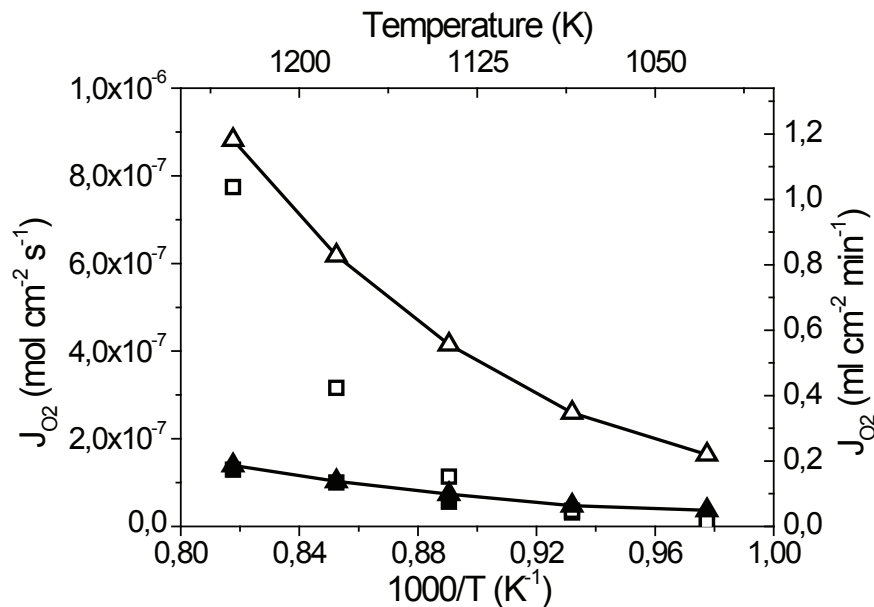


Figure 75 Oxygen model flux ( $L=1\text{mm}$ :  $\blacktriangle$  and  $L=20\mu\text{m}$ :  $\triangle$ ) versus experimental data from Betz et al.<sup>14</sup> ( $1\text{mm}$ :  $\blacksquare$  and  $20\mu\text{m}$ :  $\square$ )

Looking at the Langmuir adsorption constant at 1073K and  $P_{O_2}=21$  kPa, the adsorption is easiest in the case of LSCF than BSCF, while the desorption step is hardest (Table 31). This can be explained by the high capabilities of BSCF to be reduced. On the other side, the desorption step is more limiting in the case of BSCF than LSCF. This is in good agreement with the literature. About the time constant for

the diffusion, it is higher in the case of LSCF. When corrected by the crystallite size, the diffusion is about 40 times higher in the case of BSCF. BSCF is known for its high conduction capabilities. Indeed, the oxygen conductivities for LSCF calculated at 1073K, at 1 kPa and 21 kPa are 0.003 and 0.005 S cm<sup>-1</sup> respectively when for BSCF the oxygen conductivities are respectively of 1.11 and 0.14 S cm<sup>-1</sup>. These observations explained the lower flux in LSCF, and whereas many studies have been done on the optimization of LSCF design, no modifications lead to a LSCF membrane as successful as BSCF.

Table 31 Comparison between LSCF and BSCF flux characteristics at 1073K

P <sub>O2</sub> kPa	K 10 <sup>-2</sup> Pa <sup>-1</sup>		D*/r <sup>2</sup> (s-1)		D* 10 <sup>-7</sup> cm <sup>2</sup> s <sup>-1</sup>	
	LSCF	BSCF	LSCF	BSCF	LSCF	BSCF
21	3.0	0.1	36	4.6	0.09	5.5
1	0.9	1.0	54	34	0.1	4.2

### II.3. Conclusions on LSCF material and membrane

The coupling of the two analysis techniques (SSITKA/TGA) allowed the estimation of the parameters. Moreover, in the case of LSCF the variation of the vacancies concentration is very low between 1kPa and 21 kPa. This low variation leads to a non significant variation of the kinetic parameters in both conditions.

The tendencies and the values are in good agreement with Xu/Thomson results. The microkinetic approach of the estimation of the parameters works also for LSCF. But, it should be noticed that this flux is compared to the modelled flux from Xu/Thomson and not to their experimental results. However, in the case of LSCF, the use of the same parameters on each side of the membrane could be sufficient. The same values would have been obtained.

The following hypothesis can be made. For materials exhibiting a high reducibility capability and high initial oxygen vacancies content, our model should be used. While, for materials with a low reducibility level, a model such as Xu-Thomson can be used.

### III.BLF: A good alternative to BSCF

#### III.1. Characterization of the sample

##### III.1.1. Oxygen vacancies characterization and Langmuir adsorption constant determination

BLF has been described by few authors as it presents a high stability under experiment and do not contain cobalt a major issue in industry. The evolution of oxygen non-stoichiometry ( $\delta$ ) and thus oxygen vacancies ( $\theta_v$ ) of  $\text{Ba}_{0.95}\text{La}_{0.05}\text{FeO}_{3-\delta}$  with the temperature at fixed oxygen partial pressure can be followed by thermogravimetric analysis (TGA). The initial oxygen non-stoichiometry ( $\delta$ ) of  $\text{Ba}_{0.95}\text{La}_{0.05}\text{FeO}_{3-\delta}$  at room temperature has been determined by iodometric titration<sup>10,11</sup>(Table 32). Series of 10 repetitive measurements gives a value of non-stoichiometry ( $\delta$ ) equal to  $0.32 \pm 0.02$  corresponding to a fraction of oxygen vacancies ( $\theta_v$ ) of 0.107 (Table 32).

Table 32 Iodometric titration on BLF

BLF	Masse g	Ve <sub>q</sub> ml	[Na <sub>2</sub> S <sub>2</sub> O <sub>3</sub> ] mol L <sup>-1</sup>	$\delta$	M <sub>BLFi</sub> g mol <sup>-1</sup>	$\Delta\delta$
1	0.109	35.1	0.0172	0.32	236.12	0.02
2	0.103	33.6	0.0172	0.31	236.20	0.02
3	0.100	32.8	0.0169	0.32	236.17	0.02
4	0.101	32.9	0.0169	0.32	236.14	0.02
5	0.105	32.5	0.0169	0.33	236.10	0.02
6	0.104	33.2	0.0169	0.32	236.15	0.02
7	0.108	33.5	0.0169	0.32	236.16	0.02
8	0.102	33.0	0.0169	0.32	236.15	0.02
9	0.101	32.7	0.0169	0.31	236.19	0.02
10	0.106	33.3	0.0169	0.32	236.17	0.02
$\delta_{\text{BLF}} = 0.32 \pm 0.02$						

The evolution of the fraction of vacancies as a function of temperature has been measured from the weight loss of the TGA curve ( $\theta_v = \delta/3$ ) under the same conditions as before, and for the same reasons (Figure 77). The fraction of vacancies remains ( $\theta_v$ ) constant until 450 K, then increases with a linear trend with temperature in the case of  $P_{\text{O}_2} = 21 \text{ kPa}$ <sup>15-17</sup>. For lower oxygen pressure ( $P_{\text{O}_2} = 1 \text{ kPa}$ ), we can observe a marked oxygen loss at 550-850K accounting for a larger reduction of the solid then reaches a minimum. Hence, we can observe an almost constant difference of oxygen vacancy

concentration between the oxygen rich and lean conditions over the temperature range of interest.

In BLF, only Iron is reducible. The electro neutrality law can be written as follows:

$$n_0(Ba) \times 0.95 + n_0(La) \times 0.05 + n_0(Fe) = (3 - \delta) \times n_0(O)$$

$n_0(x)$  is the oxidative state of the atom, for  $n_0(Ba)=2$ ,  $n_0(La)=3$ ,  $n_0(Fe)=2;3;4=X$  and  $n_0(O)=-2$ . The average oxidative state of Iron is defined then by the following equation:

$$X = 3.95 - 2\delta$$

At room temperature, the quantity of vacancies,  $\delta_i$  is equal to 0.32 so the average oxidative state of Fe is about 3.3 at room temperature. At 900°C, the quantity of vacancies tends to a maximum for  $P_{O_2} = 1$  kPa.  $\delta_{max} = 0.52$ . The final oxidative state of iron is of 2.9. It should be noticed that these values are average values and the oxidative state of Iron is a mixture of  $Fe^{2+}$ ,  $Fe^{3+}$  and  $Fe^{4+}$ . The average oxidative state has also been determined using EXAFS technique (Figure 76). The deviation can be due to the literature standard<sup>18</sup> used for the calibration ( $SrFeO_{2.86}$  for the  $Fe^{4+}$ ). In order to validate on the other technique, a new standard should be tested and a new technique used, such as Mossbauer.

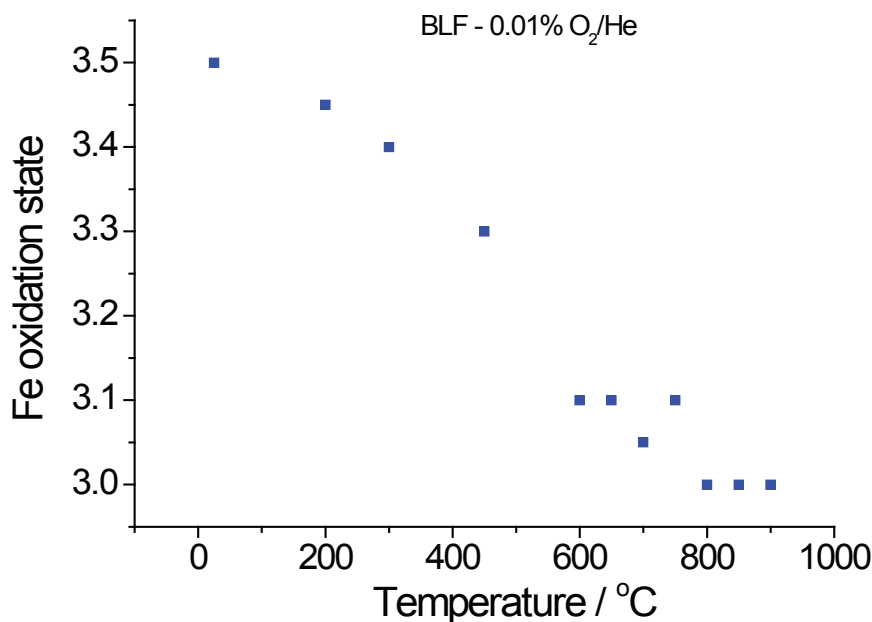


Figure 76 Average oxidative state from EXAFS analysis under  $P_{O_2} = 0.01$  kPa in Helium.

In addition, TGA measurements were carried out by keeping the sample for a longer time at a constant temperature before ramping to a next temperature level. A dwell type temperature program gave similar non-stoichiometry values  $\delta$  as those obtained by a continuous temperature ramp (Figure 77). We can therefore conclude that the oxygen adsorption/desorption and transport is faster rapid and in quasi-equilibrium compared to the change in temperature.

We have observed that after TGA measurements, cell parameters remain constant within measurement errors. In addition, we do not observe the formation of a new phase. Hence, the modification of the  $\text{Ba}_{0.95}\text{La}_{0.95}\text{FeO}_{3.6}$  material during TGA experiments, if occurring, is at least reversible. Then the Langmuir equilibrium constant are calculated and the results are recorded in Table 33.

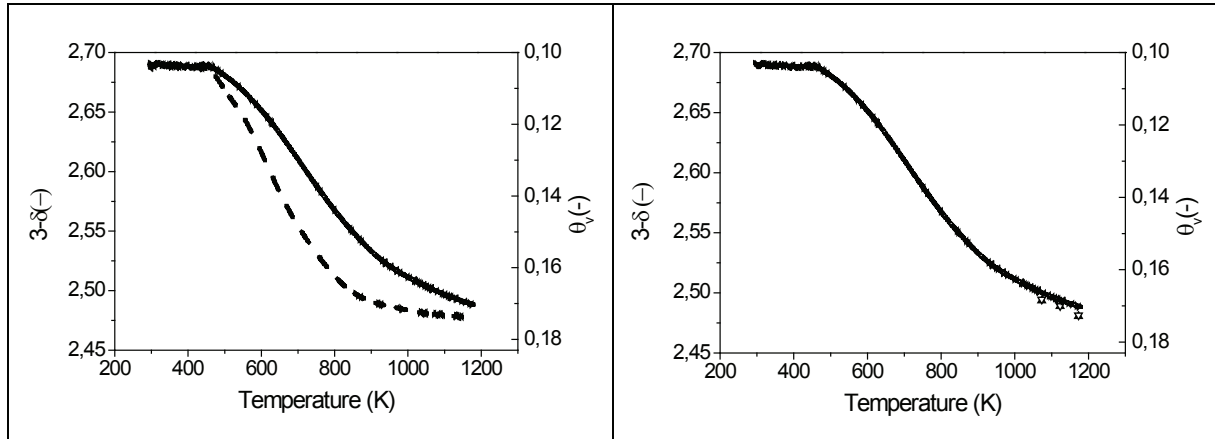


Figure 77 TGA on BLF powder under  $\text{O}_2/\text{N}_2$  flow, with  $P_{\text{O}_2}=21$  kPa (-) and  $P_{\text{O}_2}=1$  kPa (- -), dwell: at the beginning ( $\blacktriangle$ ) after 30 minutes ( $\Delta$ )

Table 33 Langmuir adsorption equilibrium constant

$P_{\text{O}_2}$ (kPa)	$K^{\circ}(\text{Pa}^{-1})$	$\Delta H$ ( $\text{kJ mol}^{-1}$ )
1	$4.95 \cdot 10^{-3}$	$-26.2 \pm 0.1$
21	$7.24 \cdot 10^{-1}$	$-9.8 \pm 0.1$

### Determination of the kinetic parameter with SSITKA experiments:

The oxygen exchange has been done for a wide range of temperature and two partial pressures of oxygen. Figure 78 shows an example of oxygen exchange experiments for two partial pressures of oxygen at three temperatures. The exchange takes about 6 times longer at  $P_{\text{O}_2}=1$  kPa than at  $P_{\text{O}_2}=21$  kPa. At low temperatures the temperature has a small effect but the effect levels out quickly above 900 K. Integration of the  $0.5 \cdot P^{32}\text{O}_2 + P^{16}\text{O}^{18}\text{O}$  signals gives the amount of exchanged oxygen. At  $T=973\text{K}$  and  $P_{\text{O}_2}=21$  kPa, 95% of all oxygen atoms in BLF are exchanged. At the same temperature and  $P_{\text{O}_2}=1$  kPa this amounts to only 50%, due to the lower exchange rate, the exchange curves were not recorded until the end of the exchange.

The oxygen exchange curves ( $P^{16}\text{O}_2$  &  $P^{16}\text{O}^{18}\text{O}$ ) have been modelled for each level of oxygen partial pressure separately, but including all temperatures simultaneously. Initial regression analysis showed that quasi-equilibrium of the exchange rates is established at the time scale of the experiment. Thus

only the forward rate parameters ( $k_f$ ) have been estimated during the regression analysis and the reverse rates parameters ( $k_r$ ) are calculated from the equilibrium rate constants ( $K=k_f/k_r$ ) determined from the TGA experiments (Table 33). In addition to the oxygen exchange parameters, the characteristic time constant ( $D/r^2$ ) for oxygen transport is estimated from the isotopic exchange response curves. Figure 78 compares the model predicted response curves with the experimental ones. A good fit is obtained at both oxygen partial pressures and at all temperatures. The surface parameter and diffusion estimates are reported in Table 34 and Table 35, respectively.

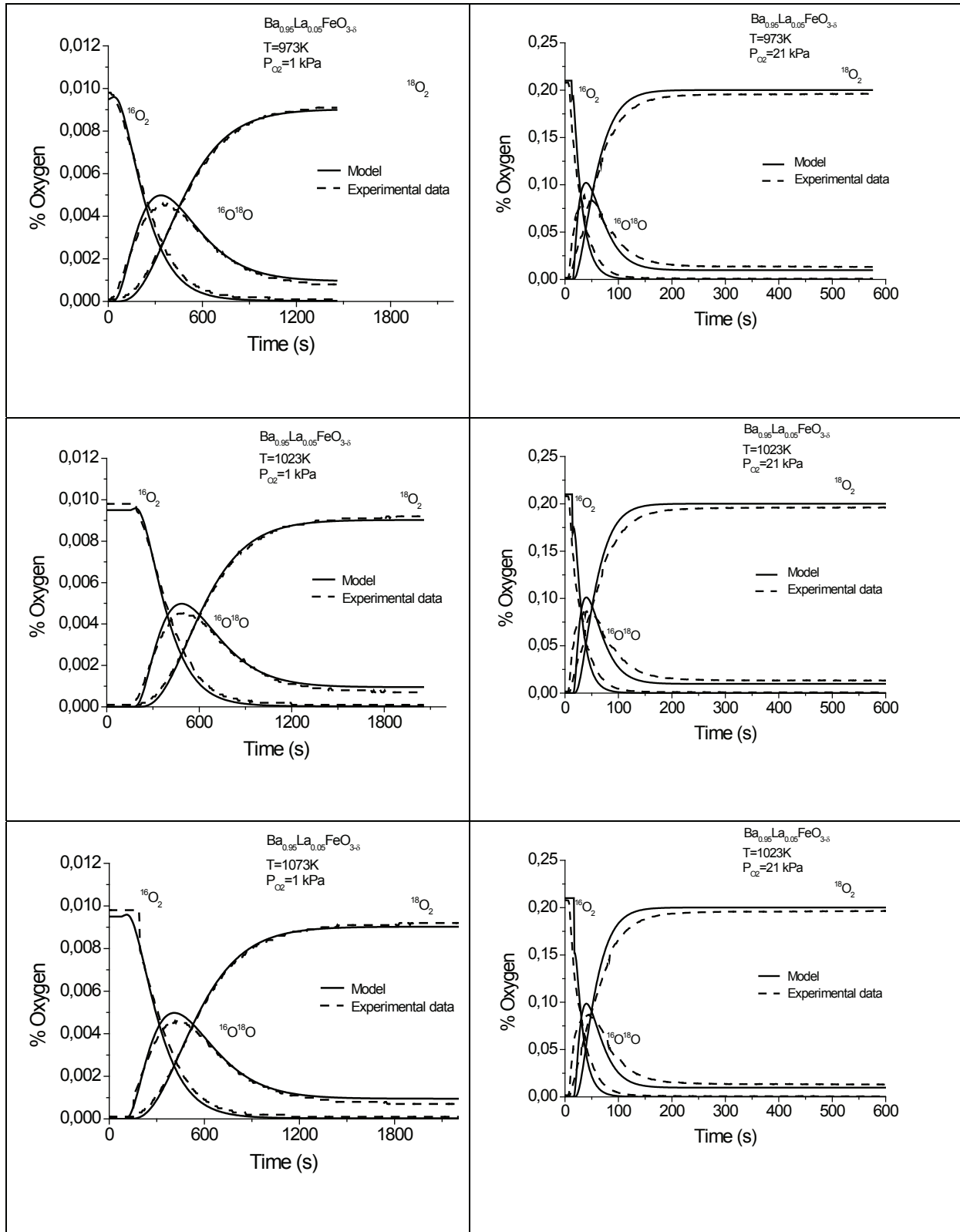


Figure 78 SSITKA experiments (plain) and model curve (dash),  $^{16}\text{O}_2(\text{g})$ ,  $^{16}\text{O}^{18}\text{O}(\text{g})$ ,  $^{18}\text{O}_2(\text{g})$  at different partial pressure of oxygen and different temperatures.

Table 34 Kinetic parameters estimated from regression analysis of the isotopic oxygen exchange response curves for BLF. The confidence intervals estimated at 95%. For comparison, the estimated parameters obtained on LSCF membrane semi-permeability data from Xu

	Shape	P <sub>O<sub>2</sub></sub> kPa	Surface	reverse	kinetic	Surface	forward	kinetic	ref
			parameter			parameter			
			kr° s <sup>-1</sup>	Er kJ mol <sup>-1</sup>		kf° Pa <sup>-1</sup> s <sup>-1</sup>	Ef kJ mol <sup>-1</sup>		
BLF	Powder	21	(2.5±0.1).10 <sup>11</sup>	225.4±30		(6.7±0.2) 10 <sup>7</sup>	215.6±30		This work
BLF	Powder	1	(2.9±0.04). 10 <sup>11</sup>	238.6±25		(1.7±0.02) 10 <sup>7</sup>	212.4±25		This work
		kPa	mol cm <sup>-2</sup> s <sup>-1</sup>	kJ mol <sup>-1</sup>		cm atm <sup>-0.5</sup> s <sup>-1</sup>	kJ mol <sup>-1</sup>		
BLF	Powder	21	(8.9±0.4).10 <sup>5</sup>	225.4±30		(1.2±0.05) 10 <sup>8</sup>	215.6±30		This work
BLF	Powder	1	(1.0±0.02). 10 <sup>6</sup>	238.6±25		(8.4±0.1) 10 <sup>8</sup>	212.4±25		This work
LSCF	Membrane	NA	(2.07±0.02) 10 <sup>4</sup>	241.3±0.1		(5.90±0.08) 10 <sup>6</sup>	226.9±0.2		<sup>12</sup>

#### About the diffusion:

Oxygen exchange experiments give access to the characteristic diffusion time, which is the ratio of the diffusion coefficient to the square of the characteristic length ( $D^*/r^2$ ). The crystallite diameter can be estimated directly from SEM image analysis (Figure 79). The size distribution of the crystallites was measured by counting 250 crystallites (Figure 79). The distribution is centred at 3.5  $\mu\text{m}$  using a non-linear Gauss curve fit (Figure 79). Independently, the mean diameter of crystallite with an accessible surface was determined by N<sub>2</sub> adsorption measurements at 77 K. The BET surface area is equal to 373±1 m<sup>2</sup> kg<sup>-1</sup> (with  $\rho=6.21$  g cm<sup>-3</sup>), which leads to a crystallite diameter ( $d_{\text{crys}}$ ) of 2.6  $\mu\text{m}$  lower than SEM image analysis. On the SEM analysis, we can observe many tiny crystallites, a small overestimation can lead to an overestimation of the crystallite size. So we decide to use the crystallite diameter obtained with BET experiments.

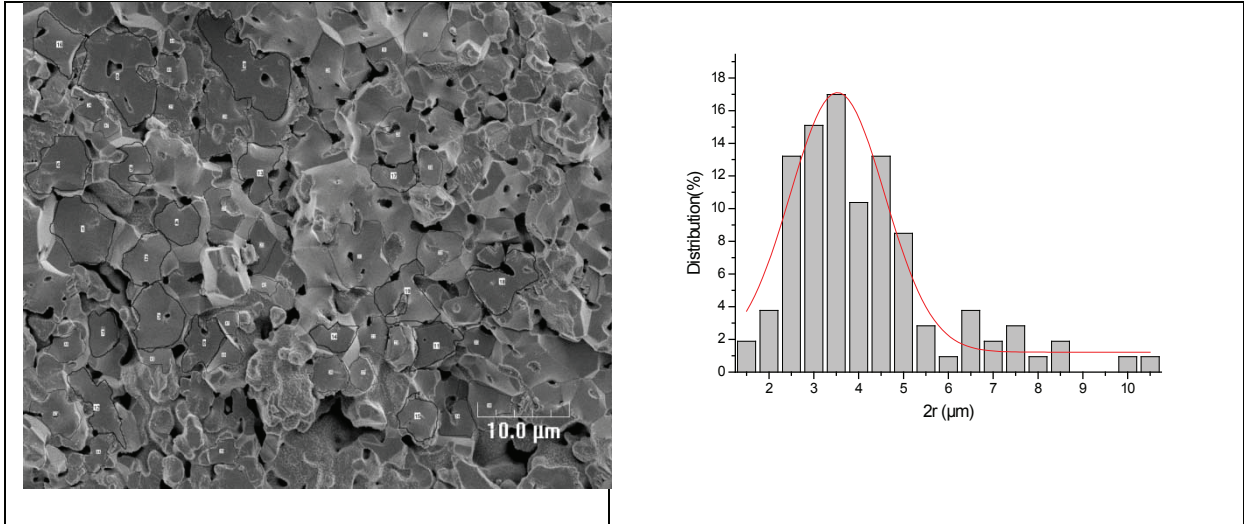


Figure 79 SEM pictures (x2000) and particle size distribution (obtained with ImagJ software)

Table 35 Characteristic time constants for diffusion estimates from regression analysis of the oxygen exchange response curve between 700-900°C, and self diffusion parameter calculated using the crystallite radius (r) equal to 1.3μm. The confidence intervals estimated at 95% level.

Pressure	$D^{*o}/r^2$	$D^{*o}$	$E_d$
kPa	$s^{-1}$	$cm^2 s^{-1}$	$kJ mol^{-1}$
21	$(2.1 \pm 0.2)10^3$	$(3.5 \pm 0.2)10^{-5}$	26±12
1	$(5.0 \pm 1.3)10^4$	$(8.5 \pm 2.1)10^{-4}$	42±15

## III.2. Estimation of the oxygen flux through the dense membrane:

### III.2.1. Impact of the experimental conditions:

Only few results were obtained on the dense membrane, so no estimation of the kinetic parameters has been achieved on this membrane, our model cannot be compared to the Xu/Thomson model. The oxygen flux has been measured as a function of the temperature, from 1073K to 1173K and as a function of the partial pressure of oxygen on the air side. Although, the oxygen flux through BLF remains lower than with BSCF membrane, BLF is known to be a very promising replacement for BSCF. The microkinetic parameters obtained for BLF (Table 34 and Table 35) are in flux models presented in chapter 5. Simulated fluxes have been calculated in a wide range of conditions of temperature (from 923 K to 1173 K),  $P''_{O_2}$  (from 1 kPa to 6 kPa) and  $P'_{O_2}$  (from 4 kPa to 80 kPa).

The flux has been calculated from model #1 and model #3 although model #3 has been validated on BSCF and LSCF (Figure 80). Models describe well the trends from 1073K to 1173K and from  $P'_{O_2}= 21$  kPa to 100kPa. It should be noticed that model #1 slightly overestimated the oxygen flux and model #3 slightly underestimate the oxygen flux. For the oxygen flux as a function of the partial pressure in the sweep side, no experimental data have been obtained, but looking at the results on LSCF and BSCF, the oxygen flux should be between model #1 and model #3 from 1 kPa to 2 kPa and higher than these values for  $P''_{O_2}$  higher than 2 kPa.

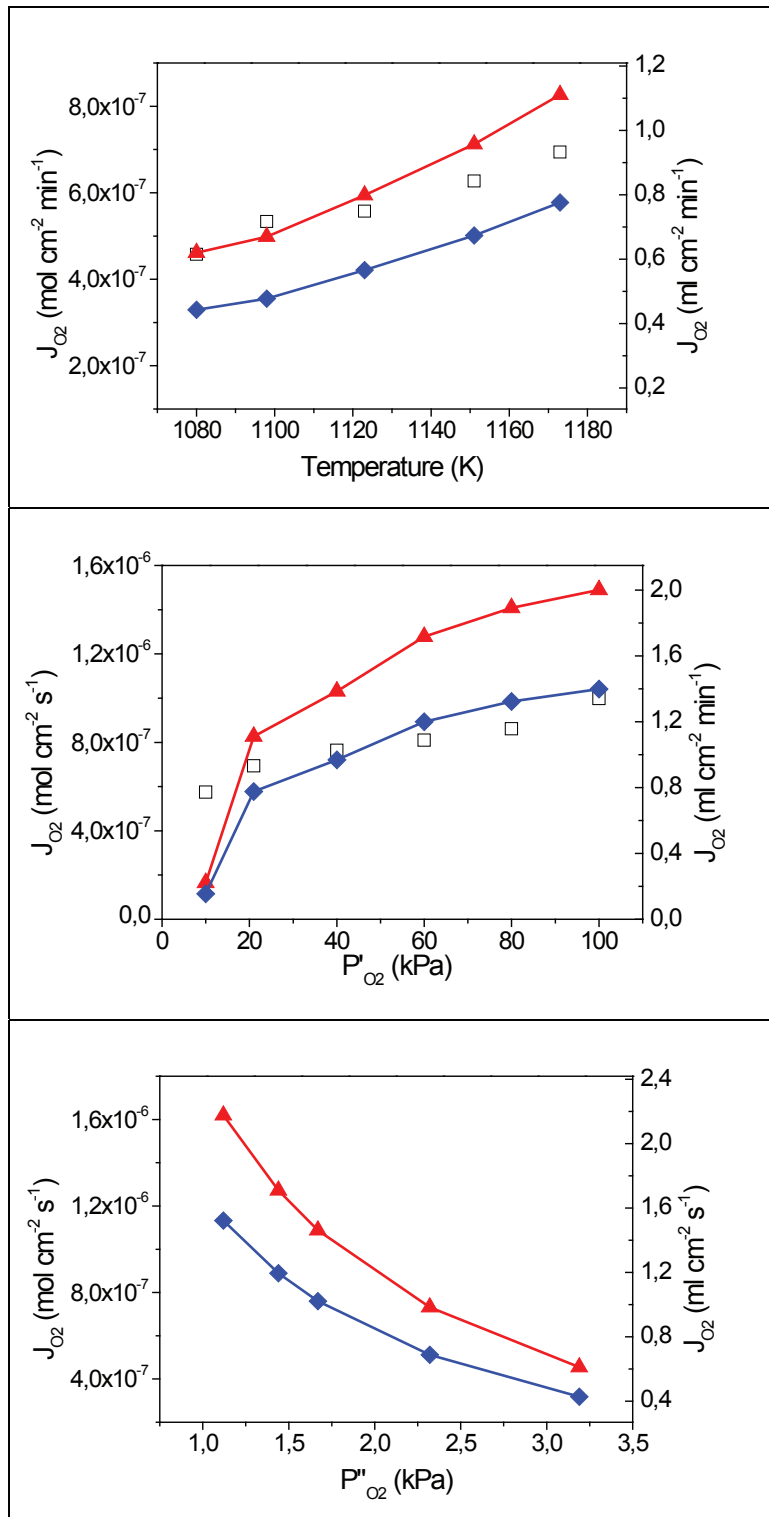


Figure 80 Comparison between the experimental flux ( $\square$ ) and different flux models (#1,  $\blacktriangle$ ), (#3,  $\blacklozenge$ ) as a function of the temperature at  $P'_{O_2}=21$  kPa and  $P''_{O_2}=1$  kPa (top), of the partial pressure of oxygen on the feed side at 1173 K and  $P''_{O_2} = 1$  kPa (medium) and of the partial pressure of oxygen on the sweep side with no experimental data at 1173 K and  $P'_{O_2}=80$  kPa (bottom).

### III.2.2. Impact of the thickness

The impact of the thickness of the membrane on the oxygen flux has been studied as a function the temperature and the partial pressure of oxygen. Our modelled values are compared to the experimental data obtained by Watenabe et al. <sup>9</sup>.

The first set of oxygen flux have been measured as a function of the temperature with  $P'_{O_2} = 21$  kPa and  $P''_{O_2} = 1$  kPa. For totally dense membranes (Figure 81 a), it appears that the predicted fluxes are in good agreements with the experimental data. However, the predicted fluxes for the supported membrane strongly overestimate the experimental data (Figure 81 b). The strong variation at higher temperature can be explained by a limitation of the diffusion in the porous layer for the supported membrane.

An optimized thickness as been determined which is able to describe properly the oxygen fluxes through the dense membrane. Using this thickness value, the oxygen flux has been calculated as a function of the partial pressure of oxygen in the air side (Figure 82). It appears that the oxygen flux is in agreement with the boundary limits ( $P'_{O_2} = 21$  kPa and 100 kPa) in contrast it does not describe the middle value, it highly overestimated it. As only three experimental values have been measured no assumption can be made on the validity of our model in these conditions.

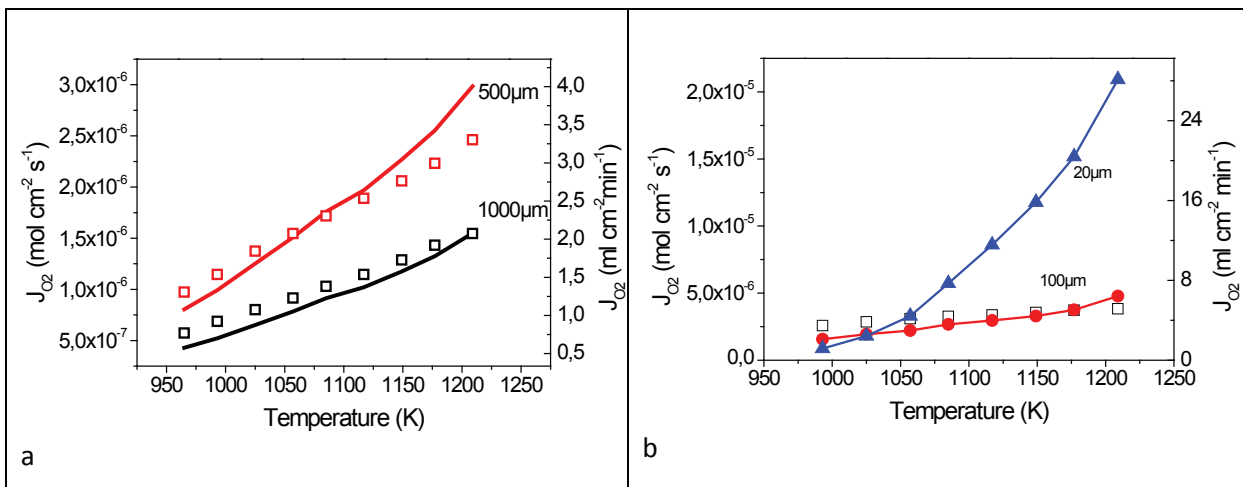


Figure 81 Oxygen flux through the dense membrane compared to experimental data from Watenabe et al. <sup>9</sup>; oxygen flux as a function of the temperature with  $P'_{O_2} = 21$  kPa and  $P''_{O_2} = 1$  kPa a) for two thickness: 1000  $\mu\text{m}$  (measured:  $\square$  modelled:  $\text{—}$ ) and 500  $\mu\text{m}$  (measured:  $\square$  modelled:  $\text{—}$ ) b) for a supported membrane (experimental:  $\square$  modelled 100  $\mu\text{m}$   $\bullet$  and 20  $\mu\text{m}$   $\blacktriangle$ ).

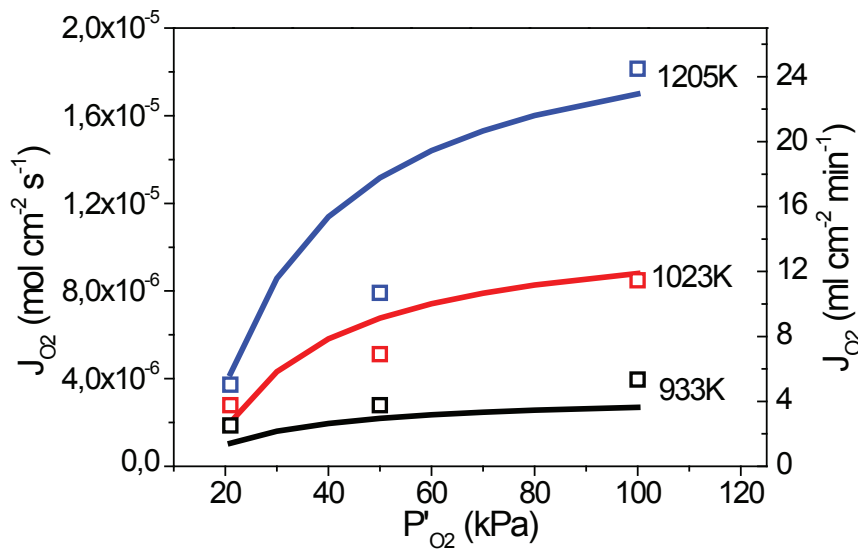


Figure 82 Dependence of the oxygen permeability on the partial pressure of the feed gas for supported dense BLF membrane for three temperatures 933K; 1023K and 1205K: Comparison between the experimental data obtained by Watanabe et al.<sup>9</sup> (□) and the model values (—)

The impact of the thickness of the membrane on the oxygen flux as a function of the partial pressure of oxygen in the air side has been compared for BSCF and BLF (Figure 83). The impact of the thickness variation at  $P'_{O_2} = 21$  kPa is stronger for BSCF. However, the increase of this partial pressure has a stronger impact in the case of BLF. BLF can replace BSCF material in order to increase the oxygen flux in this configuration. The conditions used for the modelling are reported in chapter 4-p138.

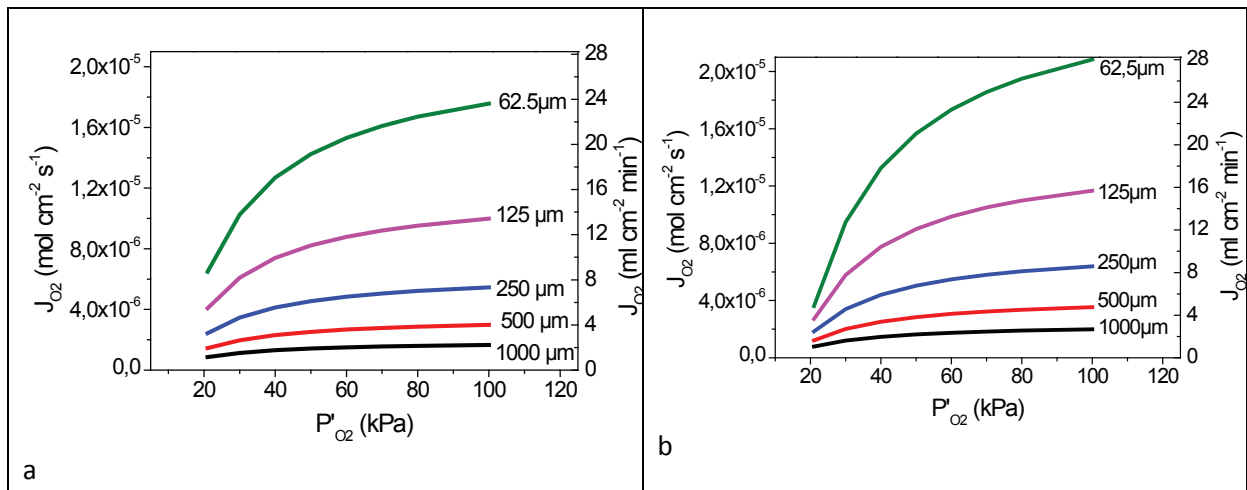


Figure 83 Impact of  $P'_{O_2}$  on the flux for different thickness: (a) BSCF (b) BLF at  $T=1173K$

### III.3. Conclusion on BLF material

The use of both TGA and SSITKA techniques allows the estimation of the parameters in good agreement with the experimental data. Looking at comparison between BLF and BSCF (Table 36), desorption step than the adsorption step remains easier in the case of BSCF although it is very close.

About the diffusion coefficient, it is much higher for BLF while the oxygen vacancies quantity is lower. BLF oxygen flux should be more limited by the surface in the sweep side than BSCF.

Moreover, in standard configuration, i.e. fully dense membrane of about 1.5 to 2mm, the oxygen flux in BSCF membrane remains higher. In this case, BSCF membrane is highly recommended for its high oxygen flux. On the other hand, the BLF membrane gives better results in thin layer configuration under strong oxygen gradient.

Table 36 Comparison between BLF and BSCF flux characteristics at 1073K

P <sub>O<sub>2</sub></sub> kPa	K 10 <sup>-2</sup> Pa <sup>-1</sup>		D*/r <sup>2</sup> (s-1)		D* 10 <sup>-7</sup> cm <sup>2</sup> s <sup>-1</sup>	
	BLF	BSCF	BLF	BSCF	BLF	BSCF
21	0.2	0.1	114	4.6	19.0	5.5
1	5.5	1.0	451	34	76.7	4.2

## IV. Conclusions

This methodology has been validated on LSCF. However, the use of a easier model considering that the kinetic parameters are equal on both side of the membrane would be sufficient. The flux model of Xu/Thomson is satisfactory.

The results obtained on BLF gives good information on this material, if the oxygen flux is sufficient in standard conditions (i.e. temperature from 700 to 900°C, P'<sub>O<sub>2</sub></sub>= 21 kPa and P''<sub>O<sub>2</sub></sub>= 1 kPa and the membrane thickness of 2 mm). However, to increase the flux the use of a thin membrane with a higher P'<sub>O<sub>2</sub></sub> is stronger with BLF than BSCF. This material can be a good alternative to BSCF in these conditions. These conclusions are based on modelling results and do not take in account the stability of the membrane over reaction.

# Bibliography

---

1. Y. Teraoka, Z. Hua-Min, S. Furukawa and N. Yamazoe, *Chem. Lett.*, 1985, 1743–1746.
2. J. E. Elshof, H. J. M. Bouwmeester and H. Verweij, *Solid State Ionics*, 1995, **81**, 97–109.
3. H. Iwahara, T. Esaka and T. Mangahara, *J. Appl. Electrochem.*, 1988, **18**, 173–177.
4. Y. Teraoka, H. Shimokawa, C. Kang, H. Kusaba and K. Sasaki, *Solid State Ionics*, 2006, **177**, 2245–2248.
5. T. Ishihara, T. Yamada, H. Arikawa, H. Nishiguchi and Y. Takita, *Solid State Ionics*, 2000, **135**, 631–636.
6. X. Zhu, H. Wang and W. Yang, *Solid State Ionics*, 2006, **177**, 2917–2921.
7. H. Wang, C. Tablet, A. Feldhoff and J. Caro, *Adv. Mater.*, 2005, **17**, 1785–1788.
8. K. Watanabe, S. Ninomiya, M. Yuasa, T. Kida, N. Yamazoe, H. Haneda and K. Shimanoe, *J. Am. Ceram. Soc.*, 2010, **93**, 2012–2017.
9. K. Watanabe, M. Yuasa, T. Kida, Y. Teraoka, N. Yamazoe and K. Shimanoe, *Adv. Mater.*, 2010, **22**, 2367–70.
10. A. Manthiram, J. S. Swinnea, Z. T. Sui, H. Steinfink and J. B. Goodenough, *Am. Chem. Soc.*, 1987, **109**, 6667–6669.
11. L. Rørmark, K. Wiik and T. Grande, *Society*, 2002.
12. S. J. Xu and W. J. Thomson, *Chem. Eng. Sci.*, 1999, **54**, 3839–3850.
13. H. Ullmann, N. Trofimenko, F. Tietz, D. Stöver and A. Ahmad-Khanlou, *Solid State Ionics*, 2000, **138**, 79–90.
14. M. Betz, F. Schulze-Küppers, S. Baumann, W. A. Meulenber and D. Stöver, *Adv. Sci. Technol.*, 2010, **72**, 93–98.
15. E. Bucher, A. Egger, P. Ried, W. Sitte and P. Holtappels, *Solid State Ionics*, 2008, **179**, 1032–1035.
16. R. Kriegel, R. Kircheisen and J. Töpfer, *Solid State Ionics*, 2010, **181**, 64–70.
17. S. Mcintosh, J. F. Vente, W. G. Haije, D. H. A. Blank and H. J. M. Bouwmeester, *Solid State Ionics*, 2006, **177**, 1737 – 1742.
18. D. N. Mueller, R. A. De Souza, J. Brendt, D. Samuelis and M. Martin, *J. Mater. Chem.*, 2009, **19**, 1960.





# CHAPTER 6-Oxidative coupling of methane in membrane reactor

---

## I. Introduction

Despite decades of efforts of development on the oxidative coupling methane, selectivities in ethylene and ethane are still much too low for allowing an industrial perspective. Among the reactor technologies, perovskite based ceramic membranes are considered as possible reactor solutions for this reaction. Efforts concentrate on  $\text{Ba}_x\text{Sr}_{1-x}\text{Co}_y\text{Fe}_{1-y}\text{O}_{3-\delta}$  and  $\text{La}_x\text{Sr}_{1-x}\text{Co}_y\text{Fe}_{1-y}\text{O}_{3-\delta}$  due to its high oxygen permeation<sup>1</sup>. The main drawback is their low catalytic selectivity in  $\text{C}_2$ . In order to drive the selectivity to desired products, different catalyst coatings have been studied for the ceramic dense membranes<sup>2</sup>. Different combinations have been considered (Figure 84).

The first studies have been carried out without catalyst coatings (Figure 84 A). Taheri et al.<sup>3</sup> studied the reactivity of  $\text{La}_{0.6}\text{Sr}_{0.4}\text{Co}_{0.8}\text{Fe}_{0.2}\text{O}_{3-\delta}$  for the oxidative coupling of methane. They compared the results obtained in a fixed bed reactor and in a bare membrane reactor. In the first design, they observed a  $\text{C}_2$  selectivity of 37.5% at 1123K in the fixed bed reactor against a 100%  $\text{C}_2$  selectivity for the dense membrane reactor. However, a direct comparison shall take into account the conversion levels. In the fixed bed reactor the maximum methane conversion was of 22% at 1153K whereas it was only 5% in the dense membrane reactor. We shall note that this result has not been confirmed nor reproduced by others.

Wang et al.<sup>2</sup> compared the impact of the addition of LaSr/CaO catalyst bed on the membrane reactor (Figure 84 B). They obtained an improvement of the  $\text{C}_2$  selectivity about +50% and a  $\text{CH}_4$  conversion of 20 times more. However, it has to be mentioned that the results in the dense membrane reactor with a bed of catalyst do not overstep the performances in a fixed bed reactor fill with LaSr/CaO catalyst. We can assume that the combination of a fixed bed in a membrane reactor may lead to a recombination of oxygen anions at the membrane surface and desorption in the gas phase before the anionic oxygen reacts with the  $\text{CH}_4$ . In this scenario, the opportunity to use anionic oxygen as source of selective oxygen is lost. The advantages remaining are still the distribution of  $\text{O}_2$  along the reactor with the absence of  $\text{N}_2$  in the gas phase.

An alternative approach for coatings consists in the modification of the membrane surface by a thin layer of catalyst on the membrane (Figure 84 C) which allows the conduction of ionic oxygen

until the surface of the catalyst, and so a contact between the activated oxygen, the catalyst and the methane. To the best of our knowledge, this solution has not been investigated in depth for the OCM reaction while the same approach has been studied in our group for the oxidative dehydrogenation of ethane<sup>4,5</sup>.

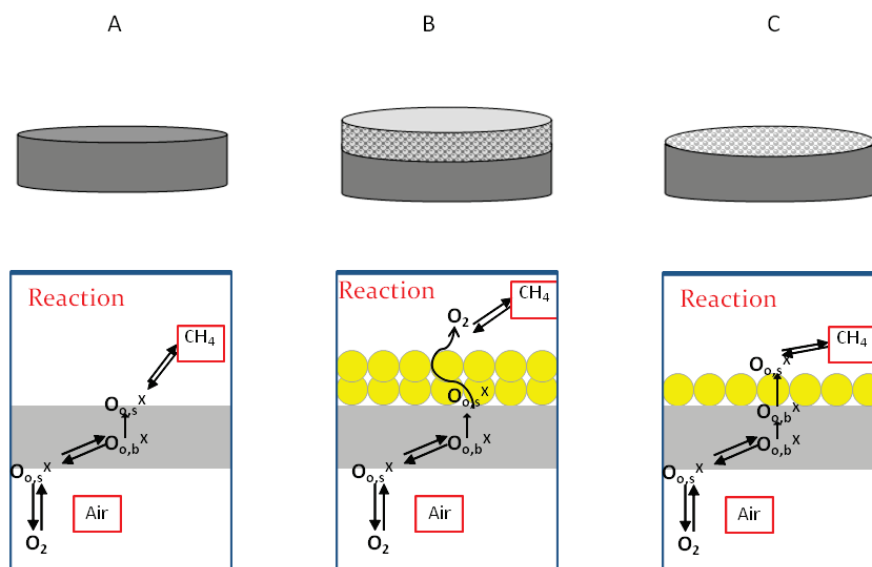


Figure 84 Membranes for the oxidative coupling of methane with or without coating

The objectives of this chapter are to describe the effects of a catalytic thin coating on the surface of the membrane for the OCM reaction. First we will evaluate the performance of the ceramic membrane BSCF without any modifications for the oxidative coupling of methane. Then a thin layer of catalyst is added on the dense membrane and its impact is studied. Two catalysts have been selected: Mn/NaWO<sub>4</sub> which is reported to be highly selective in fixed bed and LaSr/CaO which is known to be highly active.

## II. Description of the membrane reactor

The membrane has been tested in a reactor bench which can host a membrane disk of 25 mm (Figure 85). The size of hot zone which is considered as the reaction volume has been estimated. We assume that the reaction can occur at a minimum of 600°C in the gas phase. Thus the hot zone length has been taken equal to 5 cm which leads to a gas phase reaction volume of  $V=14.2 \text{ cm}^3$  while the exposed surface of the membrane is of  $S=3.8 \text{ cm}^2$ .

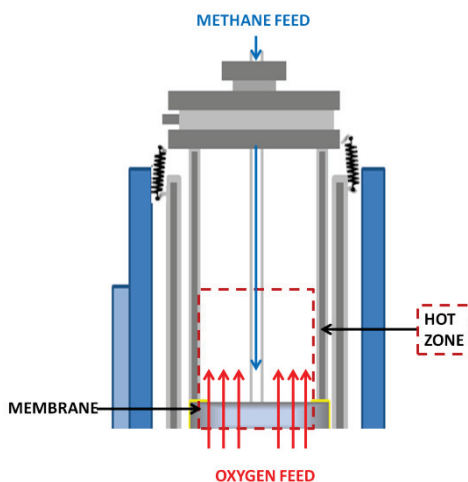


Figure 85 Reaction side configuration

The residence time ( $t_r$ ) is a key parameter in catalytic reaction. It has been calculated by the following equation:

$$t_r = \frac{V}{F} \tag{1}$$

With  $V$ , the volume of the gas phase in the hot zone, i. e.  $14.2 \text{ cm}^3$  and  $F$  the flow rate in the reaction side in  $\text{cm}^3 \text{ s}^{-1}$ .

The thickness of the coating is between  $50$  and  $100\mu\text{m}$  and thus does not change the volume reaction. The loading of catalyst is discussed in details in part III.2.1.1.

Various experimental conditions have been tested (Table 37). In order to study the impact of the partial pressure in the reaction side and the residence time in this part of the reactor, the flow rate in the reaction side has been modified from  $47.5$  to  $200 \text{ ml min}^{-1}$ . The range of temperature was taken from  $923$  to  $1173\text{K}$ . Then the partial pressure of oxygen in the air side has been study at  $21 \text{ kPa}$  and  $80 \text{ kPa}$  while the partial pressure of methane in the reaction side has been taken equal to  $4 \text{ kPa}$  and  $6 \text{ kPa}$ .

Table 37 Experimental conditions for bare BSCF membrane

$F_{\text{reaction side}}$	$P_{\text{CH}_4}$	Temperature	$P'_{\text{O}_2}$ range	$F_{\text{air side}}$
$\text{ml min}^{-1}$ (STP)	kPa	K	kPa	$\text{ml min}^{-1}$ (STP)
47.5-200	4-6	923-1173	21-80	200

## II.1. OCM results on bare BSCF membrane

### II.1.1. Impact of flow rate in the reaction side.

The impact of the total flow rate in the reaction side ( $\text{CH}_4/\text{He}$ ) has been studied at constant temperature 1173 K, constant conditions in the air side (flow rate in air of  $200 \text{ ml min}^{-1}$  and  $P'_{\text{O}_2} = 21 \text{ kPa}$ ) (Figure 86). The conversion of methane and the ratio  $\text{C}_2\text{H}_4/\text{C}_2\text{H}_6$  decreases while the flow rate in the reaction side increases. In the same time, the selectivity in  $\text{C}_2$  increases and the yield in  $\text{C}_2$  reaches a maximum of 8% for  $80 \text{ ml min}^{-1}$ . The partial pressure of methane does not impact the trends but the conversion of methane is lower in the case of a higher partial pressure of methane.

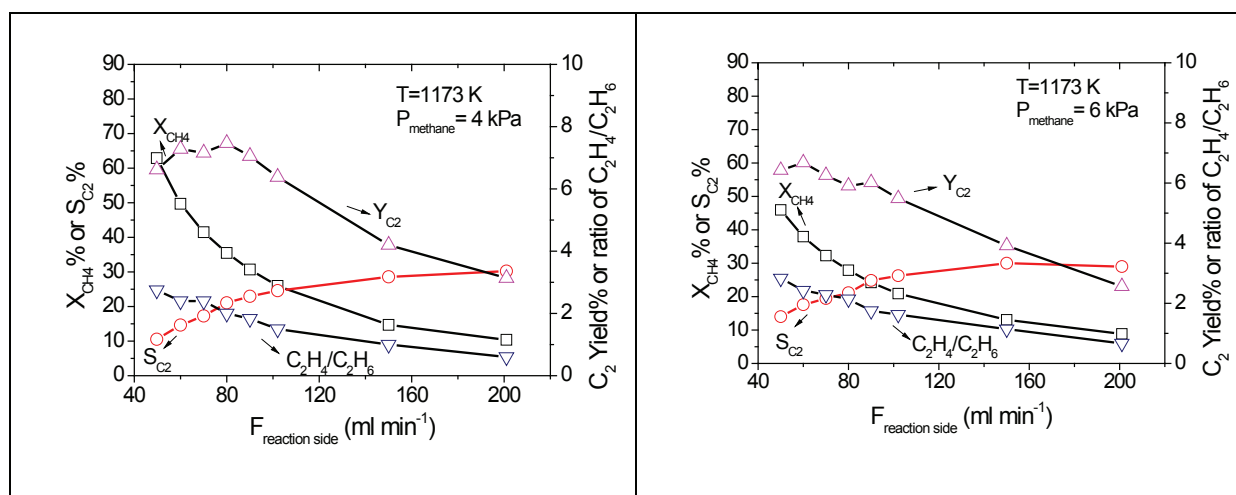


Figure 86 Impact of the flow rate in the reaction side on the methane conversion ( $\square$ ),  $\text{C}_2$  selectivity ( $\circ$ ),  $\text{C}_2$  yield ( $\Delta$ ) and  $\text{C}_2\text{H}_4/\text{C}_2\text{H}_6$  ratio ( $\nabla$ ) with 4.3% of methane in Helium and a flow rate of  $50 \text{ mL} \cdot \text{min}^{-1}$  in air side with 21%  $\text{O}_2/\text{N}_2$

The oxygen conversion follows the same trend as the methane conversion (Figure 87). The decrease of the oxygen and methane conversion is linked to an increase of the  $\text{C}_2$  selectivity. A low residence time (i. e. a high flow rate) tends to favour the selectivity in  $\text{C}_2$ .

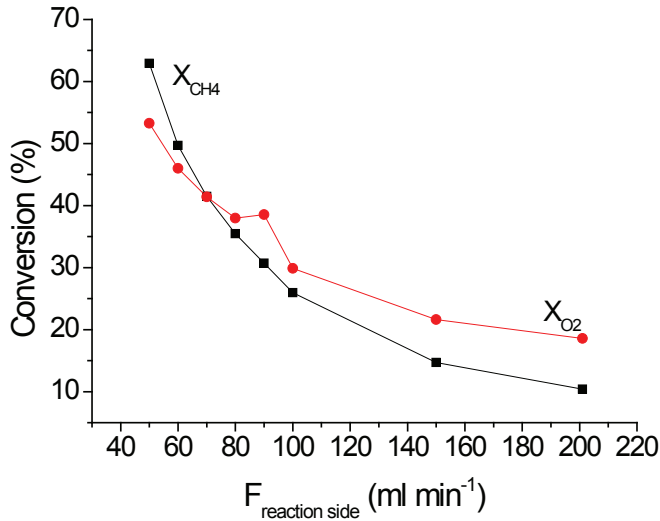


Figure 87 Impact of the flow rate in the reaction side on the methane conversion (■), oxygen conversion (●) with 4.3% of methane in Helium and a flow rate of 50mL.min<sup>-1</sup> in air side with 21%O<sub>2</sub>/N<sub>2</sub>

The oxygen flux through the dense membrane increases as a function of the flow rate in the reaction side for both conditions with and without reaction (Figure 88). The oxygen flux increases with the flow rate in the reaction side in the case of pure helium. When the reaction occurs at low flow rate of CH<sub>4</sub>/He, the oxygen flux is higher than without reaction. With the increase of the flow rate, the oxygen flux remains constant which can be explain by a strong loss of methane and oxygen conversion.

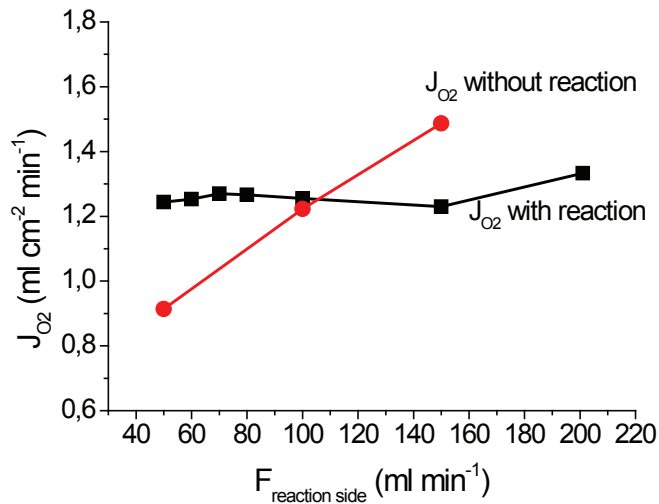


Figure 88 Impact of the reaction on the oxygen on oxygen flux in BSCF membrane in the planar reactor with a total flow rate of 100mL.min<sup>-1</sup> (STP) on the air side ( $P'_{\text{O}_2}$ =21 kPa in N<sub>2</sub>): with reaction (■); without reaction (●).

### II.1.2. Impact of the partial pressure in the air side.

The impact of the partial pressure in the air side ( $P'_{O_2}$ ), i.e change of oxygen gradient in the retentate, is plotted in Figure 89. As expected, the methane conversion increases with the partial pressure of oxygen in the air side since more oxygen is fed although not all oxygen is consumed. Indeed, the conversion of oxygen decreases from 24 to 18.5%. As the  $C_2$  selectivity increases slightly, the  $C_2$  yield is improved while the ratio  $C_2H_4/C_2H_6$  remains constant.

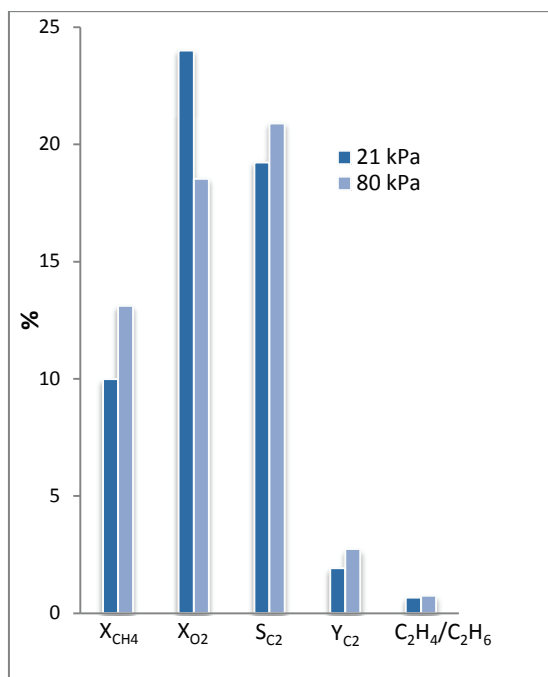


Figure 89 Methane and oxygen conversions;  $C_2$  selectivity ;  $C_2$  yield and  $C_2H_4/C_2H_6$  ratio as a function of the partial pressure of oxygen in the air side with total flow rate in both compartment of  $200 \text{ ml min}^{-1}$  (STP); the temperature of 1173K and 4% $CH_4/He$

The oxygen flux increases with the partial pressure of oxygen in the retentate side ( $P'_{O_2}$ ). At low partial pressure, from 4 to 21 kPa, the oxygen flux increases by a factor of 1.3 when the partial pressure is multiplied by 2.5 (Figure 90). At higher partial pressure, the impact becomes lower. Indeed, when  $P'_{O_2}$  increases from 21 to 60 (i.e. multiplied by 3), the oxygen flux increases of x 1.2 and then reaches a plateau. The oxygen flux is not really modified in reaction conditions.

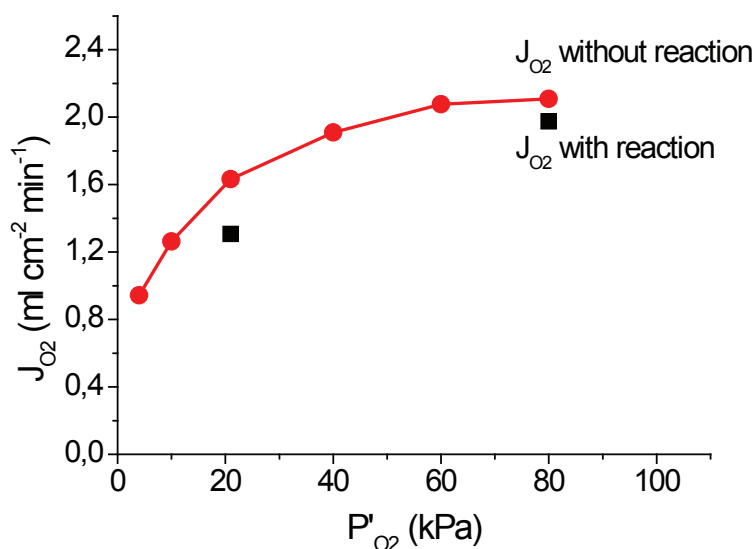


Figure 90 Impact of the partial pressure of oxygen in the air side at 1173K on the flux of oxygen (with both side of 200 ml  $min^{-1}$ ) with reaction (■) and without reaction (●).

### II.1.3. Impact of the temperature

The temperature is a key parameter in the case of the oxidative coupling of methane. Most authors agree on the optimal temperature ranging from 1073 to 1173K<sup>20</sup>. The conversion is increased from 10% to 60% (i.e. 6 times) within this temperature window (Figure 91). The  $C_2$  selectivity is rather constant from 1073 to 1160K at of 12%, resulting in a  $C_2$  yield 3 times higher. The highest ratio ethylene on ethane as well as the yield of  $C_2$  is obtained at 1173K.

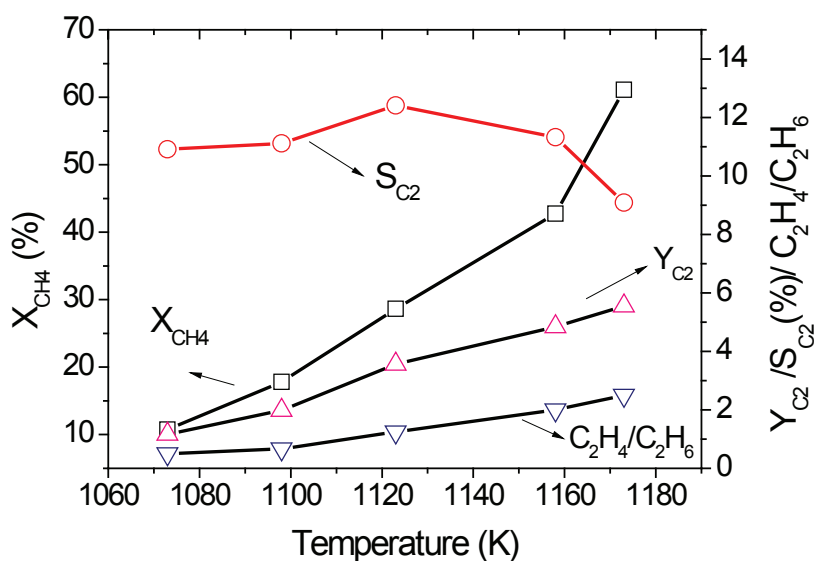


Figure 91 Methane conversion (□),  $C_2$  selectivity (○)  $C_2$  yield (Δ) and ratio of  $C_2H_4/C_2H_6$  (▼) as a function of the temperature with a total flow rate of 50ml. $min^{-1}$ . On the air side, 21% $O_2/N_2$  flows at 200ml. $min^{-1}$

The oxygen conversion follows the same trend than the methane conversion (Figure 92). With the temperature the conversion increases. Moreover the selectivity decreases. The increase of the temperature leads to higher by-products selectivity.

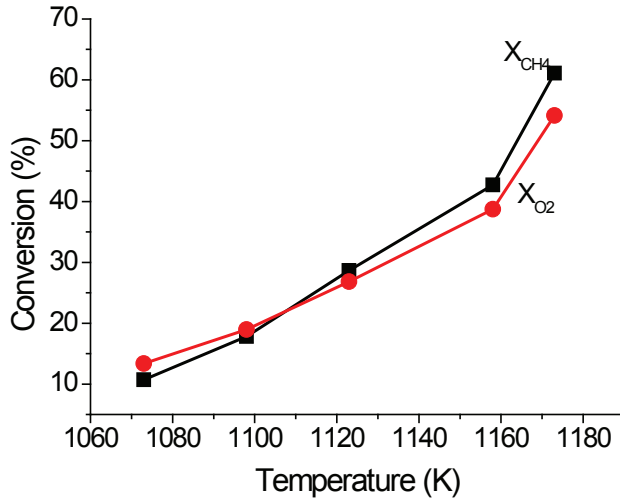


Figure 92 Oxygen (●) and methane (■) conversions as a function of the temperature with a total flow rate of 50ml.min<sup>-1</sup>. On the air side, 21%O<sub>2</sub>/N<sub>2</sub> flows at 200ml.min<sup>-1</sup>

Looking at the oxygen flux as a function of the temperature without reaction, the flux is 1.4 times higher from 1073K to 1173K (Figure 93). The flux with reaction increases much more (about 2.5 times). At low temperature, and so low methane and oxygen conversion, the oxygen flux in reaction conditions is lower than the oxygen flux without reaction. Over 1115K, the oxygen flux with reaction is getting much higher than without reaction (about 1.7 times).

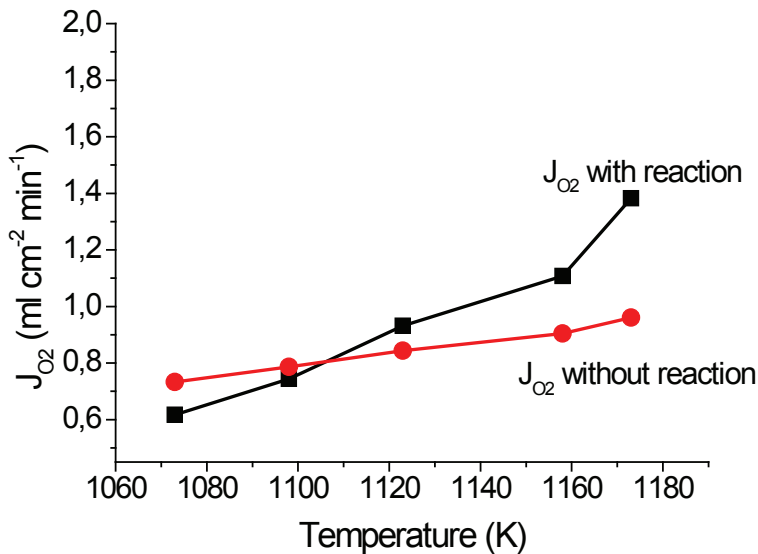


Figure 93 Oxygen flux with (■) and without reaction (●) as a function of the temperature: with P'<sub>O<sub>2</sub></sub>= 21 kPa and flow rate on both side of 200 ml min<sup>-1</sup> and Methane conversion and oxygen conversion as a function of the temperature in the same conditions.

## II.2. Discussion

BSCF membrane is active for the oxidative coupling of methane. The maximum methane conversion reaches 70% when the maximum C<sub>2</sub> selectivity is of 30%. This material is active but not selective enough for industrial perspectives. Gaseous oxygen is observed in the gas phase. A decrease of the oxygen flux would lower the methane conversion but would not necessarily result in higher selectivity. We assume that a catalyst coating might lead to an enhancement of the C<sub>2</sub> selectivity and might also impact the oxygen flux.

About the different parameters impact on the reaction conditions, the partial pressure of oxygen in the air side has a slight impact on the OCM results. Then the flow rate in the reaction side (i. e. the residence time) has a stronger impact on the results. An optimum should be found between the methane conversion and the C<sub>2</sub> selectivity. The highest methane conversion and C<sub>2</sub> yield are obtained for a long residence time, higher than 4 s (in our case, this correspond to a flow rate about 50 ml min<sup>-1</sup>). In the same time, the best C<sub>2</sub> selectivity is obtained for a residence time around 1 s (about 200 ml min<sup>-1</sup>).

The temperature shows the strongest impact of catalytic performances. The highest selectivity is obtained for 1123K, when the methane conversion increases with the temperature.

In a nutshell for the bare BSCF membrane, the best methane conversion and C<sub>2</sub> yield are reached for high residence time about 4s and high temperature, around 1173K. For the C<sub>2</sub> selectivity, the best conditions are a low residence time (about 1s) and an average temperature of 1123K.

The impact of surface modification by applying a catalyst coating is studied in same experimental conditions.

## II.3. Stability of BSCF membrane in OCM conditions

The stability of the BSCF membrane has been studied by SEM after 4 weeks of use in OCM conditions (Figure 94). The surface of the side exposed to air remains the same after experiment, no defects appear. Looking at the edge same, some rare defects appeared. In order to characterize the defects in the structure, line scans have been carried out on the edge and on the surface of the membrane exposed to air. The line scan on the surface showed no variations. Looking at the edge, the line scan shows a defect in the structure with the appearance of SrO oxide. At higher magnification, only rare defects can be observed. There are all present across the 2.5µm close to the surface, which correspond to 1/1000 of the thickness of the membrane.

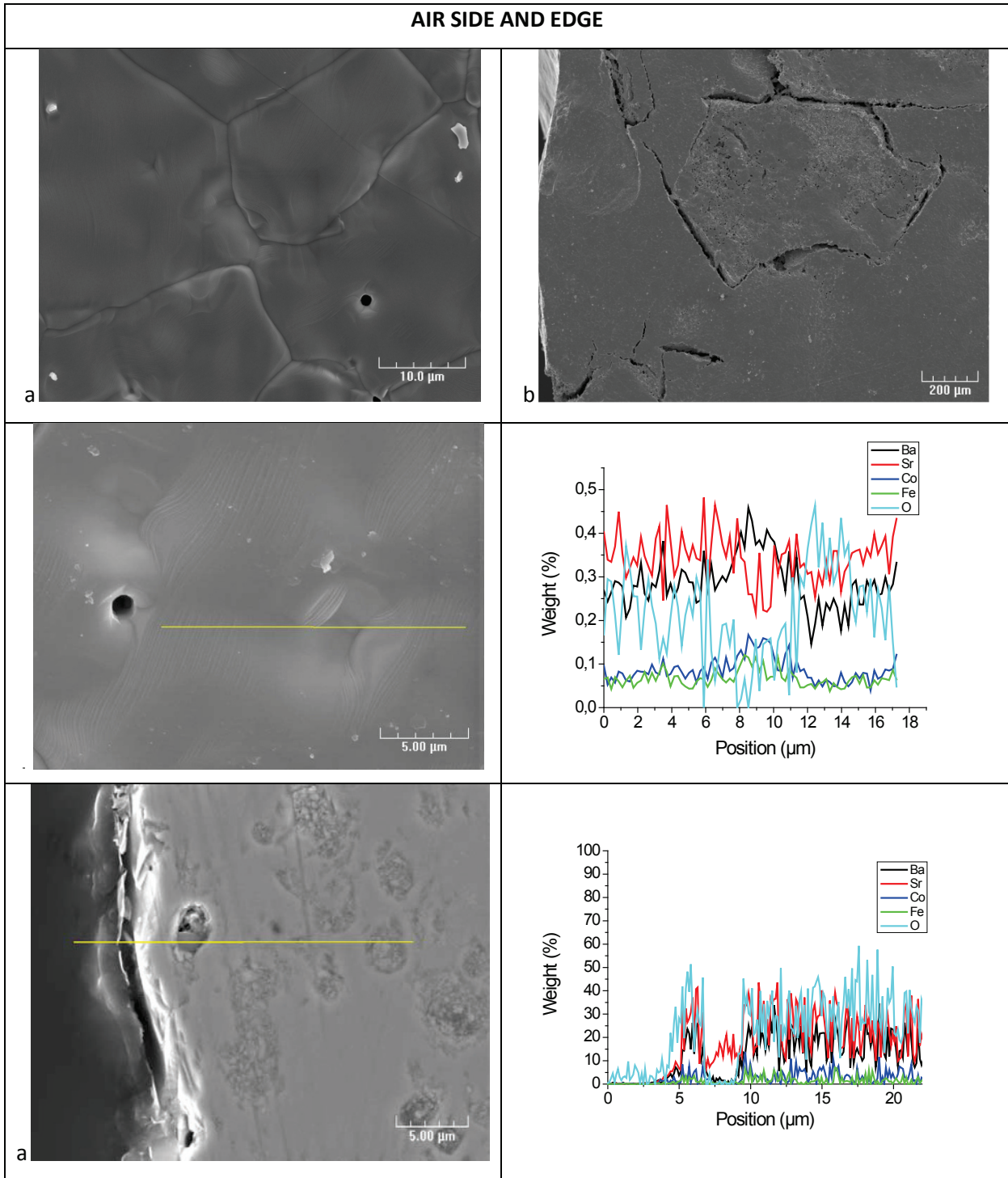


Figure 94 Surface of the sample after reaction on air side (a: x2000 and b:x 80) and Edge on the air side (c: x4000 d:x4000)

For the reaction side, the picture of the surface shows many defects, the characterization pointed out the segregation of cobalt oxides (Figure 95 b). Looking at the edge (Figure 95 c), these defects are present to a certain thickness (about 10  $\mu\text{m}$ ; 10 thousandth of the thickness).

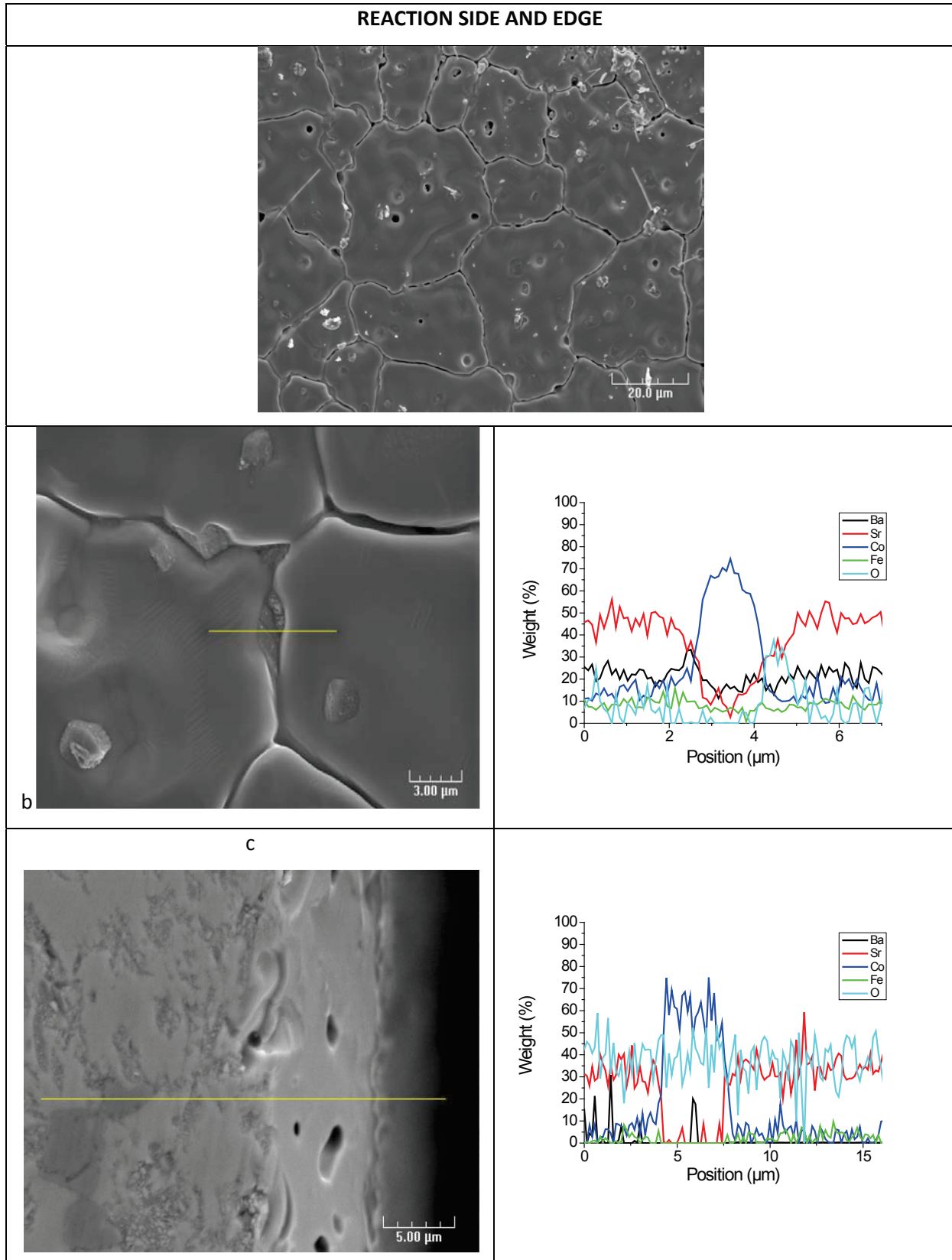


Figure 95 Line scan on the membrane: a) the edge on the air side (x1100), b) the surface on the reaction side (x5000) and c) the edge on the reaction side (x4000)

In order to characterize the defects in the structure, both sides of the membranes have been studied in Raman spectroscopy (Figure 96). The two Raman spectra show the same pattern. However, on the reaction side, an extra peak appears at  $743.0\text{cm}^{-1}$  shift. This shift is characteristic of  $\text{Co}_3\text{O}_4$  oxide.

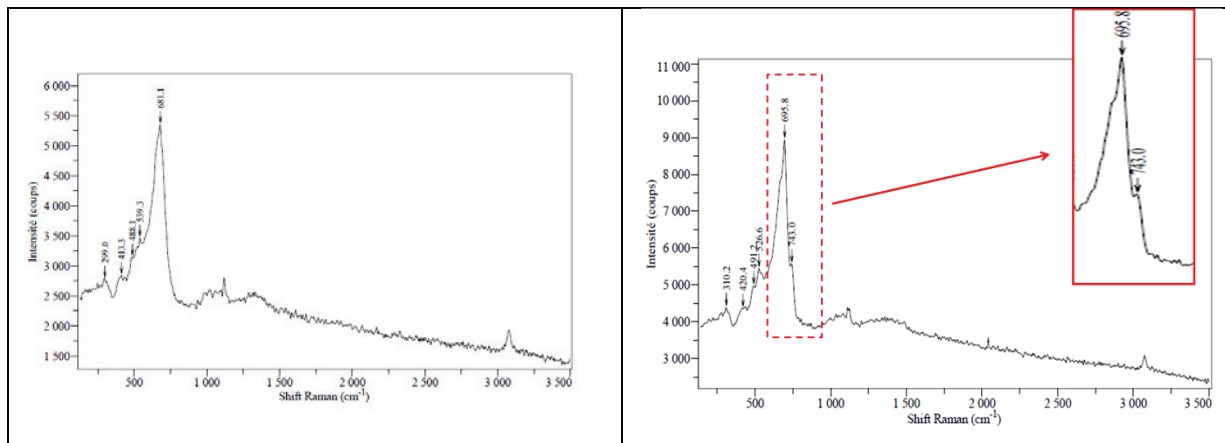


Figure 96 Raman Spectrum on BSCF dense membrane after experiment: a: air side; b: reaction side

In a nutshell, the side of the sample exposed to air remains stable, in spite of the appearance of few defects mainly composed of strontium. While on the reaction side, the appearance of cobalt based defects is confirmed by Raman spectroscopy. These defects are mainly  $\text{Co}_3\text{O}_4$  oxides.

The stability of the BSCF perovskite over a reaction is a highly controversial subject. Indeed some authors report a chemical stability<sup>21–23</sup>. Other authors agreed on the chemical non-stability of BSCF membrane<sup>24,25</sup>. Zhen and al.<sup>26</sup> found a small amount of  $\text{CoO}$  on the surface of the membrane. Nevertheless, a degradation of oxygen permeation in containing  $\text{CO}_2$  atmospheres is generally acknowledged<sup>27</sup>.

Our results show a formation of  $\text{CoOx}$  at the reaction side but on a deepness which is non significant with respect to the thickness of the membrane. In addition, some catalytic test on a membrane last for more than 4 weeks without obvious degradation.

### III. I.1. OCM results using a catalyst coating on BSCF membrane

LaSrCaO and Mn/NaWO<sub>4</sub> on silica are considered as most promising catalyst candidates for the oxidative coupling of methane. LaSrCaO allows a high conversion of methane but a low selectivity, the yield of C<sub>2</sub> reported in the literature can almost reach 25%. In the case of Mn/NaWO<sub>4</sub>, selectivity in C<sub>2</sub> up to 80% have been reported but the yield remains lower than 25%.

For each catalyst coating, the membrane flux without reaction was first tested. Then, methane (CH<sub>4</sub>/He) has been feed to the reaction side and catalytic performances recorded at various conditions.

#### III.1. Tungsten based catalyst

Li and co-workers<sup>28,29</sup> first studied Mn/NaWO<sub>4</sub> on silica in two reactors configurations: fluidized bed reactor and fixed bed reactor. This catalyst presents a high stability about 450 hours under stream. Moreover, the presence of Mn<sub>2</sub>O<sub>3</sub> and Na<sub>2</sub>WO<sub>4</sub> phases has been reported. The loading of NaWO<sub>4</sub> has an impact of the reactivity and the highest OCM activity has been reported for 4wt% NaWO<sub>4</sub> loading on amorphous SiO<sub>2</sub>. Mn/SiO<sub>2</sub> is also an active site. Under the high temperature conditions, a phase transition occurred from amorphous silica to  $\alpha$ -cristobalite. The first study from Li as well as Density Functional Theory (DFT)<sup>30</sup> calculations for tetrahedral WO<sub>4</sub> either on  $\alpha$ -cristobalite demonstrate tetrahedral WO<sub>4</sub> species are formed of one W=O bond and three W-O-Si bonds. Mn interacts with a single oxygen bridge forming either dispersed MnO<sub>4</sub> or it exists as oxide clusters.

The best composition<sup>31</sup> has been chosen 13.3/18.3/4.6 wt% Mn/W/Na on silica. About 50 mg of catalyst was coated on the membrane using the spray coating method. A suspension of catalyst in ethylene glycol, glycerol and propan-2-ol (chapter 2) was prepared in a ball mill for 1 hour. Then the sample was coated. After sintering, the adhesion of the coating was tested on an ultrasonic bench. Then the sample was loaded in the reactor.

##### III.1.1. Flux without reaction

The flux of oxygen through the dense membrane has been measured on bare BSCF and coated membrane. Figure 97 shows the impact of the partial pressure of oxygen in the feed side on the oxygen flux through the dense membrane. The flux of oxygen for the coated membrane is about 5 times lower than the flux across the bare membrane. Moreover the partial pressure of oxygen on the feed side has a no real impact on this flux. In a first approach, we can conclude that one of the compound poisoned the flux, the desorption rate of oxygen in the reaction side is lowered and seems

to be the limiting step. In order to define which compound poisoned the flux, we coated various compounds  $\text{Na}_2\text{WO}_4$  without silica and manganese, and then directly the tungsten oxide ( $\text{WO}_3$ ) and a new layer based on a mixture of  $\text{WO}_3$  and BSCF. The different catalyst configurations are plotted in Figure 97 and in Table 38. The maximum value of the flux remains the one with  $\text{Na}_2\text{WO}_4$ . Authors studied  $\text{Mn-Na}_2\text{WO}_4/\text{SiO}_2$  catalyst for the oxidative coupling of methane. They showed that the formulation  $\text{Mn-Na}_2\text{WO}_4/\text{SiO}_2$  is hardly reducible since any desorption oxygen occur until  $800^\circ\text{C}^{28,29}$  in  $\text{O}_2$ -TPD experiments.

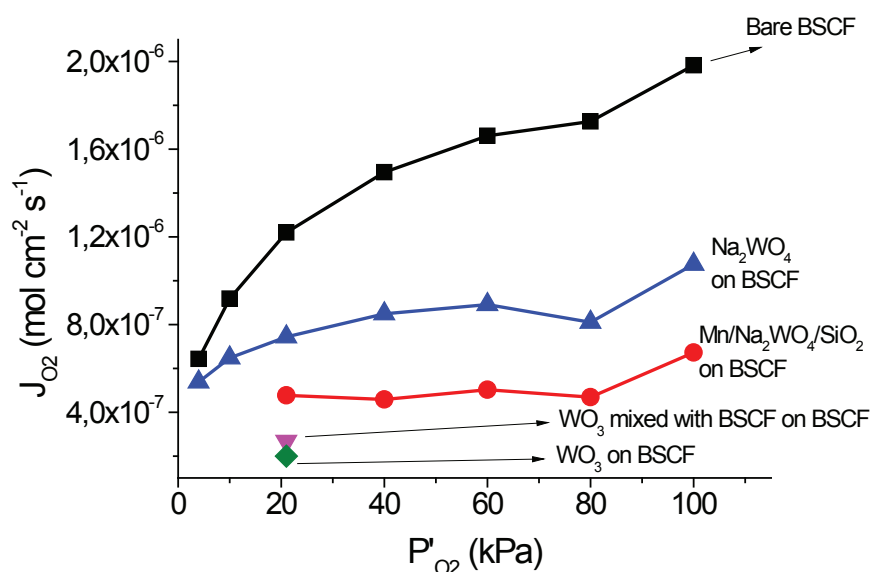


Figure 97 Impact of the partial pressure of oxygen in the feed side on the oxygen flux through the dense membrane at  $1173\text{K}$  and  $200\text{mL}\cdot\text{min}^{-1}$  (STP) flow rate on each side of the membrane for bare BSCF membrane (■) and for the membrane coated with:  $\text{Mn}/\text{Na}_2\text{WO}_4$  (●);  $\text{Na}_2\text{WO}_4$  (▲)

Table 38 Summary of the oxygen flux through BSCF with different coatings at  $1173\text{K}$ , total flow rate on each side of  $200\text{mL}\cdot\text{min}^{-1}$  (STP) and with  $21\%\text{O}_2$  in  $\text{N}_2$  in the feed side

Catalyst on BSCF	$J_{\text{O}_2}$ $1\text{E-}6\cdot\text{mol}\cdot\text{cm}^{-2}\cdot\text{s}^{-1}$
None	1.22
$\text{Mn}/\text{Na}_2\text{WO}_4$ on Silica	0.48
$\text{Na}_2\text{WO}_4$	0.74
$\text{WO}_3$ mixed in BSCF	0.36
$\text{WO}_3$	0.27

### III.1.2. Catalytic results of W-based coatings on BSCF membranes

The catalytic results of the W-based catalysts are recorded in Table 39. The conversion of methane for tungsten based catalyst is in a range of 5-10% while in the literature methane conversions up to 30% are reported. The two best candidates are  $\text{Na}_2\text{WO}_4$  and  $\text{WO}_3$  mixed with BSCF, no improvement of the methane conversion is observed. With  $\text{Mn}/\text{Na}_2\text{WO}_4$  on Silica and  $\text{WO}_3$ , the methane conversion is lower than with bare BSCF membrane. The  $\text{C}_2$  selectivity varies from 10 to 60% against 70-80% as reported in the literature.  $\text{Mn}/\text{Na}_2\text{WO}_4$  on Silica shows the lowest selectivity. However, for the  $\text{Na}_2\text{WO}_4$ , the  $\text{C}_2$  selectivity is increased by a factor 1.5 as a comparison of the bare BSCF membrane.  $\text{WO}_3$  catalysts (in thin layer or mixed with BSCF) show the highest selectivity (62.9 and 53.1% respectively).

Table 39 Summary of the results obtain with tungsten based catalyst with 4% $\text{CH}_4/\text{He}$  and 21% $\text{O}_2/\text{N}_2$  with a flow rate in each side of 200ml.min<sup>-1</sup> at 1173K.

Catalyst on BSCF	$X_{\text{CH}_4}\%$	$X_{\text{O}_2}\%$	$S_{\text{C}_2}$	$Y_{\text{C}_2}$	$\text{C}_2\text{H}_4/\text{C}_2\text{H}_6$
None	10.1	50	20.2	2.0	0.5
$\text{Mn}/\text{Na}_2\text{WO}_4$ on Silica	5.4	100	11.0	0.6	0.3
$\text{Na}_2\text{WO}_4$	10.3	60	31.4	3.2	1.0
$\text{WO}_3$ mixed with BSCF	10.1	100	53.1	5.4	0.1
$\text{WO}_3$	8.0	100	62.9	5.0	0.1

For the flux with reaction, no real increase of the oxygen flux can be observed (Table 40). Looking at the conclusions on the bare BSCF membrane, for a low methane conversion, the oxygen flux with reaction is equivalent or slightly higher/lower than the oxygen flux without reaction.

Table 40 Summary of the fluxes obtained with tungsten based catalyst with 4% $\text{CH}_4/\text{He}$  and 21% $\text{O}_2/\text{N}_2$  with a flow rate in each side of 200ml.min<sup>-1</sup> at 1173K and without reaction in the same  $P'_{\text{O}_2}$  and Temperature conditions.

Catalyst on BSCF	$X_{\text{CH}_4}$ %	$J_{\text{O}_2}$ (without reaction) 1E-6.mol.cm <sup>-2</sup> .s <sup>-1</sup>	$J_{\text{O}_2}$ (with reaction) 1E-6.mol.cm <sup>-2</sup> .s <sup>-1</sup>
None	10.1	1.22	1.33
$\text{Mn}/\text{Na}_2\text{WO}_4$ on Silica	5.4	0.48	0.45
$\text{Na}_2\text{WO}_4$	10.3	0.74	0.77
$\text{WO}_3$ mixed with BSCF	10.1	0.36	0.27
$\text{WO}_3$	8.0	0.27	0.17

Tungsten based catalysts poisoned the oxygen flux through the membrane and there is no improvement on the methane conversion. On the other hand, the C<sub>2</sub> selectivity is higher and leads to a higher C<sub>2</sub> yield. The tungsten based catalysts are not the best candidates due to their oxygen flux poisoning but these experiments validates the interest of the addition of a catalyst thin layer on the membrane.

## III.2. Lanthanum based catalyst

Lanthanum based catalysts have attracted most attention in the OCM reaction. Over the past decades, Marin group extensively studied using a microkinetic approach the impact of catalyst features on the oxidative coupling of methane. They first developed a micro kinetic model on Li/MgO<sup>32</sup> catalyst, then on Sn/Li/MgO<sup>7,33</sup>, to finally adapt it on lanthanum based catalysts<sup>34,35</sup>. They compare the results for each catalyst and they pointed out that the methane activity of Sr/La<sub>2</sub>O<sub>3</sub> (which has been proved to be lowest than LaSr/CaO catalyst) is 33 times and 5 time higher than that of Li/MgO and Sn-Li/MgO, respectively. They attribute the high activity of Sr/La<sub>2</sub>O<sub>3</sub> to the higher stability of adsorbed hydroxyl and oxygen and also to the higher active site density. Moreover, they linked to C<sub>2</sub> selectivity to the methyl radical sticking coefficient and the stability of adsorbed oxygen. The recombination of oxygen to gaseous oxygen should be avoided (leading to a low loading per square meter and a high quantity of active sites) in order to increase both selectivity and conversion.

### III.2.1. Coating of LaSrCaO and LaSrO on BSCF membrane

Details of the catalyst coating are described in chapter 2. The catalyst was deposited as thin film by a spray coating method. The coating was about 50µm-70µm thick for a deposition of 50 mg in total. All the tested were done with a 50 mg coating except for the test of the impact of the catalyst loading, which tests were carried out with 20 and 60 mg. Adhesion of the catalyst was tested by ultrasonic bench after sintering. Then the coated membrane is directly set up in the reactor in order to avoid a loss of adherence which is experienced when the sample stand a long time in air. We suspect the segregation of Lanthanum hydroxides in air upon time.

### III.2.2. Impact of La-coatings on oxygen flux without reaction

Oxygen fluxes were measured in air separation configuration (without reaction with methane) (Figure 98). At low partial pressure of oxygen in the air side (lower than 40 kPa), the coating of La based catalyst does not affect the oxygen flux. In contrast at higher partial pressure of oxygen (>40 kPa), the impact of the catalyst loading is significant; the oxygen flux is obviously decreased by La/Sr/Ca catalyst coating. In this condition, we can assume that the oxygen flux is limited by the desorption in the sweep side. In contrast, surface modifications by the addition of so called active layers of the same composition than the membrane<sup>36</sup> or a noble metal particle deposition<sup>4</sup> on BSCF have shown to increase the oxygen flux due to a faster desorption of oxygen in the sweep side. In both cases, we can assume that the recombination is facilitated by either the

larger surface area or by spill-over mechanism of metal particles. In our case, the coating is an oxide formulation which contains La and Ca which are not present in the composition of BSCF. We can suggest that the catalyst coating modify the solid structure on the interface leading to a slower adsorption.

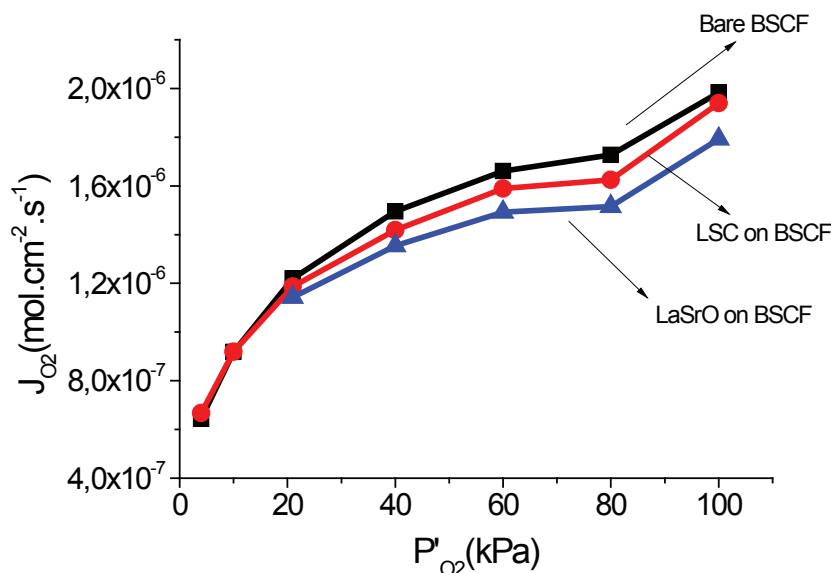


Figure 98 Oxygen flux through the membrane as a function of the partial pressure of oxygen in the air side at 1173K, and a total flow rate on both side of  $200 \text{ mL min}^{-1}$  (STP) for bare BSCF (■), coated BSCF with LaSrCa (●) and LaSr (▲).

### III.2.1. Impact of La-based coatings on OCM reaction in Membrane Reactor

Figure 99b shows the surface aspect of the catalyst depending on the catalyst loading, the catalyst has been not spread uniformly. The upper part of the picture shows a low loading, the catalyst consists of small agglomerates. The lower part of the picture shows a high loading of catalyst. The agglomerates are bigger and the pore size is smaller which may make the mass transport slower in the gas.

The following picture (Figure 99 a) shows a slice of the catalyst supported on the membrane in the case of a high loading. We can observed that the layer is divided in two main part, a layer which looks like the low loading layer and a extra layer which looks like a high loading layer.

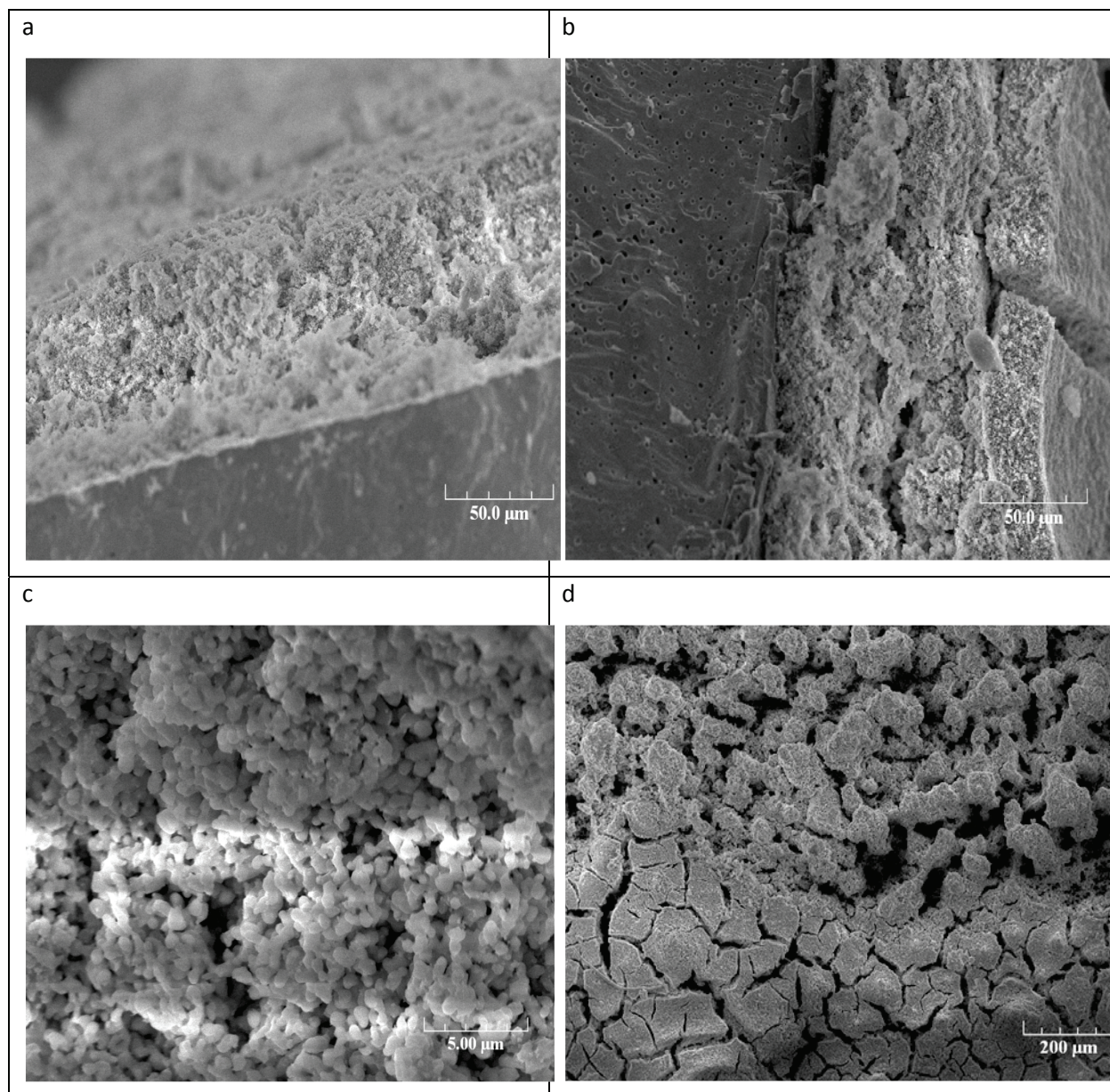


Figure 99 Edge (top) and surface (bottom) aspect for different catalyst loading (20 mg left and 60 mg right) (a: x500; b: x500, c:x5000, d: x100)

### III.2.1.1. Impact of the La-based catalyst loading on OCM performances

The conversion of methane is 50% larger for larger catalyst loading (Figure 100) while the  $C_2$  yield and the  $C_2H_4/C_2H_6$  ratio remain almost constant. On the other hand the increase of the loading of the catalyst has a negative impact on the selectivity; which is 6% lower.

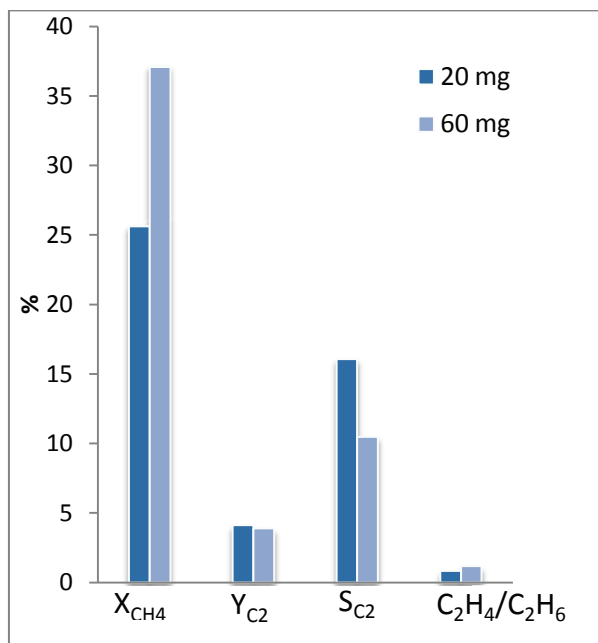


Figure 100 Methane conversion;  $C_2$  yield;  $C_2$  selectivity;  $C_2H_4/C_2H_6$  ratio

The productivity in ethylene expressed by unit of mass of coating doubled when the catalyst loading is divided by 3. Similarly, the catalyst activity is 50% larger (Figure 101). Clearly a high catalyst loading is detrimental in the case of the La based catalysts as the selectivity and the productivity in ethylene drop. The amount of 20mg on the membrane surface represents a loading of  $5\text{ mg cm}^{-2}$  of membrane.

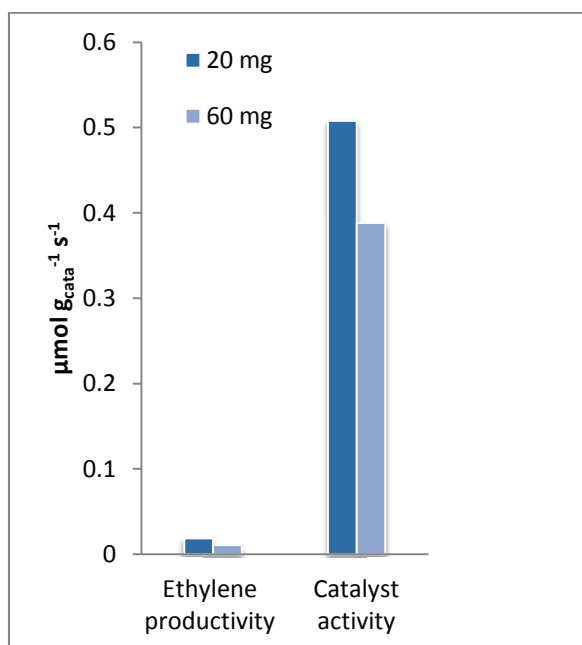


Figure 101 Productivity in ethylene and activity of the catalyst: for 20mg of catalyst and 60mg of catalyst

The oxygen flux with reaction is much higher than without reaction (Figure 102). The conversion of methane is high for LaSrCa. Moreover, an increase of the catalytic loading leads to an increase of the

methane conversion and an increase of the oxygen flux through the dense membrane. This is also directly linked to a loss of  $C_2$  selectivity. The variation of these two parameters leads to a balance of the  $C_2$  yield.

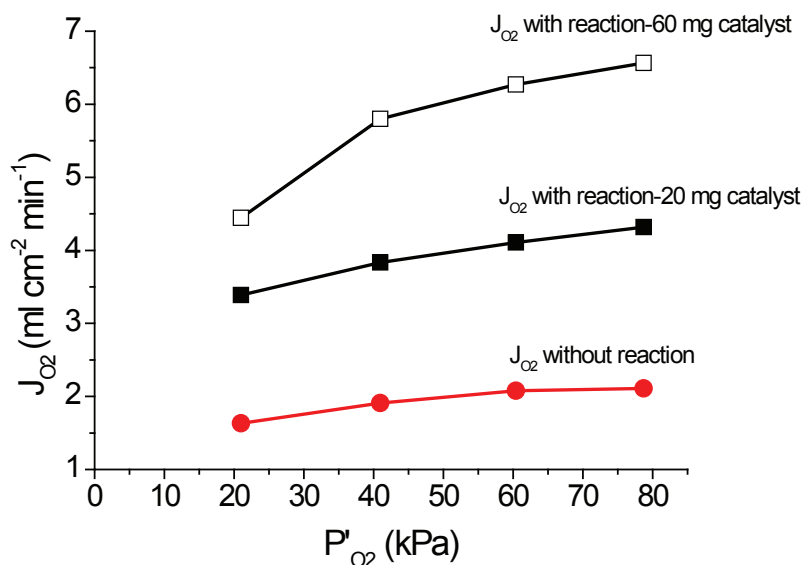


Figure 102 Oxygen flux as a function of  $P'_{O_2}$  with (■) and without reaction (●): with a flow rate of  $200\text{mL}\cdot\text{min}^{-1}$  on air side and  $200\text{mL}\cdot\text{min}^{-1}$  in the reaction side with a methane ratio in Helium of 10%: for 20mg of catalyst (plain) and 60mg of catalyst (open)

The addition of LaSrCa catalyst leads to an increase of the methane conversion. The increase of the amount of the loading leads to an increase of the methane conversion and the oxygen flux (and so the oxygen provided in the reaction side). This also leads to a loss of  $C_2$  selectivity.

Indeed the conversion of methane for 60mg is 60% higher than for 20mg of catalyst. But the selectivity is 40% lower. In both cases, the surface of the membrane remains constant, but with 60mg of catalyst the layer is thicker. The thicker layer prevents methane diffusion in the catalyst layer and leads to a recombination of oxygen before entering the reaction side, which leads to a higher selectivity in by-products  $CO_x$ . In order to increase the conversion and avoid the decrease of the selectivity, the amount of catalyst should be increase as well as the membrane surface. The use of tubular membrane reactor could be a good alternative.

In the following, the catalytic results are presented with the catalyst coating of 50-60mg.

### III.2.1.2. Impact of the Temperature

The impact of the temperature has been studied in the same conditions than for the bare BSCF membrane from 1073 to 1173 K (Figure 103). The conversion of methane increases with the

temperature while the selectivity decreases. The highest methane conversion and  $C_2$  yield are obtained at 1173 K when the highest selectivity is obtained at 1123K. This is similar to the case of bare BSCF membrane. In order to highlight the effect of the addition of a catalyst coating, results were compared for the two designs at 1173 K (Figure 104). The methane conversion is 4 times lower for bare BSCF membrane when the  $C_2$  selectivity is slightly lower the  $C_2$  selectivity of the coated membrane. The  $C_2$  yield is higher for the coated membrane (about 4 times) as well as the  $C_2H_4/C_2H_6$  ratio. Thus, we can again conclude on the positive effects of the application of a La-based catalyst layer on the dense membrane. In addition, the thickness of this layer should be well controlled in order to avoid a loss of  $C_2$  selectivity and of ethylene production.

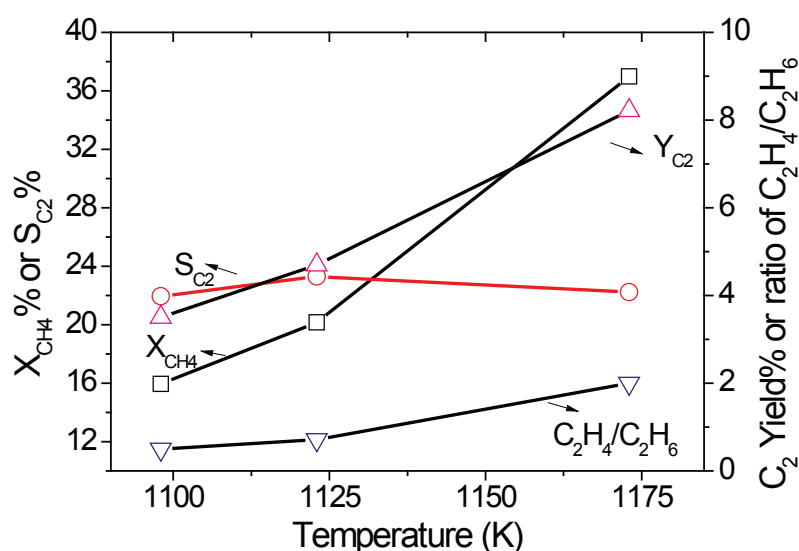


Figure 103 Impact of the temperature on Methane conversion (□),  $C_2$  selectivity (○)  $C_2$  yield (Δ) and ratio of  $C_2H_4/C_2H_6$  (▼) for  $P_{methane}=4$  kPa,  $P_{O_2}=21$ kPa, Flow rate in both side of  $200$  ml  $min^{-1}$  with 50mg of catalyst

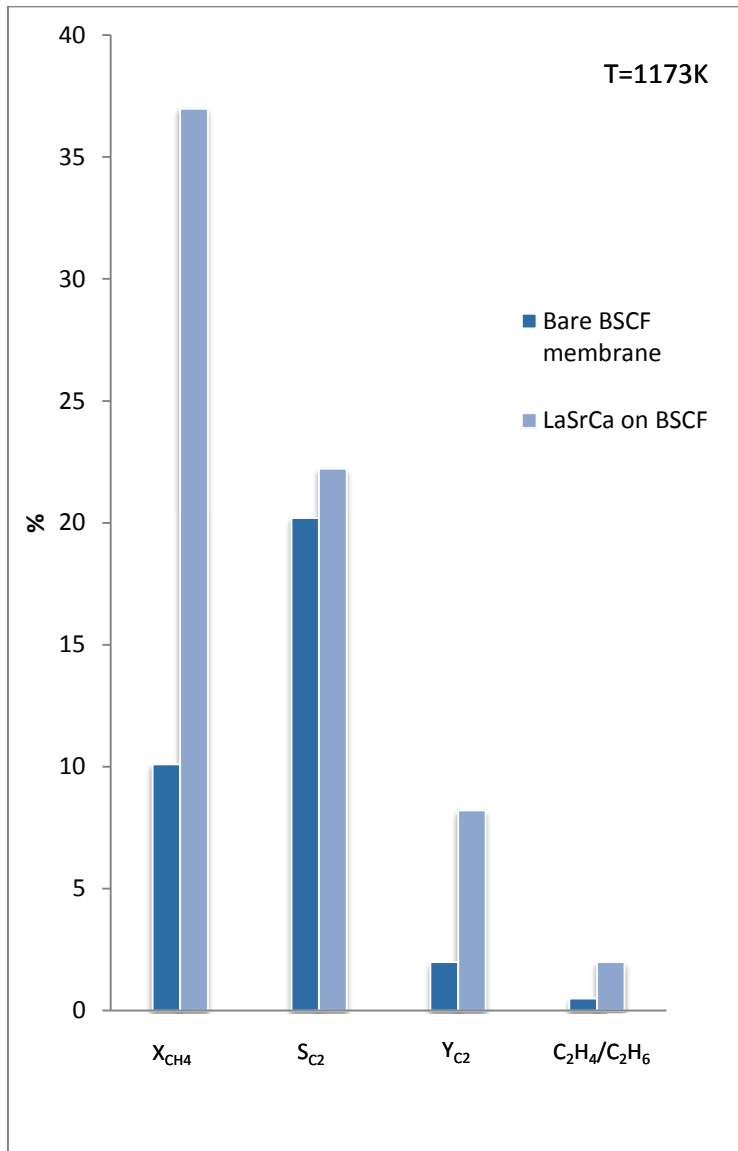


Figure 104 Methane conversion,  $C_2$  selectivity and  $C_2$  yield without and with catalyst at two temperatures (left  $T=1173K$  and right  $T=1123K$ ) with  $P_{methane}=4$  kPa,  $P_{O_2}= 21kPa$ , Flow rate in both side of  $200$  ml  $min^{-1}$  with 50mg of catalyst of LaSrCaO.

The oxygen flux is much higher in reaction condition and increases with the methane conversion (Figure 105). These results are in good agreement with the results observed until now.

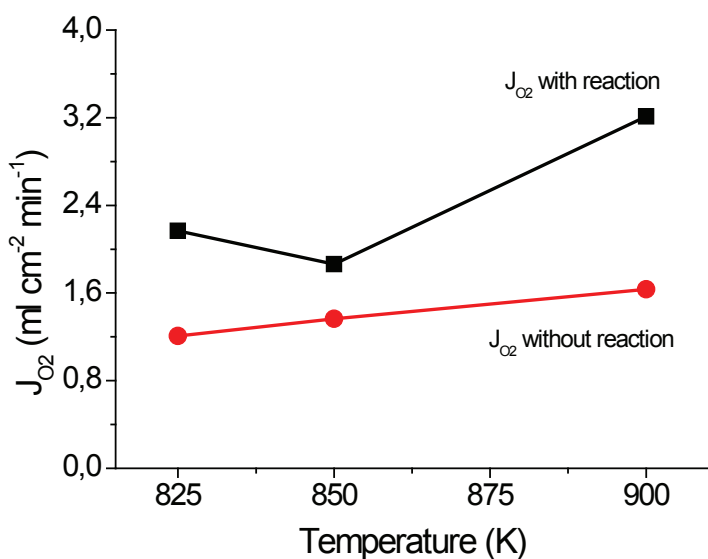


Figure 105 Oxygen flux as a function of  $P'_{O_2}$  with (■) and without reaction (●): for  $P_{\text{methane}}=4$  kPa,  $P_{O_2}=21$  kPa, Flow rate in both side of  $200$  ml min<sup>-1</sup> with 50mg of catalyst

### III.2.1.3. Impact of flow rate on each side of the membrane:

The study of the bare membrane showed the relevancy of the optimization of the flow rates on both side of the membrane in order to find an optimum between conversion and selectivity.

#### III.2.1.3.1. Impact of the flow rate in the reaction side

The effect of the variation of the flow rate in the reaction side has been measured at two different methane partial pressures (4 and 8 kPa) and at different temperatures (Figure 106). The increase of the flow rate has two consequences: i) the dilution of the oxygen partial pressure ( $P''_{O_2}$ ) in the reaction side and ii) the decrease of the residence time.

In all cases, we observe that the conversion decreases while the  $C_2$  selectivity increases with the flow rates. The results are in line to what would be expected by decreasing the residence time in a fixed bed type of reactor. The  $C_2$  selectivity is higher for  $P_{CH_4}=8$  kPa while the methane conversion is lower. At 1173K, the yield of  $C_2$  reaches a plateau for  $F_{\text{reaction side}}$  higher than  $120$  ml min<sup>-1</sup>. For 1123K, the reaction is strongly limited by the oxygen feeding. The conversion of methane decreases from 50% to 20% and from 60% to 20% for  $P_{CH_4}=4$  kPa respectively  $P_{CH_4}=8$  kPa. The yield of  $C_2$  increases until reaches a maximum for  $F_{\text{reaction side}}=120$  ml min<sup>-1</sup> and  $F_{\text{reaction side}}$  from 120 to 150 ml min<sup>-1</sup> for  $P_{CH_4}=4$  kPa respectively  $P_{CH_4}=8$  kPa.

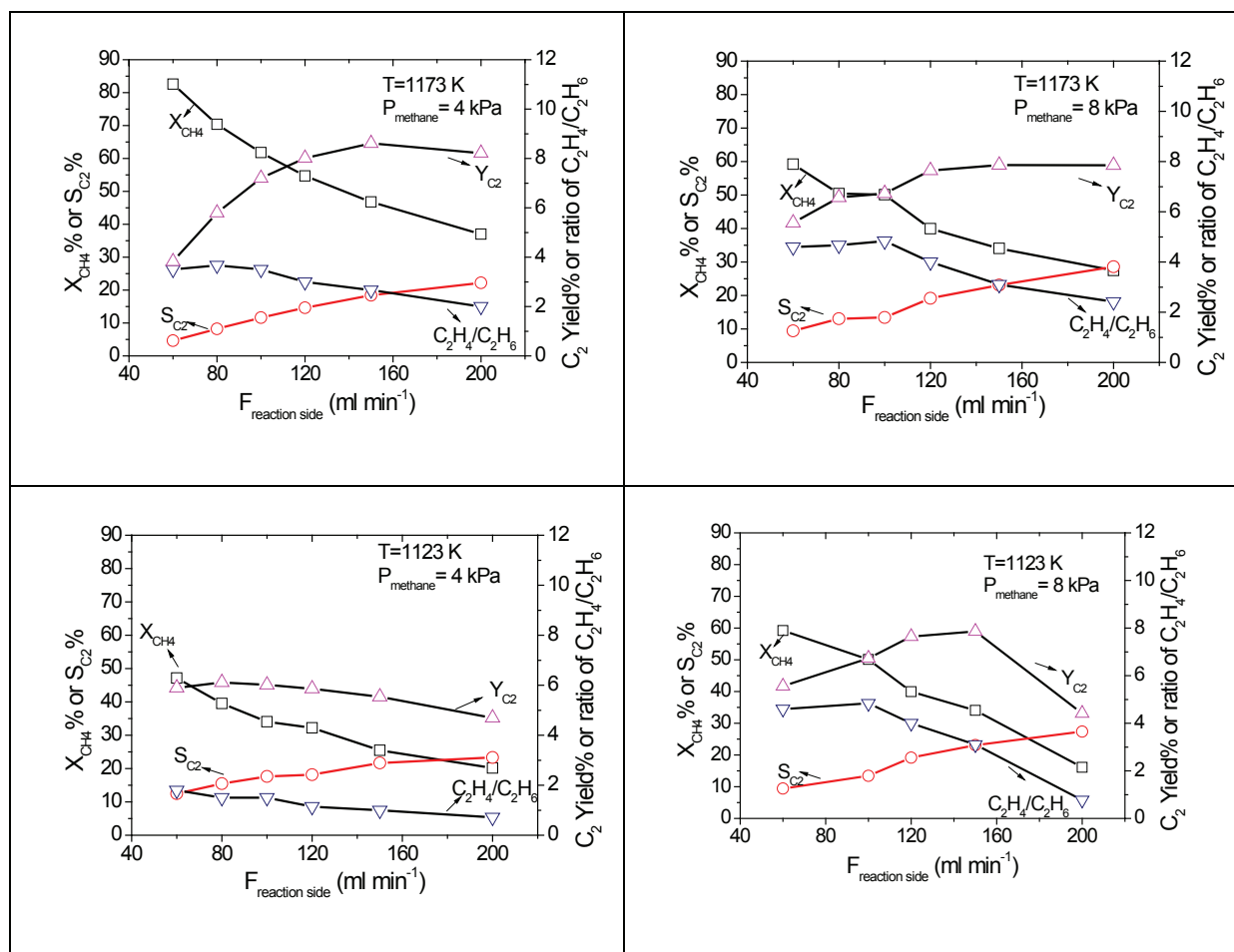


Figure 106 Impact of the flow rate in the reaction side on Methane conversion (□),  $\text{C}_2$  selectivity (○),  $\text{C}_2$  yield (Δ) and ratio of  $\text{C}_2\text{H}_4/\text{C}_2\text{H}_6$  (▼) at 1173K with  $P_{\text{methane}} = 40\text{ kPa}$  and  $\text{PO}_2 = 21\text{ kPa}$  with a flow rate of  $200\text{ ml min}^{-1}$  (STP) in the air side with  $50\text{ mg}$  of catalyst

The oxygen flux increases with the temperature (Figure 107). Moreover, the oxygen flux estimated during the reaction is higher than the oxygen flux measured without reaction.

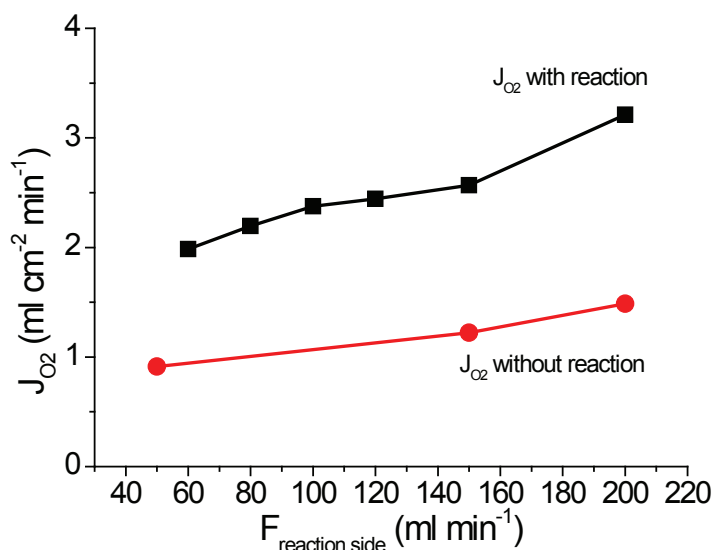


Figure 107 Impact of the reaction on the oxygen flux through the dense membrane at 1173K with  $P_{\text{CH}_4}=4$  kPa with 21%O<sub>2</sub>/N<sub>2</sub> in the air side with a flow rate of 200mL.min<sup>-1</sup> (STP): oxygen flux without reaction (●) and with reaction (■) with 50 mg of catalyst.

The impact of the flow rate in the reaction side is the same than for the bare membrane except that the maximum yield is obtained between 120 and 150 ml min<sup>-1</sup> against a range from 60 to 80 ml min<sup>-1</sup> with the bare membrane. Moreover, although the methane conversion is much higher 85% against 50% in the same conditions, the yield of C<sub>2</sub> is remaining similar and the selectivity is lower. On the other hand, the productivity in C<sub>2</sub> is higher with a catalyst.

### III.2.1.3.2. Impact of the flow rate in the air side

The impact of the residence in the air side has been studied keeping the flow rate in the reaction side constant and equal at 200mL min<sup>-1</sup>. The conversion of methane, the selectivity in C<sub>2</sub> and the C<sub>2</sub> yield are constant in this range of flow rate (Figure 108).

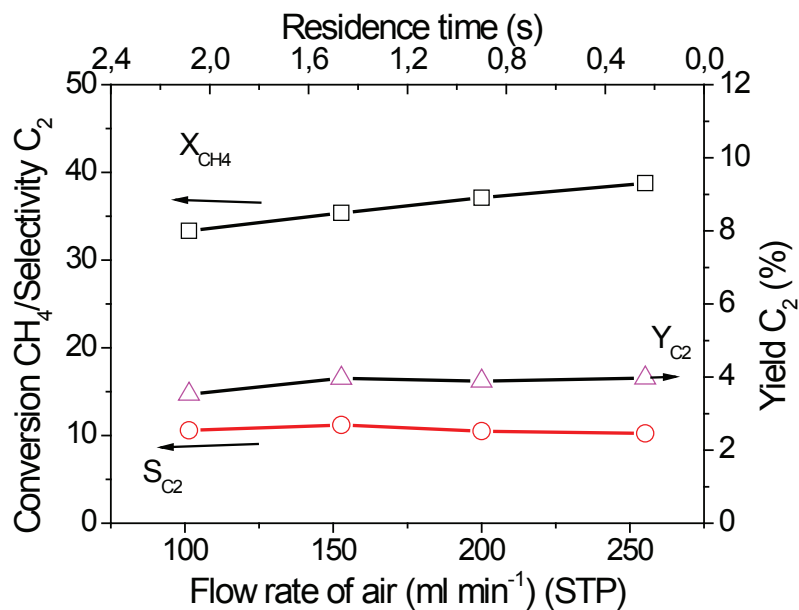


Figure 108 Impact of 21%O<sub>2</sub>/N<sub>2</sub> flow rate on the conversion of methane (□), selectivity in C<sub>2</sub> (○) and C<sub>2</sub> yield (Δ) with a flow rate of 200mL.min<sup>-1</sup> in the reaction side with a methane ratio in Helium of 10% at 1173K with 60 mg of catalyst

The oxygen flux is higher with the reaction and increase with the total flow rate in the feed side (Figure 109). Nevertheless, no real impact of this parameter has been shown. The flow rate is sufficient to insure a total renewal of the oxygen leading to a constant concentration on close to the surface of the membrane.

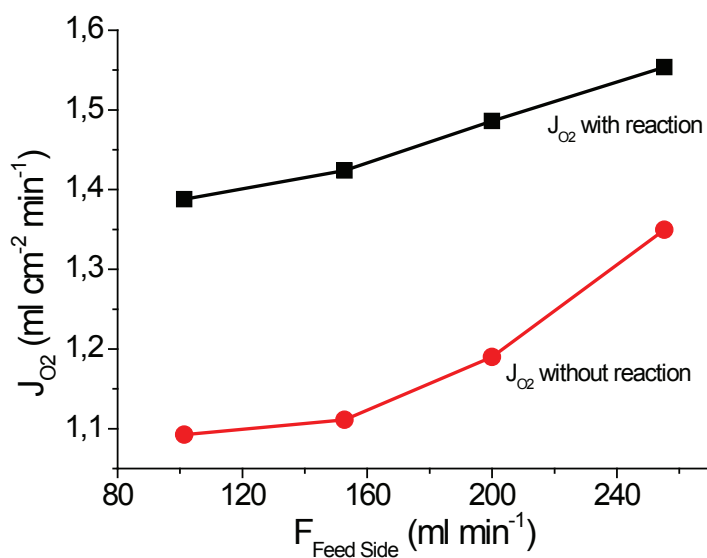


Figure 109 Oxygen flux as a function of  $P'_{O_2}$  with (■) and without reaction (●); with a flow rate of 200mL.min<sup>-1</sup> in the reaction side with a methane ratio in Helium of 10% at 1173K with 60 mg of catalyst

### III.2.1.4. Impact of the Partial pressure of Oxygen

The impact of the partial pressure of oxygen in the air side is very low (Figure 110). The methane conversion slightly increases while the  $C_2$  selectivity decreases and the  $C_2$  yield remain constant. The conclusions are the same as the bare BSCF membrane and so the use of air is sufficient. Moreover, the oxygen flux with the reaction is much higher than without (Figure 111).

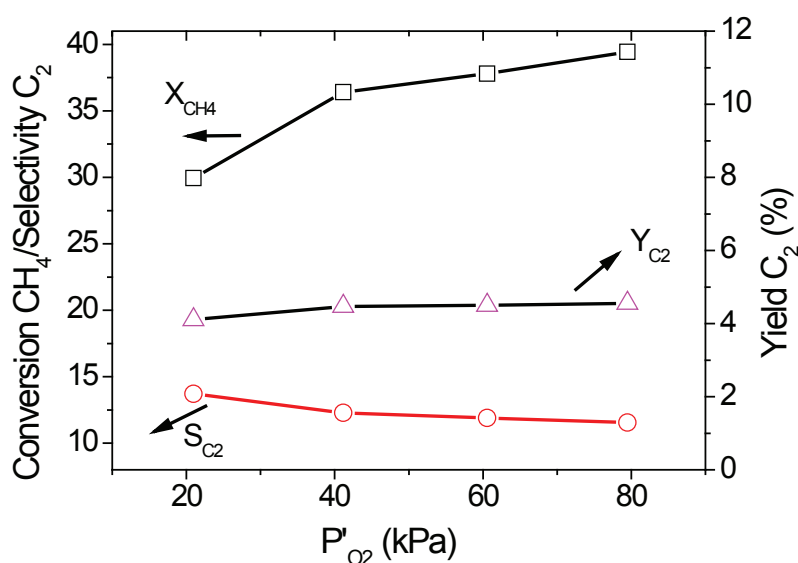


Figure 110 Impact of the ratio  $O_2/N_2$  on the conversion of methane ( $\square$ ), selectivity in  $C_2$  ( $\circ$ ) and  $C_2$  yield ( $\Delta$ ) with a flow rate of  $150\text{mL}\cdot\text{min}^{-1}$  on air side and  $250\text{mL}\cdot\text{min}^{-1}$  in the reaction side with a methane ratio in Helium of 10% with 60 mg of catalyst

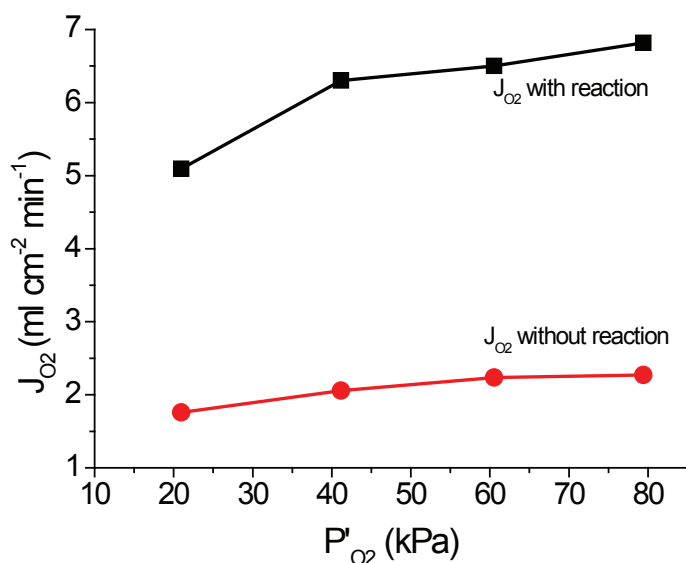


Figure 111 Oxygen flux as a function of  $P'_{O_2}$  with ( $\blacksquare$ ) and without reaction ( $\bullet$ ): with a flow rate of  $150\text{mL}\cdot\text{min}^{-1}$  on air side and  $250\text{mL}\cdot\text{min}^{-1}$  in the reaction side with a methane ratio in Helium of 10% with 60 mg of catalyst

## III.2.1.5. Impact of the Partial pressure of Methane

At 1173K, the selectivity in  $C_2$  increases from 22% to 34% (i.e. +50%) when the methane partial pressure is increased by a factor of 2.5 (Figure 112). The methane conversion decreases while the oxygen flux with the reaction strongly increases (Figure 113). The conversion of methane is lower but the total quantity of methane converted in moles is twice higher. This explains the increase of the oxygen flux with the reaction with the increases of the partial pressure of methane.

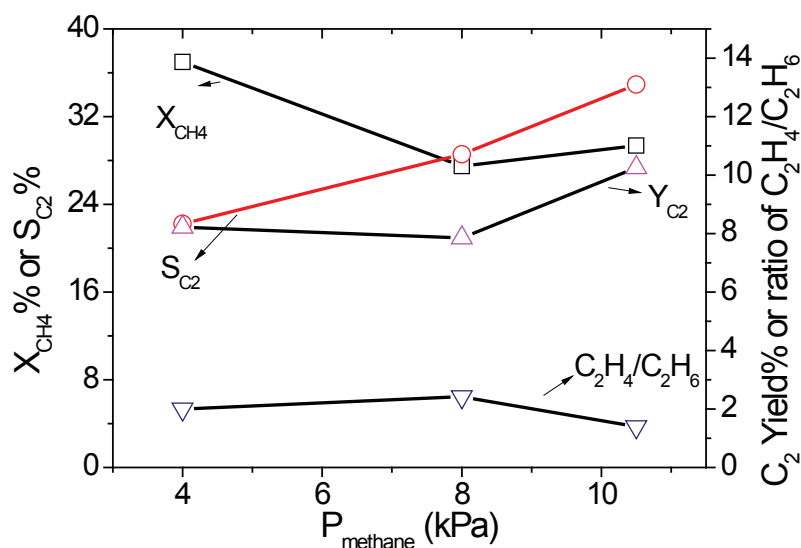


Figure 112 Impact of the  $P_{\text{methane}}$  on Methane conversion (□),  $C_2$  selectivity (○)  $C_2$  yield (△) and ratio of  $C_2H_4/C_2H_6$  (▼) with a total flow rate on both side of  $200 \text{ ml min}^{-1}$  and  $P_{\text{O}_2}^i = 21 \text{ kPa}$  at 1173 K and 50 mg of catalyst loading

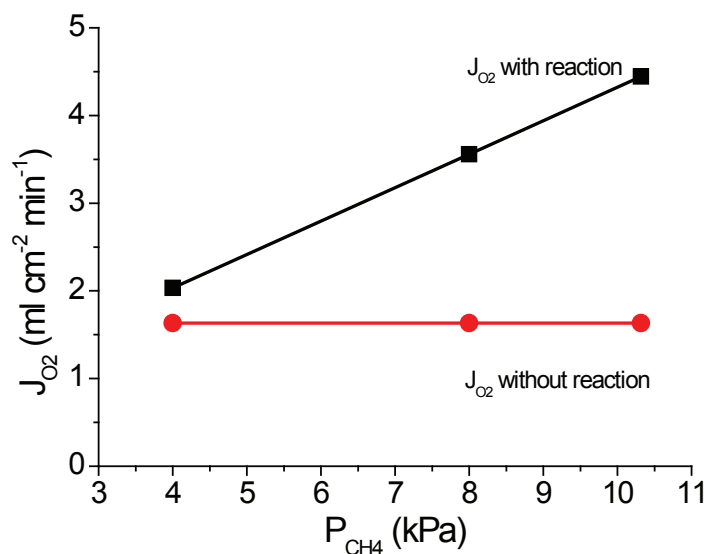


Figure 113 Oxygen flux as a function of the partial pressure of methane with the total flow rate of  $200 \text{ ml min}^{-1}$  on both side, at 1173K and  $P_{\text{O}_2}^i = 21 \text{ kPa}$  for 50 mg of catalyst

### III.3. Stability of LaSrCa catalytic coating on BSCF membrane

After two months of experiments, the catalytic coating poorly stuck to the disk. When the membrane has been removed from the bench test, the catalyst went away. Nevertheless, the membrane, post-mortem, has been characterized by SEM in order to characterize the interfaces between the catalyst and the perovskite membrane.

Looking at the air side on the membrane (Figure 114), the solid is mostly homogenous on all the thickness. Contrary to the bare BSCF membrane, no strontium oxide has been found. On this side the membrane can be considered as stable.

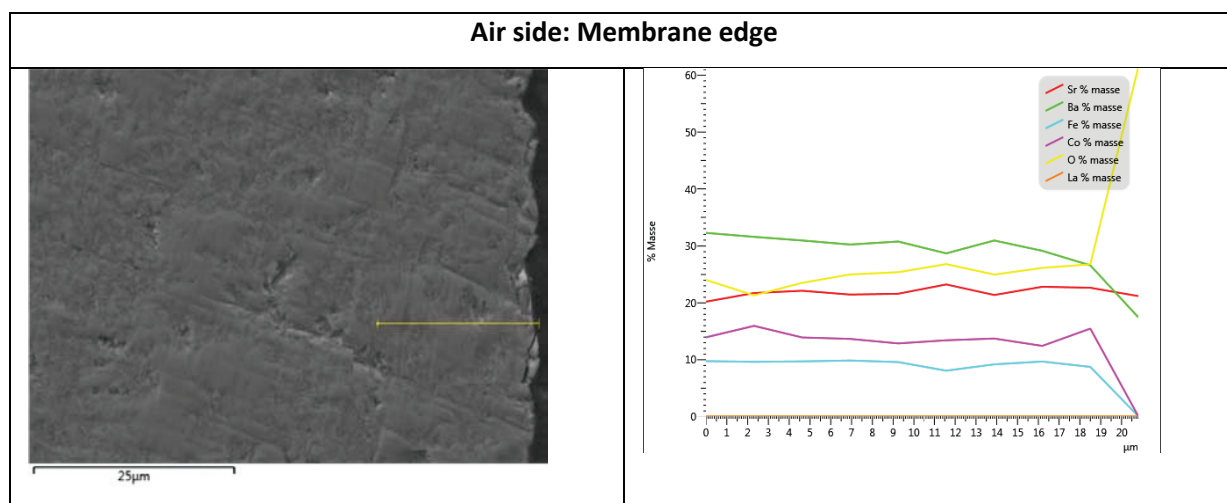


Figure 114 Membrane edge on the air side after two months of testing (x1000)

On the reaction side, the conclusions are the same (Figure 115). Despite the loss of catalyst on the membrane, a very thin layer seems to strongly stick on the membrane. And contrary to the dense membrane, no cobalt oxide has been found and the membrane seems homogeneous.

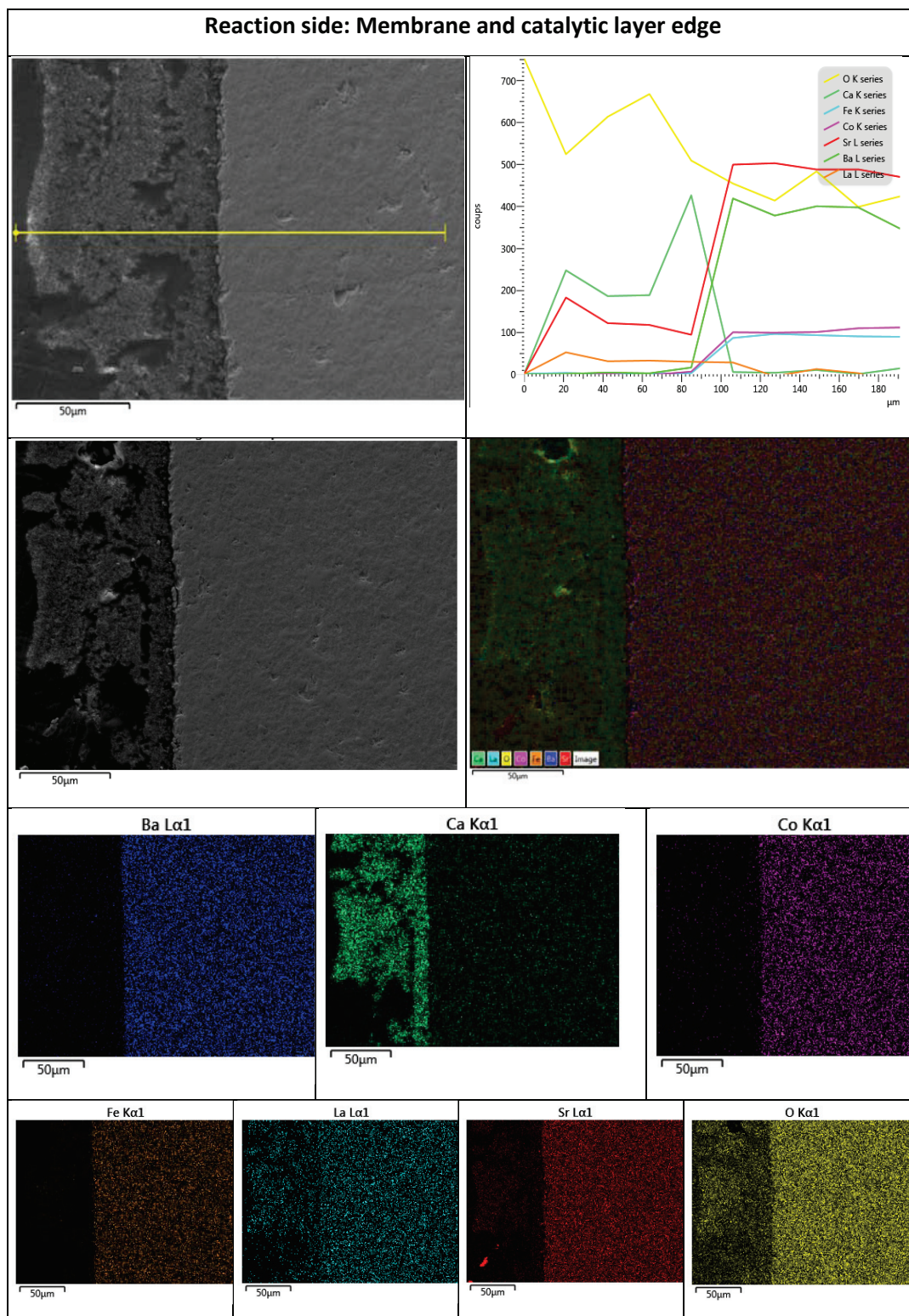


Figure 115 Membrane with catalytic layer look on the edge on the reaction side (x500)

### III.4. Discussion

The addition of a lanthanum based catalyst on the surface of the dense membrane leads to an increase of the activity and a slight increase of the  $C_2$  selectivity. The maximum methane conversion reaches 85% while the maximum  $C_2$  selectivity is of 30%. Contrary to bare BSCF membrane, the oxygen is most of the time fully consumed especially at high methane conversion (Figure 116).

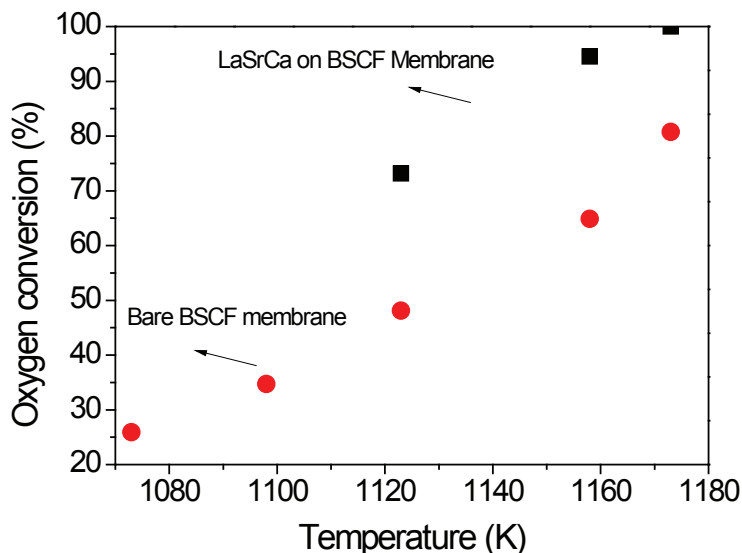


Figure 116 Oxygen conversion as a function of the temperature with a total flow rate of  $200 \text{ ml min}^{-1}$  on both side of the membrane and  $P'O_2 = 21 \text{ kPa}$  and  $PCH_4 = 4 \text{ kPa}$  for a bare BSCF membrane (●), and a BSCF membrane with a catalytic coating of 50 mg of LaSrCa (■).

About the effect of process parameters, the results are in line with the bare BSCF membrane. We can sort the parameters by increasing order of significance. The partial pressure of oxygen in the air side has a slight impact on the OCM results. The flow rate in the reaction side (i. e. the residence time) has a stronger impact. The highest methane conversion and  $C_2$  yield are obtained for a long residence time, higher than 4 s (in our case, this correspond to a flow rate about  $50 \text{ ml min}^{-1}$ ). In the same time, the best  $C_2$  selectivity is obtained for a residence time around 1 s (about  $200 \text{ ml min}^{-1}$ ). Obviously, the temperature has the strongest impact since it plays a major role in the transport of oxygen through the membrane, the activation of the substrates and also the reactions which occur in the gas phase.

BSCF membrane is slightly active and selective for the oxidative coupling of methane. A catalytic layer has then been added on the surface of the membrane in order to improve the selectivity. The two chosen catalysts show opposite trends in terms of conversion-selectivity pattern. First of all, the addition of a based tungsten catalyst leads to a drop of the oxygen flux across the membrane while the addition of lanthanum based catalyst hardly affects the oxygen flux. Looking at the methane

conversion (Figure 117), the conversion is 4 times higher for lanthanum based catalyst than for bare BSCF membrane and BSCF coated with tungsten based catalyst. The  $C_2$  selectivity is higher with an addition of a catalyst layer, slightly higher for lanthanum based catalyst and much higher, up to 3 times higher, for tungsten based catalyst. Thus, the addition of a catalyst leads to an increase of the  $C_2$  yield. However, even with the addition of a catalytic layer, the minimum specifications for industrial perspectives are not achieved.

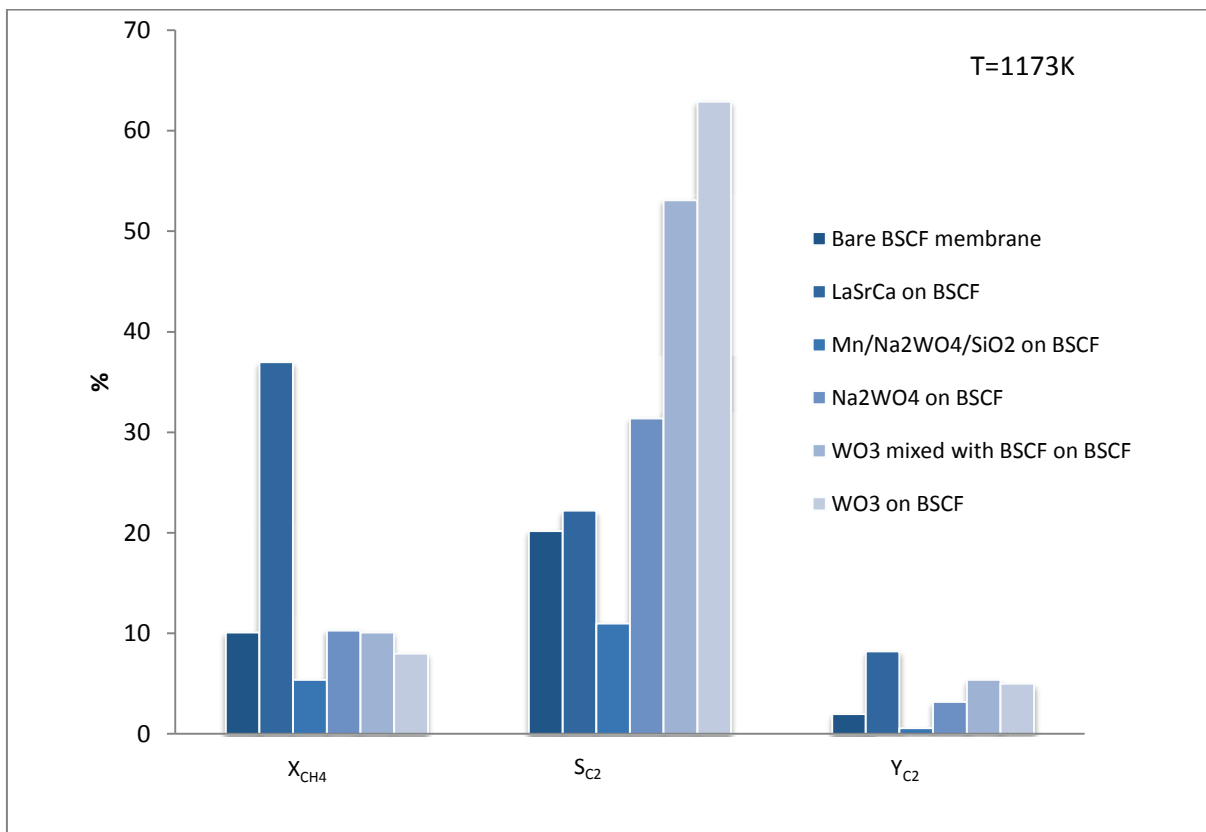


Figure 117  $C_2$  Selectivity and Yield for bare BSCF membrane and coated membranes at 1173K with a flow rate of 200 ml  $min^{-1}$  on both side of the membrane, 21% of  $O_2/N_2$  and 4% of  $CH_4/He$

All the experimental results on bare BSCF membrane and membrane coated with LaSrCa can be plotted in one graph as a function of the ratio of methane on oxygen (Figure 118). A general trend is found for methane conversion, ethane/ethylene selectivity and so ethane/ethylene yield. In both case, the highest methane conversion is obtained for the lowest methane to oxygen ratio, while the highest yield is obtained for the highest methane to oxygen ratio.

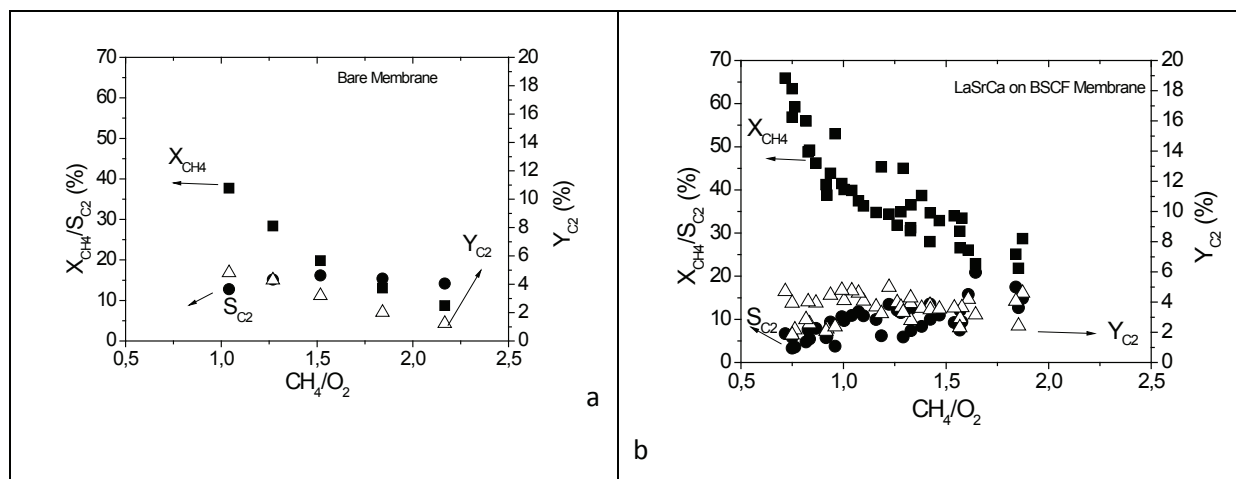


Figure 118 Summary of all tested conditions  $\text{CH}_4$  conversion (■);  $\text{C}_2$  selectivity (●) and  $\text{C}_2$  yield (Δ) as a function of the ratio  $\text{CH}_4/\text{O}_2$  : for bare BSCF (a) and BSCF with LaSr/CaO catalyst (b)

Besides the wide range of tested values, the selectivity in  $\text{C}_2$  remains lower than 20% and the yield lower than 6%. The optimization of the experimental conditions is not sufficient in order to obtain a viable industrial process. The reactor design does not allow any improvement of the selectivity in  $\text{C}_2$ . Serres showed that the conversion of methane and the selectivity in  $\text{C}_2$  depend on the ratio gas volume, surface of the catalyst. In our case, the volume of the gas may be too large as a comparison of the surface of the catalyst. The use of a thicker layer of catalyst leads to a drop in selectivity and therefore cannot be an appropriate solution. A possible solution would be to use a larger reactor surface keeping a thin layer for same volume.

Moreover the contact time is also a key factor. The contact time cannot be estimate in the case of the planar membrane reactor due to its design, but a quick estimation confirms that is much lower than the residence time. As a consequence, a solution would be to use a new design of reactor such as a tubular reactor, which increases the ratio contact time on residence time. Moreover this geometry of reactor allows a better control of the gas phase volume as a comparison of the surface of the catalytic coating (Figure 119).

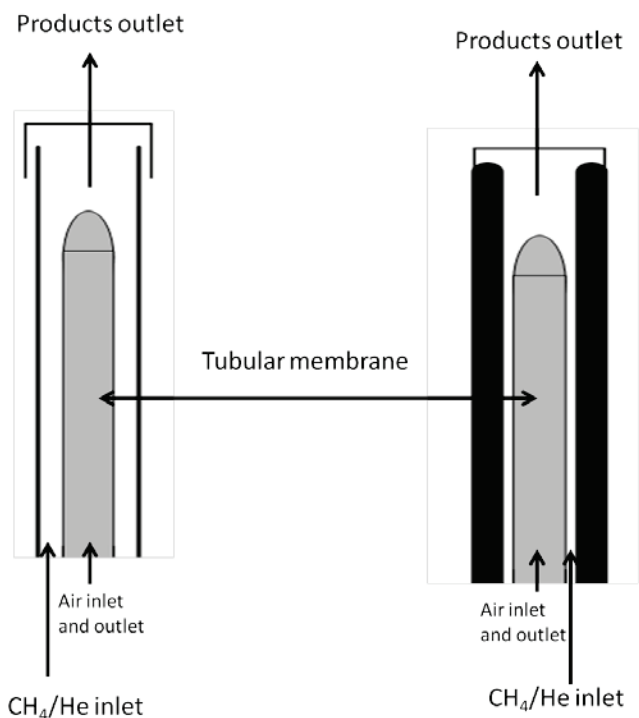


Figure 119 New reactor design with various volume of the gas phase in the reactor side

## IV. CONCLUSIONS

Bare BSCF membrane is active for the OCM reaction but not selective enough. A maximum of methane conversion (40%) is reached when  $C_2$  selectivity is minimal equal to 10%. The maximum selectivity 15% is reached for a minimal methane conversion of 10%. The yield of  $C_2$  doesn't overstep 6%.

The addition of a thin layer of catalyst leads to a great increase of the  $C_2$  selectivity for tungsten based catalyst but to a loss of activity. The final  $C_2$  yield remains very low. About the lanthanum based catalyst, the maximal conversion of methane (70%) is reached for a minimal  $C_2$  selectivity of 10%. As well the maximal  $C_2$  selectivity (20%) is reached for a methane conversion of 20%. Despite of the improvement due to the catalytic loading, the  $C_2$  yield stays very low. The increase of the loading of the catalyst leads to a loss of activity.

The modification of the experimental conditions parameters is not sufficient to reach a high  $C_2$  selectivity and a good conversion. The volume should be decrease as a comparison to the surface area. The design a new tubular reactor would allow this improvement and the ratio volume of the gas phase as a comparison of the surface of the catalyst would be controllable.

# Bibliography

1. P. Zeng, Z. Chen, W. Zhou, H. Gu, Z. Shao and S. Liu, *J. Memb. Sci.*, 2007, **291**, 148–156.
2. H. Wang, Y. Cong and W. Yang, *Catal. Today*, 2005, **104**, 160–167.
3. Z. Taheri, K. Nazari, A. A. Safekordi and N. Seyed-matin, *J. Mol. Catal. A Chem.*, 2008, **286**, 79–86.
4. M. Rebeilleau-Dassonneville, S. Rosini, a. C. Van Veen, D. Farrusseng and C. Mirodatos, *Catal. Today*, 2005, **104**, 131–137.
5. A. C. van Veen, M. Rebeilleau, D. Farrusseng and C. Mirodatos, *Chem. Commun. (Camb)*., 2003, **33**, 32–3.
6. Q. Chen, J. H. B. J. Hoebink and G. B. Marin, *Ind. Eng. Chem. Res.*, 1991, **30**, 2088–2097.
7. J. Sun, J. Thybaut and G. Marin, *Catal. Today*, 2008, **137**, 90–102.
8. T. Ito, J. Wang, C. H. Lin and Lun, *J. Am. Chem. Soc.*, 1985, **18**, p5062–5068.
9. L. M. Aparicio, S. A. Rossini, D. G. Sanfilippo, J. E. Rekoske, A. A. Treviio and J. A. Dumesic, *Ind. Eng. Chem. Res.*, 1991, **30**, 2114–2123.
10. J. G. McCarty, in *Methane Conversion by Oxidative processes*, Springer Netherlands, New York, E.E. Wolf., 1992, pp. 320–350.
11. S. C. Reyes, E. Iglesia and C. P. Kelkar, *Chem. Eng. Sci.*, 1993, **48**, 2643–2661.
12. O. V. Krylov, in *Kinetics and Catalysis*, 1993, p. 250.
13. P. J. Gellings and H. J. M. Bouwmeester, *Catal. Today*, 2000, **58**, 1–53.
14. E. Bordes, *Surf. Chem. Catal.*, 2000, **3**, 725– 733.
15. J. H. White, E. A. Needham, R. L. Cook and A. F. Sammells, *Solid State Ionics*, 1992, **53-56**, 149–161.
16. A. Bielanski and J. Haber, *Oxygen in Catalysis*, New York, M. Dekker., 1991.
17. J. C. Vedrine, *Top. Catal.*, 2002, **21**, 97–106.
18. D. Creaser and B. Andersson, *Appl. Catal. A Gen.*, 1996, **141**, 131–152.
19. D. Creaser, B. Andersson, R. R. Hudgins and P. L. Silveston, 1999, **269**, 264–269.
20. L. Mleczko and M. Baerns, *Fuel Process. Technol.*, 1995, **42**, 217–248.

21. J. H. Park, J. P. Kim, H. T. Kwon and J. Kim, *DES*, 2008, **233**, 73–81.
22. Z. Shao, W. Yang, Y. Cong, H. Dong, J. Tong and G. Xiong, *J. Memb. Sci.*, 2000, **172**, 177–188.
23. Z. Shao, W. Yang, Y. Cong, H. Dong, J. Tong and G. Xiong, *J. Memb. Sci.*, 2000, **172**, 177–188.
24. S. Engels, T. Markus, M. Modigell and L. Singheiser, *J. Memb. Sci.*, 2011, **370**, 58–69.
25. M. Arnold, H. Wang and A. Feldhoff, *J. Memb. Sci.*, 2007, **293**, 44–52.
26. Q. Zhen, Q. Yun, H. Wang, C. Ding, W. Ding and X. Lu, *Solid State Ionics*, 2011, **189**, 50–55.
27. M. Arnold, H. Wang and A. Feldhoff, *J. Memb. Sci.*, 2007, **293**, 44–52.
28. X. P. Fang, S. . Li, J. Z. Lin and Y. L. Chu, *J. Mol. Catal.*, 1992, **6**, 427–433.
29. X. P. Fang, S. . Li, J. Z. Lin, J. F. Gu and D. X. Yan, *J. Mol. Catal.*, 1992, **6**, 255–262.
30. H. S. Chen, J. . Nui, B. Zhang and S. B. Li, *Acta Physico-Chimica Sin.*, 2001, **17**, 111–115.
31. T. Serres, University of Lyon 1, 2013.
32. P. . Couwenberg, Technische Universiteit Eindhoven, 1995.
33. Q. Chen, P. M. Couwenberg and G. B. Marin, *Catal. Today*, 1994, **21**, 309–319.
34. J. W. Thybaut, J. Sun, L. Olivier, A. C. Van Veen, C. Mirodatos and G. B. Marin, *Catal. Today*, 2011, **159**, 29–36.
35. V. I. Alexiadis, J. W. Thybaut, P. N. Kechagiopoulos, M. Chaar, A. C. Van Veen, M. Muhler and G. B. Marin, *Appl. Catal. B Environ.*, 2014, **150-151**, 496–505.
36. S. Baumann, J. M. Serra, M. P. Lobera, S. Escolástico, F. Schulze-Küppers and W. a. Meulenbergh, *J. Memb. Sci.*, 2011, **377**, 198–205.



# Conclusions & Perspectives

---

The semi permeability of oxygen in an OTM membrane is generally too low to expect the industrialisation of oxygen separation membranes or membrane reactors. For the OCM, a minimum flux of  $10 \text{ ml min}^{-1}\text{cm}^{-2}$  is expected with a target of  $50 \text{ ml min}^{-1}\text{cm}^{-2}$ . With the exception of BSCF which shows promising fluxes, others materials exhibit fluxes of one to several orders of magnitude lower. The development of a membrane is carried out by a trial and error approach which is very time consuming and inefficient. The rational design of an OTM membrane based on the measurements of kinetic of elementary steps would accelerate the discovery of new materials and the development of performing membranes.

- Is it possible to determine the kinetic parameters which control oxygen transport in a membrane from experiments carried out on the corresponding powder?

An original method has been developed based on a microkinetic approach for the estimation of the oxygen transport parameters of  $\text{Ba}_{0.5}\text{Sr}_{0.5}\text{Co}_{0.8}\text{Fe}_{0.2}\text{O}_{3-\delta}$  powder. The coupling of two techniques SSITKA and TGA allows the estimation of the forward and reverse kinetic rate, thereby accounting for the oxygen vacancy concentration. In addition, the self-diffusion rate coefficient was estimated at different oxygen partial pressures. In this study, the kinetic parameters were measured in a temperature window between 873 K and 1173 K and under two pressure conditions (21 kPa and 1 kPa) chosen for their appropriateness for simulating the semi-permeability of oxygen in a membrane in a process of oxygen separation from air.

At 21kPa and 1073K, adsorption step is faster than the desorption step only in the case of  $\text{La}_{0.6}\text{Sr}_{0.4}\text{Co}_{0.2}\text{Fe}_{0.8}\text{O}_{3-\delta}$  which can be explained by a low reducibility of this material. Indeed the Langmuir constant giving the ratio between the adsorption and the desorption constant is of  $5.5 \cdot 10^{-2} \text{ Pa}^{-1}$  against  $0.1 \cdot 10^{-2} \text{ Pa}^{-1}$  for  $\text{Ba}_{0.5}\text{Sr}_{0.5}\text{Co}_{0.8}\text{Fe}_{0.2}\text{O}_{3-\delta}$  and  $0.2 \cdot 10^{-2} \text{ Pa}^{-1}$  for  $\text{Ba}_{0.95}\text{La}_{0.05}\text{FeO}_{3-\delta}$ . As for the diffusion,  $\text{Ba}_{0.95}\text{La}_{0.05}\text{FeO}_{3-\delta}$  exhibit the highest diffusion of  $19 \cdot 10^{-7} \text{ cm}^2 \text{ s}^{-1}$  while the value is 4 times lower for  $\text{Ba}_{0.5}\text{Sr}_{0.5}\text{Co}_{0.8}\text{Fe}_{0.2}\text{O}_{3-\delta}$  ( $5.5 \cdot 10^{-7} \text{ cm}^2 \text{ s}^{-1}$ ) and 4 orders of magnitude lower for  $\text{La}_{0.6}\text{Sr}_{0.4}\text{Co}_{0.2}\text{Fe}_{0.8}\text{O}_{3-\delta}$  ( $0.09 \cdot 10^{-7} \text{ cm}^2 \text{ s}^{-1}$ ). The conclusions are the same at lower partial pressure of oxygen. It should be noticed that the adsorption and desorption parameters increase onefold the order of magnitude except for the diffusion parameter in  $\text{Ba}_{0.5}\text{Sr}_{0.5}\text{Co}_{0.8}\text{Fe}_{0.2}\text{O}_{3-\delta}$  and for all the parameters in  $\text{La}_{0.6}\text{Sr}_{0.4}\text{Co}_{0.2}\text{Fe}_{0.8}\text{O}_{3-\delta}$ . Indeed, the low reducibility of  $\text{La}_{0.6}\text{Sr}_{0.4}\text{Co}_{0.2}\text{Fe}_{0.8}\text{O}_{3-\delta}$  leads to an equivalent set of parameters in both conditions.

This novel approach is based on the dependence between the kinetic parameters and the state of oxidation of the mixed oxide material. It has been assumed that the kinetic parameters are strongly dependant on the oxidative state of the materials and new material should be considered. Nevertheless, in the case of low reducible materials, the assumption of Xu/Thomson, based on the conservation of the kinetic parameters on both sides of the membrane is correct and sufficient. A preliminary step should be achieved using TGA in order to determine the reducibility of the materials, then the materials can be classified in two main groups. The first assumption is the oxidative state of the A site in the perovskite ( $ABO_{3-\delta}$ ). The lower the oxidative state it is, the stronger the reducibility of the material will be.

- Is it possible to simulate membrane fluxes from kinetic parameters?

Oxygen fluxes passing through a  $Ba_{0.5}Sr_{0.5}Co_{0.8}Fe_{0.2}O_{3-\delta}$  membrane have been modelled using microkinetic parameters in a flux model without using any fitting on experimental membrane data. The model accounts for different rate constants and diffusion coefficient in agreement with the difference in oxygen gradients in the membrane. The best models assume a constant diffusion parameter on the air side and a rapid evolution  $\phi$  on the sweep side. Nevertheless, the model assuming a linear variation of the diffusion parameters over the thickness well describes the variation of the experimental condition for a thickness of 2mm. The best model properly describes the variation of experimental conditions (temperature and oxygen partial pressure) as well as the variation of membrane thickness.

In contrast to macrokinetic approaches in which the measured rate constants are apparent, microkinetic parameters are intrinsic features of the solids and therefore can be applied to different flux models such as in a fixed bed or in a planar membrane cell (this study). A flux model for dead-end tubular membrane, which is the most appropriate for OCM reaction, has been modelled (not shown in this manuscript).

- What are the limiting steps? In which conditions can very high fluxes be achieved? Is there an alternative membrane composition or design which can compete with BSCF?

The application of this microkinetic modelling approach has been extended to  $La_{0.6}Sr_{0.4}Co_{0.2}Fe_{0.8}O_{3-\delta}$  and  $Ba_{0.95}La_{0.05}FeO_{3-\delta}$ . In the case of material with a low oxygen vacancy concentration, the microkinetic approach yield consistent parameter estimations.

Simulations carried out on thin  $Ba_{0.5}Sr_{0.5}Co_{0.8}Fe_{0.2}O_{3-\delta}$  and  $Ba_{0.95}La_{0.05}FeO_{3-\delta}$  membranes demonstrate that high fluxes can be obtained by increasing the oxygen partial pressure at the feed side. We

believe that combining high feed pressure and a thin membrane is a powerful way to significantly increase oxygen flow in  $\text{Ba}_{0.5}\text{Sr}_{0.5}\text{Co}_{0.8}\text{Fe}_{0.2}\text{O}_{3-\delta}$  and  $\text{Ba}_{0.95}\text{La}_{0.05}\text{FeO}_{3-\delta}$  membranes. However, we recognize that mechanical stability will become an issue at a certain point.

In perspectives, based on the microkinetic methodology it is now possible to screen the potentiality of OTM materials by using SSITKA and TGA measurement on powders. Hence, straightforward measurements on powders shall discriminate candidate materials for further shaping in membrane and testing.

In order to improve the modelling, the evolution of the kinetic parameter as a function of the partial pressure should be studied in order to obtain an empirical trend to link kinetic parameter, partial pressure of oxygen in the gas phase, temperature and quantity of oxygen vacancies on the material surface. If possible, this would largely improve the kinetic parameter estimations in extrapolated conditions. As a consequence, the fluxes will be estimated with higher accuracy for a wider range of experimental conditions.

Moreover using the same approach, a flux that passes through a membrane of different geometry, in which internal and external surfaces are different, can be modelled. In addition to the possibility of integrating microkinetic parameters in various reactor/membrane devices, the microkinetic rate constants remain valid over a larger operational window of temperature and pressure, making it feasible to predict performances for which experimental data can rarely be obtained, such as with ultrathin membranes.

- Does a catalytic coating drive the activity and/or selectivity of the OCM reaction?

The integration of bare BSCF in an OTM reactor shows a high conversion of methane against a poor selectivity in  $\text{C}_2$ . The addition of a catalytic coating leads to an increase of the  $\text{C}_2$  selectivity. The use of a tungsten catalyst allows the enhancement of the  $\text{C}_2$  selectivity from 20% on a bare membrane to 63% when the methane conversion is lowered by 20%. Looking at the Lanthanum based catalyst; the  $\text{C}_2$  selectivity is doubled when the methane conversion is divided by 2. In every condition, the yield in  $\text{C}_2$  could not go over 6% which is far below the initial expectations.

- Which type of membrane reactor should be investigated further?

The integration of  $\text{Ba}_{0.5}\text{Sr}_{0.5}\text{Co}_{0.8}\text{Fe}_{0.2}\text{O}_{3-\delta}$  in an OCM reactor shows no enhancement as a comparison with the literature. A total new design of reactor should be developed. The exchange surface should increase while the volume of the gas phase should be reduced, in order to obtain a lower value of the ratio  $V/S$ . The use of a tubular membrane reactor could be a clue. The flux equation and the

kinetic model of OCM should be integrated in the same model, in order to define the optimal experimental conditions as well as the catalyst coating and thickness. This will allow the enhancement of the current reactor design, as no improvement of the catalyst composition is possible.